

---

Electronic Theses and Dissertations, 2004-2019

---

2014

## Combustion Instability Mechanism of a Reacting Jet in Cross Flow at Gas Turbine Operating Conditions

Jared Pent  
*University of Central Florida*

 Part of the [Mechanical Engineering Commons](#)  
Find similar works at: <https://stars.library.ucf.edu/etd>  
University of Central Florida Libraries <http://library.ucf.edu>

This Doctoral Dissertation (Open Access) is brought to you for free and open access by STARS. It has been accepted for inclusion in Electronic Theses and Dissertations, 2004-2019 by an authorized administrator of STARS. For more information, please contact [STARS@ucf.edu](mailto:STARS@ucf.edu).

---

### STARS Citation

Pent, Jared, "Combustion Instability Mechanism of a Reacting Jet in Cross Flow at Gas Turbine Operating Conditions" (2014). *Electronic Theses and Dissertations, 2004-2019*. 1294.  
<https://stars.library.ucf.edu/etd/1294>

COMBUSTION INSTABILITY MECHANISM OF A  
REACTING JET IN CROSS FLOW AT GAS TURBINE  
OPERATING CONDITIONS

by

JARED MATTHEW PENT  
B.S. University of Central Florida, 2008  
M.S. University of Central Florida, 2009

A dissertation submitted in partial fulfillment of the requirements  
for the degree of Doctor of Philosophy in Mechanical Engineering  
in the Department of Mechanical and Aerospace Engineering  
in the College of Engineering and Computer Science  
at the University of Central Florida  
Orlando, Florida

Summer Term  
2014

Major Professor: Jayanta Kapat

© 2014 Siemens Energy, Inc.

## ABSTRACT

Modern gas turbine designs often include lean premixed combustion in order to meet stringent emission requirements. It is widely known, however, that this type of combustion process is susceptible to self-excited combustion instabilities that can lead to increases in heat loads and system vibrations. As a result, the fundamental behavior of these combustion instabilities must be understood and analyzed so that they can be affectively mitigated in the design process.

This study focuses on the flow phenomena related to an unsteady dump combustor and a reacting jet in cross flow, at typical gas turbine operating conditions. The setup provides a relatively simple combustion system that includes self-excited combustion instabilities as well as multiple reaction zones, a common scenario often seen in combustion design, known as staging technology. One of the key objectives of this study is to analyze and understand the flow physics of a reacting jet in cross flow, with specific focus given to the physical mechanisms that drive or damp the instabilities present in the combustion system due to the reacting jet in cross flow.

A three point stability trend was identified in experimental results from a related study where a reacting jet in cross flow was found to strongly drive a moderately unstable mode in the combustion chamber for one configuration, but strongly damp it for a different configuration. It was clear from the experimental results that the unsteady heat release from the JICF was coupling with the pressure waves present in the combustion chamber to either drive the baseline dump combustor mode to a significantly higher unstable point, or damp the baseline dump combustor mode to a nearly stable condition. These stability trends were used as validation data

for a set of self-excited Large Eddy Simulations of the reacting jet in cross flow, with the goal of obtaining an understanding of the physics governing the thermoacoustic stability of this combustion scenario.

The self-excited Large Eddy Simulations, run using the OpenFOAM open source toolbox, were utilized to provide a numerical modeling tool where combustion instabilities are generated solely from the interaction between heat release and acoustics, just as they are in the actual systems being studied. Both head end only configurations and multiple jet in cross flow configurations were run and validated with experimental results. Reduced order acoustic models of the combustion system were also developed and compared with both experimental and numerical results to further validate a hypothesized mechanism of combustion instability for the reacting jet in cross flow.

It was found that the self-excited Large Eddy Simulation methods applied in this study could correctly replicate the stability trends observed in the experiment when appropriate tuning of the combustion model was applied to account for differences in the reaction behavior of a co-flow jet as compared to a reacting jet in cross flow. The need for this tuning would likely be eliminated with the application of a more advanced combustion model. It was found that the frequencies of the dominant modes were captured well with the simulations, however, significant under-prediction occurred in the limit cycle amplitude, attributed to unphysical transmission of the waves at the inlet boundaries.

From an investigation of the natural coherent structures of the reacting jet in cross flow, it was found that these structures occurred at frequencies too high to result in any feedback cycle with the pressure and heat release oscillations that generated combustion instabilities at the

frequencies of interest in this study of less than 500 Hz. By observing experimental and numerical flame behavior, a strong pulsing of the jet was identified to occur at the unstable frequency of interest when the jet was driving the baseline instability present in the combustion chamber. Thus, a mechanism was proposed that included a mass flow fluctuation of reactants as well as an equivalence ratio fluctuation of the mixture that resulted from the pressure oscillations present in the combustion chamber at the point of injection. Time lags were identified from the Large Eddy Simulations and implemented into a 3D thermoacoustic modeling tool as a “jet impedance time lag” and a “flame time lag”. The jet impedance is simply a function of the acoustic properties of the geometry while the flame time lag can be separated into jet velocity, equivalence ratio, and strain fluctuations, depending on the operating conditions and setup. For the specific gas turbine application investigated in this study, it was found that the jet velocity and equivalence ratio fluctuations were important, however, the effect of the strain fluctuations on the heat release were minimal due to the high operating pressure.

The stability trends observed in the experiments were also replicated with the 3D thermoacoustic modeling tool, using a derived heat release model based on the proposed mechanism of instability as a function of the velocity and pressure oscillations present in the system. Using a detailed heat release model that included terms for both the jet velocity and equivalence ratio fluctuations of the jet in cross flow, it was found that the jet velocity fluctuations contributed to damping of the system, while the equivalence ratio fluctuations contributed to driving of the system. A Generalized Instability Model was also used to generate stability maps that demonstrated how a stable system could be achieved based on the two design

parameters of the reacting jet in cross flow that were identified – the jet impedance and the overall flame time lag.

By appropriately utilizing the tools and methodologies presented in this study, a fundamental understanding of some of the key mechanisms of combustion instability in a system with a reacting jet in cross flow was achieved. Using available tools and open source software, methods were developed to model the thermoacoustic behavior of a reacting jet in cross flow that can be further extended to full engine style designs. Limitations of the existing tools were highlighted and recommendations were given on areas where the tools should be improved, mostly in the area of combustion modeling.

In modern gas turbine design, there are two general ways to mitigate the combustion instabilities that arise due to the lean premixed combustion process. The first and simplest way to mitigate these instabilities is through combustion tuning. The more robust and significantly more difficult way is to develop and implement design changes that mitigate the instabilities, without resulting in a detriment to the emissions benefits of lean premixed combustion. This study provides a fundamental understanding of a key feature in combustion design that can provide the information necessary to design for further mitigation of the combustion instabilities that are present in most of the combustion devices used in modern energy and propulsion systems.

To my dear Stef, for being my sure and steady companion and making it a precious respite to come home every day.

*“The race is not to the swift, nor the battle to the strong, nor bread to the wise, nor riches to the intelligent, nor favor to those with knowledge, but time and chance happen to them all.” Ecclesiastes 9:11*

SOLI DEO GLORIA



## ACKNOWLEDGMENTS

I would like to thank my academic advisor and Doctoral Committee Chair, Dr. Jay Kapat, for your dedicated guidance and assistance throughout the past five years of my graduate career at UCF. Your extensive knowledge in the energy field, your challenging courses in heat transfer and turbulence, and your patient mentoring throughout the years has provided me with a rewarding graduate education.

Thank you to my technical advisor, Dr. Enrique Portillo, for providing me with the opportunity to pursue a Ph.D. internship at Siemens and for your invaluable technical and professional guidance throughout my doctoral studies. Thank you for taking a sincere interest in my academic development and for investing countless hours out of your busy schedule towards my success as a student and engineer.

I would like to thank Dr. Weiwei Deng, Dr. Ali Gordon, Dr. Subith Vasu, and Dr. Scott Martin for your willingness to serve as members of my Doctoral Committee. In addition, I would like to thank Dr. Deng and Dr. Gordon for your academically challenging and relevant courses in fluid dynamics, solid mechanics, and machine design. Thank you to Dr. Martin for your unique and engaging approach in teaching the topic of compressible flow and for taking the time to provide detailed technical assistance both during and after your time at UCF and Siemens.

Thanks to the many engineers in the Combustion and Technology groups at Siemens Energy, Inc. that I have had the pleasure of working with over the past four years. Specifically, thank you to Dr. Rajesh Rajaram for not only taking a special interest in my academic and

professional career and for your valuable technical assistance that I could always rely on, but also for your thoughtfulness and support in my personal life as well. Thank you to Richard Valdes for sharing your decades of experience in the CFD world and for your ability to encourage those with less experience by taking a sincere interest in our individual studies. Thank you to Dr. Ray Laster and Dr. Vinayak Barve for your leadership in my professional career and for your wealth of experience and knowledge that I have greatly benefited from. Thank you to Dr. Cliff Johnson for your guidance in my professional career and for allowing me the opportunity to begin a full time career as a Combustion Engineer while completing my doctoral studies.

This work was greatly enhanced through many hours of discussions with Perry Johnson and Stefan Dederichs. Thank you Perry and Stefan for taking the time out of your already full research schedules to give me the opportunity to discuss my own studies with you, and for taking a sincere interest in providing feedback and assistance at so many levels. Without your invaluable comradery, this work may never have been completed.

I would like to acknowledge the University of Central Florida Stokes Advanced Research Computing Center for providing computational resources and support that have contributed to results reported in this study. Specifically, I would like to thank Dr. Sergio Tafur and Dr. Craig Finch for their assistance throughout the nearly 1.5 million computational hours utilized to complete this work.

## TABLE OF CONTENTS

LIST OF FIGURES .....	xiii
LIST OF TABLES .....	xxiii
NOMENCLATURE .....	xxiv
CHAPTER 1 – INTRODUCTION .....	1
Background of the problem.....	1
Overview of combustion instabilities.....	5
Objectives of the Current Study.....	7
CHAPTER 2 – LITERATURE REVIEW .....	11
Flow Physics of a Jet in Cross Flow .....	11
Thermoacoustics of Dump Combustors.....	19
Self-Excited LES of Combustion Instabilities .....	26
CHAPTER 3 – METHODOLOGY .....	42
Overview of Proposed Tools and Methods.....	42
Background of OpenFOAM.....	43
Background of LES.....	43
Background of Combustion Modeling.....	48
Implementation of strain and heat loss models.....	51
Numerical Procedure.....	57
Computational resources .....	59
Computational domain and meshing.....	59
Boundary Conditions .....	65
Head End and JICF Inlets .....	65
Exit.....	67
Walls .....	68
Monitor Points and Outputs .....	69
Validation with experimental results .....	71
Selection of Validation Cases from Experiment.....	74
Comparison to Thermoacoustic Modeling.....	83
3D Thermoacoustic Solver .....	83

Generalized Instability Model.....	84
CHAPTER 4 – RESULTS .....	89
RANS Head End Only Simulations .....	89
LES Head End Only Simulations.....	92
LES Head End with Jet in Cross Flow Simulations.....	102
Selection of the best fit combustion model.....	102
Qualitative combustion model tuning for Reacting Jet in Cross Flow .....	108
Dynamic Pressure Results.....	111
Rayleigh Index calculations .....	114
CHAPTER 5 – FLOW PHYSICS AND ACOUSTIC MODELING.....	118
Development of Mechanism Hypothesis .....	118
Investigation of jet in cross flow coherent structures .....	118
Proposed Mechanism of Instability.....	122
Derivation of a Heat Release Model .....	130
Application to Acoustic Modeling.....	134
Basic Heat Release Model .....	136
Detailed Heat Release Model.....	139
Generalized Instability Model.....	147
CHAPTER 6 – CONCLUSIONS AND RECOMMENDATIONS .....	151
Summary and Conclusions.....	151
Recommendations for Future Work.....	157
APPENDIX A – LESSONS LEARNED .....	160
Analysis of Computational Domain Boundaries .....	161
Reflection coefficient calculations.....	161
Boundary losses due to jet in cross flow geometry.....	171
Effect of Choked Area on Chamber Pressure .....	173
Effect of Combustion Model Tuning Parameter .....	175
Understanding the Impact of Mesh Effects.....	181
Mesh resolution.....	181
Ox-post refinement .....	186
Numerical damping of rhoPisoFoam solver .....	187
Effect of off-centering coefficient in the temporal discretization.....	189

Effect of Spatial Discretization Scheme .....	197
Asymmetric head end behavior.....	199
APPENDIX B – PRE AND POST PROCESSING METHODS .....	204
Calculating time lag information from simulations .....	205
Calculation of three-dimensional Rayleigh Index fields.....	211
Modeling the jet in cross flow fuel nozzle .....	212
APPENDIX C – DERIVATION OF HEAT RELEASE MODEL WITH STRAIN TERM.....	219
LIST OF REFERENCES .....	228

## LIST OF FIGURES

Figure 1: Siemens SGT5-8000H Gas Turbine (1-Inlet, 2-Compressor, 3-Combustion Chamber, 4-Turbine, 5-Exhaust) (Siemens, 2011).....	2
Figure 2: Competing behavior of emissions and dynamics with effects of tuning and design .....	3
Figure 3: Feedback cycle for combustion instabilities .....	5
Figure 4: Purdue Acoustic Rig (Fugger, 2011).....	9
Figure 5: Dominant flow and vortical structures associated with a jet in cross flow (Karagozian, 2010).....	11
Figure 6: Chemiluminescence data from a CH <sub>4</sub> reacting jet flame (Noble, 2011) .....	14
Figure 7: Phase-locked averaged jet dispersion patterns for 6 different cross flow configurations (Lam, 2004).....	16
Figure 8: Flow visualization from experiments of a jet injected into a steady (left) and unsteady (center, right) cross flow (Blossey, 2002).....	17
Figure 9: Contours of mean axial velocity, comparing non-reacting to reacting flow ( $\phi=0.65$ ) through a sudden expansion (Ahmed, 1992) .....	21
Figure 10: Schematic of vortex structure at the rearward facing step of a dump combustor (Schadow, 1991) .....	22
Figure 11: Interaction and roll up of vortices at a sudden expansion (Schadow, 1991).....	23
Figure 12: Plot of Rayleigh index criterion vs. combustor length (Sterling, 1987).....	25
Figure 13: Computational domain for self-excited study performed by Roux (Roux, 2010).....	28
Figure 14: Pressure spectra for two chemical schemes used by Roux (Roux, 2010) .....	29
Figure 15: Computation domain of the sector rig studied by Wolf (Wolf, 2009) .....	31

Figure 16: Pressure and temperature fluctuation levels found by Wolf (Wolf, 2009) .....	32
Figure 17: Computational domain and boundary conditions used by Roux (Roux, 2005) .....	33
Figure 18: Instantaneous temperature and pressure field solved by Staffelbach (Staffelbach, 2009).....	35
Figure 19: Computational grid used by Xia (Xia, 2011) .....	37
Figure 20: Rayleigh index from coarse grid and fine grid cases (Xia, 2011).....	38
Figure 21: PSD's of pressure traces from single step and multi-step reaction cases (Xia, 2011)	39
Figure 22: Computational domain and boundary conditions used by Lorstad (Lorstad, 2010) ...	40
Figure 23: Turbulence energy spectrum as a function of wavenumber, representing typical approaches to numerical modeling (Poinsot, 2005).....	45
Figure 24: Cantera 1D counterflow data without heat loss ( $\beta=1.0$ ) and with heat loss ( $\beta=0.92$ ), compared to Tay's model (Tay, 2009) with fitted Markstein number. ....	53
Figure 25: Normalized unstrained laminar flame speed as a function of the heat loss coefficient, taken from 1D premixed flame simulations run using Cantera and the GRI3.0 mechanism at 8bar. ....	55
Figure 26: Schematic of the PISO algorithm in a Finite Volume Code .....	58
Figure 27: Dimensions of CAD geometry used for meshing .....	61
Figure 28: Entire mesh for head end only model (flow in z direction).....	63
Figure 29: Mesh refinement at the dump plane (flow in z direction).....	63
Figure 30: Mesh at the exit nozzle (flow in z direction).....	64
Figure 31: Mesh at JICF region (cross flow in z direction, jet flow in negative y direction).....	64
Figure 32: Monitor point locations in chamber (baseline).....	70

Figure 33: Representative plot showing the energy gains and losses in a system versus the limit cycle amplitude .....	73
Figure 34: Dimensions of baseline HE only geometry, inlet and outlet are choked (moderately unstable).....	75
Figure 35: Dimensions of JICF1 geometry, inlets and outlet are choked (very unstable).....	76
Figure 36: Dimensions of JICF2 geometry, inlets and outlet are choked (stable).....	77
Figure 37: Dynamic pressure spectra from experimental pressure measurements for the three cases investigated in this study. ....	78
Figure 38: Normalized pressure amplitude measured from experiment for HE only, JICF1, and JICF 2 configurations at varying HE equivalence ratios. Note that the JICF points include additional variation in the jet equivalence ratio. ....	80
Figure 39: Dynamic pressure trace over one complete test cycle.....	81
Figure 40: Pressure spectrum comparing JICF1 fired operation to purge operation. Spectrum from HE only operation (no JICF geometry) included for reference. ....	82
Figure 41: Pressure mode shapes solved from analytical model. (Bold lines represent the axial locations of the dump plane and JICF) .....	87
Figure 42: RANS solutions for reaction progress variable at dump plane and Mach number at exit nozzle (used as initial conditions to LES simulations) .....	90
Figure 43: Pressure and Temperature from RANS simulation.....	91
Figure 44: Initial transient pressure trace from head end simulation.....	93
Figure 45: Head end simulation raw pressure trace compared to corresponding experimental pressure transducer, sampled at 1800 Hz (PT-TA-08) .....	94



Figure 46: Spectral data from experiment and baseline head end simulation, taken from 0.3 seconds of data from PT-TA-08 .....	95
Figure 47: 2L mode shapes from experimental and simulation data, calculated from raw pressure data filtered at 190 Hz.....	98
Figure 48: 4L mode shapes from experimental and simulation data, calculated from raw pressure data filtered at 400 Hz.....	99
Figure 49: 2L mode shape from simulation pressure field data, calculated using 3D DFT, filtered at 192 Hz.....	100
Figure 50: 4L mode shape from simulation pressure field data, calculated using 3D DFT, filtered at 385 Hz.....	101
Figure 51: Mean normalized CH* chemiluminescence intensity of JICF flame from Test 191343 on 01/24/2013 using JICF2 configuration. White line represents Holdeman scalar trajectory for a non-reacting JICF.....	104
Figure 52: Normalized heat release contours from LES simulations with strain model off (left), strain model on (middle), and strain and heat loss models on (right). White corresponds to maximum heat release, black corresponds to zero heat release. Black or grey isolines represent reaction progress variable of 0.1, white line represents Holdeman trajectory for a non-reacting JICF.....	105
Figure 53: Normalized 1D plots of CH* intensity (EXP) and heat release (LES) .....	106
Figure 54: Normalized heat release contours from simulations with strain model for varying combustion model constants. White corresponds to maximum heat release, black corresponds to zero heat release. Dark isolines represent reaction progress variable of 0.1, white line represents Holdeman trajectory for a non-reacting JICF. ....	109

Figure 55: Normalized 1D plots of CH* intensity (EXP) and heat release (LES) for varying combustion model constants. ....	110
Figure 56: Dynamic spectrum for unstable (JICF1) and stable (JICF2) configurations.....	111
Figure 57: Representative filtered signals from experiment and simulation for unstable (JICF1) and stable (JICF2) configurations. ....	112
Figure 58: Representative filtered signal from LES simulations for unstable (JICF1) and stable (JICF2) configurations. ....	113
Figure 59: Normalized Rayleigh Index contours for unstable (JICF1) and stable (JICF2) cases, white line represents Holdeman trajectory for a non-reacting JICF. ....	114
Figure 60: Normalized Rayleigh's Index contours of Test 174826 on 08/18/2011 using JICF1 configuration, calculated using a POD technique. White line represents Holdeman trajectory for a non-reacting JICF. ....	116
Figure 61: Instantaneous contours of mixture fraction used to measure the physical distance between vortices in the jet shear layer. ....	120
Figure 62: FRF of preliminary LES simulation, showing the Helmholtz resonator behavior of the JICF geometry.....	121
Figure 63: 200Hz acoustic pressure mode shape distributed along JICF2 geometry. ....	123
Figure 64: Instantaneous pressure contours in the JICF region over one cycle of oscillation (timestep is 1/20 <sup>th</sup> of a period, red=max, blue=min, approximate range = 815,000 to 830,000 Pa). ....	124
Figure 65: Instantaneous Y-velocity contours in the JICF region over one cycle of oscillation (timestep is 1/20 <sup>th</sup> of a period, red=max, blue=min, approximate range = -70 to 30 m/s). ....	124

Figure 66: Instantaneous mixture fraction contours in the JICF region over one cycle of oscillation (timestep is $1/20^{\text{th}}$ of a period, red=max, blue=min, approximate range = 0 to $0.05 \text{ kg}_{\text{fuel}}/\text{kg}_{\text{mixture}}$ ).....	125
Figure 67: Instantaneous heat release contours in the JICF region over one cycle of oscillation (timestep is $1/20^{\text{th}}$ of a period, red=max, blue=min, approximate range = 0 to $100 \text{ kg}_{\text{fuel}}/\text{m}^3\text{s}$ ). 125	
Figure 68: Schematic representing the proposed mechanism with effective time lags. ....	127
Figure 69: Time lags calculated from self-excited LES simulations for unstable (JICF1) and stable (JICF2) cases, shown on a pressure-heat release stability map.....	129
Figure 70: Regions defined for heat release derivation. ....	131
Figure 71: Filtered acoustic pressure signals for baseline JICF1 and JICF2 cases from TA3D, no JICF heat release model. ....	135
Figure 72: Sender and receiver regions for basic TA3D heat release model for the JICF .....	137
Figure 73: Filtered acoustic pressure signals for JICF1 and JICF2 cases from TA3D, with basic JICF heat release model (note the different axes for clarity).....	138
Figure 74: Sender and receiver regions used for detailed JICF heat release modeling in TA3D. ....	144
Figure 75: Filtered acoustic pressure signals for JICF1 and JICF2 cases from TA3D, with detailed JICF heat release model. ....	145
Figure 76: Summary of experimental data and TA3D results with detailed JICF heat release model.....	147
Figure 77: Schematic representation of the GIM model with the location of the applied heat release model shown relative to the 200 and 400 Hz pressure mode shapes.....	148

Figure 78: Normalized growth rate for 200 and 400 Hz modes using a 1D linear heat release model in GIM. Red and green points represent the JICF1 and JICF2 configurations, respectively, as calculated from SELES. Black lines represent stability boundaries. ....	149
Figure 79: Experimental spectrum comparing the first two dominant modes in the HE only, JICF1, and JICF2 configurations. ....	150
Figure 80: Schematic of two-microphone method setup applied to computational domain boundary analysis. ....	162
Figure 81: Domain used for inlet boundary reflection calculations .....	162
Figure 82: Calculated magnitude and phase of reflection coefficient for inlet boundary .....	163
Figure 83: Representative pressure spectra for the head end only simulation with a constant velocity inlet boundary condition .....	164
Figure 84: Domain used for transonic inlet boundary calculations, colored by temporal mean Mach number .....	167
Figure 85: Calculated magnitude and phase of reflection coefficient for all inlet boundary configurations tested .....	167
Figure 86: Representative pressure spectra for the head end only simulation comparing the standard inlet to a transonic inlet for various temporal discretization off-centering coefficients. ....	168
Figure 87: Domain used for exit boundary calculations, colored by Mach number. Black line represents isoline of Mach = 1.0 .....	169
Figure 88: Calculated magnitude and phase of reflection coefficient for exit boundary.....	170
Figure 89: HE only and JICF1 network models used one-dimensional transfer matrix code to quantify boundary damping .....	171

Figure 90: Relative damping coefficient at 200 and 400 Hz for HE only and JICF1 one-dimensional models. rhoPisoFoam numerical damping included for reference.....	172
Figure 91: Comparison of choked area between long and short expansion section. Black line represents isoline of Mach=1.0.....	174
Figure 92: Representative pressure traces for short nozzle case, compared to experimental pressure.....	175
Figure 93: Clip plane through primary flame for four values of $A$ , colored by instantaneous reaction progress variable.....	177
Figure 94: Mean heat release profiles for varying $A$ factors.....	178
Figure 95: Axial location of mean heat release profiles with respect to 1L, 2L, and 4L acoustic pressure modes shapes.....	179
Figure 96: Representative pressure spectrum for minimum and maximum $A$ factor cases.....	180
Figure 97: Coarse mesh YZ and XZ clip planes colored by mean reaction progress variable, representing the mean flame shape at the dump plane. Black isoline at $b_{Mean} = 0.5$ .....	182
Figure 98: Fine mesh YZ and XZ clip planes colored by mean reaction progress variable, representing the mean flame shape at the dump plane. Black isoline at $b_{Mean} = 0.5$ .....	183
Figure 99: Representative pressure spectrum for mesh resolution study (Note that this data was taken from only 0.25 seconds of raw pressure data, compared to the standard 0.3 seconds of data used in other figures throughout this document).....	185
Figure 100: Ox-post mesh refinement levels.....	186
Figure 101: Damping coefficient versus cells per wavelength for rhoPisoFoam solver using two off-centering factors.....	188
Figure 102: Representative pressure spectrum for temporal discretization study.....	191

Figure 103: Zoomed in view of representative pressure spectrum for temporal discretization study.....	192
Figure 104: Representative pressure spectrum for JICF temporal discretization study (note the different scales on the simulation plots for clarity) .....	194
Figure 105: Comparison of numerical and acoustic modes for JICF case using the CN1.0 temporal discretization scheme.....	196
Figure 106: Representative pressure spectra for spatial discretization comparison .....	198
Figure 107: Orthogonal clip planes colored by mean reaction progress variable showing asymmetric mean flame shape. Isoline represents a value of 0.5. ....	199
Figure 108: Orthogonal views of the coarse mesh in the head end region .....	201
Figure 109: Orthogonal clip planes colored by mean axial velocity showing asymmetric recirculation region. Isoline represents a value of 0. ....	202
Figure 110: Representation of the volume used for calculating the temporal signals of reacting JICF heat release and jet nozzle pressure. Instantaneous contours of heat release rate included in lower plot .....	206
Figure 111: Representation of the volume used for calculating the temporal signals of jet velocity, including instantaneous contours of y-velocity .....	207
Figure 112: Velocity and pressure fluctuation signals filtered at 200Hz (upper) and corresponding transfer function phase calculated from the corresponding raw signals (lower)	208
Figure 113: Velocity and heat release fluctuation signals filtered at 200Hz (upper) and corresponding transfer function phase calculated from the corresponding raw signals (lower)	209
Figure 114: Phase-frequency relation for various jet air supply line choke points (distance specified from jet manifold).....	210

Figure 115: Schematic of air and fuel supply to reacting JICF .....	213
Figure 116: Contours of instantaneous mixture fraction, demonstrating the difference between a partially, or technically, premixed JICF and perfectly premixed JICF (note different scales for clarity).....	216
Figure 117: Normalized mixing profiles at scoop exit for JICF case with mixture fraction source term (left) and a honeycomb nozzle mixing study computed using CFX RANS (right). .....	217
Figure 118: Regions defined for heat release derivation. ....	221
Figure 119: Representative instantaneous isosurface of reaction progress variable at 0.1, used to calculate fluctuating strain and velocity fields at the flame front. Colored by strain magnitude. ....	225
Figure 120: Fluctuating strain and scaled velocity fields, used verify to proportionality between fluctuating strain and acoustic velocity.....	226

## LIST OF TABLES

Table 1: Objectives of the current study .....	10
Table 2: Summary of flame speeds used in expanded expression for the reaction rate .....	57
Table 3: Summary of Boundary Conditions for OpenFOAM Simulations .....	71
Table 4: Flow conditions for head end only reference design, taken from experiment.....	75
Table 5: Summary of 3-point stability trend from experimental results, used to validate the acoustic modeling techniques described in this study. Dynamic pressure measured near the exit of the combustor (pressure anti-node). .....	79
Table 6: Flow conditions for baseline head end only simulations.....	92
Table 7: Time lag calculations from LES simulations.....	141
Table 8: Constants used to calculate the gain terms in the JICF heat release model.....	141
Table 9: Gain expressions and relative values applied to JICF heat release model. Phase values are shown for reference and are calculated from the time lags shown in Table 8. ....	142
Table 10: Objectives of the current study and summary of results.....	157
Table 11: Critical parameters for mesh resolution study .....	181



## NOMENCLATURE

### *Latin Letters*

- $A$  = Area ( $m^2$ ), Bradley model constant
- $Co$  = Courant number
- $CFL$  = Courant-Frederich Lewis number
- $D$  = Mass diffusivity ( $m^2/s$ ), Diameter ( $m$ )
- $DFT$  = Discrete Fourier Transform
- $D_\lambda$  = Thermal diffusion coefficient
- $H_f$  = Lower Heating Value ( $J/kg$ )
- $Ka$  = Karlovitz Number
- $Le$  = Lewis number
- $Ma$  = Markstein number
- $Pr$  = Prandlt number
- $Q$  = Heat release ( $W$ )
- $R$  = Receiver region
- $Re$  = Reynolds number
- $Sc$  = Schmidt number
- $S_L$  = Strained laminar flame speed ( $m/s$ )
- $S_{L0}$  = Unstrained laminar flame speed ( $m/s$ )
- $S_T$  = Turbulent flame speed ( $m/s$ )
- $T$  = Temperature ( $K$ )
- $V$  = Volume ( $m^3$ )
- $Y$  = Species mass fraction, Fuel concentration
- $b$  = Reaction progress variable
- $c$  = Sound speed ( $m/s$ )

$f_T$	= Mixture fraction
$h$	= Enthalpy ( $J/kg.K$ )
$m$	= Mass ( $kg$ )
$n$	= Gain factor
$p$	= Pressure ( $N/m^2$ )
$q$	= Heat release ( $W$ )
$t$	= Time ( $s$ )
$u$	= Velocity ( $m/s$ )
$x$	= Spatial direction ( $m$ )
$y$	= Spatial direction ( $m$ )
$z$	= Spatial direction ( $m$ )

### ***Greek Letters***

$\alpha$	= Thermal diffusivity ( $m^2/s$ )
$\beta$	= Heat loss coefficient
$\Delta$	= Filter Width
$\gamma$	= Ratio of specific heats
$\kappa$	= Strain rate ( $1/s$ )
$\Phi$	= Equivalence Ratio
$\mu$	= Dynamic viscosity ( $N.s/m^2$ )
$\rho$	= Density ( $kg/m^3$ )
$\Sigma$	= Wrinkling factor
$\sigma$	= Effective strain rate
$\tau$	= Time lag, period ( $s$ )
$\omega_R$	= Reaction rate ( $kg/m^2.s$ )
$\chi$	= Heat loss parameter

### ***Abbreviations***

CAD	= Computer Aided Design
CFD	= Computational Fluid Dynamics
CN	= Crank-Nicholson
CPU	= Central Processing Unit
CVP	= Counter-Rotating Vortex Pair
DES	= Detached Eddy Simulations
DNS	= Direct Numerical Simulation
FTF	= Flame Transfer Function
GIM	= Generalized Instability Model
GRI	= Gas Research Institute
HE	= Head End
HRT	= Helmholtz Resonator Tool
JICF	= Jet in Cross Flow
LDV	= Laser Doppler Velocimeter
LES	= Large Eddy Simulations
MP	= Monitor Points
ParPM	= Partially Premixed
PerPM	= Perfectly Premixed
PISO	= Pressure Implicit with Splitting of Operators
PIV	= Particle Image Velocimetry
POD	= Proper Orthogonal Decomposition
PSD	= Power Spectral Density
PT	= Pressure Transducer

RANS = Reynolds Averaged Navier Stokes

RI = Rayleigh Index

STL = Stereolithography file format

TA3D = Thermoacoustic 3D

TFC = Turbulent Flamespeed Closure

### *Subscripts*

$F$  = Fuel

$k$  = Arbitrary species

$O$  = Oxidizer

$T$  = Turbulent component

$u$  = Unburnt

### *Accents*

$x'$  = Fluctuating component

$\bar{x}$  = Mean component

$\tilde{x}$  = Favre averaged component

$\dot{x}$  = Rate

# CHAPTER 1 – INTRODUCTION

## Background of the problem

Increasing emissions regulations have been a driving force in modern gas turbine design and have led to the development of lean premixed combustion. It has been found however, that the lean premixed combustion process is susceptible to self-excited combustion oscillations, known as combustion instability (Gentemann, 2004). Combustion instability is a damaging and dangerous phenomenon that is present in most combustion devices, particularly those that undergo lean premixed combustion processes. It occurs when oscillations in the combustion process couple with the acoustics of the combustion chamber. If these oscillations are in phase, strong pressure oscillations may appear in the absence of strong damping mechanisms (Crocco, 1951). This leads to an increase in heat loads and system vibrations that may render an engine inoperative. To avoid this, the combustion system must be analyzed for thermoacoustic stability and solutions must be developed to mitigate any damaging instabilities that may occur.

The general focus of this study is on the combustion instabilities that develop in the combustion chamber of a stationary gas turbine. An example of a modern gas turbine is shown in Figure 1. The basic operation of a stationary gas turbine begins with air entering into the engine at atmospheric conditions (1) and being compressed in the compressor section (2) up to pressures as high as 20 bars. This pressurized air enters the burners where fuel, such as natural gas, is mixed with the air. The mixture is then ignited in the combustion chamber (3) and burned at temperatures as high as 2200 Kelvin. The hot combustion gases then enter the turbine (4) and are expanded back to atmospheric pressure. The rotation of the turbine drives a shaft that is

connected to both the compressor as well as a generator, generating large amounts of electrical power. The exhaust gases (5) are often passed through a heat exchanger to generate steam that can be run through a steam turbine. Such a combined cycle is capable of producing more than 570 MW of power at efficiencies higher than 60% (Siemens, 2011).

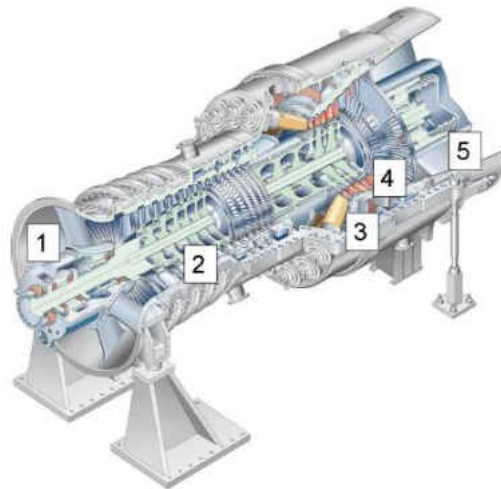


Figure 1: Siemens SGT5-8000H Gas Turbine (1-Inlet, 2-Compressor, 3-Combustion Chamber, 4-Turbine, 5-Exhaust) (Siemens, 2011)

One difficulty that arises in designing gas turbine combustion systems for power generation is that the turbines are not always run at the same conditions. Startup conditions, fluctuations in power demand, and even atmospheric changes such as differing inlet temperatures can all have an effect on the operation of the turbine, including both the frequencies and amplitudes of the combustion instabilities that are seen in the engine. These operational conditions also have an effect on the NO<sub>x</sub> and CO emissions which must be maintained below specific limits. As a result, many combustors typically employ what is known as staging technology. This technology utilizes multiple fuel injection configurations at different locations within the combustor, all of which can be tuned individually depending on the operating

conditions and stability and emissions requirements. It is important to understand, however, that tuning an engine to meet emissions requirements while maintaining operation below stability limits is a complex process, as the emissions and dynamics of a system generally behave with opposite trends. This behavior is shown schematically in Figure 2, which shows a qualitative plot of emissions versus dynamics, or acoustic oscillations.

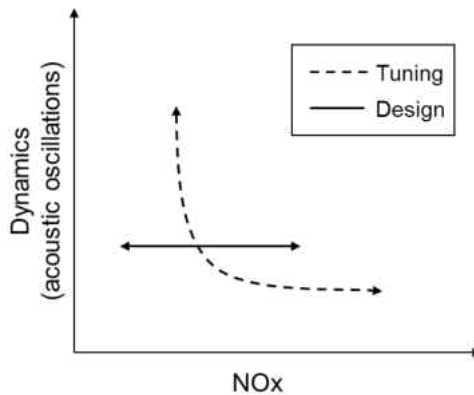


Figure 2: Competing behavior of emissions and dynamics with effects of tuning and design

It is well known that if an engine is tuned to reduce the emissions, the dynamics will often increase. Conversely, if an engine is tuned to reduce dynamics, the emissions will often increase. These trends are represented by the dashed curve in Figure 2. The only way to reduce the emissions and increase the stability of an engine is to modify the design of the combustion system. This is represented by the solid line in Figure 2, which demonstrates that the dashed curve can be moved to the left with appropriate design changes. In order to effectively implement such design changes, it is important to have a fundamental understanding of how a particular combustion design feature will behave within a particular system and how it will impact both the dynamics as well as the emissions of the engine over the entire operational range

that it will experience. This fundamental understanding is often achieved through experimental rig tests, as well as complementary numerical simulations and analytical modeling.

While experimental combustion rig tests are often used as a part of the design stage to verify the stability of a particular design, these tests can be very costly and difficult to achieve. As a result, it is also desirable to provide thermoacoustic stability analysis using additional modeling tools so that further studies can be performed without the cost of additional experimentation (Martin, 2006). Each type of tool is useful for different aspects of the combustion system analysis. While low order analytical tools are useful for quick, low cost approximations of the stability of a given system, high fidelity numerical models provide the details necessary to investigate the complex flow physics of the combustion system and can be used to determine the specific mechanisms that are driving the instability in a given scenario. Each type of tool, from low order analytical models, to high pressure experimental rigs, to massively parallel numerical simulations, should be used in combination with each other to understand and quantify a given system.

While investigating specific engine configurations is a necessary step in the design process, it is also important to model and understand more general setups so that the fundamental physics of the flow can be determined. This fundamental knowledge is critical as it provides a general understanding and directly applies to many practical applications. It also aids in developing experimental methods and modeling tools that can be extended to a given engine configuration. The current work seeks to perform such a fundamental study by developing and applying modeling techniques to investigate how a reacting jet behaves when injected into an unstable cross flow at typical stationary gas turbine operating conditions. While this study will



help to understand the general rules for designing staging technologies, its focus is on the flow physics of the problem, and thus, contains many more applications to various engine configurations as each configuration is governed by the general physics of the problem.

### **Overview of combustion instabilities**

Combustion instabilities occur in nearly all types of gas turbine combustors, as well as rocket engines and other combustion devices. These instabilities are often referred to as thermoacoustics, where a coupling can develop between unsteady heat release and acoustic waves within the chamber, resulting in oscillatory instabilities. The unsteady heat release generated from a turbulent flame produces acoustic pressure and velocity waves within the combustion chamber. These waves travel downstream through the combustion chamber and can be reflected at the walls and other boundaries of the chamber or turbine. The reflected waves can return to the location of the flame and perturb the flame surface or cause fluctuations in the mass flow of fresh reactants. Both the flame perturbations and the reactant mass flow fluctuations can cause additional oscillations of heat release. Depending on the phase between the acoustic fluctuations and the heat release fluctuations, a feedback cycle can result that causes the amplitude of the acoustic waves to increase. A schematic of this feedback cycle is shown in Figure 3.

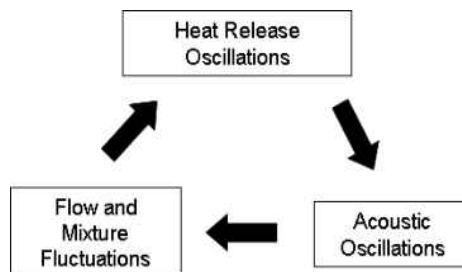


Figure 3: Feedback cycle for combustion instabilities

If the energy driving the combustion instabilities is greater than the energy damping the instabilities, a growth of the oscillations will occur until a limit cycle is achieved due to non-linear effects. The phase and energy required to result in growing thermoacoustic instabilities was quantified by Rayleigh in 1945 (Rayleigh, 1945). According to Rayleigh's criterion, thermoacoustic instabilities can grow if the phase between acoustic pressure and heat release oscillations is between -90 and 90 degrees. If the phase is out of this range, the instabilities will be damped. Rayleigh also developed an expression, represented by Equation (1), which states that the integral over volume and time of the pressure fluctuations multiplied by the heat release fluctuations must be greater than zero for thermoacoustic instabilities to grow.

$$\int\int_{V_0}^T p'Q'dtdV > 0 \quad (1)$$

As stated above, however, the necessary energy and phase between pressure and heat release oscillations will only cause the instabilities to increase if this energy driving the instabilities is greater than the energy damping the instabilities. An extension of Rayleigh's criterion, shown in Equation (2), has been developed that adds an additional integration to the right hand side of the equation to account for losses that can dampen the acoustic waves present in the system (Poinsot, 2005).

$$\frac{\gamma - 1}{\mathcal{M}_o} \int\int_{V_0}^T p'Q'dtdV > \int\int_{A_0}^T p'utdA \quad (2)$$

In summary, if the correct phase relation exists between pressure and heat release oscillations and if the energy driving the instabilities is greater than the energy damping the instabilities, self-sustained combustion instabilities will grow until a limit cycle is achieved due to non-linear effects. This thermoacoustic limit cycle must be kept within certain limits for the entire operational envelope of the engine.

Due to the detrimental effects that combustion instabilities can have on the operation of gas turbines and other combustion systems, an extensive amount of research has been done on the mechanisms that cause these instabilities as well as practical ways to mitigate their effects and control the instabilities. Several mechanisms have been identified that contribute to the amplification of thermoacoustic instabilities. These include equivalence ratio fluctuations, reactant mass flow rate fluctuations, convective acoustic waves, entropy waves, and vortex shedding (Ibrahim, 2005). Common mechanisms associated with instabilities in dump combustors and other recirculation stabilized flame combustors include vortex shedding and reactant mass flow fluctuations. Details of these mechanisms, specifically how they apply to dump combustors, will be outlined below in the literature review.

### **Objectives of the Current Study**

The primary objective of this study is to analyze and understand the flow phenomena related to a reacting jet injected into an unstable cross flow, generated by a specially designed dump combustor. This primary objective is crucial to provide a solid framework on which to base future investigations. A detailed literature review is provided that summarizes the extensive amount of fundamental studies that have been done, investigating areas such as non-reacting sudden expansions flows, reacting dump combustor flows and their relation to combustion

instabilities, non-reacting and reacting jets in cross flow, and forced jets in cross flow. Focus is given to the physics that govern these different flows, including vortex structures and the mechanisms of instability. A review is also included that gives an overview of the self-excited Large Eddy Simulations (LES) that have been performed in recent research, as this is proposed to be an effective tool for investigating the combustion instability issues mentioned above.

Once a solid understanding of the complex flows related to this study is obtained, a baseline model must be setup using the proposed tool. This was achieved by applying a method known as self-excited LES to an experimental dump combustor, focusing on the development of combustion instabilities within the combustor.

The dump combustor modeled in this study was designed at Purdue University to operate at typical gas turbine operating conditions of up to 20 bar and 2100 Kelvin (Sisco, 2011). This experimental rig was developed to allow for the investigation of multiple reaction zones within a simple combustion system, providing the resources for a fundamental understanding of technologies such as combustion staging. The length of the rig was designed so that the longitudinal modeshapes are characterized by frequencies similar to intermediate range engine frequencies, on the order of several hundred to a thousand Hertz. The area ratio of the dump combustor as well as the location of the dump plane was designed to result in the necessary coupling between heat release fluctuations and pressure fluctuations to induce combustion instabilities at specific resonant modes of the combustor. A sketch of the experimental rig, including a description of the key components, is shown below in Figure 4.

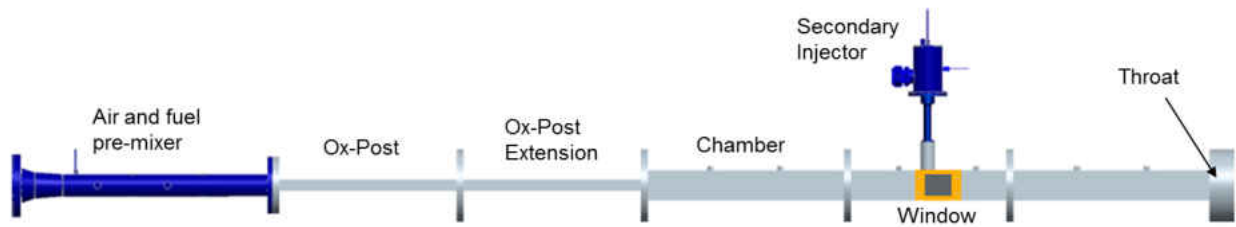


Figure 4: Purdue Acoustic Rig (Fugger, 2011)

This dump combustor provides a reliable means for generating both transverse and longitudinal instabilities and acts as an actuator to produce an acoustically unsteady cross flow inside the combustion chamber. Further downstream, a premixed jet is injected transversely into the unsteady cross flow. As soon as the premixed jet injects into the hot combustion products from the head end reaction, it ignites and burns. The response of the jet is studied experimentally using high speed flame visualization for analyzing the heat release fluctuations and multi probe measurements for analyzing the acoustic pressure and velocity fluctuations. Using these measurements and optical diagnostics, the behavior of the flame can be quantitatively analyzed (Fugger, 2011). This rig provides the necessary setup to experimentally investigate the fundamental flow physics associated with a reacting jet injected into an unsteady cross flow. The experimental results will be used to validate the LES modeling of this setup that this study seeks to achieve.

Once a head end only simulation is achieved, it can be compared to experimental results to determine if the expected self-excited instabilities present in the rig are captured using the LES methods. Upon confirming that the proposed methods are valid and obtaining an understanding of their limitations, the next objective of this study is to add the jet injection to the computational domain and develop a simulation that includes a reaction from the head end as

well as the jet reaction. The goal of the JICF simulations will be to correctly capture the stability trends observed in the experimental results for the sake of validating the LES approach, but then to use this data to complement the experimental data in identifying any potential mechanisms of instability of the reacting JICF. The proposed mechanism will then be used to develop 3D and 1D thermoacoustic modeling techniques that can be applied to reduced order modeling tools for further validation of the proposed mechanism and insight into the fundamental parameters that govern the flow.

The overall objective of this study is to first provide a detailed analysis of the physics of a reacting jet in an unsteady cross flow. Special attention will be given to identify a mechanism of combustion instability and the parameters that are important in both the modeling and design of the jet. This study also seeks to develop and validate the necessary tools and methods so that the fundamental study shown here can be extended to more specific engine design studies, such as actual combustor configurations and specific fuel injection nozzles. The objectives of this study are explicitly outlined below in Table 1.

Table 1: Objectives of the current study

Objective 1	Analyze and understand the flow phenomena related to a reacting JICF
Objective 2	Develop self-excited LES simulations of an unsteady dump combustor and reacting JICF and validate with experimental data
Objective 3	Investigate the interaction between an unsteady cross flow and a reacting jet and identify a mechanism that contributes to the stability of the system
Objective 4	Identify the necessary tools and methods so that the fundamental study shown here can be extended to more specific engine design studies

## CHAPTER 2 – LITERATURE REVIEW

### Flow Physics of a Jet in Cross Flow

The flow field associated with a jet injected into a cross flow has been extensively studied experimentally, analytically, and numerically. The large extent of JICF studies is a result of the widespread practical applications where this flow phenomenon is observed. Specific applications are commonly seen in energy and propulsion systems, largely due to the mixing characteristics in the regions near the injected jet.

A sketch detailing the dominant flow and vortical structures associated with the JICF was outlined by Fric and Roshko in 1994 (Fric, 1994). An adaptation of this sketch is shown in Figure 5.

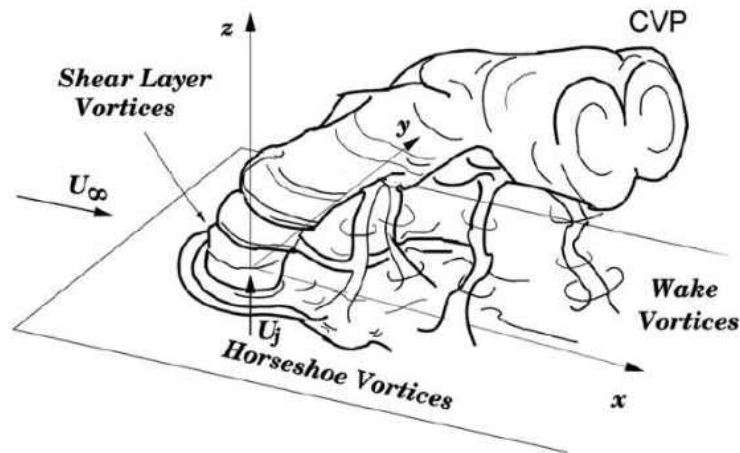


Figure 5: Dominant flow and vortical structures associated with a jet in cross flow (Karagozian, 2010)

This sketch has been included in numerous studies, as it clearly details the four most dominant vortical structures that have been observed in both experimental and numerical studies.

The most prominent vortex structure observed in a JICF is the counter-rotating vortex pair (CVP) that develops in the cross section of the jet. It has been suggested that these vortices are generated in the nearfield region of the jet through the distortion of vorticity in the evolving shear layer (Kelso, 1996; Smith, 1998; Cortelezzi, 2001).

Another common vortical structure that has been observed in jets that are injected flush from a wall is known as horseshoe vortices. It has been proposed that these horseshoe vortices arise from the displacement effect that the jet has on the wall boundary layer in the cross flow (Baker, 1990). Additional studies have shown that the horseshoe vortex system contains both oscillatory and stationary modes that appear to be a function of the jet to cross flow velocity ratio and the jet Reynold's number (Kelso, 1995).

According to a smoke visualization study performed by Fric and Roshko (Fric, 1994), the upright wake vortices that appear in the downstream wake region of the jet are initiated within the wall boundary layer and evolve periodically around and beyond the jet. The smoke studies indicated that the wake vortices allow fluid to be drawn from the boundary layer into the actual jet itself.

Many studies have suggested that the instabilities associated with the jets shear layer vortices cause a rollup of the vorticity in the nearfield of the jet, and are a major contributor to the formation of the CVP. Several DNS studies, however, have shown that the CVP forms even in steady 3D flow simulations, indicating that the periodic shear layer rollup is not necessary to initiate the CVP (Muppidi, 2007; Alves, 2006; Bagheri, 2009). This conclusion may agree with studies that have shown that the pressure difference between the upstream and downstream regions of the jet can lead to an accumulation of vorticity that is sufficient to form the CVP in the



downstream region of the jet (Muppidi, 2007). Although the shear layer instabilities of the jet may not be necessary to form the CVP, it is clear that the shear layer vorticity does contribute to the strength of the jet's structure as well as the manner in which the structure evolves (Karagozian, 2010).

While the majority of fundamental JICF studies relate to non-reacting jets, there have been recent advances in the study of reacting jets injected into cross flow. Optical diagnostics are often used to characterize the jet flame shape and length, based on the luminosity of radicals present in the reacting jet. Fundamental studies have shown that the trajectory of the jet flame follows that of the non-reactive JICF relatively closely when the reactive mixture is injected into an essentially incompressible cross flow of air (Pratte, 1967). Some PIV studies, however, have suggested that the flames penetrate slightly further into the cross flow as compared to their non-reactive counterparts (Hasselbrink, 2001). Experimental studies have also shown that, similar to the non-reacting JICF, the flame cross-section transitions from an elliptic to a kidney-like shape, consistent with the CVP (Kadota, 1990).

A study performed by Noble et al (Noble, 2011) investigated the behavior of a  $\text{CH}_4/\text{H}_2$  reacting fuel jet injected into a vitiated cross flow at 6 atm. This study concluded that the reaction initiated on the downstream side of the jet. In the near field, the centerline of the reacting jet closely coincided with non-reacting jet correlations. Farther downstream, however, it was found that the reacting jet penetrates much further into the flow than the non-reacting jet. Figure 6 shows a colorized chemiluminescence image (a) of a pure  $\text{CH}_4$  jet flame, along with a contour plot of the chemiluminescence intensity (b) and a plot of the vertical chemiluminescence intensity distribution at several axial stations (c).

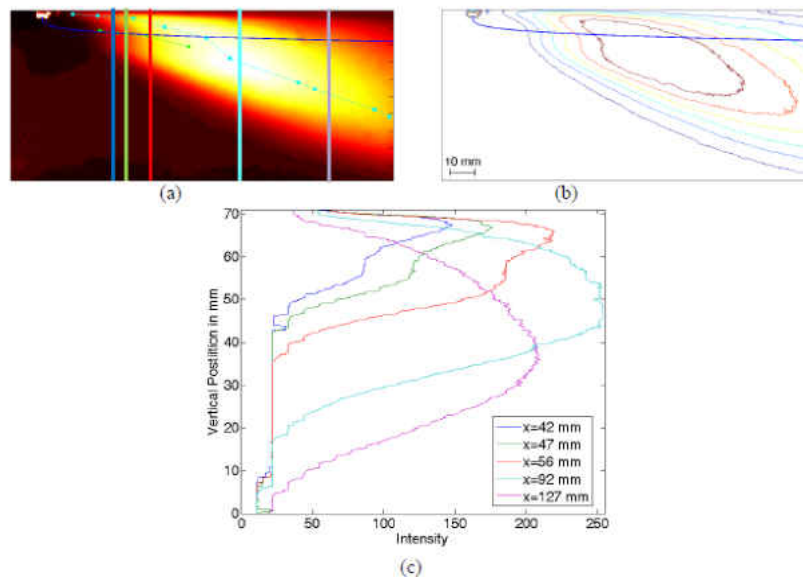


Figure 6: Chemiluminescence data from a CH<sub>4</sub> reacting jet flame (Noble, 2011)

Several points were deduced from these images. First, it is evident that the Holdeman correlation (represented by the blue line) closely tracks the jet core for the first 45 mm past the injector center. This result is consistent with other studies which have shown that the jet trajectory does not change significantly for reacting jets when compared to non-reacting jets. It was also concluded from the figure that the visible reaction initiates near the wall, but approximately 10 mm downstream of the jet centerline. It was suggested that the asymmetric intensity distribution indicates that the flame is initiated on the downstream side of the jet and does not fully wrap around the jet until about 40 mm downstream of the injector.

Yet another aspect of JICF studies includes the behavior of a jet injected into an unsteady cross flow. While these investigations are not as extensive, there are several interesting studies that have analyzed the differences that can occur when the cross flow becomes unsteady. A technique was developed by Lam and Xia in 2001 (Lam, 2001) that produced a method to

experimentally investigate the interaction of a turbulent jet with an unsteady cross flow. The effect of the unsteady cross flow, consisting of a mean flow current and a sinusoidal oscillating component, was incorporated by moving the actual injector back and forth with a controlled sinusoidal motion. Multiple unsteadiness parameters were investigated using experimental and computational studies (Lam, 2004). In general, it was found that in a cross flow characterized by a large unsteadiness parameter (defined as the ratio between the time averaged mean cross flow velocity and the amplitude of the oscillating velocity component), the jet dispersion pattern was significantly different from that of the same jet in a steady cross flow. The jet fluid became organized periodically into large-scale effluent clouds, enhancing the time-averaged mean dilution of the jet. Figure 7 is a sample of the images generated from Lam's experimental results, showing the phase-locked averaged jet dispersion patterns for various cross flow situations. This particular figure includes unsteadiness parameters of 0.25 and 0.5 and Strouhal numbers (defined by the jet diameter and mean cross flow velocity) of 0.0375, 0.0825, and 0.12.

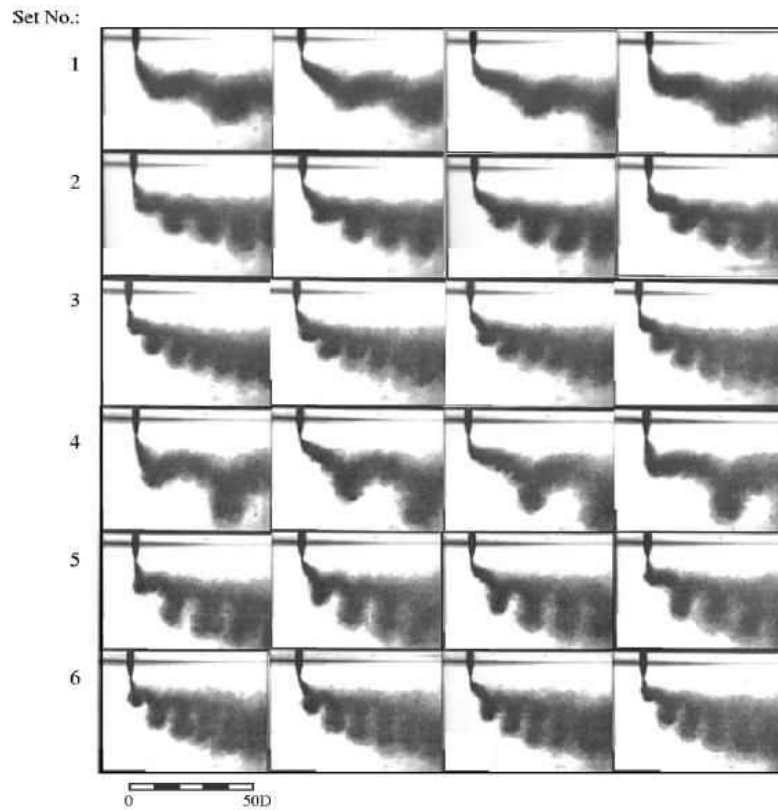


Figure 7: Phase-locked averaged jet dispersion patterns for 6 different cross flow configurations (Lam, 2004)

It was concluded that when the cross flow oscillates and changes its velocity, the vertical penetration of the jet is affected in a quasi-steady manner by the instantaneous cross flow velocity. The effluent clouds formed from the jet were convected downstream during the high-speed phase of the cross flow. Also, when compared with the corresponding width of a jet in a steady cross flow, it was found that the jet width in an unsteady cross flow was increased two to three times, determined by the unsteadiness parameter. The experimental results in Lam's study were found to agree well with similar computational results. This type of cross flow velocity oscillation likely correlates to the presence of an acoustic velocity wave in a combustion chamber, such as the experimental rig modeled in this study.

A study conducted by Blossey involved DNS and experiments to investigate the structure of a jet injected into a steady cross flow as well as a cross flow undergoing sinusoidal forcing (Blossey, 2002). The simulation results showed substantial entrainment and mixing enhancements with low frequency forcing while forcing at higher frequencies (up to a Strouhal number of 0.64) resulted in a jet which closely resembled the unforced jet in a time-averaged sense. Similar to other studies, it was also found that the forced jets showed a slight increase in penetration as well as greater spreading in the wall-normal direction, when compared to that of the unforced jet. Figure 8 shows instantaneous scalar concentration in an x-y plane through the jet centerline for the unforced jet in cross flow (left) and the jet in cross flow forced at a Strouhal number (based on the jet velocity and diameter) of 0.08 (center) and 0.1875 (right).

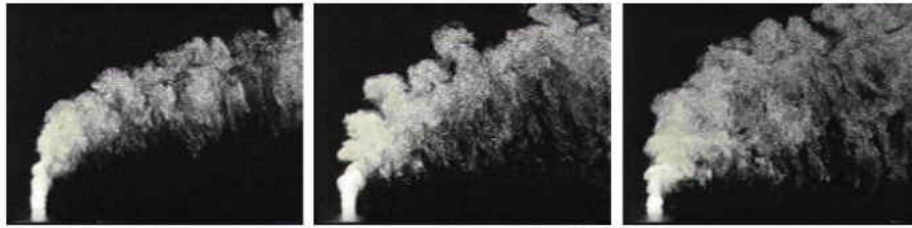


Figure 8: Flow visualization from experiments of a jet injected into a steady (left) and unsteady (center, right) cross flow (Blossey, 2002)

It was found that unsteady forcing of the jet, within the appropriate frequency range, can have a substantial impact on both the structure and mixing of the jet in cross flow. The range of forcing frequencies was chosen to enable excitation of a variety of the coherent structures of the flow, including the near field unsteady jet shear layer structures and the far field unsteady CVP structures.

When investigating possible instability mechanisms of the reacting jet in cross flow modeled in this study, it is important to have an understanding of the range of frequencies that each of a non-forced, non-reacting jet's natural coherent structures is likely to exhibit. This understanding will aid in determining if the frequencies of combustion instability of interest in the combustor are likely to have an effect or interact with the coherent structures of the jet. Smith and Mungal summarized that for jets injected flush with the cross flow wall, the Strouhal number of the wake vortices closely matches the value obtained from a cylinder with the same diameter as the jet. These Strouhal numbers based on the jet exit diameter and velocity have been observed to be approximately 0.15 for velocity ratios below 8 and to fall to about 0.06 for a velocity ratio of 20. Many studies have also shown that the horseshoe vortex system oscillates at the same Strouhal numbers as these wake vortices (Smith, 1998; Kelso, 1996).

The general opinion regarding the formation of the CVP is that it is formed from the jet shear layer, and thus, the vorticity from the jet boundary layer before it is injected into the cross flow is eventually transferred to the vorticity of the CVP (Kelso, 1996). Although the jet shear layer is present with the combustion regime of a reacting JICF and likely effects the reaction or flame surface of the jet, its contribution to the CVP is unlikely to result in a feedback cycle as the CVP forms much further downstream than the typical reaction zone. Thus the necessary feedback coupling between mixture fluctuations and heat release is not expected to develop as a result of the CVP.

The remaining known coherent structure of a non-forced, non-reacting JICF is the shear layer of the jet. There is a wide range of Strouhal numbers reported in the literature, varying from 0.1 (Narayanan, 2003) to as high as 2.0 (Smith, 1998), with commonly accepted

intermediate values around 0.3 to 0.5 for Kelvin-Helmholtz type instabilities (Schlegel, 2013; Megerian, 2007). Depending on the frequency of these shear layer instabilities, they have the potential to participate in the combustion instability feedback cycle as they can have a direct effect on the reacting jet flame surface. Literature from non-reacting jets in cross flow as well as the flow field obtained from the numerical simulations in this study will help to identify if these shear layer structures occur near the frequencies of interest for the configurations that have been run in the experiments.

### **Thermoacoustics of Dump Combustors**

Due to their relatively simple geometry, dump combustors are a classical means of investigating thermoacoustic phenomena. The dump combustor consists of a sudden area expansion where the incoming reactant mixture is ignited at the dump plane. Due to the recirculation of the flow in the corners of the sudden expansion, the reacting mixture can become anchored at the dump plane. Many studies have been performed that investigate the flow fields in non-reacting sudden expansion flows and reacting dump combustor flows, as well as the mechanisms of combustion instability that are present in dump combustor flows and how these mechanisms drive the instabilities present in the combustor.

Some of the key parameters of dump combustors that have been studied extensively include the inlet geometry, the step height, and the inlet turbulence and rotation. A study performed by Ronald et al (Ronald, 1989), investigated some of these effects using non-reacting flow in an axisymmetric tube with a sudden expansion. Ronald came to an interesting conclusion, suggesting that the net effect of the step height on the flow in the combustor is relatively small. It was found that the inlet turbulence had a direct and significant effect on the

flow in the combustor by increasing mixing and energizing the separating shear layer, causing it to reattach sooner. Although the studies that have investigated non-reacting dump combustor flows provide valuable insight into the flow physics present in sudden expansion flows, it should be noted here that many key differences have been found when comparing reacting flow to non-reacting flow in a dump combustor.

Many experimental and computational studies have been performed to characterize the differences between non-reacting and reacting flow through a sudden area expansion. One of the most well-known of these studies was conducted by Pitz and Daily in 1983 (Pitz, 1983). By investigating the reacting flow behind a step in a rectangular duct with a 2:1 area ratio, they found that the length of the recirculation zone present in the reacting flow was reduced by 20-30 percent compared to that of the non-reacting case. Another study performed by Ahmed et al (Ahmed, 1992) utilized a two-component laser doppler velocimeter (LDV) to characterize the difference between a premixed propane/air reacting flow and a non-reacting flow using nitrogen instead of propane. Figure 9 shows contours of mean axial velocity for an equivalence ratio of 0.65, compared to the non-reacting case.



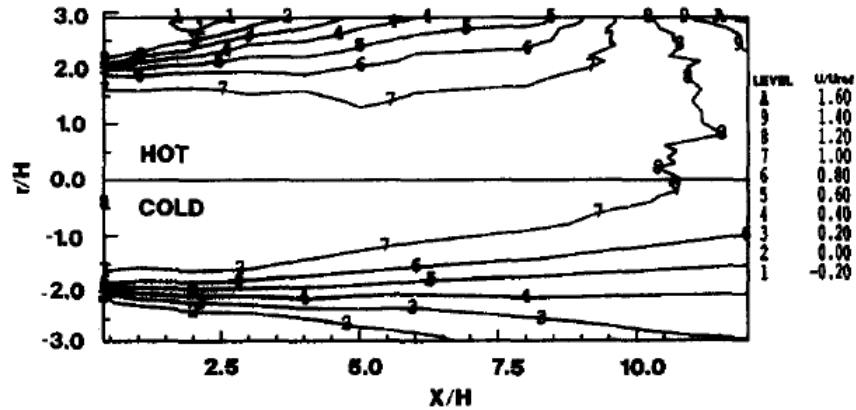


Figure 9: Contours of mean axial velocity, comparing non-reacting to reacting flow ( $\phi=0.65$ ) through a sudden expansion (Ahmed, 1992)

In this figure, the boundaries of reverse flow are defined by contour lines of  $U/U_{ref}$  of 0.0, indicating that in the presence of combustion, the length of the corner recirculation zone decreased by as much as 44 percent, from 6.7-3.75 step heights. In spite of this reduction in recirculation region length, however, the flow inside the reacting bubble is more active, shown by the higher values of negative velocity.

While much of the dump combustor literature focuses on the flow fields throughout the combustor, many studies are specifically focused on the combustion instabilities present in dump combustors. Especially for premixed cases, these instabilities are commonly attributed to the hydrodynamic behavior of the dump plane, specifically the vortex shedding that occurs off of the sudden expansion. This effect was clearly outlined in a work by Schadow (Schadow, 1991), who stated that the vortex structure has a significant influence on the combustion process. Figure 10 shows a schematic of this vortex structure at the rearward facing step of a dump combustor.

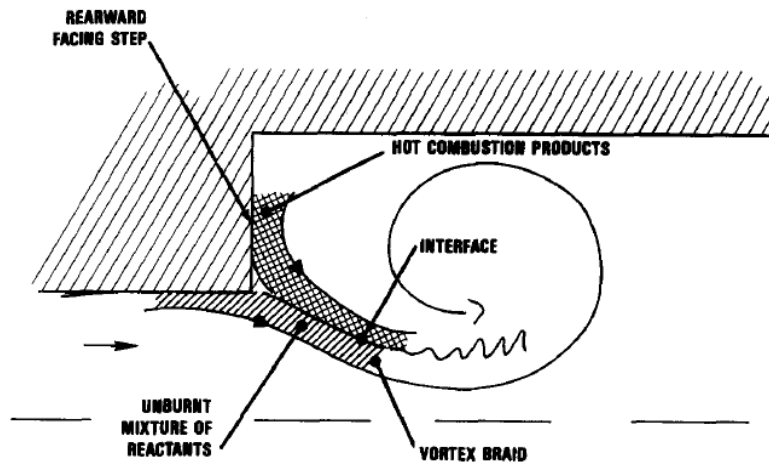


Figure 10: Schematic of vortex structure at the rearward facing step of a dump combustor (Schadow, 1991)

The high speed stream of unburnt reactants is injected into a low speed stream, composed largely of hot combustion products, where the flame-holding recirculation zone is formed behind the dump plane. In the early phase of vortex development, specifically right off of the dump plane, the fine scale mixing and burning between the unburnt mixture and the hot combustion products is limited. The instability waves developed by the initial shear layer, however, are amplified to a higher energy level and begin to roll up into vortices. As these vortices begin to roll up and interact with other vortices and chamber walls, a large interface between the air/fuel mixture and the hot combustion products develops, as outlined in the schematic in Figure 11.

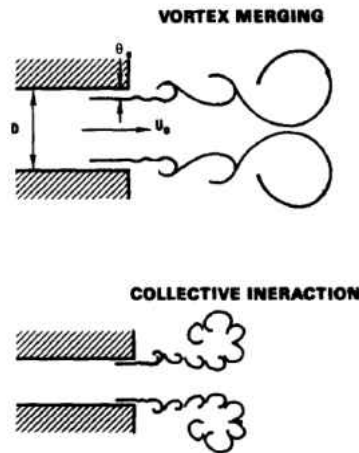


Figure 11: Interaction and roll up of vortices at a sudden expansion (Schadow, 1991)

As these larger scale vortices are created, they trap fresh gas in pockets that are convected downstream. These vortices can release the fresh gas when they unwrap at the edges of the main stream or when they collide with a wall of the chamber, for example. This causes a sudden spike in the heat release when the fresh gas is exposed to the hot combustion products and spontaneously burns. This process is repeated during each cycle of the pressure oscillations, resulting in periodic heat release. When a proper phase relationship exists between the periodic heat release and pressure oscillations, as defined by the Rayleigh criterion (Rayleigh, 1945), the pressure oscillations can be excited and the combustor will sustain combustion instabilities.

A fundamental study was performed by Ahmed et al using LDV measurement techniques on a ramjet dump combustor (Ahmed, 1995). The objective of this study was to characterize the pressure oscillations of the flow field for different combustor lengths and inlet flow velocities. The combustor length is known to have a direct effect on the combustion instabilities as it determines what the resonant frequencies of the chamber are. The inlet flow velocity also has a direct effect on the combustion instabilities as it determines the frequency of vortex shedding at

the dump plane, one of the common mechanisms attributed to combustion instabilities in dump combustors. Reacting flow was obtained by using premixed propane and air at an equivalence ratio higher than 0.6 to avoid instabilities associated with lean blow off. The intensity and frequency of oscillations were found to be dependent on the inlet velocity, combustor length, and equivalence ratio. Results showed that pressure oscillations were controlled by both vortex kinematics in the combustor as well as the acoustic response of the inlet section.

Previous studies on dump combustor instabilities have shown that these types of geometries are dominated by vortex flows that are associated with periodic heat release. In order to verify that this periodic heat release is indeed a driving force of the instabilities, however, it is necessary to have a complete knowledge of the spatial and temporal distributions of heat release and acoustic pressure (Schadow, 1991). It has been shown in previous studies that the heat release in a combustion chamber is linearly proportional to the emitted radiation (Smith, 1985). Using this comparison, a quantitative factor based on the Rayleigh criterion can be developed and measured by taking the cross spectra and phase of the pressure and radiation intensity at a given location in the combustion chamber.

This type of analysis was done by Sterling et al (Sterling, 1987) to determine the relative magnitude of the driving of the instabilities at various axial locations throughout the combustor. As shown in Figure 12, Sterling found that the driving of instabilities occurred primarily at the front of the combustor while damping of the instabilities was observed further downstream. The net value of the integral of the curve shown in Figure 12 determines if driving or damping of the instability will occur, where a positive net value implies driving and a negative net value implies damping.

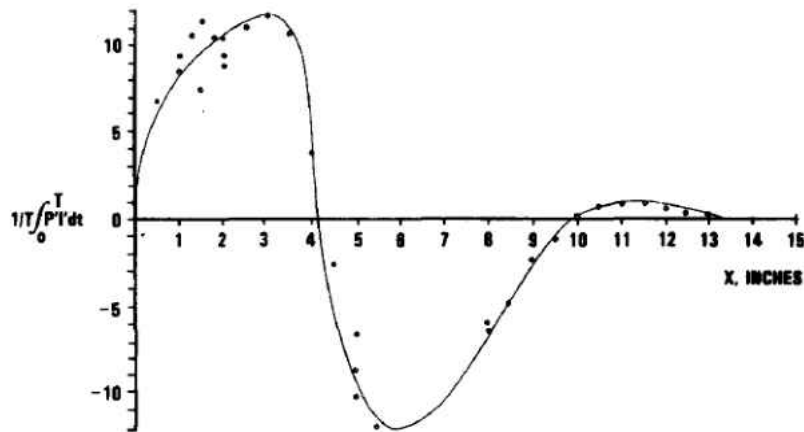


Figure 12: Plot of Rayleigh index criterion vs. combustor length (Sterling, 1987)

The net value of this Rayleigh index will change based on the parameters of the dump combustor that affect the heat release and the pressure distributions. The heat release depends on dump geometry, the initial condition of the shear layer, fuel type, and local equivalence ratio while the pressure distribution depends on the dominant acoustic modes of the combustion chamber. New research continues to be conducted that explores the effects of these key parameters on combustion instabilities of dump combustors.

There are likely many similarities between the physics governing the combustion instabilities of a dump combustor, compared to those that govern a reacting jet in cross flow like the one investigated in this study. Both scenarios include a basic jet flow of fresh reactants, anchored and self-sustained by recirculating burnt gas, although the co-flow dump combustor flame and the perpendicular jet flame clearly have very different hydrodynamic structures. In both cases, a standing pressure or velocity wave sustained in the combustion chamber can have similar effects on the hydrodynamics of the incoming reactants and the resultant feedback cycle necessary to impact the combustion instabilities. Because dump combustors and their

combustion instabilities have been studied extensively, it is helpful to have an overview of these studies, as there is likely relevance to that of a reacting jet in cross flow where little to no research on reacting JICF combustion instabilities has been conducted.

### **Self-Excited LES of Combustion Instabilities**

A powerful modeling tool for combustion systems is the use of high fidelity numerical simulations that can capture both the complex physics of unsteady heat release oscillations as well as the acoustic phenomena represented by the compressible fluid mechanics equations. This allows for the simulation of the coupling between the unsteady heat release and the acoustics of the flow, known to be the source of combustion instabilities. Self-excited LES provides one of the most accurate numerical modeling tools, as no artificial forcing is applied to the flow. Instabilities are generated solely from the interaction between heat release and acoustics, just as they are in the actual system being studied.

It is well known that LES simulations, in general, require relatively fine meshes in order to obtain useful results as well as small time steps to maintain the stability of the solver. This combination results in computationally expensive simulations that have been largely impractical until even the most recent advances in computational systems. The large computational resources that are required for LES are significantly increased when the goal of the simulation is to obtain self-excited combustion instabilities. In order to accurately model the coupling between the heat release fluctuations and the acoustic phenomena within the domain, it is necessary to include enough of the domain so that clean acoustic boundary conditions can be specified at the inlets and exits of the computational domain. These boundary conditions must properly reflect the acoustic waves traveling within the domain so that a minimal amount of artificial damping or

reflecting of waves is present. This often requires geometrically large computational domains, adding to the computational expense of the simulations. As a result of the high computational cost of self-excited LES studies, there are only a limited number of studies that have been done. As computational resources are continually being improved, however, it is becoming more feasible to complete these simulations.

As stated above, the acoustics of compressible flows are naturally captured by compressible LES, provided that the proper boundary conditions are applied. How to model the combustion and chemistry, however, remains a critical issue for complex applications. Roux, et al (Roux, 2010) performed a study using LES of a side-dump ramjet combustor to investigate how the combustion and chemistry modeling affects the numerical predictions of the problem. The first simulation was based on a one-step chemistry model that is known to overestimate the laminar flame speed in fuel rich conditions. The second simulation was based on the same scheme, but with a correction of reaction rates for rich flames. The laminar flame speed is fitted to provide the proper behavior at rich equivalence ratio values.

The configuration in this study, shown in Figure 13, was acoustically choked and consisted of a choked air intake by specifying a constant mass flow rate and stagnation temperature, and a choked nozzle exit.

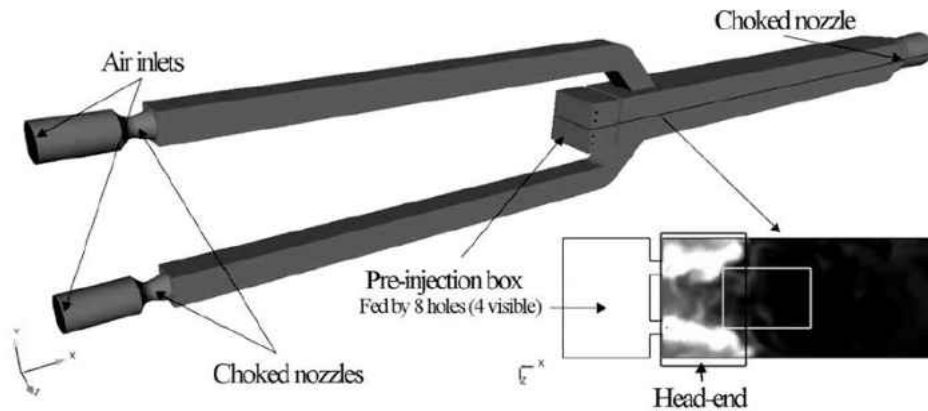


Figure 13: Computational domain for self-excited study performed by Roux (Roux, 2010)

This allowed for the comparison between the results found from the simulations and experimental results. The computational domain included a minimum grid size of approximately 1mm, resulting in a mesh of 5 million tetrahedral elements. The acoustic CFL number was maintained at 0.7 and the time step was 3E-07 seconds. The chamber walls were assumed to be non-slip and adiabatic. It was noted, however, that the impact of adiabatic walls as compared to fixed temperature walls did not show significant impact on the two LES limit cycles. Gaseous propane was the fuel used in both the experiment and numerical study. Two simplified one-step chemical schemes were used, both accounting for 5 species and a global one-step irreversible reaction. The parallel LES code solved the fully compressible Navier Stokes equations using an explicit cell-vertex approximation. This provided third-order accuracy on hybrid meshes, adequate for the low dissipation requirements of LES.

Roux found that one key difference between the two LES simulations was the position of the flame. The fitted one-step scheme matched the experimental results closely, showing a stabilized flame in the main chamber and away from the air inlets. The standard one-step scheme



incorrectly produced combustion in the head end region of the combustor, attributed to the fact that this standard scheme allows combustion to proceed, even for high equivalence ratios. This difference in flame position resulted in different thermoacoustic coupling mechanisms for each simulation. Pressure spectra for both cases are shown below in Figure 14.

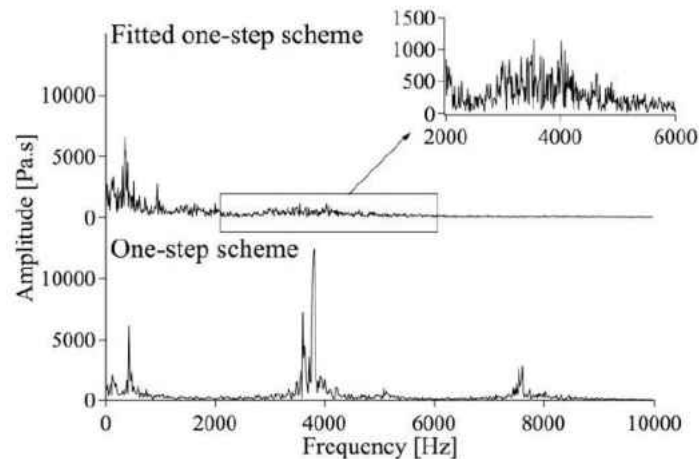


Figure 14: Pressure spectra for two chemical schemes used by Roux (Roux, 2010)

Results obtained with the standard one-step chemistry exhibited high frequency self-sustained oscillations, however, those high frequencies were damped with the fitted scheme. When compared to the experiment, the fitted one-step scheme yielded better predictions than the standard scheme. For the standard one-step chemistry scheme, combustion proceeded, even for high equivalence ratios; however, because of the rich side corrections introduced in the fitted one-step scheme, flow speeds in the head-end zone were large enough to prevent combustion in this region, as observed experimentally. Roux concluded that the chemical scheme for this ramjet burner exhibited a strong impact on the predicted stability. Roux suggested that approximate chemical schemes, even in a limited range of equivalence ratios, can lead to the occurrence of non-physical combustion oscillations. However, it was noted that this strong role that the

chemistry plays on the stability of the combustor may only apply to these ramjet combustors due to the absence of the flame holder in the combustion chamber. While the slight differences in flame location in this study altered the thermoacoustic coupling mechanism that was present, the same effect may or may not be observed for different geometrical scenarios.

Wolf et al (Wolf, 2009) investigated full Large Eddy Simulations of two annular helicopter combustors, each with a different swirler design. A fully compressible unstructured explicit code was used to solve the reactive multi-species Navier Stokes equations. A third order finite element scheme was used for both time and space and subgrid scales were modeling using Smagorinsky turbulence modeling. The chemistry in the simulations was computed by a reduced one-step mechanism for JP-10 and air flames, and to better capture flame/turbulence interactions, the dynamic thickened flame model was used. To avoid uncertainty in the boundary conditions, the whole chamber was computed, including the casing. The computational domain started immediately after the compressor's outlet, where the inlet profiles were known, and extended to a choked nozzle, corresponding to the throat of the high pressure distributor. A 1/15<sup>th</sup> sector is shown in Figure 15.

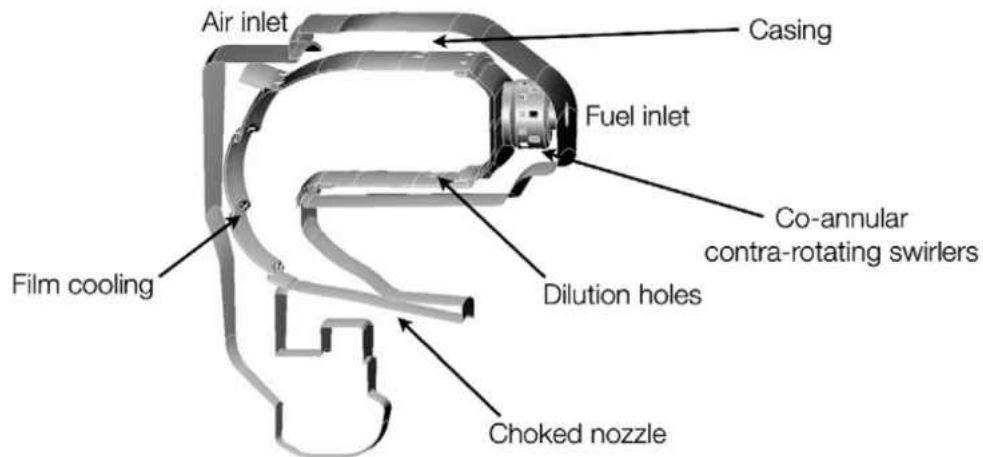


Figure 15: Computation domain of the sector rig studied by Wolf (Wolf, 2009)

This computational domain resulted in mesh sizes between 37-42 million elements. Time steps were between  $5.9\text{E-}8$  and  $7.5\text{E-}8$  seconds and 0.1 seconds of physical solution time was achieved, after nearly 400,000 CPU hours. This massive computational expense is typical of self-excited LES simulations.

Both cases (differing only by the geometry of the swirler) showed different thermoacoustic responses and limit-cycles for the self-excited rotating azimuthal modes that were captured by the LES. The pressure and temperature fluctuation levels for one of the cases are represented by the cylindrical cut surfaces shown in Figure 16.

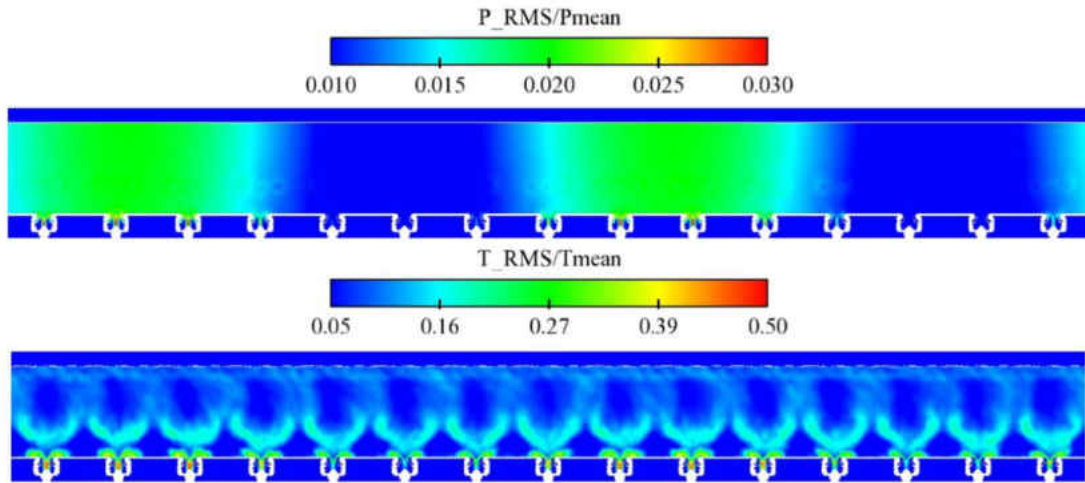


Figure 16: Pressure and temperature fluctuation levels found by Wolf (Wolf, 2009)

As can be seen from the pressure fluctuation, a clear azimuthal acoustic mode developed in the domain, demonstrating the potential of LES as a much needed design tool relating to gas turbine combustion instabilities.

Results found that both swirlers revealed self-excited azimuthal acoustic modes and the resulting rotating pressure waves perturbed the flame axially and azimuthally. This study clearly exhibited that with sufficient computational resources, LES is an invaluable tool for full scale analysis of combustion systems. It not only provides the thermoacoustic analysis of a system in terms of frequencies and limit cycles amplitudes, but also can be used to investigate the physics of the flow, including how flames are perturbed and interact with each other in a particular chamber.

Another study performed by Roux et al (Roux, 2005) investigated the turbulent flow within a complex swirled combustor using compressible LES, acoustic analysis, and experimental results. To allow for a more direct evaluation of the capabilities and limitations of

the LES and acoustic analysis, the boundary conditions were kept simple: a constant mass flow rate was imposed at the inlet while an atmospheric pressure was specified far away from the exhaust. Adding a part of the exhaust atmosphere to the computational domain was computationally expensive, but Roux claimed that it was necessary so that the acoustic waves reaching the chamber exhaust were properly transmitted or reflected without having to specify an acoustic impedance at the exhaust section. This atmospheric pressure region was meshed with progressively larger elements to damp perturbations. Characteristic methods were used to specify boundary conditions. The boundary conditions used in this study are detailed in Figure 17.

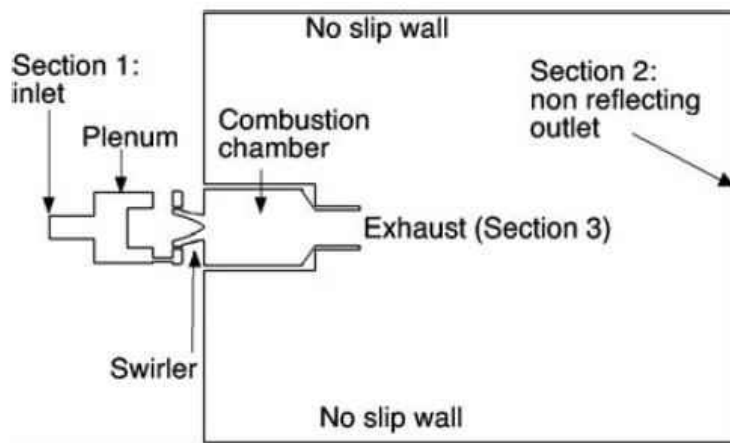


Figure 17: Computational domain and boundary conditions used by Roux (Roux, 2005)

The walls of the combustor were treated as adiabatic in the simulation. Subgrid stresses were modeled using the Wale model and a thickened flame efficiency function model was used with 6 species and 2 reactions for the methane/air combustion. The computational domain consisted of 3 million elements and time steps for the simulation were approximately  $1.5E-06$  seconds. The mesh size near the walls was not refined enough to correctly resolve the turbulent boundary layer, however, it was found that this had limited effects on the results, as shown by

comparing the LES results to the experimental LDV results. Most of the turbulent activity was generated by velocity gradients inside the chamber, which were well resolved on the grid.

In conjunction with the LES, an acoustic solver was used that solved the Helmholtz equation applied to the same unstructured grid. The acoustic boundary conditions were matched to those of the LES by treating the inlet as a velocity node and the boundary of the atmospheric region as a pressure node. For the reacting flow, two self-excited modes were present in the experimental study, around 300 and 570 Hz. Using the Helmholtz solver, these two modes were identified as the  $\frac{1}{4}$  wave and  $\frac{3}{4}$  wave modes of the combustor. The frequency of the self-excited mode from the LES simulations was determined to be 500 Hz. This slight deviation from the experimental and analytical results is attributed to inaccuracies in the acoustic boundary conditions of the LES.

The comparison of the LES results with experimental LDV confirmed the remarkable predictive capacity of LES methods and also highlighted the need for well-defined boundary conditions. In this study specifically, the computation had to include the swirler vanes and could not start at the chamber inlet plane.

Similar to the study performed by Wolf, Staffelbach et al (Staffelbach, 2009) presented an LES simulation of a full helicopter annular combustion chamber in which a self-excited azimuthal mode developed naturally. A strong oscillation of the transverse velocity component appeared at 740 Hz. This frequency matched with the frequency of the first azimuthal mode of the chamber which was also obtained using a Helmholtz solver, assuming the mean temperature distribution in the combustor. Transfer functions were measured for each individual burner in the chamber.

Similar to other studies, the Smagorinsky turbulence model was used for modeling the subgrid scales. The combustion of the JP10/air flames was modeled using an Arrhenius type reaction with a one-step scheme. The turbulence flame interaction was modeled using a dynamic thickened flame approach. The inlet of the 42 million tetrahedral mesh was specified as a non-reflective boundary while the outlet was choked. The time step was  $6.7E-8$  seconds.

By observing the temperature field on a cylindrical plane through the chamber, Staffelbach concluded that the flames oscillated azimuthally, moving from left to right at a frequency near 740 Hz. This azimuthal motion was accompanied by an axial displacement of the flames. Figure 18 shows an instantaneous temperature and pressure field, demonstrating how the distance between the flames and the burner exit planes changes. The pattern oscillated at the frequency of the azimuthal mode.

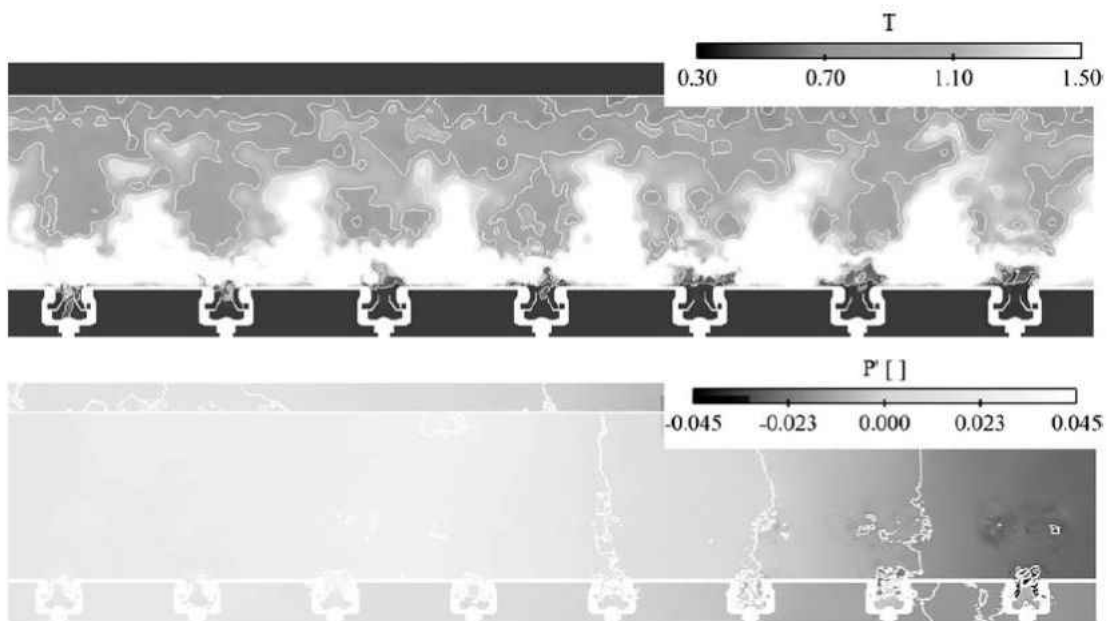


Figure 18: Instantaneous temperature and pressure field solved by Staffelbach (Staffelbach, 2009)

From the results of this study it was concluded that for this particular setup, the burners reacted only to axial flow rate perturbations and did not interact with neighboring burners when a limit cycle was induced by the azimuthal mode. It was claimed that this finding confirms that models based on simple quasi-dimensional networks of the annular chamber are adequate to study the stability of annular combustion chambers, assuming that the burners transfer function is known. This conclusion, however, is specific to the particular setup considered here and could not have been verified without the self-excited LES simulations. Also, while the flame transfer function for this particular geometry could be computed from LES or experimental results on a single sector, this may not always be the case for geometries where the flames from adjacent burners interact with each other.

Recent studies at Purdue University employ the use of an in-house hybrid RANS/LES, or detached eddy simulation (DES), code to numerically investigate combustion instabilities and compare with experimental results. Xia et al (Xia, 2011) studied self-excited combustion instabilities present in an axisymmetric dump combustor fed by separate fuel (JP-8) and oxidizer ( $H_2O_2$ ) streams. The General Equation and Mesh Solver (GEMS) code used in this study solves the Navier Stokes equations, in conjunction with species equations and a relevant turbulence model. 2<sup>nd</sup> order accurate methods in space and time are employed and a finite volume solution method allows for the use of unstructured grids.

The computational domain of the combustor included choked oxidizer slots, fuel inlet passages, and a converging diverging nozzle at the exit of the chamber that exhibited choked flow at the throat of the nozzle. Figure 19 shows details of the computational grid used in the



study. Comparative studies were performed to determine the effect of mesh resolution and the chemical kinetic modeling on the frequencies and amplitudes of the self-excited instabilities.

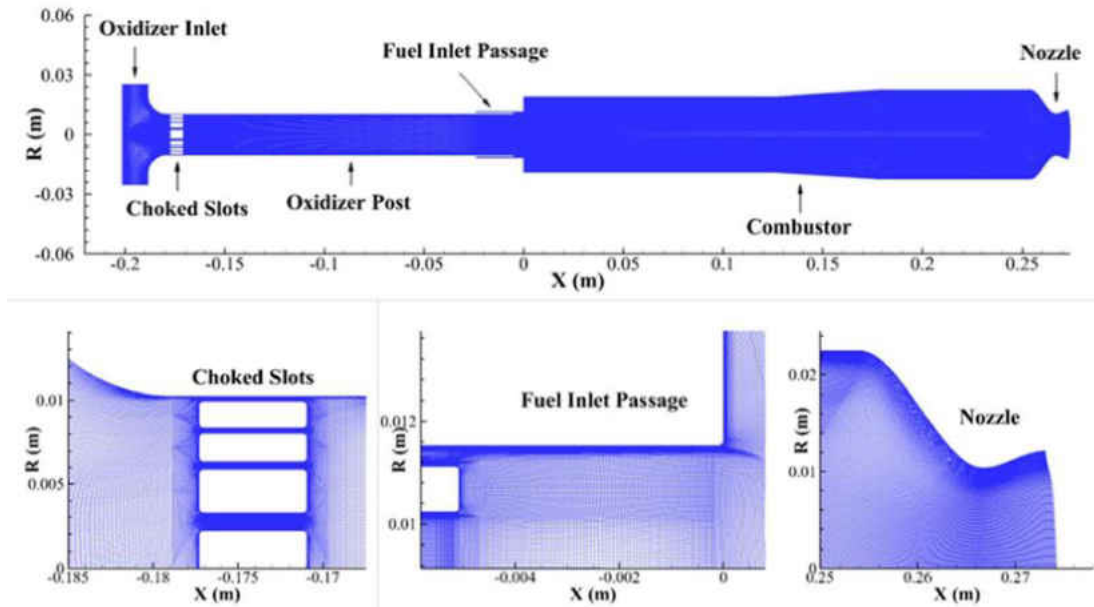


Figure 19: Computational grid used by Xia (Xia, 2011)

The grid resolution comparison consisted of a two-dimensional simulation with a coarse grid of 195,000 cells and a fine grid of 495,000 cells. From observing the pressure traces as well as the corresponding PSD's of the pressure signals, it was found that the first dominant mode, corresponding to the 1L mode of the combustor, was weaker in the coarse grid results. The second and third modes were barely visible from the pressure traces. The frequency of the first mode was 1875 Hz for the coarse grid, compared to 2000 Hz for the fine grid. These effects were attributed to the fact that the fuel burns faster and the oxidizer is consumed more completely in the fine grid case. It was also found that the heat release is stronger in the fine grid case, which, when coupled with the pressure oscillation at the head end of the combustor (located at a pressure anti-node), results in a stronger instability. The peak value of the Rayleigh index was

found to be nearly twice as high in the fine grid case as compared to the coarse grid case, as shown in Figure 20.

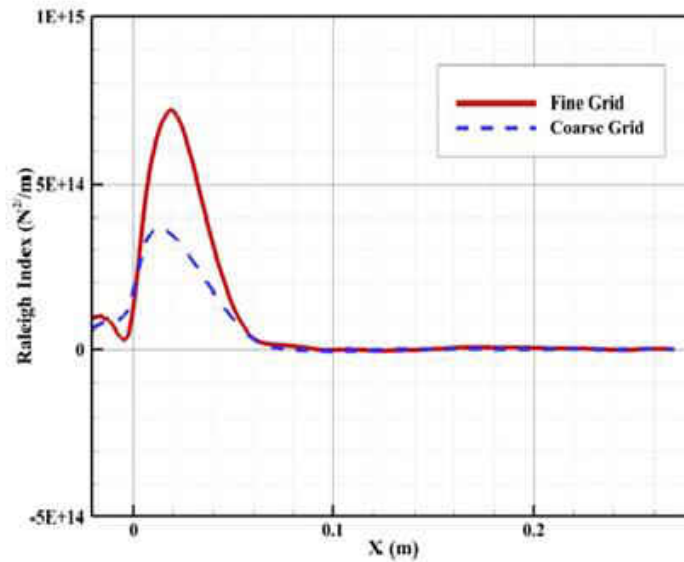


Figure 20: Rayleigh index from coarse grid and fine grid cases (Xia, 2011)

For this particular study, it was found that the single step and multiple step reactions gave close results. The first longitudinal mode peaked slightly higher with the multistep reaction and the frequency was slightly lower, and actually further from the frequency observed in the experiment. This is attributed to a relatively shorter cold region of reaction and overall hotter chamber temperature for the single step reaction. The Rayleigh index for the multistep reaction was also found to be slightly higher than that of the single step reaction. PSD's of the pressure traces comparing the single step reaction with the multistep reaction are shown below in Figure 21.

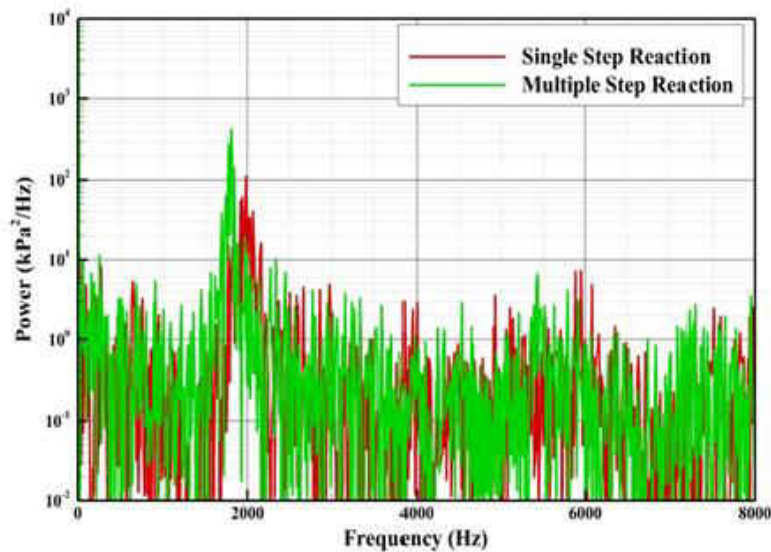


Figure 21: PSD's of pressure traces from single step and multi-step reaction cases (Xia, 2011)

While a limited number of self-excited reacting LES studies have been performed with the goal of studying combustion instabilities, they typically have been done using custom solvers developed by the research organization performing the study. There are only a few studies, at most, that have performed self-excited LES simulations using a commercial or open source CFD code that is available to the public. One such study was recently performed by Lorstad et al (Lorstad, 2010), who modeled a Siemens combustor rig equipped with an SGT-800 DLE burner using experimental and LES calculations. The LES model was based on OpenFOAM's unstructured finite volume framework and solved the filtered compressible reactive Navier Stokes equations. The methane/air combustion was modeled using a three-step combustion model. Both an atmospheric case and a higher pressure case were investigated, where high pressure effects were considered by incorporating pre-exponential factors scaled by the pressure ratio to the power of -0.92. A representation of the LES boundary conditions is shown in Figure 22, where velocity and temperature were specified for the pilot and main air and fuel inlets. Wall

temperatures were set according to the measured rig wall temperatures and the outlet of the domain utilized a wave-transmissive boundary condition to minimize reflection.

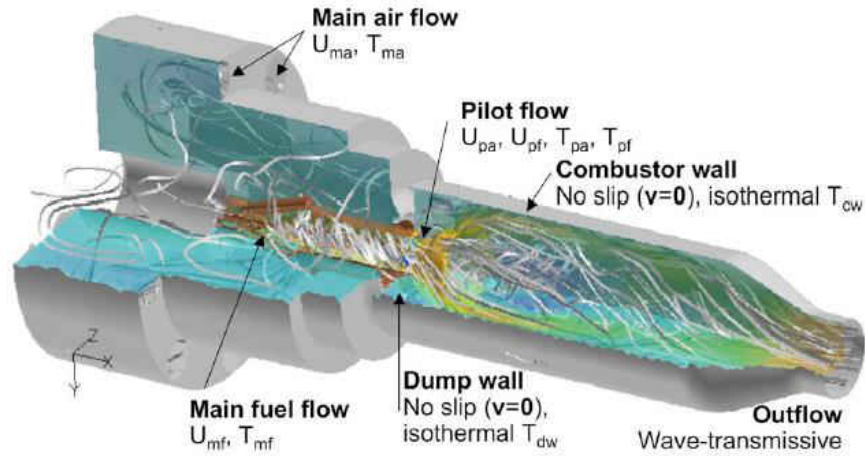


Figure 22: Computational domain and boundary conditions used by Lorstad (Lorstad, 2010)

The atmospheric case predicted strong combustion dynamics and indicated the existence of a strong axial mode. The increase in pressure from atmospheric to the full load gas turbine operating conditions significantly affected the dynamics. Good agreement was found between the dominant frequency obtained in LES and the frequencies detected during combustion tests, again verifying that LES is a promising tool for predicting combustion dynamics.

This review of self-excited LES studies has shown the capability of high fidelity numerical modeling tools that can capture both the complex physics of unsteady heat release oscillations as well as the acoustic phenomena represented by the compressible fluid mechanics equations. This review has shown that such studies can provide a much needed designed tool for modeling of gas turbine combustion systems. As each specific geometry and flow configuration has a direct effect on the flow physics of combustion instabilities present in the combustor, one

solution to the general problem cannot exist. Rather, detailed models must be made specific to each case. While some general guidelines can be implemented, it is apparent that some techniques may prove useful for one particular case while causing significant discrepancies in other cases. Consequently, care should always be given to understand how each technique or method will affect the specific case being studied.

An additional conclusion that can be drawn from this review is that while several self-excited combustion instability studies have been performed relating to specific geometries, fundamental studies are lacking that investigate the coupling between the heat release and pressure oscillations using high fidelity numerical models. Also, while there are a limited number of studies on reacting and non-reacting jets injected into unsteady cross flows, there are no numerical studies that incorporate both the full physics of the self-excited unsteady cross flow with the response of a reacting jet at high pressure conditions. This study will begin to fill these gaps by investigating full, self-excited LES simulations of a reacting jet injected into an unsteady cross flow. The unsteady cross flow is naturally generated by modeling a dump combustor, designed to be unstable at the longitudinal frequencies of the geometry. The simulations are run at typical gas turbine operating conditions, including similar temperatures, high pressures, and frequencies of combustion instability. This will provide detailed insight into the fundamental mechanisms of combustion instability at the head end reaction and at the reacting jet, with direct application to the gas turbine industry. All of the simulations will be validated against experimental and analytical results.

## **CHAPTER 3 – METHODOLOGY**

### **Overview of Proposed Tools and Methods**

When presented with a problem in industry that needs to be solved or analyzed, there are a broad range of tools and methods that can be used, many of which can provide valuable results with varying levels of required time and resources. As a result, it is important to focus on the objectives of a particular study and determine what tools have the most potential to provide a complete solution to the problem being investigated, within the required time frame and available resources.

As this study seeks to analyze and understand the flow phenomena related to a reacting JICF with application to combustion instabilities, a tool is necessary that can capture the physics of the flow as well as the source of the combustion instability. Whenever practically possible, one of the most widely used tools for this type of analysis is LES. This is because LES can capture both the complex physics of unsteady heat release oscillations as well as the acoustic phenomena represented by the compressible fluid mechanics equations. As mentioned earlier, this allows for the simulation of the coupling between the unsteady heat release and the acoustics of the flow, known to be the source of combustion instabilities. A specific type of LES modeling is known as self-excited LES, where the combustion instabilities present in the system develop naturally from the accurate calculation of the flow physics, as well as the correct implementation of boundary conditions. Self-excited LES provides one of the most accurate numerical modeling tools, as no artificial forcing is applied to the flow. Instabilities are generated solely from the interaction between heat release and acoustics, just as they are in the actual system being studied. For fundamental studies, this type of analysis can provide a significant amount of insight that

other tools may lack. As the combustion system modeled in this study is relatively simple, these self-excited LES simulations can be run in a reasonable length of time, given a sufficient amount of computational resources.

### **Background of OpenFOAM**

The simulations in this study are run using the OpenFOAM library (SGI, 2011), specifically the v1.7.x release. OpenFOAM (Open Field Operation And Manipulation) is a C++ based open source CFD toolbox for the numerical simulation of complex fluid flows including chemical reactions, turbulence, and heat transfer. OpenFOAM constructs matrix equations separately for each equation using the finite volume method applied to arbitrary shaped cells. OpenFOAM contains a variety of discretization schemes, generally limited to second-order accuracy, to enable reliable solutions. The source code for OpenFOAM is completely open source and can be utilized in parallel on an unlimited number of processors without any licensing costs. This makes it highly desirable from an economic standpoint, especially for computationally expensive simulations that would require an extensive amount of commercial licenses to run in parallel.

### **Background of LES**

Numerical modeling of turbulent flow is typically achieved using one of three general methods, all of which solve some form of the Navier Stokes equations. The most computationally expensive method is to use Direct Numerical Simulations (DNS) where no turbulence modeling is used and all turbulent scales are solved explicitly. This requires extremely fine meshes, however, as the mesh resolution has to be lower than the characteristic

length of the smallest scales present in the flow. Even with recent computational advances, DNS studies are difficult to achieve and are often not practical for specific engineering applications.

Currently the most often used method of numerical modeling involves what are known as the Reynold's Averaged Navier Stokes (RANS) equations. These equations describe the mean flow field and include some type of turbulence model for closure of the Reynold's stress term. The benefit of such modeling is that the computational cost is relatively low and the RANS methods provide useful predictions of the mean flow field. However, these models are limited by the averaging procedures and turbulence models that must be used and do not solve the equations in the temporal domain.

Large Eddy Simulations (LES) are becoming increasingly popular as they provide somewhat of a compromise between the extensive computational resources required by DNS and the limited results that are generated from RANS. LES simulations solve for the large scale structures of the flow, but model the smaller scale structures of the flow that are more isotropic and easier to accurately model. The smaller scales also contain less energy and thus, any potential inaccuracies involved in modeling them have less of an effect on the overall flow. Figure 23 shows a representation of the typical approaches to numerical modeling, in terms of the energy and wavenumber of the structures that are modeled and computed. For LES, the critical wave number is often defined by the mesh size and should be within the self-similar range of turbulence.



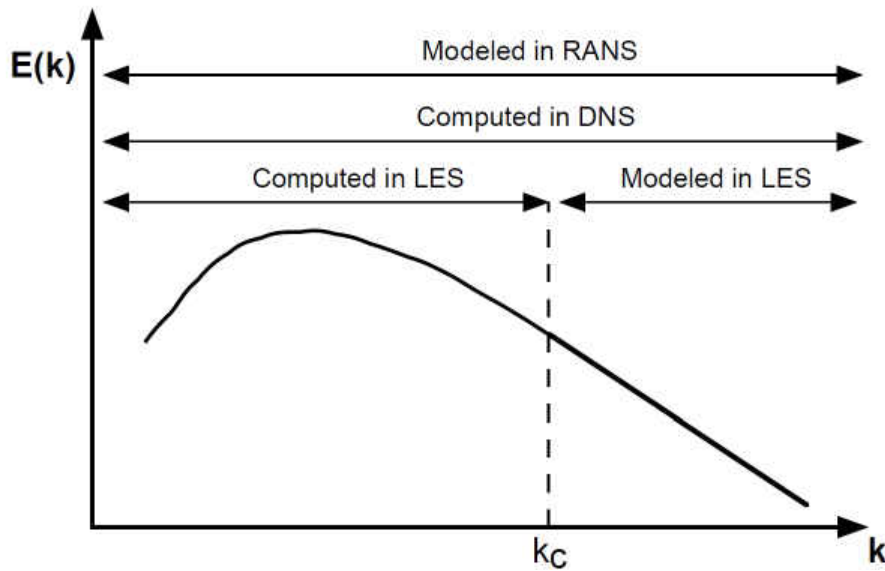


Figure 23: Turbulence energy spectrum as a function of wavenumber, representing typical approaches to numerical modeling (Poinsot, 2005)

An LES solver, FSDFOAM (Beck, 2009; Di Domenico, 2011), is used for the simulations run in this project that solves the fully compressible Navier Stokes Equations. FSDFOAM uses a standard Pressure Implicit with Splitting of Operators (PISO) algorithm (Versteeg, 1995). This same PISO algorithm is used by the standard supersonic solvers that are provided with OpenFOAM. Based on discussions with Aleksandar Jemcov, an OpenFOAM developer with Wikki Ltd, it was concluded that pressure based solvers, like the one used for this project, are sufficient to model flows with Mach numbers less than 3, as long as high resolution in flow discontinuities is not required (such as highly resolved shocks). For flows greater than Mach 3, or for highly resolved discontinuities, it would be necessary to upgrade to a density based solver (Jemcov, 2011).

The solutions are initiated using first order discretization schemes for time (Euler) and the divergence of velocity (upwind). This allows for a stable approach until the solution converges to

a stationary solution from the specified initial condition. Once this stationary solution is achieved, second order discretization schemes are implemented for time (Crank Nicholson) and the divergence of velocity (Gauss linear).

A total of seven transport equations are solved, including mass, momentum, total enthalpy, mixture fraction, and reaction progress variable. For LES, each of the variables represented by the transport equations are filtered in physical space, where the filtered quantity,  $\bar{f}$ , is defined in Equation (3) as:

$$\bar{f}(x) = \int f(x')F(x-x')dx' \quad (3)$$

where  $F$  is the LES filter. For this project, the common approach is used that averages over a cubic box of size  $\Delta$ . The LES filter then becomes:

$$F(x) = F(x_1, x_2, x_3) = \begin{cases} 1/\Delta^3 & \text{if } |x_i| \leq \Delta/2 \\ 0 & \text{otherwise} \end{cases} \quad (4)$$

where  $\Delta$  is defined as the cubic root of the local cell volume. This resulted in an approximate filter width of 0.5 to 1.8 mm, depending on the refinement level in each region of the domain. At the dump plane, this equated to a filter width of less than one-tenth of the step height. At the exit of the jet in cross flow (JICF), this equated to a filter width of approximately 1/30<sup>th</sup> of the jet exit diameter.

For variable density flow, a mass-weighted Favre filtering is used, given by Equation (5):

$$\bar{\rho} \tilde{f}(x) = \int \rho f(x')F(x-x')dx' \quad (5)$$

This implies that LES solves for the mean value over a given cell. The filtered quantity,  $\bar{f}$ , is resolved in the numerical simulation while the  $f' = f - \bar{f}$  term corresponds to the unresolved part. This is the subgrid scale term due to unresolved flow motions that must be modeled using a specified subgrid model.

Filtering the instantaneous Navier Stokes Equations leads to the following result for the conservation of mass (Poinsot, 2005):

$$\frac{\partial \bar{\rho}}{\partial t} + \frac{\partial (\bar{\rho} \tilde{u}_i)}{\partial x_i} = 0 \quad (6)$$

and momentum:

$$\frac{\partial (\bar{\rho} \tilde{u}_i)}{\partial t} + \frac{\partial (\bar{\rho} \tilde{u}_i \tilde{u}_j)}{\partial x_j} = -\frac{\partial \bar{p}}{\partial x_i} + \frac{\partial \bar{\tau}_{ij}}{\partial x_j} + \frac{\partial T_{ij}}{\partial x_j} \quad (7)$$

Here the unresolved part of the convection term,  $T_{ij} = -\overline{\bar{\rho} u_i' u_j'}$ , must be modeled by a subgrid scale turbulence model. For this study, the Smagorinsky turbulence model is used to model these flow characteristics below the size of the filter width. This model represents the unclosed term as (Poinsot, 2005):

$$T_{ij} - \frac{\delta_{ij}}{3} T_{kk} = -\mu_T \left( \frac{\partial \tilde{u}_i}{\partial x_j} + \frac{\partial \tilde{u}_j}{\partial x_i} \right) = -2\mu_T \tilde{S}_{ij} \quad (8)$$

The turbulent viscosity is modeled as:

$$\mu_T = \bar{\rho} (C_s \Delta)^2 |\tilde{S}| = \bar{\rho} (C_s \Delta)^2 (2\tilde{S}_{ij} \tilde{S}_{ij})^{1/2} \quad (9)$$

where  $C_s$  is model constant and  $\Delta$  is the filter width, defined as the cubic root of the local cell volume. The value of  $C_s$  is taken as 0.202, the estimated value for homogeneous isotropic turbulence (Poinsot, 2005). Caution should be taken when using the Smagorinsky model, as some research has suggested that it is too dissipative (Poinsot, 2005).

The turbulent viscosity at the walls of the domain is modeled using the Spalart-Allmaras turbulence model (Spalart, 1994). This model determines the turbulent viscosity using the following equation:

$$\mu_T = \rho \nu_T \frac{\chi^3}{\chi^3 + c_{vl}^3} \quad (10)$$

where  $\chi = \frac{\nu_T}{\nu}$  and  $c_{vl}$  is a model constant, commonly taken as 7.1 (Spalart, 1994).

### Background of Combustion Modeling

The combustion model in this study was based off of the approach used by Weller and Tabor et al (Weller, 1998; Tabor, 2004) and was applied by Di Domenico et al (Di Domenico, 2011). For the energy equation, it is assumed that the energy of the viscous stresses can be neglected compared to the heat release of combustion and that thermal diffusion can be ignored (Derksen, 2005). These assumptions simplify the transport equation for total enthalpy to the following form:

$$\frac{\partial \bar{\rho} \tilde{h}}{\partial t} + \frac{\partial}{\partial x_i} \cdot (\bar{\rho} \tilde{u}_i \tilde{h}) = \frac{D\tilde{p}}{Dt} - \frac{\partial}{\partial x_i} \cdot (-\bar{\rho} \overline{u_i' h'}) \quad (11)$$

The unclosed term,  $-\bar{\rho} \overline{u_i' h'}$ , is modeled using a gradient assumption:

$$-\overline{\rho u_i' h'} = \overline{\rho} D_\lambda \frac{\partial \tilde{h}}{\partial x_i} = \frac{\mu_T}{Pr} \frac{\partial \tilde{h}}{\partial x_i} \quad (12)$$

where  $D_\lambda$  is the thermal diffusion coefficient (Derksen, 2005) and  $Pr$  is the Prandtl number.

The species mass fraction transport equation is given as:

$$\frac{\partial(\overline{\rho} \tilde{Y}_k)}{\partial t} + \frac{\partial(\overline{\rho} \tilde{u}_i \tilde{Y}_k)}{\partial x_i} = \frac{\partial}{\partial x_i} \cdot \left( \overline{\rho} \overline{D}_k \frac{\partial \tilde{Y}_k}{\partial x_i} \right) + \frac{\partial \Psi_{kj}}{\partial x_j} + \tilde{\omega}_k \quad (13)$$

Here the  $\Psi_{kj} = -\overline{\rho u_j' Y_k'}$  term describes the sub grid fluctuations of the species mass fractions and must be modelled by a sub grid scale model.

Assuming a single step, two species reaction (fuel and oxidizer), the species mass fraction transport equation can be rewritten as a function of the mixture fraction,  $f_T$ , and the reaction progress variable,  $b$ , which are defined as:

$$f_T = \frac{Y_k - Y_{kO}}{Y_{kF} - Y_{kO}} \quad (14)$$

$$b = \frac{Y_k - Y_{k,unburnt}}{Y_{k,burnt} - Y_{k,unburnt}} \quad (15)$$

where  $Y_k$  represents the species mass fraction of species  $k$  and the subscripts  $F$  and  $O$  represent the fuel and oxidizer, respectively.

As seen from the definitions above, the mixture fraction indicates the ratio between fuel and oxidizer while the reaction progress variable is a non-dimensional parameter that represents

the degree of completeness of the reaction. The reaction progress term varies from one in the unburnt reactants to zero in the fully burnt products (note that this is opposite of the standard definition of what is commonly called the regress variable). Again, modeling the unclosed terms using a gradient assumption, the following form of the final two transport equations can be derived:

$$\frac{\partial(\bar{\rho} \tilde{f}_T)}{\partial t} + \frac{\partial(\bar{\rho} \tilde{u}_i \tilde{f}_T)}{\partial x_i} = \frac{\partial^2}{\partial x_i \partial x_i} \left( \bar{\rho} \bar{D} + \frac{\mu_T}{S_C} \tilde{f}_T \right) \quad (16)$$

$$\frac{\partial(\bar{\rho} \tilde{b})}{\partial t} + \frac{\partial(\bar{\rho} \tilde{u}_i \tilde{b})}{\partial x_i} = \frac{\partial^2}{\partial x_i \partial x_i} \left( \bar{\rho} \bar{D} + \frac{\mu_T}{S_C} \tilde{b} \right) + \tilde{\omega}_R \quad (17)$$

where  $D$  and  $S_C$  represent the mass diffusivity and Schmidt number, respectively.

Closure of the source term present in the reaction progress transport equation is obtained using a turbulent flame speed closure (TFC) combustion model. This gives the following relation for the reaction source term (Poinsot, 2005):

$$\tilde{\omega}_R = \bar{\rho}_u S_T |\nabla \tilde{b}| = \bar{\rho}_u S_L \Sigma |\nabla \tilde{b}| \quad (18)$$

The ratio between the turbulent and laminar flame speed, or wrinkling factor, is determined from the Bradley correlation (Beck, 2010) which gives the following relation for the wrinkling factor,  $\Sigma$ , where  $A$  is a constant (Bradley, 1992):

$$\Sigma = 1 + \frac{(0.95A)}{Le} (\text{Re}_T \text{Pr})^{0.5} \quad (19)$$

For this study, the constant  $A$  was taken as 0.5 for the head end flame, while a value of 0.3 was applied for the JICF flame. Studies have shown that for co-flow methane/air jet flames it is recommended to use a value between 0.25 and 0.5 (Govert, 2011). The sensitivity of the simulation results to this constant was investigated and is detailed below.

### ***Implementation of strain and heat loss models***

Recent extensions to turbulent flame speed type combustion models have included additional factors in the equation for the reaction rate that account for strain and heat loss effects on the laminar flame speed. A model developed by Tay et al (Tay, 2009) was implemented into the current combustion model to allow for the investigation of strain and heat loss effects in the simulations. The model provides improvement to the calculation of the reaction rate in regions of large strain and regions close to non-adiabatic walls where heat loss can increase the sensitivity of the flame to strain.

An effective strain rate is defined as the ratio of the strained laminar flame speed to the unstrained laminar flame speed. This parameter is a 3D field that is calculated during simulation run time, and varies from 0 (fully quenched) to 1 (unstrained). The strain rate is applied to the equation for the reaction rate, as shown below, where  $\rho_u$  is the density of the unburnt gas,  $S_{L0}$  is the unstrained laminar flame speed,  $\Sigma$  is the stretch factor (ratio of turbulent to laminar flame speed),  $\sigma$  is the effective strain rate, and  $b$  is the reaction progress variable.

$$\dot{\omega}_R = \rho_u S_{L0} \Sigma \sigma |\nabla b| \tag{20}$$

As is evident from this relation, the effective strain rate, shown below, has a direct impact on the reaction rate.

$$\sigma = \frac{S_L}{S_L^0} = \exp(-KaMa - Ka\chi) \quad (21)$$

where the Karlovitz number,  $Ka$ , represents the non-dimensional strain,

$$Ka = \frac{\alpha K}{S_L^{0.2}} \quad (22)$$

and  $Ma$  and  $\chi$  represent the Markstein number and a heat loss parameter, respectively. A common procedure used to determine the Markstein number is to run counter-flow flame simulations, using a 1D kinetics tool such as Cantera, to obtain data for the strained laminar flame speed as a function of strain. The Markstein number in the model is then tuned to obtain the best fit between the model curve and the Cantera data (Doost, 2013; Krediet, 2012). Applying this method to the high pressure and preheat temperature conditions present in this study resulted in a fitted Markstein number of approximately 0.1, as shown below in Figure 24.



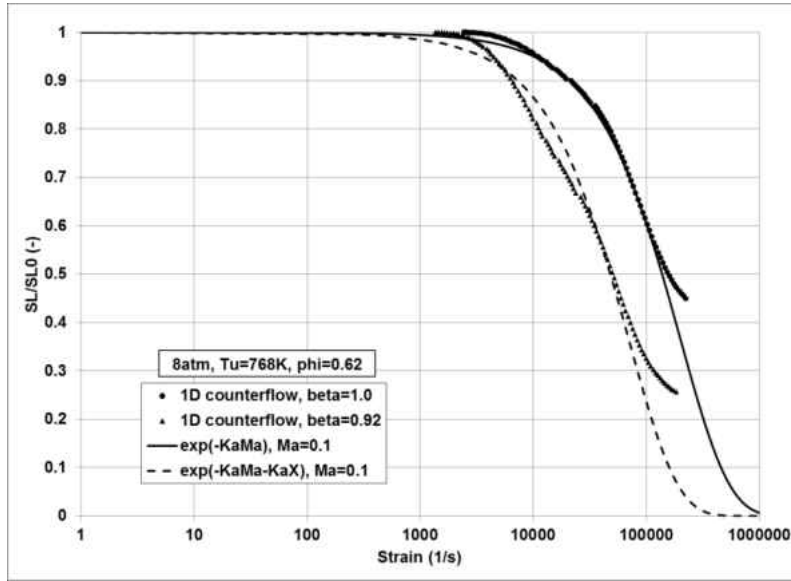


Figure 24: Cantera 1D counterflow data without heat loss ( $\beta=1.0$ ) and with heat loss ( $\beta=0.92$ ), compared to Tay's model (Tay, 2009) with fitted Markstein number.

Because the combustion model source term is a direct function of the gradient of reaction progress variable, it was found that the reaction rate is over predicted in the region immediately after JICF injection where the gradient of reaction progress is very high. This is a known drawback of using a simplified combustion model that includes a limited amount of kinetics in the model. It should be noted, however, that this region immediately after injection is also a high strain region, resulting in a reduction of the reaction rate in this region when the strain model is applied, assuming that the Markstein number is high enough.

The heat loss parameter,  $\chi$ , is defined by Tay as,

$$\chi = \left[ \left( \frac{Ze}{2} \right) \left( \frac{1-\beta}{\beta^3} \right) \right] \quad (23)$$

where the Zeldovich number,  $Ze$ , is defined as,

$$Ze = \left( \frac{E_a}{2RT_{adiab}^2} \right) (T_{adiab} - T_{unburnt}) \quad (24)$$

with  $E_a$  and  $R$  representing the activation energy and the universal gas constant, respectively. The heat loss coefficient,  $\beta$ , is defined as:

$$\beta = \frac{(T_{product} - T_{unburnt})}{(T_{adiabatic} - T_{unburnt})} \approx 1 - \frac{(h_{product} - h_{unburnt})}{H_f Y_f} \quad (25)$$

This heat loss parameter is calculated as a full three-dimensional field during run time.

While the strain and heat loss model discussed above includes a term to account for heat loss in the strained laminar flame speed, it does not account for heat loss in the unstrained laminar flame speed. To determine the effect of heat loss on the unstrained laminar flame speed, multiple premixed 1D flame simulations were run using Cantera and the GRI3.0 mechanism over a range of equivalence ratios and heat loss parameters, at a pressure of 8 bars. The unstrained laminar flame speeds from these calculations were normalized by their corresponding adiabatic unstrained laminar flame speeds and plotted against the heat loss coefficient,  $\beta$ , defined above in Equation (25). The results from these calculations are shown in Figure 25, along with an exponential curve fit of the data.

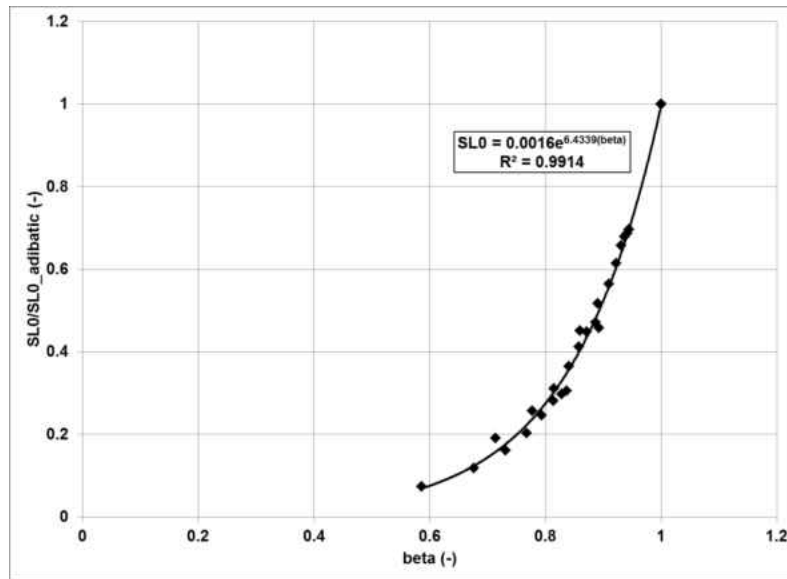


Figure 25: Normalized unstrained laminar flame speed as a function of the heat loss coefficient, taken from 1D premixed flame simulations run using Cantera and the GRI3.0 mechanism at 8bar.

From the 1D premixed flame data, it is evident that even small percentages of heat loss (or an enthalpy reduction from adiabatic conditions) can result in a significant reduction in the unstrained laminar flame speed. In the particular JICF setup investigated in this study, a sufficient amount of heat loss is expected through the walls of the combustor between the head end flame and the JICF flame that could play an important role in the behavior of the JICF reaction.

Several simulations were run to investigate this effect on the JICF flame by implementing the exponential curve fit shown in Figure 25 into the equation for the reaction rate source term, similar to the approach used by Tay et al (Tay, 2009). This resulted in an additional factor that was equal to one when no heat loss was present, but decreased exponentially for values of  $\beta$  less than one. This expression was defined as

$$\frac{S_{L,diab}^0}{S_{L,adiab}^0} = a_1 \exp(a_2 \beta) \quad (26)$$

where  $a_1$  and  $a_2$  are constants, defined from the curve fit as 0.0016 and 6.4339, respectively.

The addition of both the strain and heat loss models results in a final expanded expression for the reaction rate, or source term in the combustion model:

$$\dot{\omega}_R = \rho_u S_{L,adiab}^0 \frac{S_{L,diab}^0}{S_{L,adiab}^0} \frac{S_T}{S_L} \frac{S_L}{S_{L,diab}^0} |\nabla b| \quad (27)$$

The unstrained, adiabatic laminar flamespeed required by the reaction rate source term equation is assumed to be only a function of equivalence ratio for the preheat temperature and pressure of each case run in this study. For a given simulation, the laminar flame speed is tabulated based on these conditions of the methane/air flame using a Cantera based network reactor modeling tool.

Table 2 summarizes the various flame speeds used in Equation (27), as well as the correlations used for each of the flame speed ratios.

Table 2: Summary of flame speeds used in expanded expression for the reaction rate

Variable	Description	Expression	Source	Validity Range
$S_{L,adiab}^0$	Unstrained, adiabatic laminar flame speed	NA	1D premix flame (Cantera, GRI 3.0)	GRI3.0 mechanism developed using data at 1-19.7atm, 300-400K
$\frac{S_{L,diab}^0}{S_{L,adiab}^0}$	Ratio of unstrained diabatic to unstrained adiabatic laminar flame speed	$a_1 \exp(a_2 \beta)$	Current study	Correlation developed using data at 8bar, 468-786K
$\frac{S_T}{S_L}$	Ratio of turbulent to strained laminar flame speed	$1 + \frac{0.95A}{Le} (\text{Re}_T \text{Pr})^{0.5}$	(Bradley, 1992)	Correlation developed using data at 0.1-1atm, 290-583K
$\frac{S_L}{S_{L,diab}^0}$	Ratio of strained to unstrained diabatic laminar flame speed	$\exp(-KaMa - Ka\chi)$	(Tay, 2013)	Correlation developed using data at 1atm, 293K

### Numerical Procedure

The seven transport equations shown above are discretized in time and space and then solved using the PISO algorithm, as mentioned above. Various temporal and spatial discretization schemes were applied to determine their effect on the simulation results, however, the selected discretization schemes included a Crank-Nicholson scheme for the temporal derivatives and linear Gaussian scheme for the spatial derivatives. Further details on the discretization scheme investigations are provided in Appendix A.

The PISO algorithm is a semi-implicit method that first solves the momentum equations to obtain a velocity field. Next, the transport equations for mixture fraction, reaction progress variable, enthalpy, and pressure are solved within the PISO loop. Each equation is solved

sequentially, but multiple times within one time step, until the desired convergence is achieved.

Figure 26 shows a schematic of the PISO algorithm as it is utilized in a finite volume code.

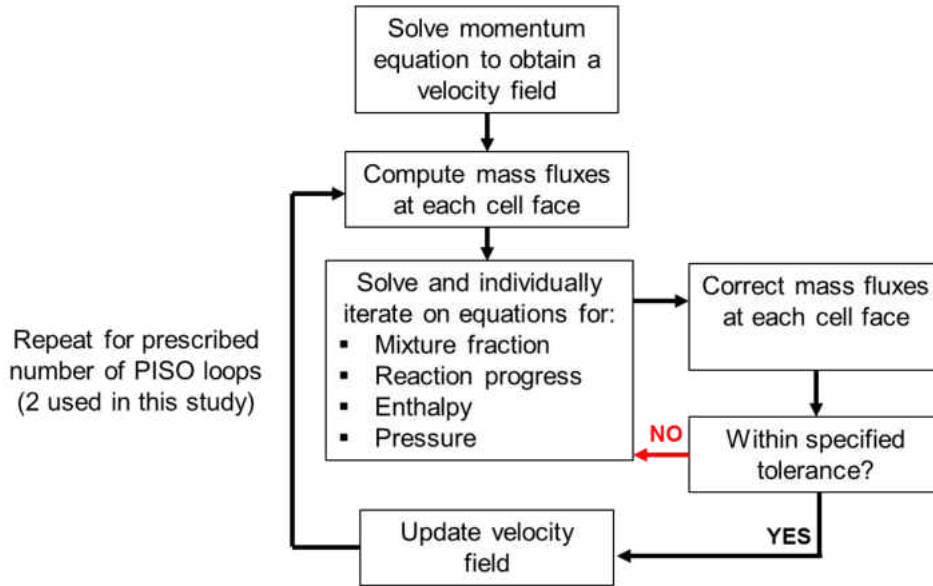


Figure 26: Schematic of the PISO algorithm in a Finite Volume Code

The time step for the simulations is based on the Courant number ( $Co$ ) as well as the Courant-Frederich Lewis number (CFL). The Courant number is given by Equation (28) and is based on the convective velocity, while the CFL number is given by Equation (29) and is based on the speed of sound. For a stable numerical solution using the PISO algorithm, the  $Co$  number must be less than 0.3. Although the value of the CFL number is not restricted when using the PISO algorithm, it has been found to have an effect on the dissipation of acoustic waves (Krediet, 2012). As a result, the CFL number must be chosen based on the frequency range of the instabilities that are to be resolved.

$$Co = \frac{|u|\Delta t}{\Delta x} \quad (28)$$

$$CFL = \frac{(|u| + c)\Delta t}{\Delta x} \quad (29)$$

### **Computational resources**

Parallel processing was performed on up to 296 processors at the Stokes High Performance Computing Center located at the University of Central Florida (Stokes, 2014). Run times vary from approximately 0.2 to 1.5 seconds per iteration, depending on the number of processors used as well as the domain being solved. As of May 2014, the Stokes computing center contains 3450 processors that are interconnected using QDR (40GB/s) and DDR (20GB/s) Infiniband interconnection. The system contains over 7.5 TB of RAM and over 144 TB of configured storage space. For more information on the UCF Stokes Computing Center, see reference (Stokes, 2014).

### **Computational domain and meshing**

One of the objectives of the LES modeling for this project is to obtain simulations that are self-excited, allowing for direct validation with the experimental rig which was designed to exhibit specific self-excited combustion instabilities. In order to achieve this goal, it is necessary to include the entire experimental combustor geometry in the computational domain to ensure that physically accurate boundary conditions can be implemented into the model. These boundary conditions must correctly represent both the acoustic and hydrodynamic boundaries that are seen in the experimental rig. Figure 4, shown previously, shows a schematic of the experimental rig.

The computational domain includes the entire combustor geometry, from the inlet choke plate through the exit nozzle. As will be discussed in detail below, it was also necessary to add

an expansion section to the computational exit nozzle, which is not present in the experimental rig. This ensured that the flow in the throat of the nozzle remained choked, representing the choked acoustic boundary condition found in the experimental rig.

The flow parameters of the baseline head end simulation are matched as closely as possible to one of the experimental runs to allow for direct validation. The head end experimental run chosen for comparison was test E-0-2-x, as labeled by Purdue University. This test was run during the June 2009 test campaign and used pure methane gas as the fuel. An equivalence ratio of 0.62 was achieved and the total mass flow rate of premixed fuel and air was approximately 0.4 kg/s. Based on these testing parameters, the mass flow rate of the premixed fuel and air in the simulation is set to 0.4 kg/s and the thermodynamic properties are determined for a methane/air mixture at an equivalence ratio of 0.62. Similar head end conditions were used for the JICF cases, however, the specific details of these cases will be given in the corresponding results section.

The meshing of the computational domain is performed using snappyHexMesh (SGI, 2011), an unstructured, hex dominant meshing tool that is a part of the OpenFOAM package. Refinement regions are included at critical locations such as the dump plane, the JICF injection region, the exit nozzle, and the wall boundaries.

The first step in the meshing process was to create a CAD model with dimensions that corresponded to the experimental rig. This was done using the Pro Engineer software where an STL file is generated that is required by the snappyHexMesh utility. The baseline CAD drawing is shown in Figure 27, detailing the dimensions that correspond to the experimental rig.



Additional geometries that include the reacting JICF will be given in the corresponding results section.

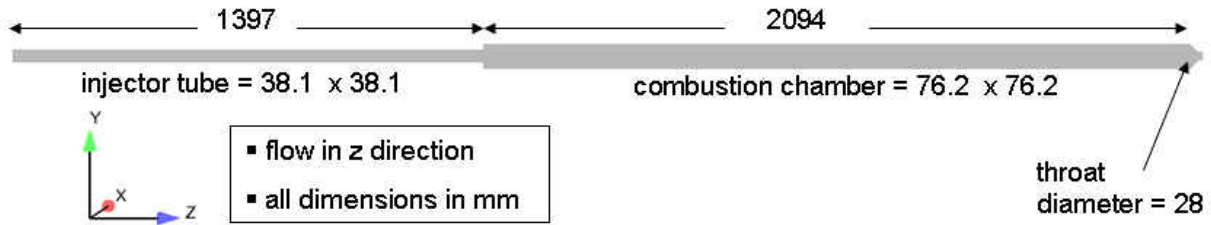


Figure 27: Dimensions of CAD geometry used for meshing

Based on procedures in the literature and industry, baseline refinement levels are chosen within the snappy utility such that the inlet of the domain includes 18 cells per inlet height, the dump plane includes 36 cells per chamber height, and the exit nozzle included 14 cells per exit diameter. A mesh refinement study was conducted to determine the effects of mesh resolution on the results of the simulation. The details of the study are included in the Appendix A, however, it was concluded that for the objectives of this work, the baseline mesh resolution described here was sufficient for the majority of the simulations. Note that further refinement was added in the JICF region for the simulations that included the reacting jet in cross flow, typically ensuring that the diameter of the incoming jet included approximately 30 cells.

Originally, three to five cell layers were added at the wall boundaries such that each cells thickness increased uniformly from the wall by 20-30% until the original cell size was reached. The goal was to ensure that the  $y^+$  values were typically between 30 and 100 (Versteeg, 1995), however, due to deficiencies in the meshing tool, this wall refinement resulted in several skewed cells throughout the mesh that would not allow 2<sup>nd</sup> order discretization schemes. Consequently, no wall refinement was used in the final meshes. The effect of the inlet mesh on the head end

flame was investigated and details are provided in Appendix A. Since no additional refinement near the walls was included, the  $y^+$  values near the wall were typically larger than 30. As a result, the near wall profile assumed a curve fit of the log law profile in the wall region. Because the objectives of this project do not require detailed results in the boundary layer region, it was concluded that removing wall refinement would not negatively impact the validity of the solutions found in this study. This assumption also agrees with similar studies found in the literature (Roux, 2005). It should be noted however, that in cases where it is proposed that the shear layer of an anchored flame or a jet in cross flow can contribute to the mechanisms of combustion instability, it is important to include enough boundary layer refinement to sufficiently capture the shear layer. Although no specific boundary layer refinement was included in the simulations run in this study, it was found that the baseline mesh was refined enough to generate the known instabilities in the chamber, and thus further boundary layer refinement was not used.

Figure 28 shows the entire mesh of the head end only model. Figure 29 and Figure 30 show the mesh in the region of the dump plane and the exit nozzle, respectively. Figure 31 shows the mesh detail around the JICF region.



Figure 28: Entire mesh for head end only model (flow in z direction)

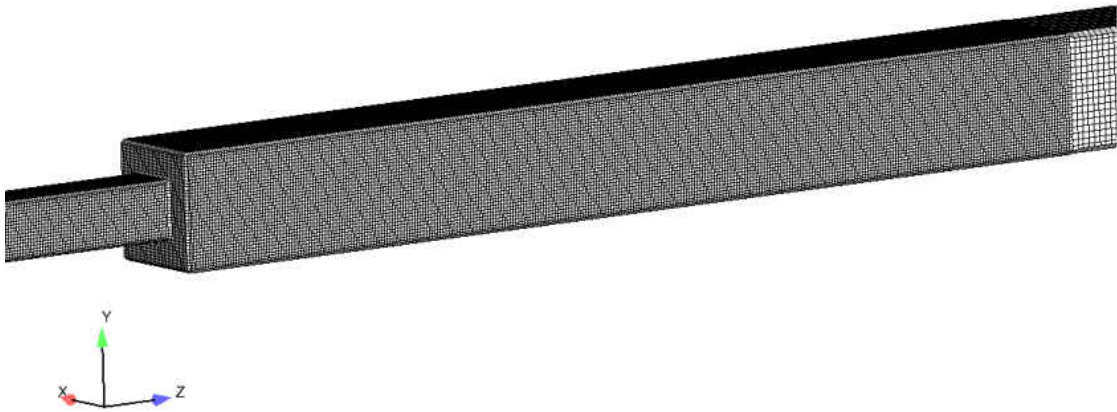


Figure 29: Mesh refinement at the dump plane (flow in z direction)

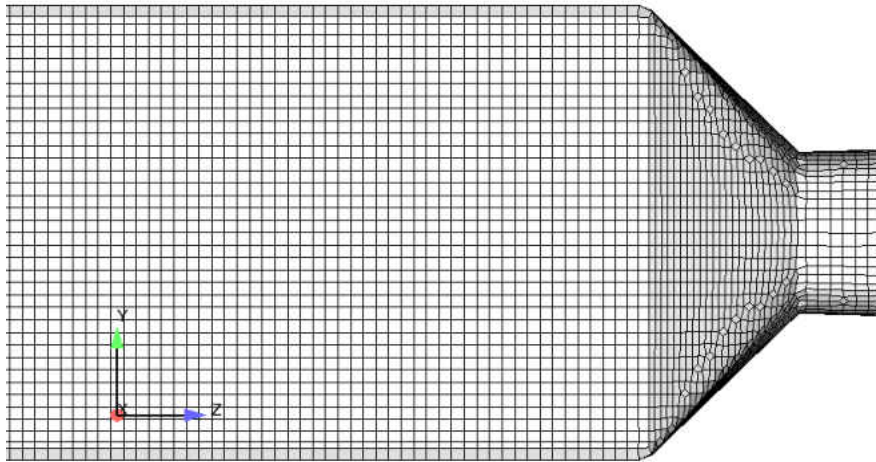


Figure 30: Mesh at the exit nozzle (flow in z direction)

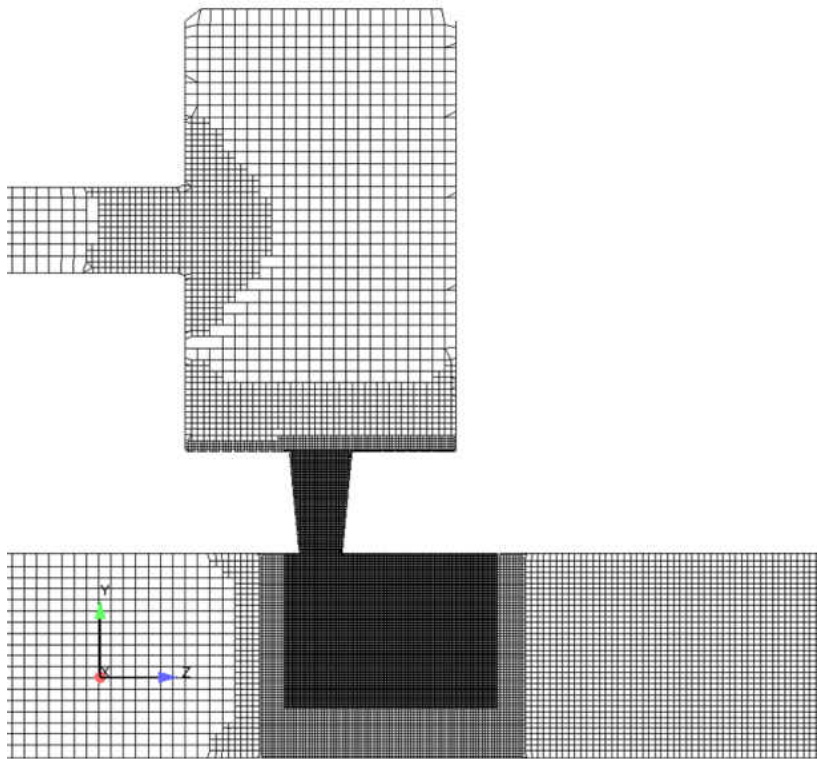


Figure 31: Mesh at JICF region (cross flow in z direction, jet flow in negative y direction)

OpenFOAM's checkMesh utility was run on all of the meshes used in this project to ensure that important parameters such as the skewness and non-orthogonality of the mesh are not outside the desired limits. The max skewness was kept below 3 while the max non-orthogonality was kept below 65 degrees. Note, however, that the average non-orthogonality was as low as 1.5 degrees throughout the mesh. Cell counts for the meshes were typically between 1.8 and 4.7 million cells with the actual cell lengths ranging from approximately 0.5 to 1.8 mm.

## **Boundary Conditions**

### ***Head End and JICF Inlets***

In the experimental rig, premixed, preheated air and fuel pass through a choke plate before entering the head end injector tube. This choke plate consists of nine 4.5 mm diameter holes that the mixture is forced through, ensuring that a clean acoustic boundary condition is achieved at the inlet of the rig. To avoid the computational expense of meshing the small features of the inlet choke plate, the inlet boundary condition for the computational domain was imposed on an inlet section area similar to the combined area of the nine choke plate holes. The inlet area in the computational domain had to be slightly increased to avoid choking at the inlet that resulted in numerical instability due to supersonic jet flow. The inlet area jumped to the actual injector tube dimensions a few cells downstream of the inlet. A similar setup was applied to the air line that supplied the flow to the JICF plenum and the same approach was used to model this boundary in the computational domain. The only difference is that the JICF inlet only consisted of preheated air, as the fuel was introduced through a specially designed nozzle downstream of the JICF plenum. The JICF fuel in the simulations was not applied as a boundary condition, but was modeled as a source term, described in the corresponding results section.

The hydrodynamic inlet boundaries of the experiment consist of a constant specified mass flow rate of air or premixed air and fuel entering at constant preheat temperatures. This is represented in the simulation by specifying a constant mass flow rate at the inlets as well as a constant total temperature. The gradient of pressure at the inlet of the computational domain is set to zero. The acoustic inlet boundary condition of the experiment is choked, due to the orifice holes of the injector plate. By specifying a constant mass flow rate and total temperature at the inlet of the computational domain, an acoustically choked condition is approximated, as no mass flow fluctuations are present at the inlet of the domain. This setup for the inlet boundary condition has also been successfully used in similar studies (Smith, 2006). It was unnecessary to specify any turbulence boundary condition at the inlet as it was assumed that any turbulent kinetic energy resulting from the choke holes in the experiment would be dissipated by the time the flow reached the dump plane or passed through the JICF plenum. This assumption was based on the relatively long injector tube (1.4 m) and the path through the JICF plenum. Any potential random fluctuations and unphysical acoustic waves were also avoided by not specifying turbulence at the inlet.

It was found that the constant mass flow and total temperature inlet boundary condition did not provide as high a reflection coefficient as would be expected for a theoretical choked inlet. The impact of this boundary condition on the acoustics within the simulation is detailed in Appendix A. Because the actual values of the limit cycle amplitude are not expected to be accurately predicted, the additional acoustic losses at the inlets of the domain are acceptable, given the objectives of these simulations. It must be understood, however, that these unphysical losses are present.

### *Exit*

The experimental rig consists of a short nozzle exiting to atmospheric conditions, with no expansion downstream of the choke point. Due to non-uniformities in the flow at this exit plane, however, it is not feasible to apply a boundary condition at the exit of the throat in the computational domain. Instead, a small expansion section was added to the nozzle, causing the flow to become supersonic after it chokes at the throat. For an arbitrary exit to throat area ratio, if the pressure at the exit of the expansion section is permitted to be low enough, the flow will exit from the converging-diverging nozzle with no internal shock waves. OpenFOAM's `waveTransmissive` boundary condition was applied at the exit of the nozzle for the pressure, while the velocity and temperature boundary conditions were set to a gradient of zero. The `waveTransmissive` boundary condition utilizes an eigenvalue analysis to separate out decoupled waves. Based on the speed of the wave at the boundary, determined by summing the component of the velocity normal to the boundary and the speed of sound, the `waveTransmissive` function then determines whether to use an upwind method at the boundary or to specify an appropriate condition based on the parameters given by the user (shown in Table 3). Note that the variables *lInf* and *fieldInf* represent a measure of how far away the far field condition should be and the value of the pressure at this far field location, respectively (MediaWikki, 2011). This allows any pressure waves that pass through the throat to exit the domain, while still partially imposing a pressure low enough to ensure that the flow remains choked at the throat.

The hydrodynamic exit boundary condition of the experiment is governed by the diameter of the throat. The throat diameter in the computational domain identically matched with that of the

experiment to ensure that the same chamber pressure would be achieved in the simulation. This throat diameter was designed to choke the flow, providing an acoustically choked exit boundary condition in the experiment. The acoustic exit boundary for the simulation is also choked, as long as the back pressure at the exit nozzle is low enough to allow the flow to become supersonic through the exit of the computational domain.

Although both the inlet and exit boundaries were theoretically choked, corresponding to the experimental rig, it was unknown how the boundaries would actually reflect acoustic waves, given the numerical errors that can arise in the simulations. A detailed study was performed to quantify the acoustic properties of the inlet and exit boundary conditions to determine the effect of the numerical procedures on the boundaries. It was found that the choked exit nozzle behaved closely to what would be expected from theory, reflecting approximately 90% of acoustic waves over all frequencies. The constant mass flow inlet, however, only reflected approximately 60% of the acoustic waves for all frequencies. This is a limitation of the numerical procedures used in this study and could not be corrected within the scope of this project. However, it is understood that this effectively can add artificial damping of the acoustic waves in the simulation and must be considered when analyzing the results. Further details of this boundary condition study are shown in Appendix A.

### ***Walls***

The air in the experiment is preheated to 400-450°C before it enters the injector tube and JICF air supply line. Once the air is preheated, it is run through the rig for several hours, with nitrogen purging the fuel lines, until all of the chamber walls have reached a steady state temperature equal to the preheat temperature. Fuel is then added and, after ignition, the reaction



occurs for approximately 12-14 seconds while data is being taken. For the purpose of these simulations, it is assumed that the walls remain at the preheat temperature due to this short run time. In reality, the inside wall temperature would certainly rise upon ignition, resulting in a slightly decreasing amount of heat loss through the walls of the chamber. Using simple heat transfer calculations, it can be shown that this effect was negligible for the purposes of these simulations, and thus, all of the walls of the computational domain were set to a fixed value equal to the preheat temperature. This is an approximation that will result in slightly lower than actual chamber temperatures and it may be beneficial in a future work to run a comparative simulation with adiabatic walls. This would provide an upper limit to the solution and would demonstrate how much of an effect the heat loss has on the results of the simulations. The pressure boundary condition at the walls is set to a gradient of zero, representing an acoustically perfectly reflecting wall, while the velocity is set to a no slip condition.

### ***Monitor Points and Outputs***

Monitor points (MP) are placed at locations corresponding to the pressure taps in the experimental rig. This allows for direct comparison between the pressure signals from the simulations and the experiment. At each axial pressure tap location one monitor point was placed adjacent to the wall and one was placed along the center line of the combustor. An additional monitor point was also placed in the center of the throat, at the center of the JICF exit, and inside the JICF manifold (for the JICF simulations). A sketch of the monitor point locations throughout the baseline computational domain is shown in Figure 32. The probes are labeled in the figure according to the nomenclature used in the experiment. Note that PT-TA-07 and PT-TA-08 were swapped in the experimental tests, depending on the rig configuration. For the head end only

runs, Figure 32 shows the correct locations, while they were swapped for the JICF runs discussed in this study.

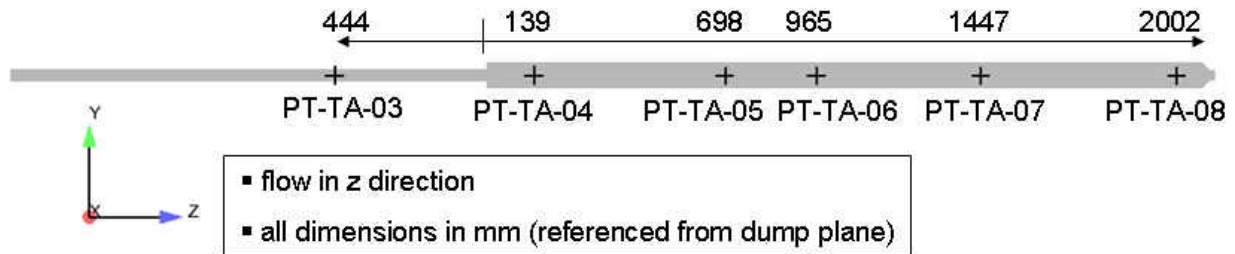


Figure 32: Monitor point locations in chamber (baseline)

Pressure, temperature, heat release, mixture fraction, and x, y, and z components of velocity were output at every timestep, or approximately every 0.1-0.3 microseconds. This provides an upper frequency limit above 1.5 MHz, which is significantly higher than the desired upper frequency limit of less than 1000 Hz. Full data sets of all variables were also output every millisecond, providing a 500 Hz upper frequency limit for any additional data, as determined from the Nyquist criterion. Once a stationary solution was achieved for a given simulation, approximately 0.3 seconds of simulation time was solved, corresponding to nearly five flow-through times through the computational domain. This gives a lower frequency limit of approximately 3 Hz. Table 3 summarizes the boundary conditions (using OpenFOAM v1.7.x syntax) and outputs of the simulations used in this project.

Table 3: Summary of Boundary Conditions for OpenFOAM Simulations

	Pressure	Temperature	Velocity
Inlet	zeroGradient	totalTemperature	flowRateInletVelocity
Exit	waveTransmissive	zeroGradient	zeroGradient
Walls	zeroGradient	fixedValue	fixedValue
MP locations	Axial locations correspond to rig pressure taps (1 centered, 1 at wall); additional MP located at center of throat, JICF exit, and manifold		
Output Intervals	p, U, T, ft, omegaLoc at every time step; full data set every 0.001 seconds		

### Validation with experimental results

Each of the simulations run in this study were chosen to correspond with experimental tests run at Purdue University. This allowed for a direct comparison between numerical and experimental results, providing the necessary data for validating the modeling methods and setup. Because no optical measurements were taken from the head end only cases, the validation for these simulations will be done using the pressure measurements and corresponding spectral analysis. Pressure probes for each simulation are located as close as possible to the locations of pressure transducers in the experimental rig for the corresponding test. Key parameters that will be validated with experimental results include the mean chamber pressure as well as the amplitude and dominant frequencies of the pressure oscillations in the chamber. 1D mode shapes of the pressure waves through chamber can also be determined from the pressure probes for each of the dominant modes. Further confirmation of these modes shapes was done using the full pressure field and a Discrete Fourier Transform, providing 3D pressure mode shapes throughout the computational domain. These mode shapes were compared with similar results from the pressure transducers in the experiment. Accurately capturing all of these parameters within

reasonable accuracy will serve to confirm that the general physics of the flow, as well as the thermoacoustics of the problem, are properly determined from the simulations.

The JICF simulations require an additional set of validation methods, as optical measurements are taken of the reacting jet in the region of injection. Qualitative comparison can be made between the LES results and the images of filtered combustion light; however, line-of-sight effects and the lack of radical species in the simulations will prevent any quantitative comparison between the data. These qualitative comparisons will provide a method of validation for the length, shape, and location of the jet flame that will help to validate the combustion model used in the simulations and determine any limitations of the model.

One of the most important validation techniques, however, is to compare the stability trends observed in the experiments and the simulations. As with any self-excited LES, it is important to observe stability trends in the simulation, and not necessarily quantitative values of the limit cycle amplitudes. This important concept is demonstrated by the sketch shown below in Figure 33, which plots the energy gains and losses versus limit cycle amplitude for two different systems.

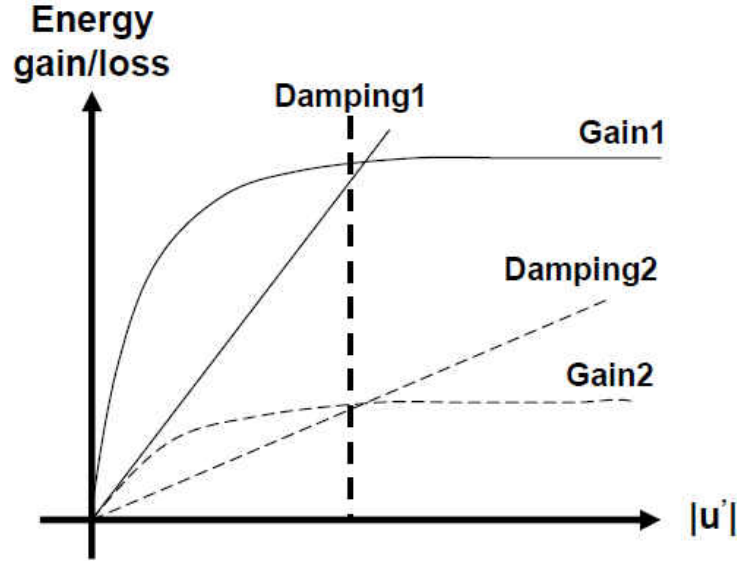


Figure 33: Representative plot showing the energy gains and losses in a system versus the limit cycle amplitude

By observing the representative systems in Figure 33, it is apparent that the same limit cycle amplitude can be reached by two systems that have completely different levels of damping and gain. In a self-excited simulation, there are many sources of both losses and gains that cannot be quantitatively analyzed, some that are physical (such as viscous effects) and some which are not physical (such as numerical damping or boundary losses). Because the relation between the gains and losses is what determines the limit cycle amplitude of the system, it is possible to have completely arbitrary levels of damping and gain in a given simulation that are physically unrealistic, but still predict a limit cycle amplitude that matches with experimental data. Or, it is possible to correctly predict the gain in a given system, but due to numerical losses, be unable to match the limit cycle amplitude from experimental data. Because of this difficulty with any numerical simulation, it is important for self-excited LES to be able to predict trends, such as modeling both a stable and unstable point and matching the trends between these two points.

Because the main objective of this study is to identify a mechanism of instability for the reacting JICF, this proposed mechanism must be shown to accurately replicate the stability trends seen in the experiments. This will be done by comparing the relative amplitudes of the unstable modes of interest between stable and unstable cases, as well as by quantifying the phases between the pressure, velocity, and heat release in the JICF region.

### *Selection of Validation Cases from Experiment*

Because predicting stability trends is a critical aspect of this study, it is ideal to identify a two or three point stability trend from experimental results that can be replicated by the simulations and modeling, either by a change in operating conditions or a change in the JICF geometry. During experimental testing, a three point stability trend was identified between the baseline head end only configuration and two JICF configurations.

The reference design, or baseline configuration for this study, included a head end only test run at the baseline operating conditions of the Purdue experimental studies. The baseline head end experimental run chosen for comparison was test E-0-2-x, as labeled by Purdue University, corresponding to data files 160006 and 160541. This test was run during the June 2009 test campaign and used pure methane gas as the fuel, with an equivalence ratio of 0.62. The total mass flow rate of premixed fuel and air was approximately 0.4 kg/s. Based on these testing parameters, the mass flow rate of the premixed fuel and air in the simulation was set to 0.4 kg/s and the thermodynamic properties were determined for a methane/air mixture at an equivalence ratio of 0.62, a preheat temperature of 768 Kelvin, and a pressure of 8 bars. Using the GRI3.0 mechanism, implemented into a network reactor modeling tool, the laminar flame speed at these conditions was calculated to be 0.531 m/s. The key flow conditions for the baseline head end

only simulations are summarized below in Table 6. Note that the target adiabatic flame temperature for the JICF cases is the same as that of the head end reaction, resulting in a temperature rise between the head end and reacting JICF very close to zero.

Table 4: Flow conditions for head end only reference design, taken from experiment.

	$\dot{m}_{total}$	$\phi$	$T_{ox}$	$S_L^0$	P	$P'_{2L}/pBar$	$T_{adiab}$
Baseline head end simulations	0.4 kg/s	0.62 (methane/air)	768 K	0.531 m/s	8 bars	0.0130	2050 K

Figure 27 shows the baseline head end configuration modeled in this study, including critical dimensions. Note that the expansion section after the throat of the exit nozzle is added to the computational domain and is not included in the experimental rig. This is necessary to maintain choked conditions at the throat and ensure a numerically stable specification of the exit boundary condition.

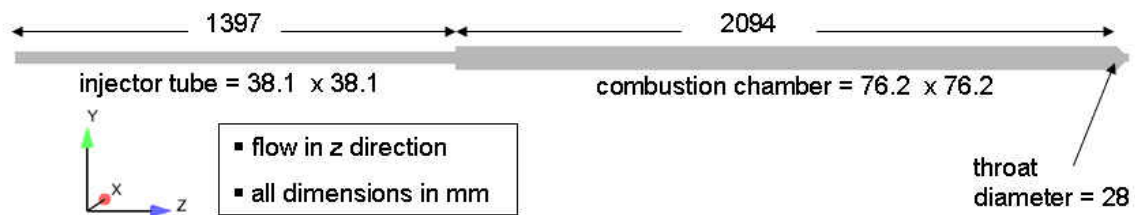


Figure 34: Dimensions of baseline HE only geometry, inlet and outlet are choked (moderately unstable).

The two additional geometries that were considered in this study were known from experiment to provide this clear, three point stability trend (including the reference design). The geometrical difference between the reference design and the additional configurations was the

addition of the JICF geometry. The only geometrical difference between the JICF1 and JICF2 configuration was the location of the choke point in the air supply line to the JICF manifold. This choke point, achieved by a choke plate in the actual test rig, defines the location of the acoustic boundary and thus the inlet of the computational domain. This alters the acoustic impedance of the JICF configuration, and results in a significant change to the overall stability of the system, as will be shown below. The critical dimensions of these additional geometries are shown below in Figure 35 and Figure 36, referred to as JICF1 and JICF2, respectively.

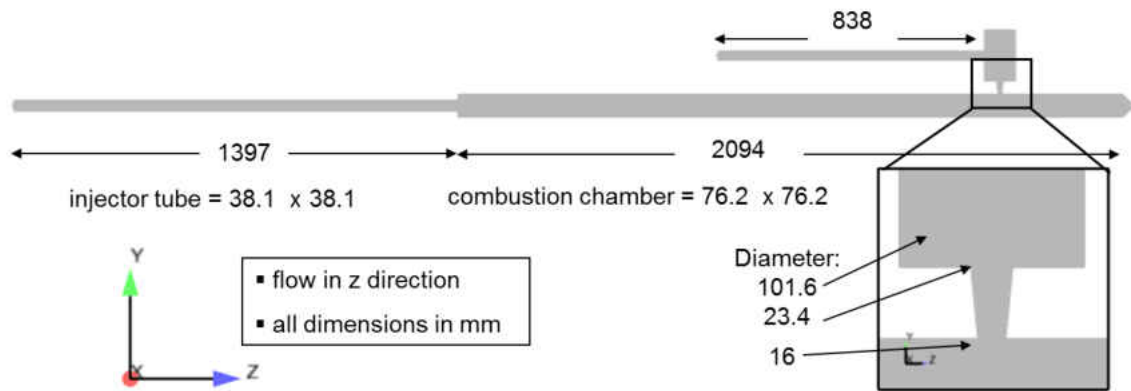


Figure 35: Dimensions of JICF1 geometry, inlets and outlet are choked (very unstable).



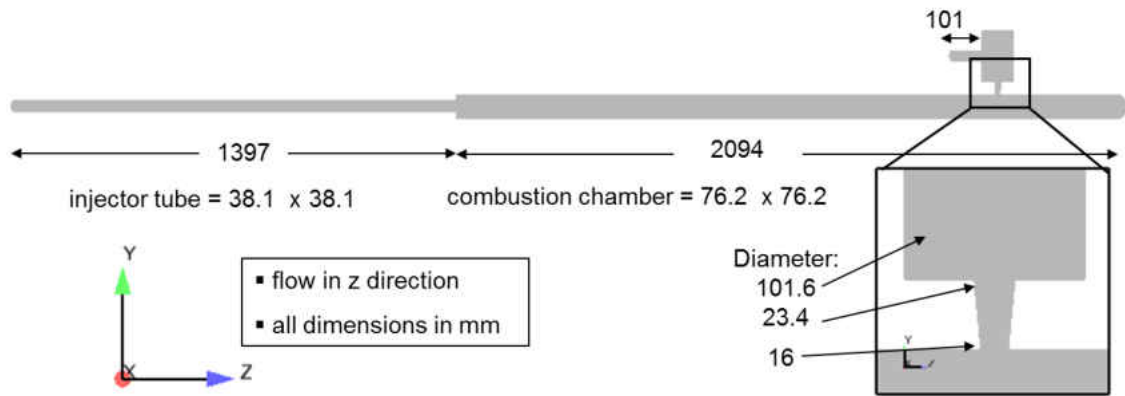


Figure 36: Dimensions of JICF2 geometry, inlets and outlet are choked (stable).

The dynamic pressure spectra for each of these cases are shown below in Figure 37, taken from dynamic pressure measurements near the exit of the combustor (pressure anti-node). Note that there is a slight frequency shift for the mode in the JICF1 case due to the three-dimensional behavior of the mode shape in the JICF geometry, however, the unstable mode is still the 2<sup>nd</sup> longitudinal mode of the dump combustor.

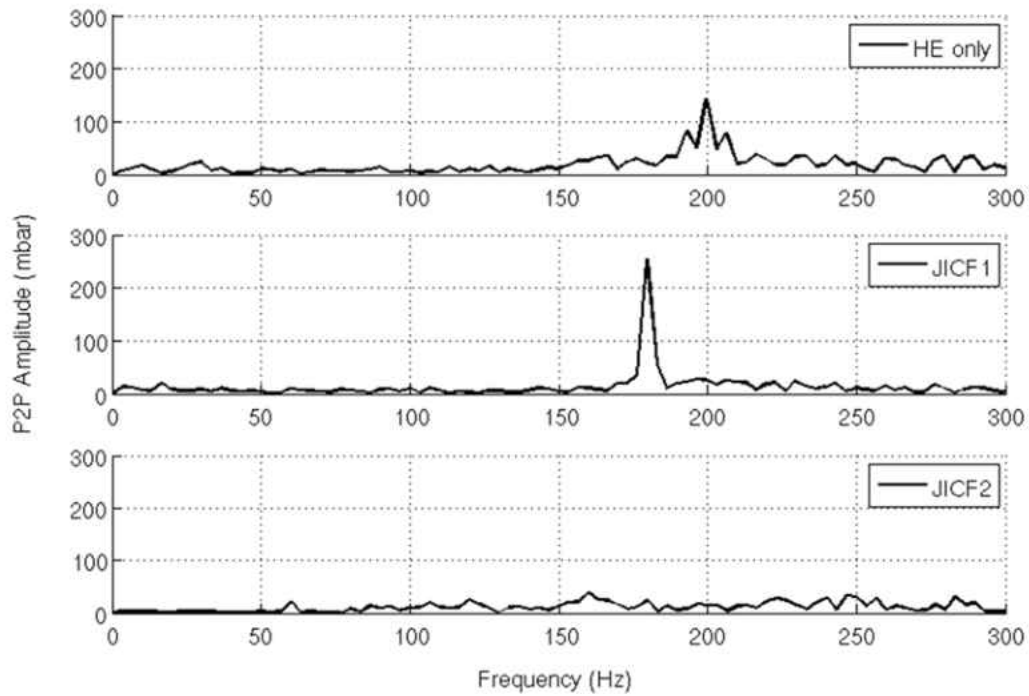





Figure 37: Dynamic pressure spectra from experimental pressure measurements for the three cases investigated in this study.

This three point stability trend is summarized below in Table 5, showing results from the experimental rig.

Table 5: Summary of 3-point stability trend from experimental results, used to validate the acoustic modeling techniques described in this study. Dynamic pressure measured near the exit of the combustor (pressure anti-node).

<b>Nomenclature</b>	<b>Cross section</b>	<b><math>P'_{2L}/pBar</math></b>	<b>Description</b>
<b>HE only</b>		<b>0.0130</b>	<b>Moderately unstable</b>
<b>JICF1</b>		<b>0.0432</b>	<b>Very unstable</b>
		<b>0.0112</b>	<b>Moderately unstable (JICF reaction off)</b>
<b>JICF2</b>		<b>0.0020</b>	<b>Stable</b>
		<b>0.0044</b>	<b>Stable (JICF reaction off)</b>

In the simulation results, a direct comparison could not be included with the HE only simulation, as the JICF domains resulted in a much higher level of acoustic boundary losses than the HE only domain (discussed in Appendix A). Thus, for the sake of the JICF validation, only the JICF1 and JICF2 configurations were used, as these domains were characterized by very similar levels of acoustic boundary losses and could be compared directly with each other. The significant change observed in the stability of the HE only geometry compared to the JICF1 and JICF2 geometries occurred over a wide range of HE equivalence ratios and JICF equivalence ratios. These data points are plotted in Figure 38. The three points selected to define the stability trend used in this study were chosen at the nominal conditions where the HE and JICF equivalence ratios were approximately equal, near 0.62.

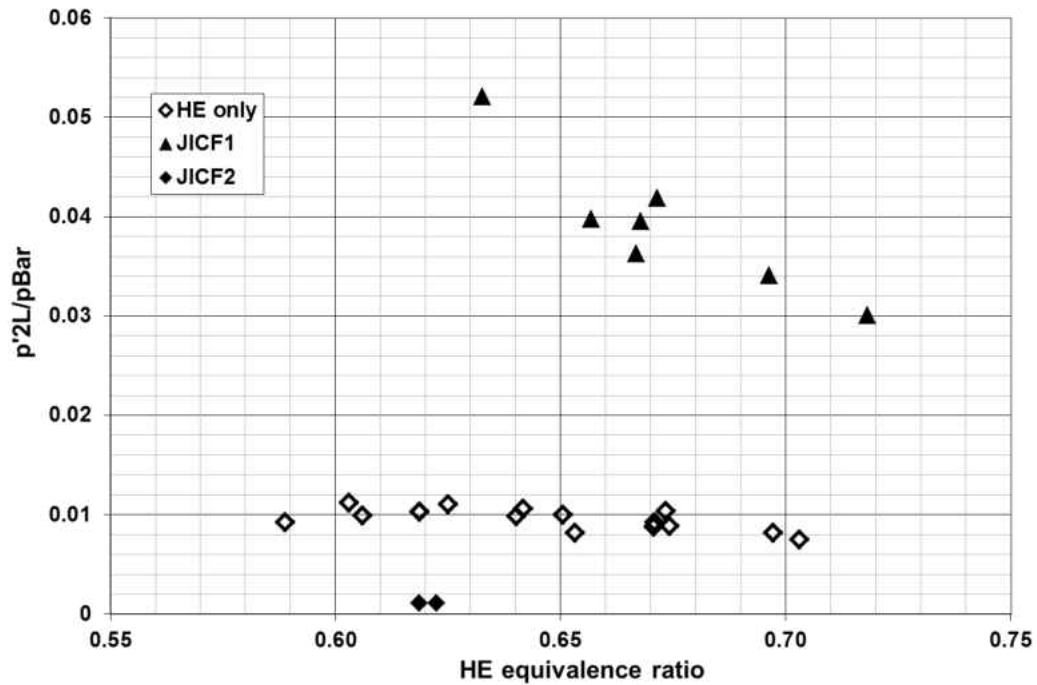


Figure 38: Normalized pressure amplitude measured from experiment for HE only, JICF1, and JICF 2 configurations at varying HE equivalence ratios. Note that the JICF points include additional variation in the jet equivalence ratio.

The test procedure for the experimental rig typically included a period of HE only reaction where the JICF fuel line was purged with nitrogen, allowing for a direct comparison between the JICF geometry with and without reaction. This test procedure is demonstrated in the following plot of the dynamic pressure measurement from one of the sensors during a complete test cycle.

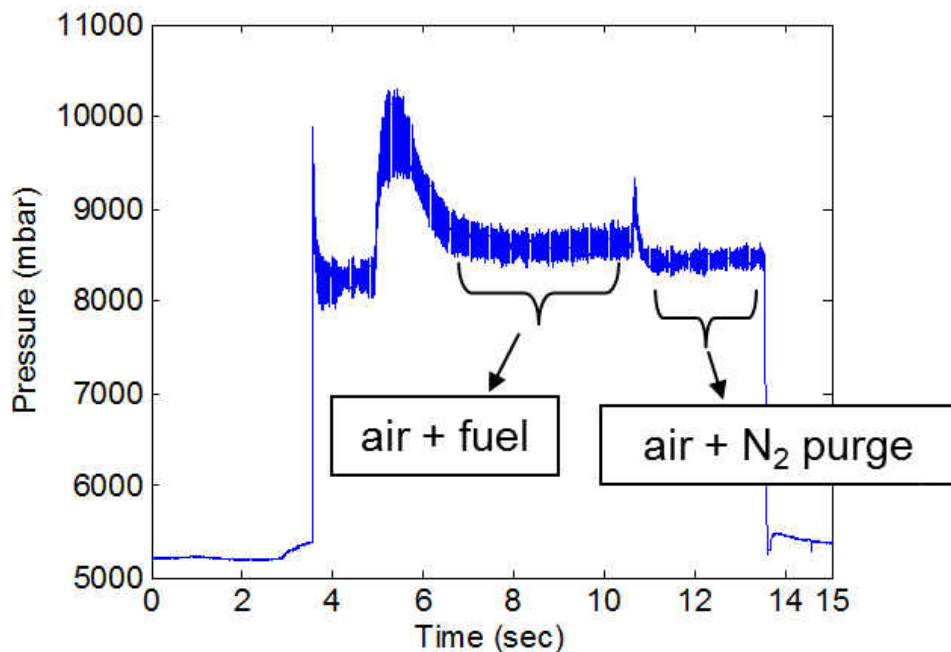


Figure 39: Dynamic pressure trace over one complete test cycle

From approximately 0-4 seconds, preheated air is flowing through the head end and JICF with nitrogen purge in place of the fuel. Just before 4 seconds, the nitrogen to the HE is replaced with fuel and the HE flame is ignited. The rig is run for just under 2 seconds before the JICF nitrogen purge is replaced by fuel and the JICF spontaneously ignites. After approximately 4 seconds of JICF reaction, the JICF fuel is switched back to nitrogen purge and another 3-4 seconds of data is taken. Finally, the HE fuel is replaced with nitrogen to end the HE reaction and complete the test sequence. This procedure provides a direct comparison between operation with and without the JICF reaction, with data taken from the two regions highlighted in Figure 39.

It was found that the strong driving of the chamber mode from the JICF1 configuration was a direct result of the JICF reaction, as adding inert purge flow (nitrogen) in place of the

reacting mixture did not have any noticeable effect of the baseline instability from the head end flame. This is demonstrated in Figure 40, which shows pressure spectrum taken from the transducer measurements during JICF1 fired operation compared to JICF1 purge operation. A spectrum from the corresponding transducer during HE only operation is included to provide a reference of the level of the instability during HE only operation (no JICF geometry installed).

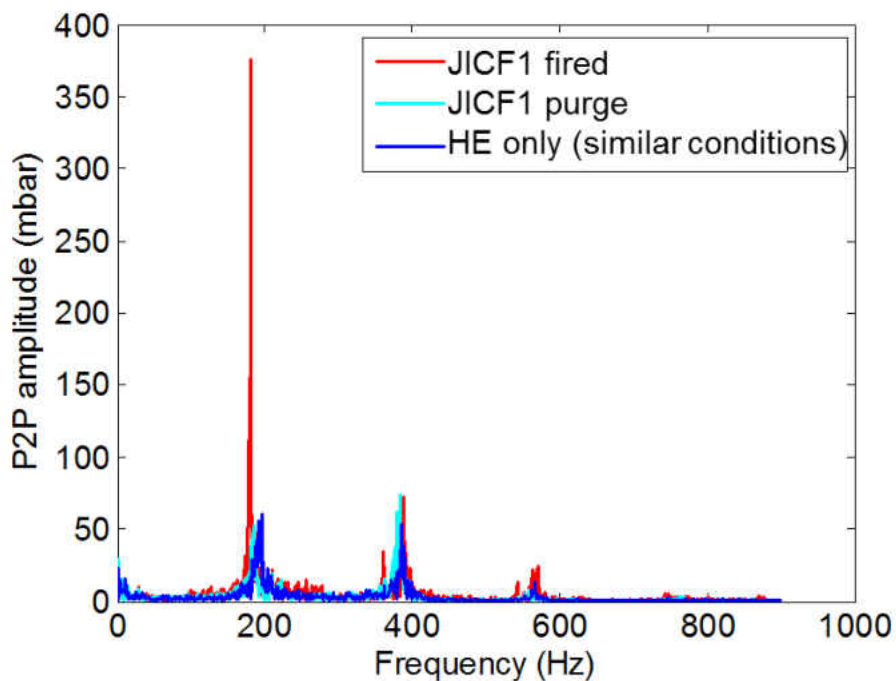


Figure 40: Pressure spectrum comparing JICF1 fired operation to purge operation. Spectrum from HE only operation (no JICF geometry) included for reference.

This figure makes it clear that the strong driving of the first dominant chamber mode is a direct result of the JICF reaction and not simply a phenomenon of the JICF geometry. This suggests that a positive feedback mechanism between the JICF heat release and chamber pressure is present, as required by Rayleigh's Criterion to drive a given mode. If the components of this feedback mechanism can be understood and quantified, a design could theoretically be

achieved that provides a negative feedback between the JICF heat release and chamber pressure and damps a mode that would otherwise be driven by the HE flame. Identifying and modeling this mechanism is one of the key objectives of this study, as listed above in Table 1. Part of this analysis is based on experimental results with additional analysis based on the simulation data. The proposed mechanism is then verified using reduced order acoustic modeling techniques.

## **Comparison to Thermoacoustic Modeling**

### ***3D Thermoacoustic Solver***

Thermoacoustic modeling was performed using a three-dimensional acoustic modeling tool implemented into OpenFOAM to identify if the trends observed in the experimental data and numerical simulations could be predicted using a reduced order tool. The successful use of this tool could potentially allow for parametric studies on full geometries, without the expense of LES. The tool used in this study, referred to as TA3D, solves the linearized Euler equations on arbitrary three-dimensional meshes where linear and non-linear heat release models can be applied to account for the interaction between acoustics and heat release (Johnson, 2013). Mean fields taken from the LES simulations, which utilized a hex-dominant mesh of approximately 2.54 million cells, were interpolated onto purely hexahedral acoustic meshes of approximately 180,000 cells that were developed of the JICF1 and JICF2 geometries investigated in this study. TA3D solves for the pressure and velocity fluctuations throughout the domain, as well as the contributing effect of a modeled heat release “field” through the implementation of various heat release models.

The heat release modeling is the key parameter to successful predictions using TA3D. The generic form of the heat release modeling in TA3D is given as

$$q' = n\bar{q}R \frac{\phi'_s(t - \tau)}{\bar{\phi}_s} \quad (30)$$

where  $q$  represents the unsteady heat release,  $n$  represents the gain,  $R$  is the receiver field (0 or 1),  $\phi_s$  is the sender-field averaged acoustic quantify (such as pressure or velocity), and the bar and prime accents represent the mean and fluctuating components, respectively. The sender and receiver regions are specified based on the proposed origination of acoustic instabilities (sender regions) and resultant location of heat release perturbations (receiver regions). Separate sender and receiver regions can be defined for each heat release model implemented into the TA3D simulation. It is evident from Equation (30) that if the receiver field encloses the mean heat release profile (as is always the case in this study), the resultant heat release fluctuation will only occur at the cells where the mean heat release field is non-zero. The calculated unsteady heat release from the model is then applied as the source term in the energy equation in TA3D's governing equations. For more details on the background and approach of TA3D, refer to Johnson (Johnson, 2013). Details on the heat release models developed for this study, including the proposed sender and receiver regions, will be given in the corresponding results section.

### ***Generalized Instability Model***

An additional component of this study included the development and analysis of an instability model directly based off of the experimental and numerical setups. This instability model was created using the Generalized Instability Model (GIM), a low-order acoustic modeling tool developed in cooperation with Purdue University, InSpace LLC, and Siemens Energy, Inc. (Portillo, 2007). GIM allows models to be created using geometric properties and flow effects along with unsteady heat response functions to parametrically study the



thermoacoustic stability of a given system. GIM solves an unsteady, inhomogeneous wave equation for the acoustic pressure perturbation,  $p'$ , of the gas phase inside a combustion chamber:

$$\nabla^2 p' - \frac{1}{c^2} \frac{\partial^2 p'}{\partial t^2} = h \quad (31)$$

with wall boundary conditions:

$$\hat{n} \cdot \nabla p' = -f \quad (32)$$

where  $c$  is the sonic velocity,  $n$  is the unit normal vector, and  $h$  and  $f$  are inhomogeneous terms that include all other effects, among them the unsteady combustion processes, damping mechanisms, mean flow variations, and nonlinear effects such as higher order acoustics, mean flow, and acoustic interactions.

For the solution of the pressure wave equation, a modified Galerkin method is used that splits the perturbation variables into temporal and spatial modes (Portillo, 2006). This approach decouples the wave equation into two ordinary differential equations, one dependent only on the spatial coordinate and one dependent on time. The forcing due to unsteadiness in the combustion process can be added as a forcing term in the temporal differential equation, along with boundary conditions and other forcing terms.

In deriving the equations used in GIM, it is assumed that the acoustic fluctuations are linear. This is a valid assumption for acoustic pressures that are small compared to the mean pressure, as is the case for many of the applications that can utilize GIM. For more detailed

derivations of the equations used by GIM for the calculation of cylindrical geometries, refer to Portillo et al (Portillo, 2007).

The boundary conditions for the GIM model were specified as closed, to correspond as closely as possible to the acoustically choked inlet and exit boundary conditions found in the experiment and the simulations.

An analytical model was developed that included the geometric features of the experimental rig, including the length and area, as well as the flow properties such as temperature, pressure, and specific heat ratio. The acoustic mode shapes and frequencies of each dominant mode were determined and compared with the experimental results. Figure 41 shows a representative plot of the 2<sup>nd</sup> and 4<sup>th</sup> longitudinal mode shapes determined from a preliminary analytical model. Note that several solutions are shown to represent how the pressure modes oscillate as a function of time. The bold lines represent the axial locations of the dump plane and JICF injection.

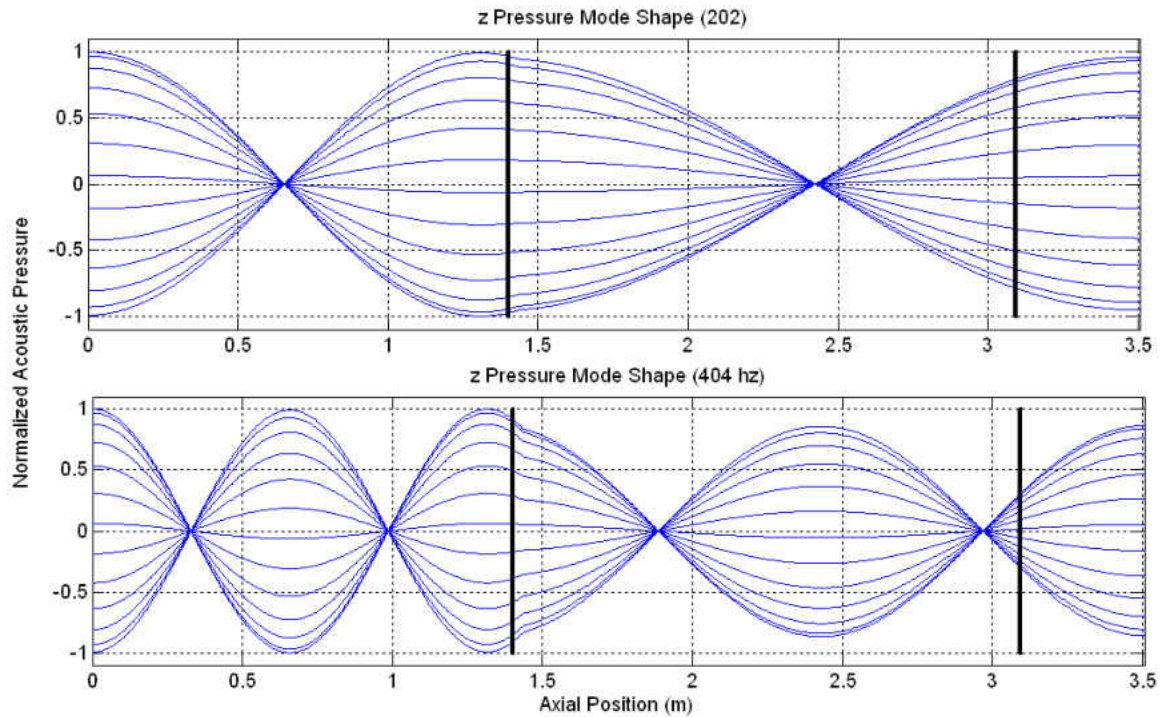


Figure 41: Pressure mode shapes solved from analytical model. (Bold lines represent the axial locations of the dump plane and JICF)

An unsteady heat release model was developed and implemented into the analytical model, based on the mechanism of instability proposed from experimental and numerical results. This heat release model allowed for a linear stability analysis of the dominant modes and included terms that represent the unsteady heat release that occurs at the reacting JICF. The total heat release that is implemented into the model was determined from the heating value and mass flow rate of the fuel. The fuel mass flow rate is calculated from the equivalence ratio and the known air mass flow rate. Equation (33) gives the relationship between the total heat release and the equivalence ratio

$$\bar{Q} = H_{fuel} \dot{m}_{air} \varphi \left( \frac{m_{fuel}}{m_{air}} \right)_{stoich} \quad (33)$$

where  $H_{fuel}$  is the lower heating value of the fuel in  $J/kg$ . Additional parameters required for the unsteady heat release model included the time lags, which were determined from experimental and numerical results. Finally, a linear stability analysis was performed by sweeping through the parameters determined to govern the system and generating stability maps for each mode of interest. Approximated operational points were determined from numerical results to understand where each flow condition lies on the stability maps and what the effect of varying the different parameters were, in terms of the stability of each mode.

## **CHAPTER 4 – RESULTS**

### **RANS Head End Only Simulations**

The first simulations run for this project were cold flow and reacting RANS cases. These were used to verify that the selected computational domain and boundary conditions would result in a solvable problem with physically realistic results. The reacting RANS solution is also used as the initial condition for reacting LES cases. A standard k-epsilon turbulence model is used for the RANS solution and the same combustion model presented above is used for the reacting flow. The mesh and boundary conditions are identical to those used for the LES simulations, as detailed above.

Figure 42 shows the reaction progress variable at the dump plane for a reacting RANS simulation. The inset of Figure 42 shows the Mach number at the exit nozzle, verifying that the flow is indeed choked at the throat and becomes supersonic through the expansion section.

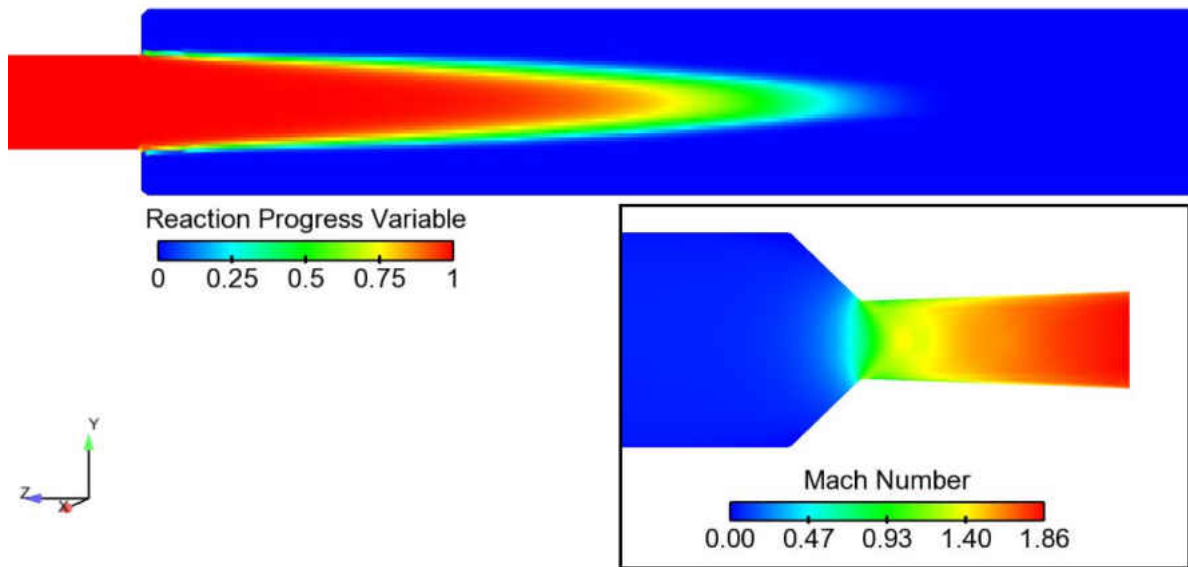


Figure 42: RANS solutions for reaction progress variable at dump plane and Mach number at exit nozzle (used as initial conditions to LES simulations)

As expected, it can be seen from the plot of reaction progress variable that a symmetric “flame” develops that is anchored at the dump plane. Note that based on the definition of the reaction progress variable, a value of one represents fresh gas and a value of zero represents burnt gas.

Figure 43 shows a plot of the pressure and temperature throughout the computational domain.

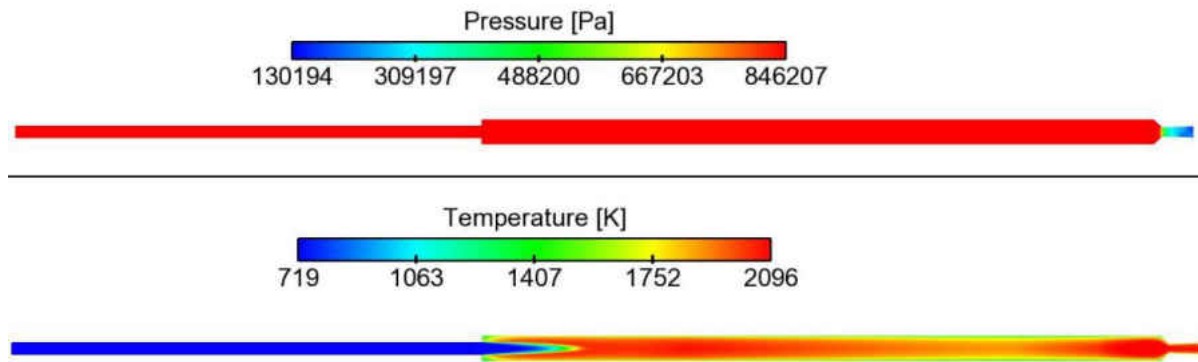


Figure 43: Pressure and Temperature from RANS simulation

It can be seen from the pressure plot that the chamber pressure is close to the experimental results that show an expected mean chamber pressure of around 8 bars. The maximum temperature given from the RANS solution was 2096 K, very close to the calculated adiabatic flame temperature of 2100 K, for the specified equivalence ratio. It is apparent from the temperature plot that the burnt products within the chamber begin to cool slightly towards the exit of the domain due to the heat loss through the walls. The temperature increases again as the flow is accelerated through the converging-diverging nozzle. It is important to note that because the main purpose of the RANS simulations is to achieve a reasonable initial condition for the LES simulations, it was not necessary to ensure that the RANS solution was completely converged in order to obtain an accurate final LES solution. However, it is certainly advantageous to achieve a converged RANS solution before beginning LES so that the computationally expensive LES simulation will not be needed to converge to the “stationary” solution that can be obtained from RANS. Note that RANS solutions were not obtained of the JICF configurations, but rather, these simulations were initialized using LES fields and assumed jump conditions.

### LES Head End Only Simulations

The first LES simulations run in this study included only the head end reaction and no JICF injection, referred to as “head end only” simulations. The purpose of these initial head end only simulations was to verify that the modeling approach detailed in the preceding chapters would be able to capture the self-excited combustion instabilities present in the experimental rig. As with every simulation run in this study, a corresponding set of experimental data was available to be used for validation of the simulation results. As stated above, the baseline head end experimental run chosen for comparison was test E-0-2-x, as labeled by Purdue University, corresponding to data files 160006 and 160541. This test was run during the June 2009 test campaign and used pure Methane gas as the fuel. An equivalence ratio of 0.62 was achieved and the total mass flow rate of premixed fuel and air was approximately 0.4 kg/s. Based on these testing parameters, the mass flow rate of the premixed fuel and air in the simulation was set to 0.4 kg/s and the thermodynamic properties were determined for a methane/air mixture at an equivalence ratio of 0.62, a preheat temperature of 768 Kelvin, and a pressure of 8 bars. This resulted in a calculated laminar flame speed of 0.531 m/s. The important flow conditions for the baseline head end only simulations are summarized below in Table 6.

Table 6: Flow conditions for baseline head end only simulations

	$\dot{m}$	$\phi$	Tox	SL	P
Baseline head end simulations	0.4 kg/s	0.62 (methane/air)	768 K	0.531 m/s	8 bars

For the first LES simulations, the RANS solution was typically used as the initial conditions. Depending on the available initial conditions, the transient simulation time required



to achieve a stationary solution was generally found to be 0.1 to 0.2 seconds in the head end simulations. Figure 44 shows a representative pressure trace acquired from the head end only simulation, demonstrating the initial transient portion of the simulation.

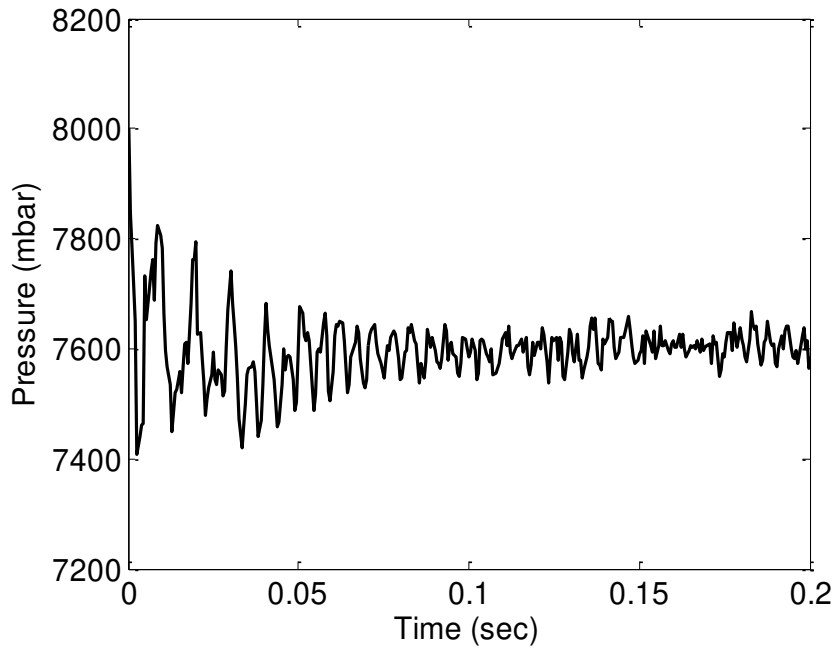


Figure 44: Initial transient pressure trace from head end simulation

Before any data was taken for post-processing, it was ensured that approximately five flow through times of data with a stationary mean pressure was achieved at all monitor points. This corresponded to about 0.3 seconds of simulation time, which was taken as a general guideline for the window of data used for post-processing. Figure 45 shows a raw pressure trace from the head end simulation compared to the corresponding experiment pressure transducer, PT-TA-08 (Refer back to Figure 32 for the axial location of these measurements). It should be noted here that the time vector used in the raw pressure plots is always re-set to zero for post-

processing, and thus should not be always be considered to represent the simulation time from the beginning of the solution.

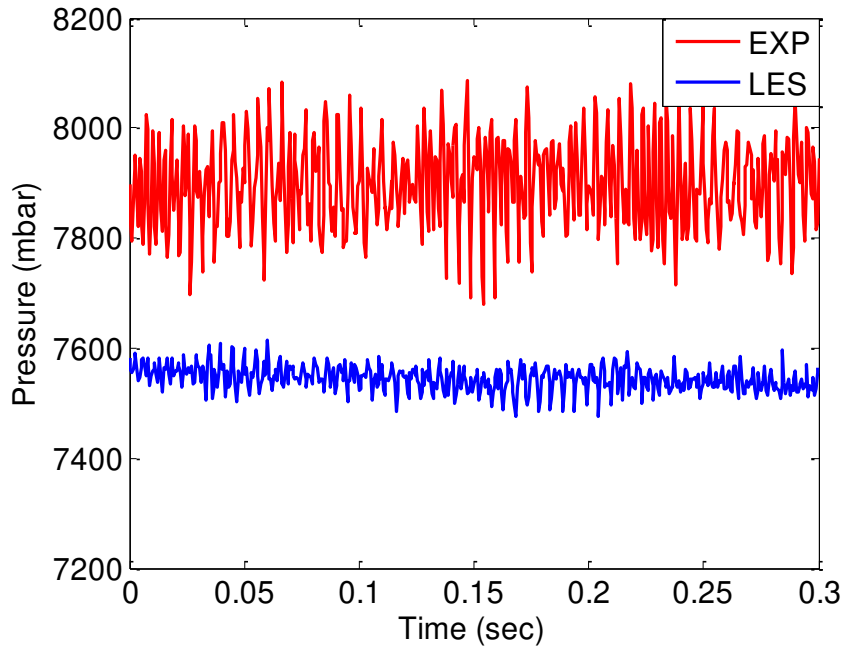


Figure 45: Head end simulation raw pressure trace compared to corresponding experimental pressure transducer, sampled at 1800 Hz (PT-TA-08)

It is apparent from the figure that both the mean chamber pressure and the overall pressure oscillations are lower in the simulation. The discrepancy in the mean chamber pressure is attributed to an increase in the effective choked area at the throat of the exit nozzle in the simulations. Because an expansion section after the throat was required in the computational domain for the sake of numerical stability at the exit boundary, the simulation resulted in a convex choked surface at the throat, as opposed to a flat plane. Although the actual throat area in the mesh corresponded to the throat area in the experimental rig, this increase in the effective choked area caused a drop in the mean chamber pressure. It was determined that the mean chamber pressure in the simulations was generally only 3-4% lower than that observed in the

experiments, and thus, it is not expected to significantly affect the overall stability of the system. This conclusion is based on experimental data which showed a negligible change in stability for small changes in chamber pressure. Further details on the effective choked area are provided in Appendix A.

Once a sufficient amount of stationary data was achieved from the head end simulations, spectral analysis of the raw pressure data could be taken to determine the frequency and amplitude of any oscillations seen in the combustion chamber. Figure 46 shows a plot of the peak-to-peak amplitude of the PT-TA-08 pressure transducer compared to the corresponding monitor point in the simulation.

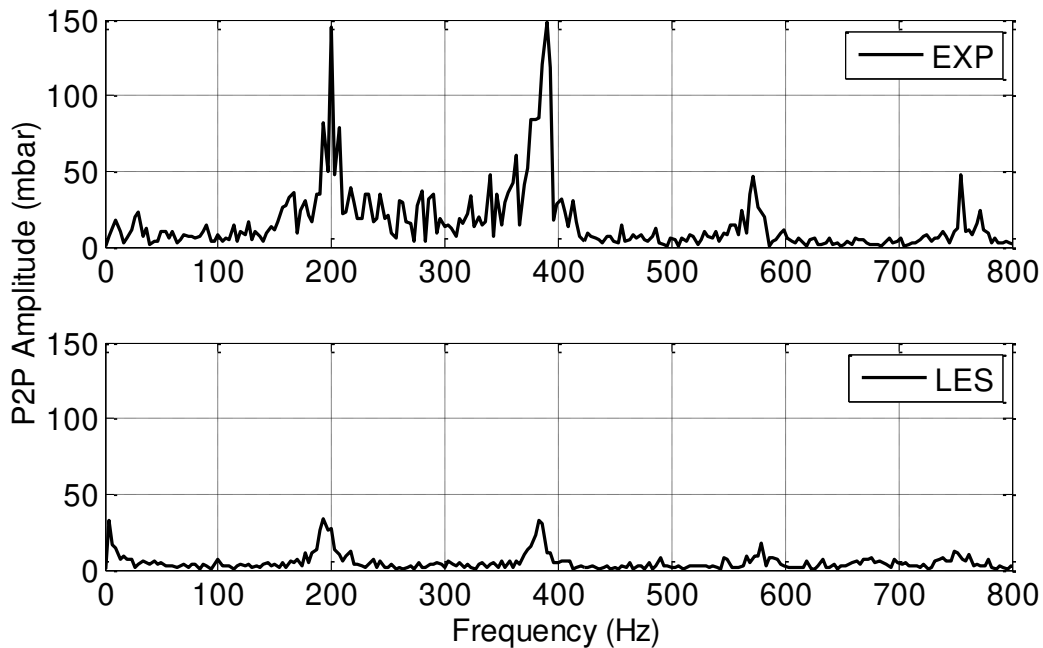


Figure 46: Spectral data from experiment and baseline head end simulation, taken from 0.3 seconds of data from PT-TA-08

The frequencies of the excited modes in the simulations match almost identically with those seen in the experiment. The two clearest modes in the simulation are seen at 193 and 383 Hz, with another slight peak at 580 Hz. It was found that the higher frequency modes, near 600 and 800 Hz, typically became stronger if the simulation was continued beyond the standard 0.3 seconds, however, because the focus of this study is on the mode near 200 Hz, the simulation was not continued to avoid the extended run time.

As expected from the raw pressure data, the peak-to-peak amplitudes seen in the simulation are significantly lower than those in the experiment. The simulation predicted an amplitude of approximately 33 mbars for both the 200 and 400 Hz modes, compared to the experimental amplitudes of approximately 145 and 148 mbars for the 200 and 400 Hz modes, respectively. This under predicted amplitude is attributed to a combination of numerical damping as well as acoustic losses from the boundaries of the computational domain. If the mesh was not sufficiently refined, the numerical damping could be high, however, a mesh resolution study did not show consistent improvements in the amplitude prediction for the modes observed here. The details of this mesh resolution study are provided in Appendix A.

It was found that another source of acoustic losses in the simulation comes from the inlet boundary. Specific boundary simulations determined that the magnitude of the reflection coefficient at the inlet of the domain was at least 30% lower than the expected theoretical value. The exit of the domain, through the choked throat, was found to allow very little acoustic loss, and is not considered to be a contributor to the under predicted amplitudes. The details of the calculations used to determine the acoustic losses through the boundaries are provided in Appendix A.

Although the frequencies of the unstable modes were predicted very well by the simulations, it is necessary to verify that these frequencies indeed correspond to the standing pressure waves measured in the experimental rig. This verification was done by calculating pressure mode shapes from the monitor point data as well as performing a 3D discrete Fourier transform (DFT) of the pressure field and filtering at the appropriate frequencies. The pressure mode shapes from the monitor point data, referred to as 1D mode shapes, were calculated by filtering the raw pressure signal at the frequency of interest, and plotting the pressure values from each chamber measurement location through a minimum of one period of oscillation of the mode of interest. This provided the filtered peak-to-peak pressure amplitude at each axial location of the monitor points through the combustor. The 1D mode shapes for the second longitudinal mode are shown in Figure 47, comparing the experimental data to the simulation data for the measurement points located within the combustion chamber.

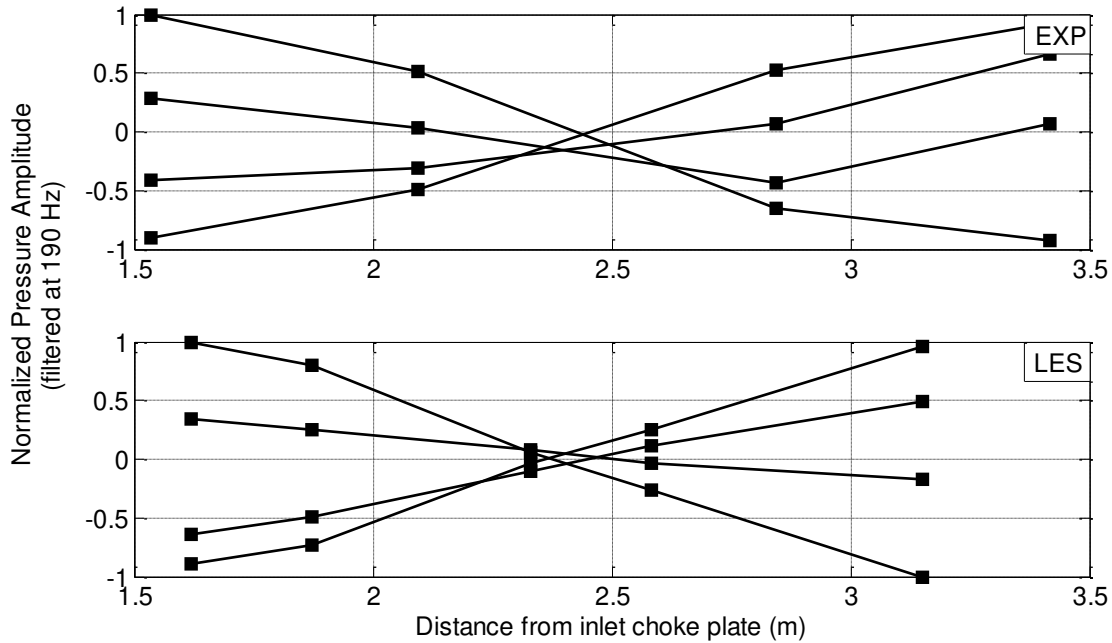


Figure 47: 2L mode shapes from experimental and simulation data, calculated from raw pressure data filtered at 190 Hz

It is apparent from the experimental data that a pressure node for the 2L mode is located inside the chamber at approximately 2.4 meters from the inlet choke plate. This node lines up almost identically with the pressure node observed in the simulation data, demonstrating that the peak near 200 Hz seen in the simulation corresponds to the 2L standing wave in the rig. It should be noted here that the pressure data from the simulation was normalized with only the simulation data, and thus, the maximum normalized amplitude for both the experimental and numerical data is equal to one, even though their real amplitudes differ significantly. Also, it can be seen in Figure 47 that the locations of the monitor points in the simulation do not correspond identically to the pressure transducer locations. This resulted from incorrect drawings of the experimental rig that were not discovered until after the simulations had been run. While the monitor point

locations were updated for future runs, it was determined that the head end simulations would not be re-run as the general conclusions would not be affected by the re-located monitor points.

The 1D mode shapes for the fourth longitudinal mode are shown in Figure 48, comparing the experimental data for the measurement points located within the combustion chamber.

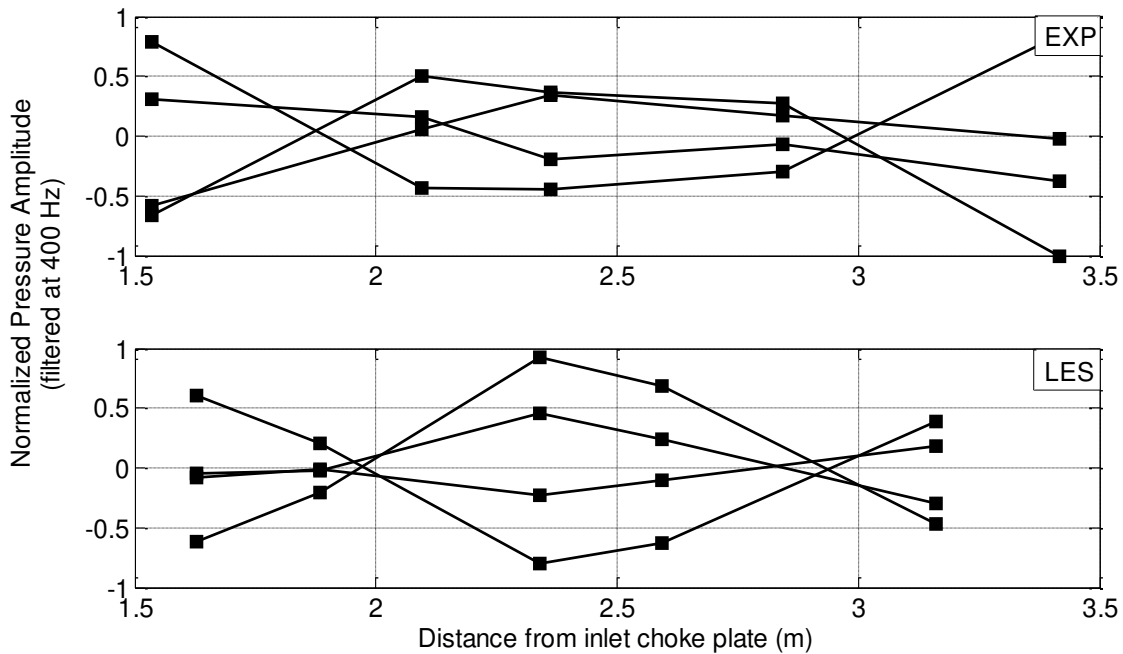


Figure 48: 4L mode shapes from experimental and simulation data, calculated from raw pressure data filtered at 400 Hz

For the 4L, it is apparent from the experimental data that a pressure node exists in the chamber at approximately 1.9 meters and then again at 2.8 meters downstream of the inlet choke plate. Again, the corresponding nodes from the simulation data line up almost identically, verifying that the peak near 400 Hz seen in the simulation corresponds to the 4L standing wave in the rig.

A three-dimensional DFT utility was applied to the entire pressure field output at every 0.001 seconds by the simulation. This utility reads the pressure field at each cell within the mesh and stores this information for each timestep. A DFT is then taken of each data point, and both the amplitude and phase of pressure at each cell is calculated from the DFT information. From this data, three dimensional mode shapes can be identified for modes with frequencies below 500 Hz. Clip planes colored by the normalized pressure amplitude and pressure phase are shown Figure 49, filtered at 192 Hz. These three-dimensional amplitude and phase fields clearly show a 2L standing wave within the domain, where a pressure node is located in both the ox-post and the combustion chamber. As expected, the pressure between these nodes is 180 degrees out of phase with the pressure on the outside of the nodes.

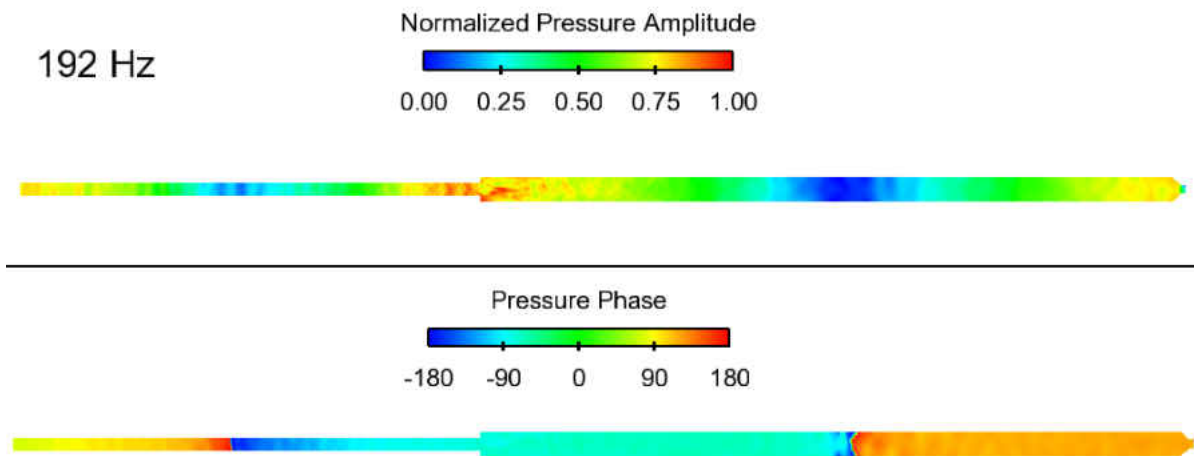


Figure 49: 2L mode shape from simulation pressure field data, calculated using 3D DFT, filtered at 192 Hz

Clip planes colored by normalized pressure amplitude and pressure phase are shown in Figure 50, filtered at 385 Hz. These three-dimensional amplitude and phase fields clearly show a 4L standing wave within the domain, where two pressure nodes are located in the ox-post and



two pressure nodes are located in the combustion chamber. Again, the pressure between nodes is 180 degrees out of phase.

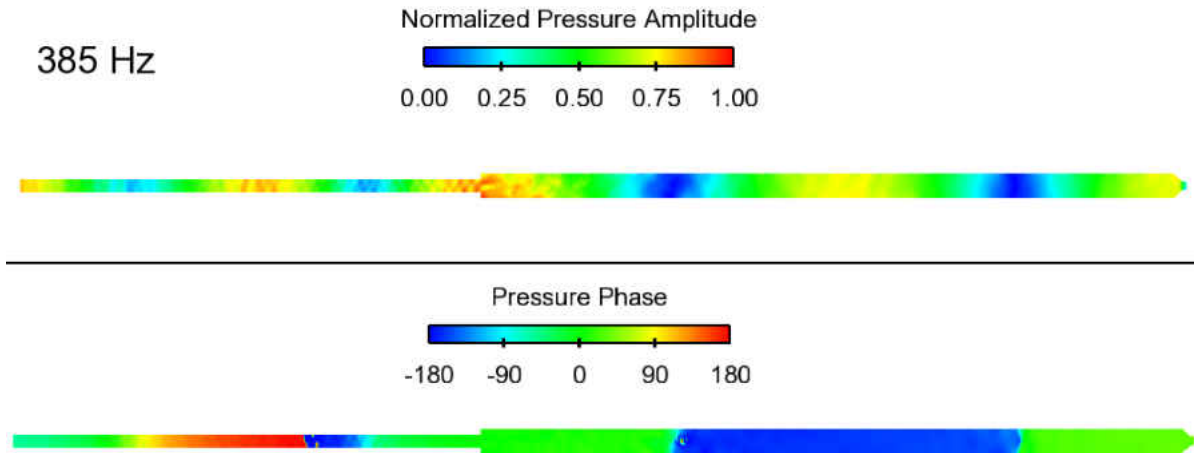


Figure 50: 4L mode shape from simulation pressure field data, calculated using 3D DFT, filtered at 385 Hz

The head end results verified that the modeling approach presented in this study was able to capture the self-excited combustion instabilities present in the experimental rig, with an accurate prediction of the frequencies and mode shapes, but with significantly under-predicted amplitudes. The discrepancy in amplitude is largely attributed to the acoustic losses through the inlet boundary. Although the implementation of higher order discretization schemes and a more acoustically accurate inlet boundary condition would likely result in simulations that match the experimental amplitudes better, such an effort is outside of the scope of this study. It was concluded that the 2L and 4L standing waves that clearly developed from the head end simulations would serve their purpose as the driving source to excite the JICF injection system.

## LES Head End with Jet in Cross Flow Simulations

### *Selection of the best fit combustion model*

Two criteria were used to determine the combustion model parameters that best matched the trends observed from experiments. These model parameters were then used in the simulations to develop and validate a mechanism of instability for the reacting JICF. The first, and most important parameter, is that the LES simulations match the experimental trends, specifically that the JICF1 configuration is shown to drive the unstable mode while the JICF2 configuration is shown to damp the unstable mode. The second parameter is the mean reacting JICF flame shape, with respect to its location, length, and distribution. Due to the limited experimental data, as well as a partially ambiguous correlation between the experimental line-of-sight CH\* chemiluminescence and the numerical planar heat release, the mean JICF flame shape is considered to be more of a qualitative parameter. However, it still provides valuable information on the physical accuracy of the applied combustion model and some insight on the limitations of the modeling techniques applied here. There are techniques that have been developed to attempt to alter the line-of-sight view of the camera to two-dimensional planar data, or to estimate a line-of-sight view from the three-dimensional simulated data. Both of these approaches would allow for a direct validation comparison between the simulated flame and the experimental flame, assuming that the radical captured through the filtered camera lens was also a variable calculated in the simulation. Otherwise, this results in an additional layer of complexity, where the intensity of the radicals in the chemiluminescence imaging is not directly available as a variable in the simulated results. For the purposes of this study, however, it was found that the qualitative comparison between the line-of-sight CH\* chemiluminescence intensity from experiment and the 2D contours of heat release from the simulation was sufficient to provide the information

necessary to understand the behavior of the simulated flame and what the limitations of the combustion model were. More quantitative analysis of the smaller scale structures of the jet flame would potentially require more direct validation techniques between experiments and simulation.

It was found that the simulations matched the experimental trends observed in the experiments for two specific combustion model setups. The first, and possibly the most physically accurate, was to apply a Markstein number of 0.1, based on the counterflow results, and include the correction term for heat loss in the unstrained laminar flame speed as developed from the 1D premixed flame results. This setup was found to be marginally unstable and did not require any additional tuning of the JICF “A factor” in the turbulent flame speed correlation (i.e., a constant value of 0.5 was applied to both the head end and JICF reaction zones).

The second setup that was observed to match the experimental stability trends was to include only the strain model developed by Tay, but increase the Markstein number from the fitted value of 0.1 to a fitted value of 0.9, determined from counterflow simulations run at 8 bar and 1 bar, respectively. This setup was of particular interest as it locally reduces the reaction rate in regions of high strain near the injection point of the JICF. The basic TFC combustion model was found to over-predict the reaction rate in this region where the gradient of the reaction progress variable is high, as experimental data has consistently shown that the jet does not ignite immediately and burn in this region, but rather ignites on the downstream surface of the jet and burns mostly in the recirculation region of the JICF. This setup was found to be strongly unstable when an A factor of 0.3 was applied locally to the JICF reaction (note that the head end A factor was always maintained at 0.5). It should be noted here that the A factor applied to the JICF

combustion region was always tuned to obtain the best possible match with the experimental stability trends and only the best tuned values are shown in this section. A representative discussion of these tuning results is provided below.

As stated above, an additional criterion used to quantify the physical accuracy of the combustion model parameters was the mean JICF flame shape. This qualitative validation is shown in Figure 51 and Figure 52, which show the mean  $\text{CH}^*$  chemiluminescence intensity of the JICF flame from Test 191343 and the normalized heat release contours from the simulations, respectively. Note that the simulation data is taken on a 2D plane while the experimental data is taken from a camera line of sight. The experimental test was run at Purdue University on 01/24/2013 using the JICF2 configuration and was relatively stable ( $P'/p\text{Bar} < 0.0025$ ) at the mode of interest near 200 Hz.

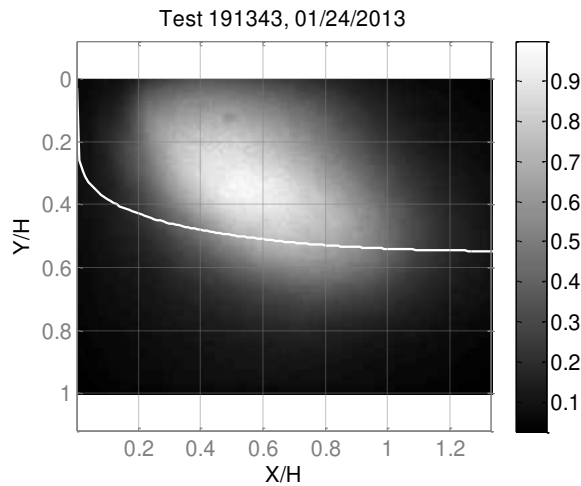


Figure 51: Mean normalized  $\text{CH}^*$  chemiluminescence intensity of JICF flame from Test 191343 on 01/24/2013 using JICF2 configuration. White line represents Holdeman scalar trajectory for a non-reacting JICF.

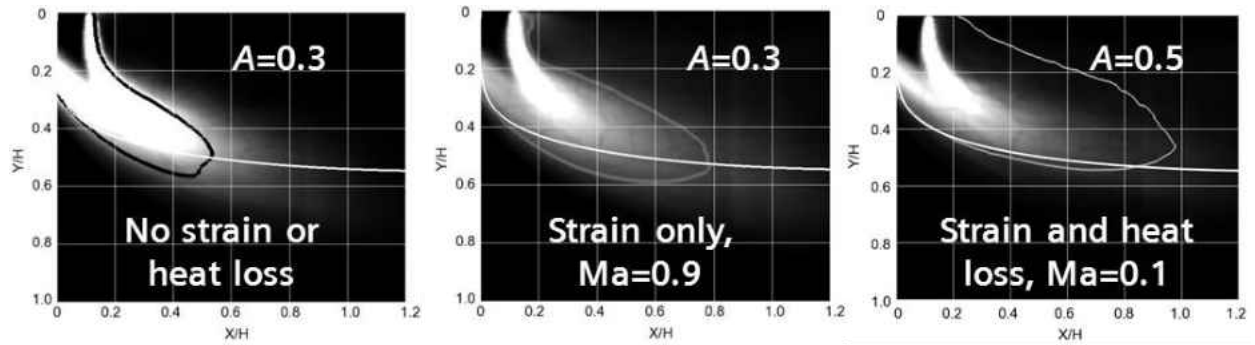


Figure 52: Normalized heat release contours from LES simulations with strain model off (left), strain model on (middle), and strain and heat loss models on (right). White corresponds to maximum heat release, black corresponds to zero heat release. Black or grey isolines represent reaction progress variable of 0.1, white line represents Holdeman trajectory for a non-reacting JICF.

In Figure 52, the mean flame shape from the basic TFC combustion model with no strain or heat loss is shown for reference (left plot). This reference simulation utilized Equation (18) for the reaction rate source term in the combustion model. The middle and right plots represent extended TFC cases that utilized Equations (20) and (27), respectively, for the reaction rate source term. Also, note that the two extended TFC cases shown in this figure (middle and right plot) include the different  $A$  factors required to match the experimental stability behavior.

It is evident from the mean heat release contours that both of the extended TFC models help to lengthen the flame and distribute the reaction over an area that is more consistent with the experimental image, as compared to the basic TFC model. It is also clear, however, that significant discrepancies still exist in both extended model cases, mainly in the jet shear layer region where the reaction rate is largely over-predicted due to the dependence of the source term on the gradient of the reaction progress variable. The most reduction in this over-predicted reaction rate is observed when the strain model is applied with a Markstein number of 0.9. This significantly reduces the upstream shear layer reaction rate and results in a longer, more

distributed flame. While this reduction in the shear layer reaction rate is not observed as strongly in the case with heat loss and a Markstein number of 0.1, it is interesting to note that the distribution of the flame is lengthened and shifted just above the Holdeman trajectory, consistent with the shift observed in the experimental flame image.

Figure 53 shows normalized 1D plots of CH\* intensity (for the experimental results) and heat release (for the simulation results) to provide a more quantitative look at the location and distribution of the flame shape. Note that the values must be normalized individually, as there is no direct correlation between the intensity and heat release.

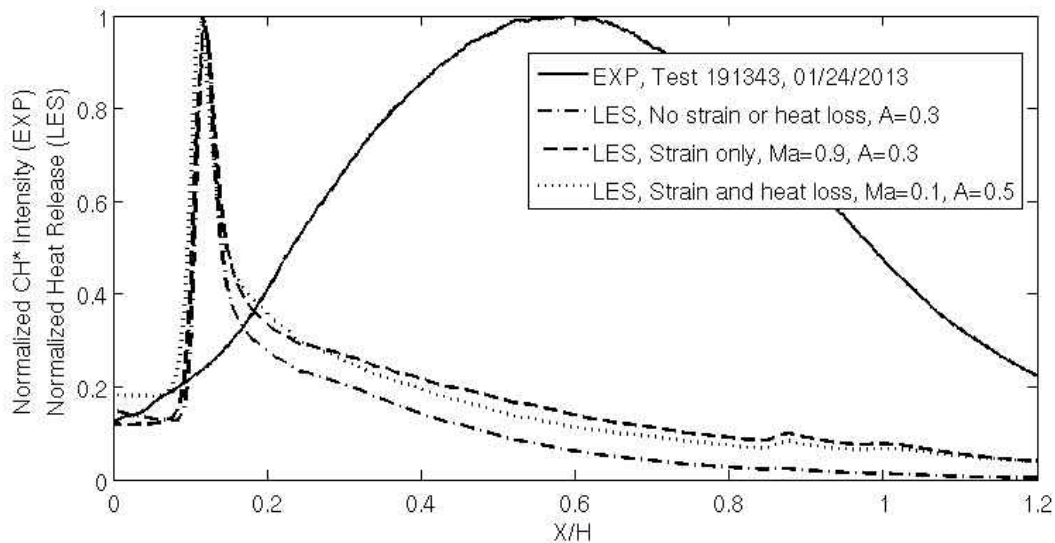


Figure 53: Normalized 1D plots of CH\* intensity (EXP) and heat release (LES)

This figure shows the same trends observed previously with the 2D contour plots, although, it shows even more clearly how much more localized the heat release distribution is in the simulations as compared to the experiment. It should be noted that while the mean distribution of heat release is significantly different in the simulations, the combustion instability

trends still have the potential to be captured, as long as the phase between the unsteady heat release and pressure correctly satisfies Rayleigh's Criterion.

Because the objective of the LES simulations in this study is to develop and validate a mechanism of instability for a reacting JICF, the extended combustion model with strain and a Markstein number of 0.9 was applied for the remainder of the simulations performed in this study. This setup was chosen as it resulted in distinct unstable operation for the JICF1 configuration, consistent with experiment. It also resulted in a mean JICF flame that was closer to the mean flame image from experiment, as the reaction rate was reduced in the shear layer immediately downstream of the injection point, forcing a delay in the reaction and a more distributed flame, consistent with the experimental flame image.

While this required "tuning" of the combustion model is expected based on the simplicity and reduced kinetics of the model, it does raise the question as to the actual physical effect that is delaying and distributing the flame in the experimental rig. Because the strain model only improves the behavior of the simulations when the Markstein number is increased above the fitted value from the Cantera data, it is concluded that the physical effect on the flame is not actually strain. Some of the most probable causes of premixed flame liftoff or reaction delay include mixing effects (if the mixture is too lean or too rich to burn) and local extinction effects due to strain and heat loss (Lyons, 2007). The full effect of these localized effects on the reaction rate cannot be properly captured with the applied combustion model and would require more detailed kinetics to be included in the combustion model. This combustion model development is outside the scope of this study as the current combustion model can be utilized with tuning parameters based on experimental results.

An evident shortfall of the existing combustion model is the ignition point of the JICF flame, which according to the simulation results, occurs immediately upon injection into the hot gas cross flow. The experimental data, however, shows that the mean region of heat release is delayed until about 0.2 chamber heights downstream of the injection location. While the addition of the strain model certainly moves the simulation results in the right direction for a reacting JICF combustion scenario, the combustion model is still limited and should only be used with a complete understanding of the model limitations. For the objectives of this study, the combustion model with strain was found to be acceptable for this application, as will be discussed in more detail below.

### ***Qualitative combustion model tuning for Reacting Jet in Cross Flow***

As detailed above, the combustion model that was utilized in this study assumes a single step, 2 species reaction (fuel and oxidizer). The reaction progress is tracked through a reaction progress transport equation where the closure for the source term is obtained using a turbulent flame speed closure combustion model. Again, the basic form of the source term, or reaction rate, is calculated from the following relation, where  $b$  represents the reaction progress variable:

$$\dot{\omega}_R = \rho_u S_T |\nabla b| = \rho_u S_{L0} \Sigma |\nabla b| \quad (34)$$

This relation requires a ratio between the turbulent and laminar flame speed to calculate the reaction rate of the mixture at every cell and timestep during the simulation. The ratio between the turbulent and laminar flame speed, or wrinkling factor, is determined from the Bradley correlation, which gives the following relation for the wrinkling factor,  $\Sigma$ , where  $A$  is a constant (Bradley, 1992):



$$\Sigma = \frac{S_T}{S_{L0}} = 1 + \frac{0.95A}{Le} (\text{Re}_T \text{Pr})^{0.5} \quad (35)$$

Various studies have shown that the value of  $A$  for methane/air flames should be set between 0.25 and 0.5 (Goevert, 2011). For the head end flame in this study, a value for  $A$  of 0.5 was found to provide the best validation with experimental results, as detailed in Appendix A. However, there have been no investigations to determine if this value can also be assumed for a reacting JICF. A three-point sweep was performed of the  $A$  factor applied to the JICF reaction region, and compared to the mean flame shape derived from experimental results. Note that the HE  $A$  factor was maintained constant at 0.5 while the JICF  $A$  factor was varied between 0.5, 0.3, and 0.1. Mean heat release contours for the simulation JICF flame (Figure 54) were compared to the mean  $\text{CH}^*$  chemiluminescence intensity from experimental test 191343, run at Purdue University on 01/24/2013 (Figure 51).

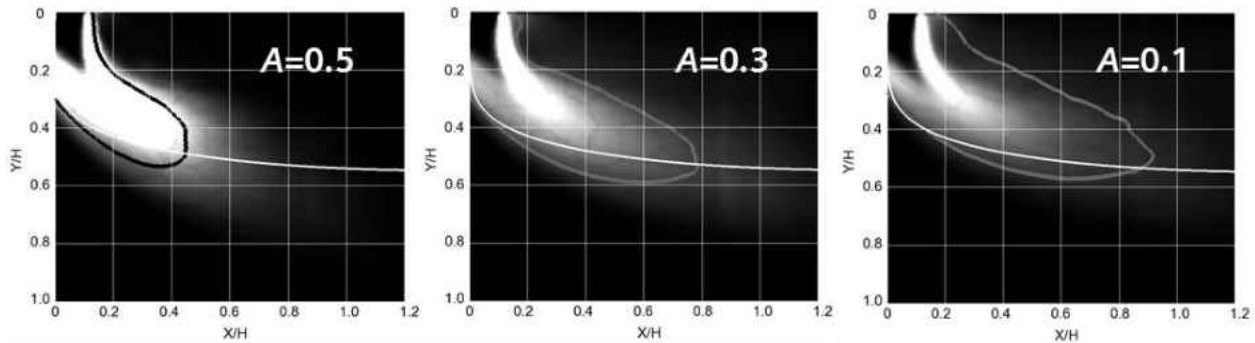


Figure 54: Normalized heat release contours from simulations with strain model for varying combustion model constants. White corresponds to maximum heat release, black corresponds to zero heat release. Dark isolines represent reaction progress variable of 0.1, white line represents Holdeman trajectory for a non-reacting JICF.

It is evident from these heat release contours that the standard  $A$  factor of 0.5 that has typically been used for premixed methane/air co-flow jet flames cannot be used for the reacting

JICF based on the extended combustion model with strain. This is shown by the left-most heat release contour that is much more compact than the representative experimental flame shown above in Figure 51, suggesting that the  $A$  factor needs to be decreased to reduce the reaction rate. The effect of decreasing the  $A$  factor is clear in Figure 54 where the flame lengthens and the heat release contours become more distributed. The same trends are observed from a more quantitative view by plotting normalized 1D plots of the heat release compared to a normalized 1D plot of the  $\text{CH}^*$  intensity obtained from experiment, shown in Figure 55.

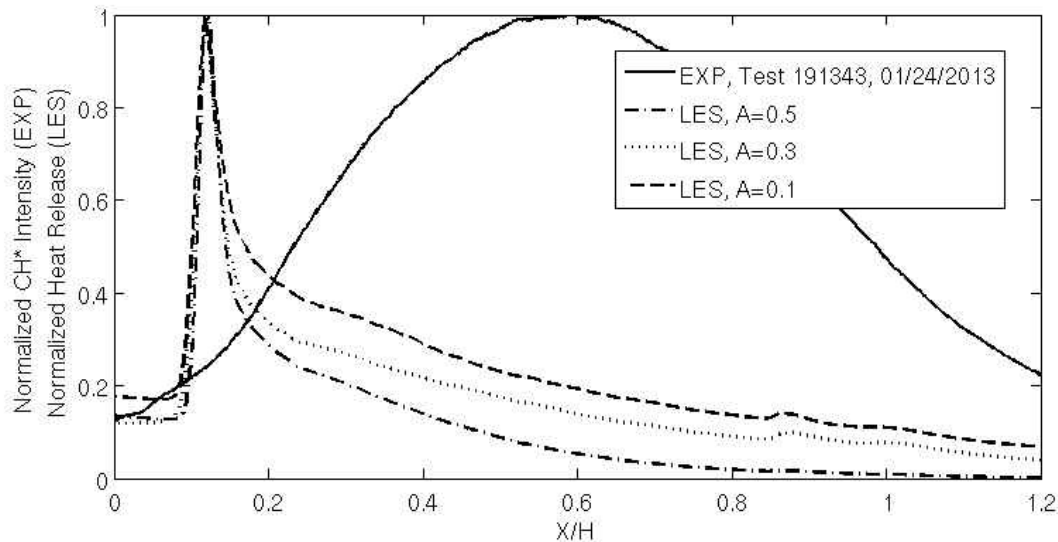


Figure 55: Normalized 1D plots of  $\text{CH}^*$  intensity (EXP) and heat release (LES) for varying combustion model constants.

Due to an incorrect prediction of stability trends and an unlikely amount of unburnt reactants downstream of the  $A=0.1$  case, it was determined that an  $A$  factor of 0.3 provided the most physical results that best matched the experimental data. As discussed in the preceding section, the existing combustion model does not accurately predict the ignition point of the JICF

flame, however, for the objectives of this study, the combustion model with strain and an  $A$  factor of 0.3 was found to be acceptable for this application.

### *Dynamic Pressure Results*

The dynamic spectrum for the stable and unstable cases is shown below in Figure 56, taken from a probe near a pressure anti-node of the dominant chamber mode. As expected, the JICF1 configuration results in a strong peak near 200 Hz while the JICF2 configuration reduces this peak almost to the level of the signal noise.

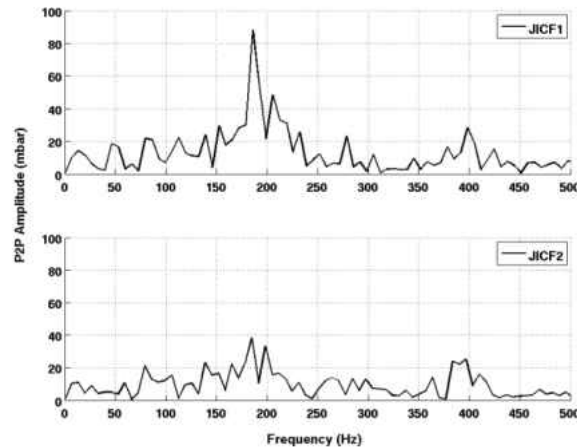


Figure 56: Dynamic spectrum for unstable (JICF1) and stable (JICF2) configurations.

It should be noted here that the actual values of the peak-to-peak amplitude observed in the experimental JICF1 case were much higher than those observed in the simulations (300-400mbars). A comparison between representative filtered signals from the experiment and simulation are shown below in Figure 57.

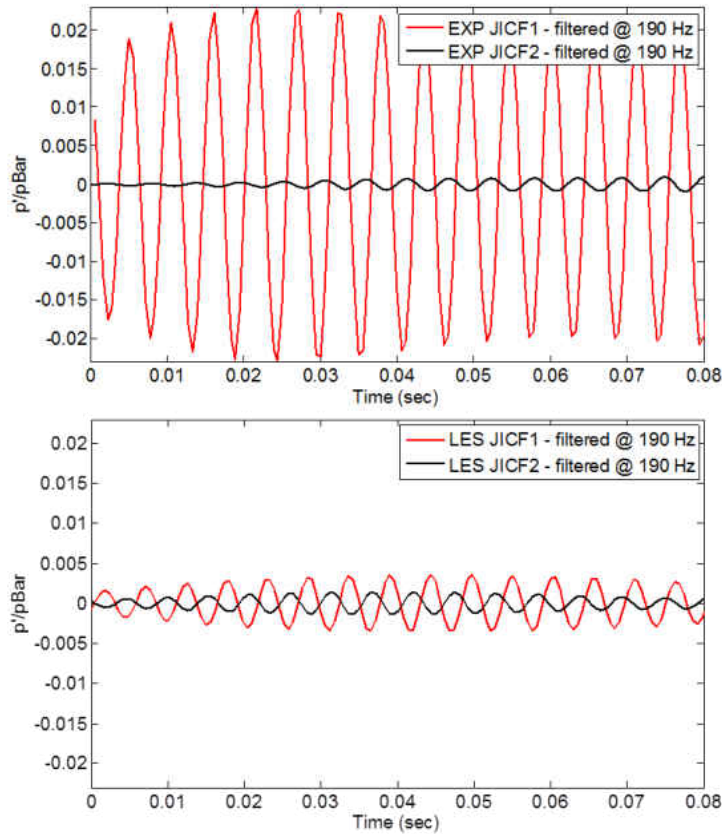


Figure 57: Representative filtered signals from experiment and simulation for unstable (JICF1) and stable (JICF2) configurations.

The discrepancy between the experimental and simulated limit cycle amplitude is largely attributed to unphysical damping at the computational domain boundaries, as described in Appendix A. However, due to the somewhat arbitrary nature of the damping present in numerical simulations, it is important to be able to predict stability trends, and not necessarily the actual limit cycle amplitude of a given mode. Although the unphysical boundary losses are quite significant and should be resolved for future applications, there was enough of a clear trend between the unstable and stable geometries to be able to further investigate the mechanism of

instability. This trend observed in the simulation is made more apparent through Figure 58, which shows the filtered signals from the LES simulations with a reduced vertical axes range.

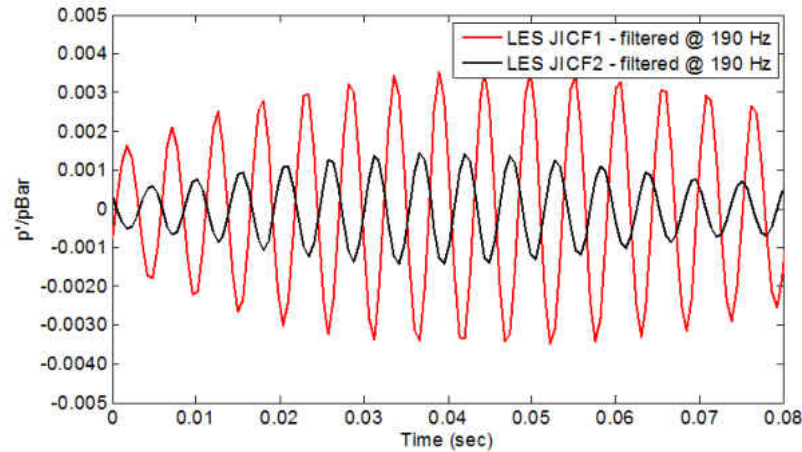


Figure 58: Representative filtered signal from LES simulations for unstable (JICF1) and stable (JICF2) configurations.

The trend seen here agrees well with that seen in the experimental results, where the JICF1 configuration strongly drove the dominant chamber mode, while the JICF2 configuration added significant damping to this mode.

It is important to note here that the JICF flame behavior is a complex result of hydrodynamic and chemical kinetics effects. Thus, a CFD tool is required to model these effects, at least with a high enough fidelity to capture the effects that contribute to the volume integrated velocity and heat release signals. The LES modeling of turbulence clearly provides an accurate method of capturing the hydrodynamic effects, while the chemical kinetics effects were modeled using the turbulent flame speed closure combustion model. It was found that this simplified model only resulted in accurate flame time lags when extensions to the model for strain and heat loss were applied. As discussed previously, these effects were found to distribute the reaction

rate of the reacting JICF. Consequently, these improvements to the combustion model delayed the flame time lags to the point where the stability trends matched those observed in the experimental rig. These time lags will be quantified in the following chapter.

### *Rayleigh Index calculations*

A method was developed based on Rayleigh's criterion (Rayleigh, 1945) to identify if any spatial regions of the reacting JICF contributed to driving or damping of the chamber mode, and what the specific contribution of the JICF was to the stability of the overall system. This method utilized 3D fields of pressure and heat release fluctuations to calculate a filtered Rayleigh Index field over the computational domain. This enabled a means to observe positive or negative contributions to the system stability, specifically at a frequency of interest. Normalized contours of this Rayleigh Index field, filtered at the frequency of the dominant chamber mode, are shown below in Figure 59.

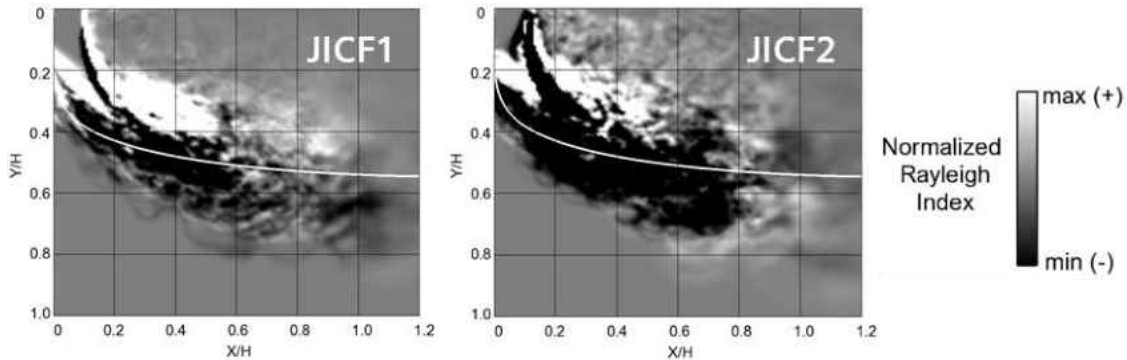


Figure 59: Normalized Rayleigh Index contours for unstable (JICF1) and stable (JICF2) cases, white line represents Holdeman trajectory for a non-reacting JICF.

Positive (white) values represent regions where the jet is driving the mode while negative (black) values represent regions where the jet is damping the mode. It is evident that a structure is consistent between both cases where the upper region of the jet is contributing to the driving of

the mode while the lower region of the jet is contributing to the damping of the mode. It is also evident that the size of the damping region in the JICF2 case is much larger than that observed in the JICF1 case. These results agree well with the experimental trends, where the JICF1 configuration drove the mode while the JICF2 configuration damped the mode.

A similar Rayleigh's Index analysis was performed using a transient video of the CH\* chemiluminescence from the experimental rig and the dynamic pressure signals obtained from the unstable JICF1 test. This analysis was completed using a Proper Orthogonal Decomposition (POD) technique (Hallum, 2012) to determine the dominant structures of the transient flame images, their frequency of oscillation, and their Rayleigh's Index contours, given the corresponding dynamic pressure field measured during the test (assumed to be uniform in the region of the jet flame, in this case). The results of this analysis, performed using 500 transient flame images (taken at 4000Hz), are shown in Figure 60.

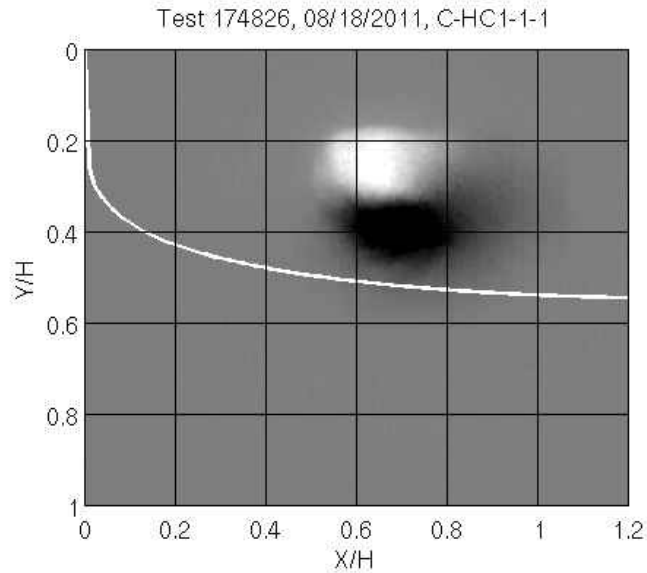


Figure 60: Normalized Rayleigh's Index contours of Test 174826 on 08/18/2011 using JICF1 configuration, calculated using a POD technique. White line represents Holdeman trajectory for a non-reacting JICF.

While the experimental data is limited, due to over-saturation of the  $\text{CH}^*$  intensity, a clear structure is observed that agrees with that seen from the simulation data where a driving region (white) is observed above a damping region (black). From the experimental data, both regions are localized in the upper region of the jet. However, there is not sufficient data to comment on how these locations correlate to the simulation data, other than that the majority of the contribution to the Rayleigh's Index occurs in the recirculating region of the JICF.

A normalized jet Rayleigh Index quantity was developed to correlate the contribution of the reacting JICF to the overall stability of the system. This quantity is defined as:



$$\bar{RI}_{jet} = \frac{\int RI \cdot dV_{jet}}{\int dV_{jet}} \div \left( \frac{\int RI \cdot dV_{HE}}{\int dV_{HE}} + \frac{\int RI \cdot dV_{jet}}{\int dV_{jet}} \right) \quad (36)$$

where  $RI$  corresponds to the filtered Rayleigh Index field (as described above), and  $V_{jet}$  and  $V_{HE}$  represent specified volumes that enclose the jet and head end flames, respectively. This normalized jet Rayleigh Index was calculated to be 0.324 for the JICF1 configuration and -1.127 for the JICF2 configuration. These values suggest that the reacting JICF is adding an additional 32% of *driving* to the existing head end instability for the JICF1 configuration and adds an additional 113% of *damping* to the existing head instability for the JICF2 configuration. These results agree well with the experimental and numerical data that has shown that the JICF1 configuration drives the existing chamber mode above the baseline instability observed from the head end flame while the JICF2 configuration almost completely damps this baseline instability. A similar type of analysis can be used in more complex cases to identify the contribution of multiple reaction zones to the overall system stability.

With the extended combustion model, it was found that the LES simulations could correctly replicate the stability trends observed between the experimental JICF1 and JICF2 configurations. While the limit cycle amplitude of the dominant unstable mode was significantly under predicted in the simulations, largely due to unphysical losses through the computational domain boundaries, the results could still be used to hypothesize the mechanism that causes the difference in stability between these two cases.

## CHAPTER 5 – FLOW PHYSICS AND ACOUSTIC MODELING

### Development of Mechanism Hypothesis

#### *Investigation of jet in cross flow coherent structures*

An important step in understanding the behavior of the reacting JICF and its effect on the combustion instabilities of the system was to investigate the natural coherent structures of the JICF and identify if any coupling between these structures and the system dynamics is possible. As highlighted previously in the literature review section, there has been an extensive amount of research on the hydrodynamics of a non-reacting JICF, as well as several more recent studies on reacting jets and the effects of forcing the jet or the cross flow. The fundamental JICF research has provided a good understanding of the four main coherent structures of a JICF, including the shear layer, horseshoe, and wake vortices, as well as the counter-rotating vortex pair (CVP) in the downstream region of the jet. Literature has shown a wide range of frequencies, or Strouhal numbers, associated with the coherent structures of the JICF. This range includes Strouhal numbers based on the jet diameter as low as 0.125 for the wake vortices to Strouhal numbers as high as 1.7 and 2.0 for the jet near field shear layer vortices (Fric, 1994; Smith, 1998). Given the velocities and jet diameters investigated in this study, this Strouhal number range corresponds to a frequency range of approximately 500-6000 Hz, however, it is difficult to provide a direct comparison as important quantities such as the jet momentum ratio, cross flow Reynolds number, and jet reaction are widely varied. The horseshoe and wake vortices are typically the lowest frequency structures in the near field region of the jet and exhibit similar Strouhal numbers, on the order of 0.125 to 0.17. These frequencies are likely still too high to result in any feedback with the dominant chamber mode, with a corresponding Strouhal number near 0.05. The shear

layer vortices typically occur at a higher frequency, with Strouhal numbers as high as 2.0. The CVP develops in the far field region of the jet, much further downstream than the region of heat release, and thus, no feedback between this structure and the system stability is expected.

Based on the information that is available in the literature, it was determined that the natural frequencies of the jet would be too high to result in any significant coupling with the combustion instability modes investigated here. This proposal was also reinforced with experimental data that shows that any variation of the parameters that have an impact on the frequency of the coherent structures of the jet, such as flow rates and jet diameter (excluding resonance effects), had a negligible impact on the unstable modes present in the chamber.

To confirm this proposal, however, an estimation of the near-field shear layer Strouhal numbers was calculated from a baseline JICF LES simulation by approximating the distance between vortices in the shear layer region of the jet. The mean velocity of the jet was divided by this distance to estimate a frequency and finally a Strouhal number associated with the jet shear layer. A representation of the data used for this calculation is shown below in Figure 61, where instantaneous contours of mixture fraction were used to identify the shear layer rollup and a spline was created to measure the physical distance between the vortices.

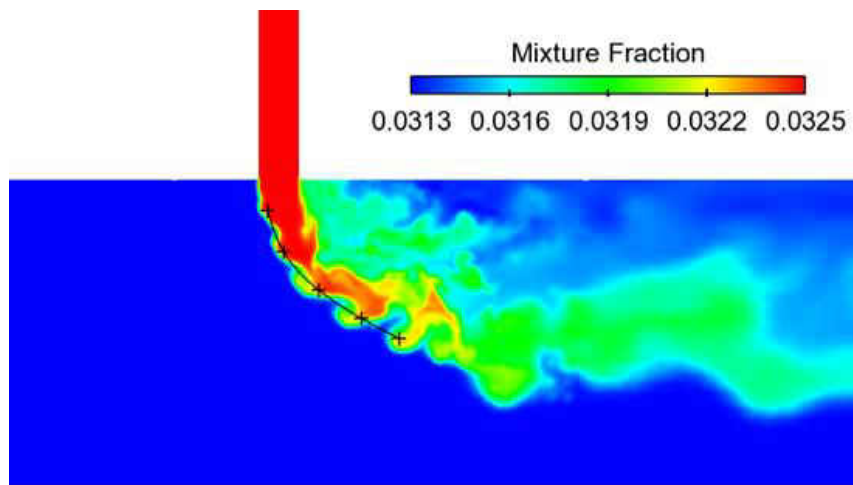


Figure 61: Instantaneous contours of mixture fraction used to measure the physical distance between vortices in the jet shear layer.

The distance between vortices was measured to be approximately 0.012 meters, and given the mean jet velocity of 60 m/s, the jet shear layer Strouhal number for this case was estimated to be 0.83. This frequency is in the middle of the range expected from literature for the natural frequencies of the JICF coherent structures, and also confirms that any coupling between the shear layer vortices and the dominant chamber mode is unlikely.

Based on the reasoning above that the coherent structures of the jet occur at too high of a frequency to effect the dominant chamber mode, it was proposed that a more global mechanism is likely in the region of the jet, as opposed to a localized mechanism. In one of the preliminary JICF simulations, an unexpected frequency in some of the monitor points was found near 120 Hz, a frequency too low to be related to the dominant chamber's second longitudinal mode. Further investigation showed that the velocity of the premixed reactants flowing to the JICF was strongly fluctuating at this frequency and a frequency response function (FRF) analysis showed that the JICF manifold and injector was behaving like a Helmholtz resonator. This FRF, taken

between a plenum probe and a chamber probe just downstream of the jet, is shown in Figure 62. The peak frequency of a Helmholtz resonator with corresponding dimensions to the JICF geometry is shown by the vertical black line, as predicted by a Helmholtz resonator tool (HRT).

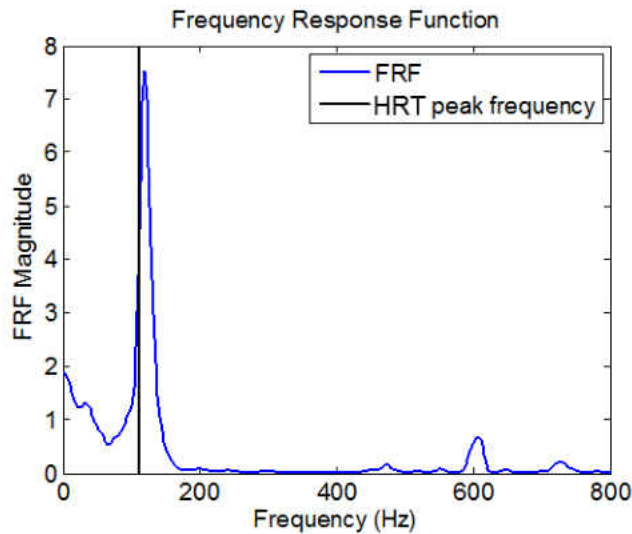


Figure 62: FRF of preliminary LES simulation, showing the Helmholtz resonator behavior of the JICF geometry.

This discovery resulted in an investigation of the resonant frequencies of all of the JICF geometries tested to determine a possible correlation between system stability and the resonant frequency of the geometries. It was found, however, that due to the three-dimensional nature of the majority of the JICF supply setups, these configurations could not always be assumed to simply be Helmholtz resonators, although the effective physics (i.e., an oscillating flow within the “resonator” neck, or jet) were similar. In a typical Helmholtz resonator setup, the flow within the neck oscillates at the resonant frequency. If you replace the purge flow with a reacting mixture, this oscillatory behavior will potentially result in an oscillatory heat release. While a non-reacting purge flow could have a damping effect on a resonant mode, a reacting “purge” flow could theoretically have a driving effect on a resonant mode, depending on the phase

between the pressure, velocity, and heat release oscillations. This was the thought process that began to provide the clues to identifying a mechanism of instability of the reacting JICF.

As discussed previously, it was found during experimental testing that a modification to the JICF air supply line choke point resulted in a drastic change in the stability of the dominant chamber mode, even when the operating conditions were kept nearly constant. While one particular setup was found to actually drive the instability much higher than the baseline head-end only instability, another setup was found to nearly completely damp this instability out. With the additional clues from the LES simulations that this stability change could be a result of “resonator-like” behavior of the JICF, a mechanism was proposed to quantify this behavior for a reacting JICF.

### **Proposed Mechanism of Instability**

For the unstable case (JICF1), transient data from the experimental rig showed a strong pulsing behavior of the reacting JICF at the frequency of the dominant chamber mode. Pixel-by-pixel analysis of the chemiluminescence images further suggested that a pulsing motion occurred when the jet was injected at an anti-node of a chamber pressure mode, while a flapping motion occurred when the jet was injected at an anti-node of a chamber velocity mode (Fugger, 2011). For the JICF configurations considered in this study, the jet is injected near a pressure anti-node of the dominant chamber mode, and thus, the incoming jet is exposed to a largely fluctuating pressure field in the chamber. This effect becomes clear in Figure 63 where the normalized mode shape of the dominant chamber mode is superimposed over the JICF2 geometry. This mode shape was calculated using the Generalized Instability Model (Portillo, 2007).

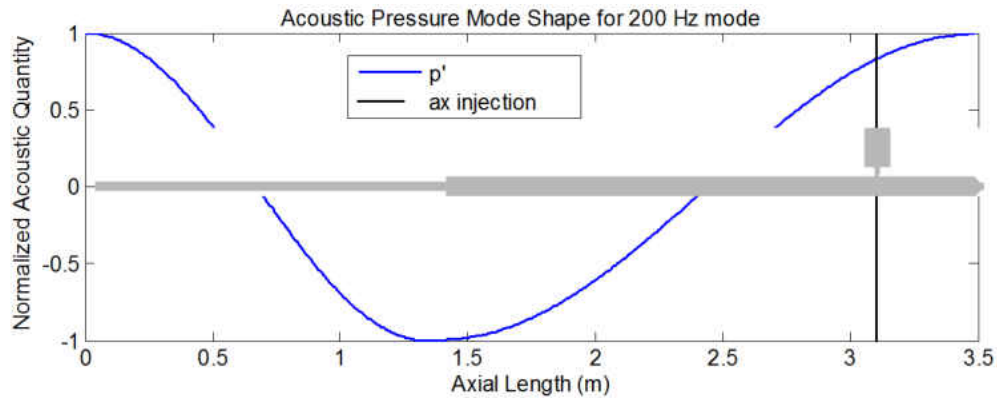


Figure 63: 200Hz acoustic pressure mode shape distributed along JICF2 geometry.

Because the incoming jet is exposed to the fluctuating pressure field in the chamber, a coupling can occur between the incoming jet reactants and this fluctuating pressure field, resulting in a fluctuation in the reactant flow at the point of injection. This mechanism is similar to an “injector coupling” that has been observed in the context of transverse modes, where it has been documented that “the oscillating pressure field over the nozzle exit creates fluctuations in mass flow through the nozzle...” (O’Connor, 2011 and 2012).

The transient behavior between the pressure, jet velocity, mixture fraction, and heat release is clearly illustrated by observing instantaneous contours of each of these quantities over one period of oscillation of the dominant chamber mode. These contours were extracted from LES animations and are shown below in Figure 64 (pressure), Figure 65 (Y-velocity), Figure 66 (mixture fraction), and Figure 67 (heat release).

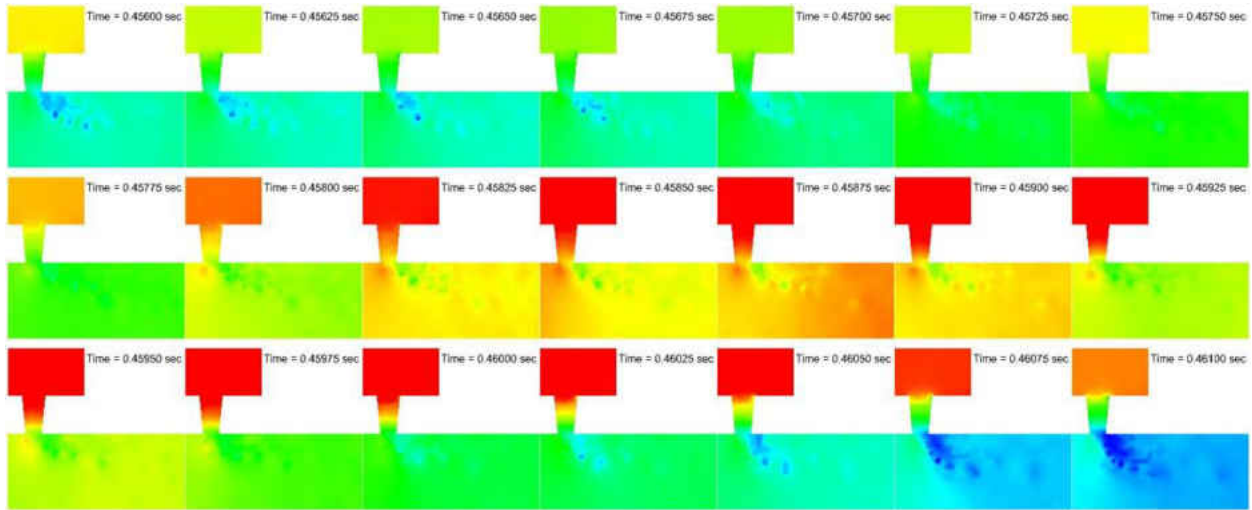


Figure 64: Instantaneous pressure contours in the JICF region over one cycle of oscillation (timestep is  $1/20^{\text{th}}$  of a period, red=max, blue=min, approximate range = 815,000 to 830,000 Pa).

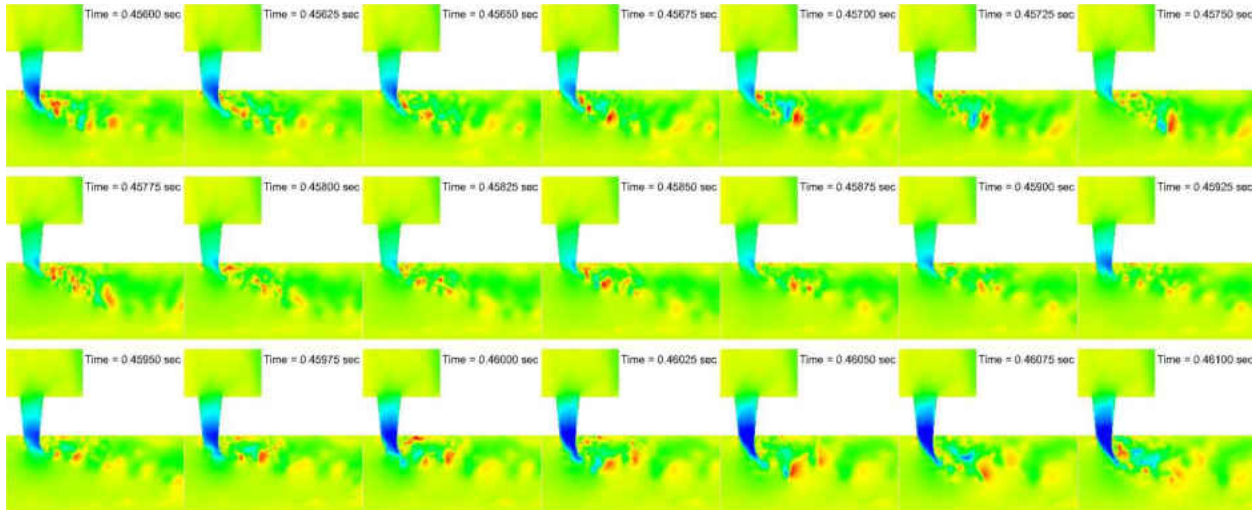


Figure 65: Instantaneous Y-velocity contours in the JICF region over one cycle of oscillation (timestep is  $1/20^{\text{th}}$  of a period, red=max, blue=min, approximate range = -70 to 30 m/s).



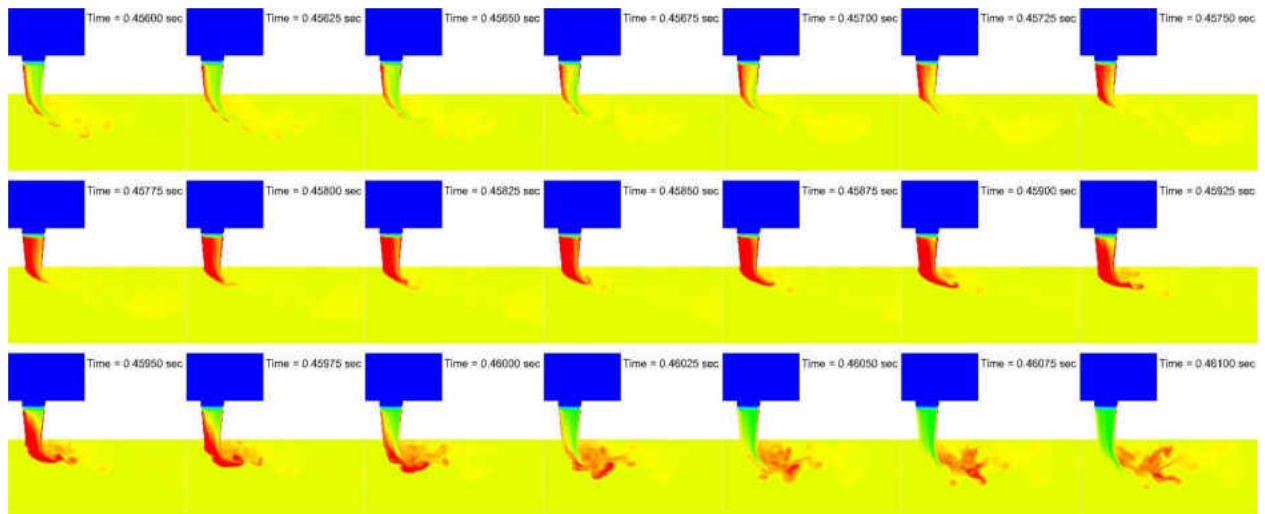


Figure 66: Instantaneous mixture fraction contours in the JICF region over one cycle of oscillation (timestep is  $1/20^{\text{th}}$  of a period, red=max, blue=min, approximate range = 0 to  $0.05 \text{ kg}_{\text{fuel}}/\text{kg}_{\text{mixture}}$ ).

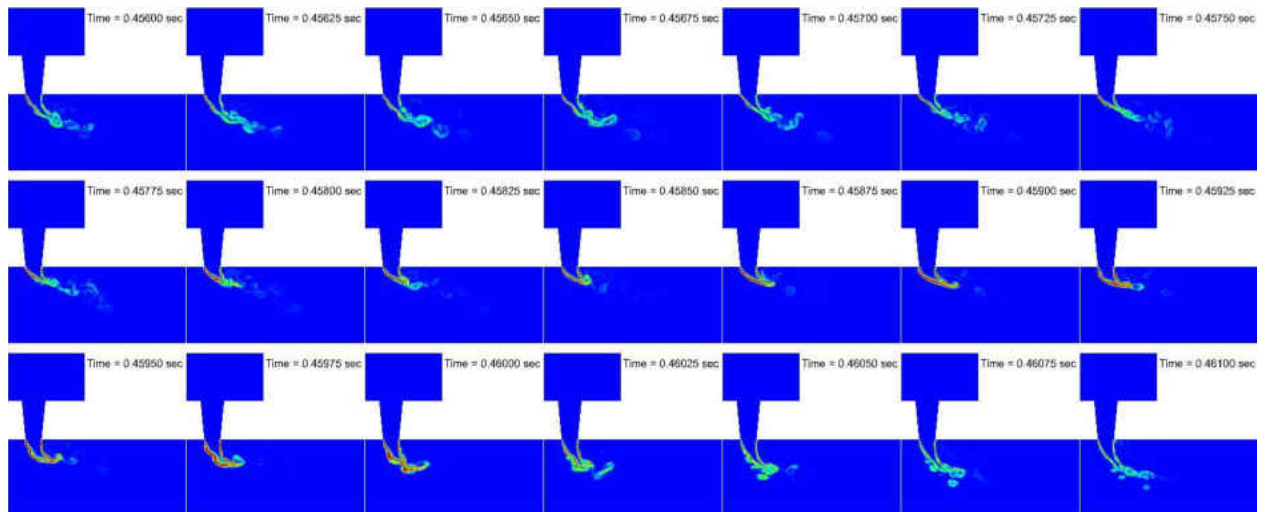


Figure 67: Instantaneous heat release contours in the JICF region over one cycle of oscillation (timestep is  $1/20^{\text{th}}$  of a period, red=max, blue=min, approximate range = 0 to  $100 \text{ kg}_{\text{fuel}}/\text{m}^3\text{s}$ ).

These contours help to illustrate the mechanism that occurs between the JICF and the unstable cross flow. It is evident from the first row of pressure images that the chamber pressure starts relatively low at the beginning of the cycle and begins to increase towards the end of the

first row of images in Figure 64. Consequently, the high jet velocity that occurs at the beginning of the cycle begins to decrease towards the end of the first row of images in Figure 65. This decrease in jet velocity (and air flow) causes an increase in the mixture fraction within the scoop (first row of images in Figure 66) as well as a decreasing penetration of the JICF heat release contours, seen in the first row of images in Figure 67.

In the middle row of images in Figure 64, the chamber pressure continues to increase to its maximum value in the middle of the period of oscillation. This produces a minimum jet velocity and air flow rate (Figure 65), and consequently a maximum mixture fraction in the scoop (Figure 66) and a significantly decreased penetration of the JICF heat release contour (Figure 67).

Finally, as observed in the final row of images in Figure 64, the chamber pressure begins to decrease to another minimum at the end of the period of oscillation. The jet velocity and air flow rate begins to increase again (Figure 65), forcing the rich mixture that had built up in the scoop out into the combustion chamber (Figure 66). This results in an increase in the penetration of the JICF heat release contour, back to its maximum point in the period of oscillation (Figure 67).

Depending on the delays between the chamber pressure fluctuation, the jet mass flow fluctuation, and the heat release that occurs from the reacting JICF, a feedback cycle can potentially develop, and based on Rayleigh's criterion, contribute to the overall system stability. This feedback cycle is shown schematically in Figure 68 where the delays between each component can be represented by effective time lags.

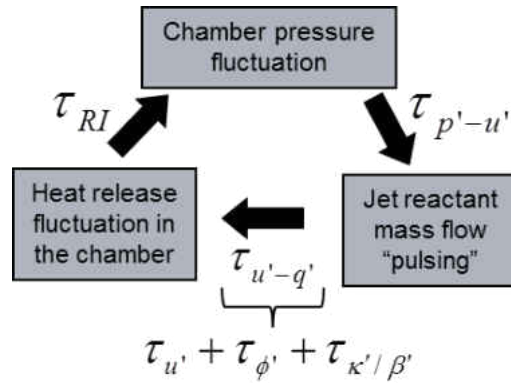


Figure 68: Schematic representing the proposed mechanism with effective time lags.

Here, the first time lag occurs between the pressure fluctuation in the chamber and the resultant mass flow (or velocity) fluctuation in the jet reactants. This time lag is a function of the JICF configuration and will be referred to as the “jet impedance”. The next time lag occurs between the fluctuation of the jet reactants and the resultant heat release fluctuation in the chamber. Depending on whether the jet reactants are perfectly or partially premixed and the kinetics of the system, this time lag can be split up into a velocity, equivalence ratio, and strain/heat loss component, forming what will be referred to as the “flame time lag”. Finally, the combined delay of each of the previous time lags results in an overall time lag between the chamber pressure fluctuation and the heat release fluctuation that occurs in the chamber due to the reacting JICF. This combined time lag will be referred to as the “Rayleigh Index time lag”, as it is this total delay that will determine whether the reacting JICF will drive or damp the mode present in the chamber.

While quantifying the actual values of each of the time lags would be difficult with experimental diagnostics, (and not possible based on the currently available results), it is straightforward to calculate these values from the 3D fields available from self-excited LES. A

process was developed during solver run time that calculates the volume integral of pressure, velocity, and heat release in pre-specified domains at a given time interval throughout the simulation. For example, a chamber pressure and heat release integration domain was setup around the jet flame while a jet velocity integration domain was setup at the location of jet injection. By integrating the respective fields in each of these domains at each timestep, a 1D signal was calculated as a function of time for each of the variables of interest. By taking the transfer function between each of these signals, the phase (or time lag) can be quantified between each variable, providing the values for the time lags necessary to validate the proposed mechanism. Note that this volume integration sampling assumes that the jet flame is acoustically compact, compared to the modes present in the chamber. This is a valid assumption as the jet flame length is less than 1% of the length of the dominant acoustic mode in the chamber.

The corresponding time lags for the JICF1 and JICF2 cases investigated here are shown below in Figure 69 where the phase values (in degrees) were calculated at the frequency of the dominant mode. Note that the flame time lag (u-q) is represented by the gray symbol, the jet impedance (p-u) is represented by the hollow symbol, and the Rayleigh Index time lag (p-q) is represented by the black symbol. Due to the physically realistic nature of the self-excited simulations, it is not possible to separate the velocity and equivalence ratio components of the flame time lag, and thus they are shown here as a combined time lag.

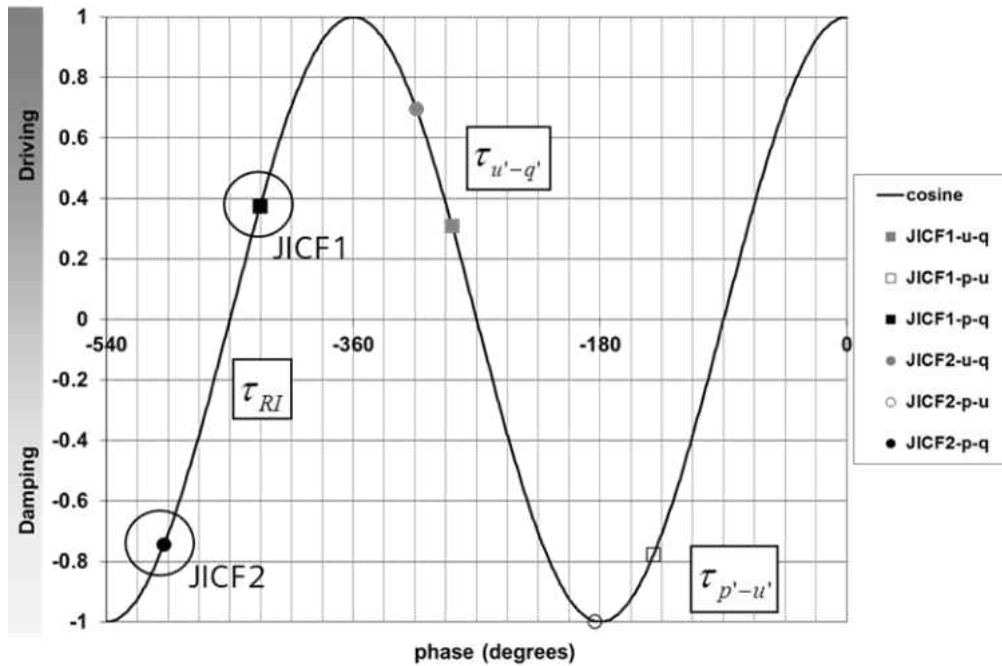


Figure 69: Time lags calculated from self-excited LES simulations for unstable (JICF1) and stable (JICF2) cases, shown on a pressure-heat release stability map.

The time lags are shown super-imposed on a cosine curve so that the combined Rayleigh Index time lags indicate driving of the instability when the cosine curve is positive and damping of the instability when the cosine curve is negative, based on Rayleigh's criterion (Rayleigh, 1945). Note that the location of the flame and jet impedance time lags on the cosine curve is not representative of driving or damping. It is evident from the data that the difference in the jet impedance time lags between the JICF1 and JICF2 cases (43 degrees) is what pushes the unstable Rayleigh Index point over the stability boundary into the stable domain. The difference in the flame time lags (26 degrees) is due to small deviations in the jet reactant mass flow rate and equivalence ratio between the two cases.

### Derivation of a Heat Release Model

A mathematical heat release model was developed from the governing equation for the unsteady heat release at the flame front of the jet. For the purposes of this study, the effects of strain and heat loss are not included explicitly in the model, as they can be assumed to be implicitly accounted for through the time lags. An additional term for strain is derived in Appendix C, based on the strain and heat loss model included in the combustion model, however, it was not included in the implemented heat release model as strain was found to have a minor effect on the combustion at the high pressures considered here (see Figure 24).

Thus, the relation for the instantaneous heat release at the flame front of the jet is defined as:

$$q(t) = Y \cdot \dot{m} \cdot H_f \quad (37)$$

where  $Y$  represents the fuel concentration,  $\dot{m}$  represents the jet mass flow rate, and  $H_f$  represents the lower heating value of the fuel.

Three regions of importance were defined for the derivation of the local heat release fluctuation: the location of the fuel injection, the exit of the jet, and the flame front, as shown in Figure 70.

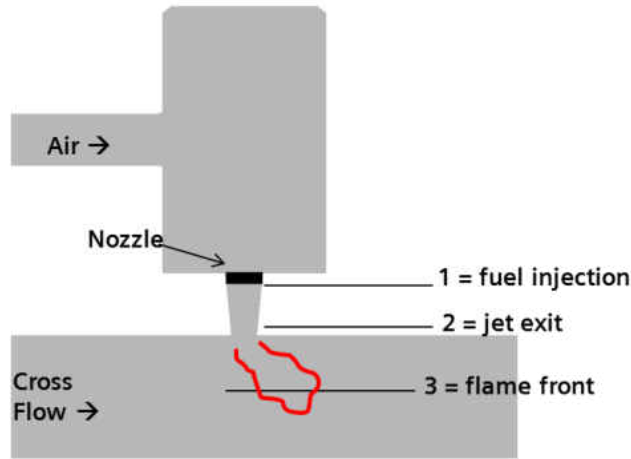


Figure 70: Regions defined for heat release derivation.

The instantaneous heat release is divided into a mean and fluctuating component and then linearized about the mean value to develop a function for the fluctuating heat release as a function of the fluctuating fuel concentration and mass flow rate:

$$q'(t) = [\bar{m}H_f Y']_1 + [\bar{Y}H_f \dot{m}']_2 \quad (38)$$

Here, the subscripts listed for each of these terms represents the location where the quantities are to be evaluated, as defined above in Figure 70. Each of these terms are then expanded about their mean values and related to acoustic quantities.

The first term on the right hand side in Equation (38) is expanded by defining the fuel concentration as a function of the fuel and air mass flow rates, but for simplicity, neglecting the contribution of the fuel mass flow to the total mass flow:

$$Y = \frac{\dot{m}_f}{\dot{m}_f + \dot{m}_{air}} \approx \frac{\dot{m}_f}{\dot{m}_{air}} = \frac{\dot{m}_f}{\rho_{air} u_{air} A_{air}} \quad (39)$$

Here, the fuel mass flow rate is assumed to be constant due to the minor contribution that it has to the overall equivalence ratio fluctuations. Based on the measured pressure drop across the fuel lines, it was calculated that the air fluctuations contributed to more than 85% of the equivalence ratio fluctuations. It may be necessary for practical cases, however, that future work be done to account for these fuel flow fluctuations by defining the fuel source term as a function of the fuel line impedance, or by actually resolving the fuel line and orifices within the computational domain.

With this approximation, and by linearizing about the mean air density and velocity, an expression for the fluctuating fuel concentration can be defined as a function of acoustic quantities:

$$Y' = \frac{-\dot{m}_f}{\bar{\rho}_{air}\bar{u}_{air}A_{air}} \left( \frac{u'_{air}}{\bar{u}_{air}} \right) - \frac{\dot{m}_f}{\bar{\rho}_{air}\bar{u}_{air}A_{air}} \left( \frac{\rho'_{air}}{\bar{\rho}_{air}} \right) = \frac{-\bar{Y}}{\bar{u}_{air}} u'_{air} - \frac{\bar{Y}}{\bar{\rho}_{air}} \rho'_{air} \quad (40)$$

Assuming isentropic flow, the density fluctuations can be related to the pressure fluctuations, giving the following expression for the fluctuating fuel concentration:

$$Y' = \frac{-\bar{Y}}{\bar{u}_{air}} u'_{air} - \frac{\bar{Y}}{\bar{\rho}_{air}c_{air}^2} p'_{air} \quad (41)$$

It is assumed that the second term in Equation (40) can be neglected, as this term is several orders of magnitude lower than the velocity term (this assumption will be verified below). Thus, an expression for the fluctuating fuel concentration can be substituted into the first term in Equation (38),



$$\bar{m}H_f Y' = \frac{-\bar{m}H_f \bar{Y}}{\bar{u}_{air}} u'(t - \tau_{injection}) \quad (42)$$

where these terms are evaluated at the location of fuel injection, or region 1 in Figure 70.

The second term in Equation (38) is expanded by linearizing the mass flow rate about its mean value to develop an expression for the fluctuating mass flow rate:

$$\bar{Y}H_f \dot{m}' = \bar{Y}H_f (\rho' \bar{u} A_{jet} + \bar{\rho} u' A_{jet}) \quad (43)$$

Assuming isentropic fluctuations, the density fluctuation can again be related to the pressure fluctuation, resulting in a relation for the fluctuating mass flow rate as a function of acoustic quantities:

$$\dot{m}' = \left( \frac{p' \bar{u} A_{jet}}{c^2} + \bar{\rho} u' A_{jet} \right) \quad (44)$$

Again, the pressure term in Equation (44) is several orders of magnitude lower than the velocity term, and thus, the fluctuating mass flow rate can be approximated as:

$$\dot{m}' \approx \bar{\rho} u' A_{jet} \quad (45)$$

The second term in Equation (38) then becomes:

$$\bar{Y}H_f \dot{m}' = \bar{Y} \bar{\rho} A_{jet} H_f u'(t - \tau_{jet}) \quad (46)$$

Substituting Equations (42) and (46) back into Equation (38) produces a final expression for the instantaneous heat release fluctuation of the JICF, as a function of acoustic quantities:

$$q'(t) = \left[ \frac{-\bar{m}H_f\bar{Y}}{\bar{u}_{air}} u'(t - \tau_{injection}) \right]_1 + \left[ \bar{Y} \cdot \bar{\rho}A_{jet}H_f u'(t - \tau_{jet}) \right]_2 \quad (47)$$

Note that the subscripts listed for each of these terms represent the location where the quantities are to be evaluated, as defined above in Figure 70. A summary of the assumptions made in deriving this model is provided below. Note that these assumptions are case specific and should be re-evaluated for additional configurations.

- The reacting JICF can be assumed to be a “thin” flame, with respect to the chamber acoustic wavelengths of interest (jet flame length is less than 1% of 2L wavelength)
- Isentropic fluctuations
- Density/pressure terms can be neglected (see Table 9)
- The contribution of the jet fuel mass flow to the total jet flow can be neglected (fuel mass flow is ~ 3% of total jet flow)
- Jet fuel mass flow is constant (based on the pressure drop across the nozzle orifices)

### **Application to Acoustic Modeling**

As mentioned above, a three-dimensional acoustic modeling tool was used to identify if the trends observed in the experimental data and numerical simulations could be predicted using a lower-order tool. The successful use of this tool could potentially allow for parametric studies, without the expense of LES. The tool used in this study, referred to as TA3D, solves the linearized Euler equations on arbitrary three-dimensional meshes where linear and non-linear heat release models can be applied to account for the interaction between acoustics and heat release (Johnson, 2013).

A baseline non-linear heat release model for the head end flame was developed by Johnson (Johnson, 2013) and applied to the JICF1 and JICF2 configurations. The first set of TA3D simulations was run using only this head end heat release model to determine the potential damping effect that the non-reacting JICF has on the overall system. By first understanding the behavior of the non-reacting JICF, the effect of the JICF heat release model on the system stability would be able to be distinguished when this model was added to the baseline head end heat release model. Because a non-linear head end model was used, a limit cycle was achieved, and is shown below in Figure 60 for the JICF1 and JICF2 configurations.

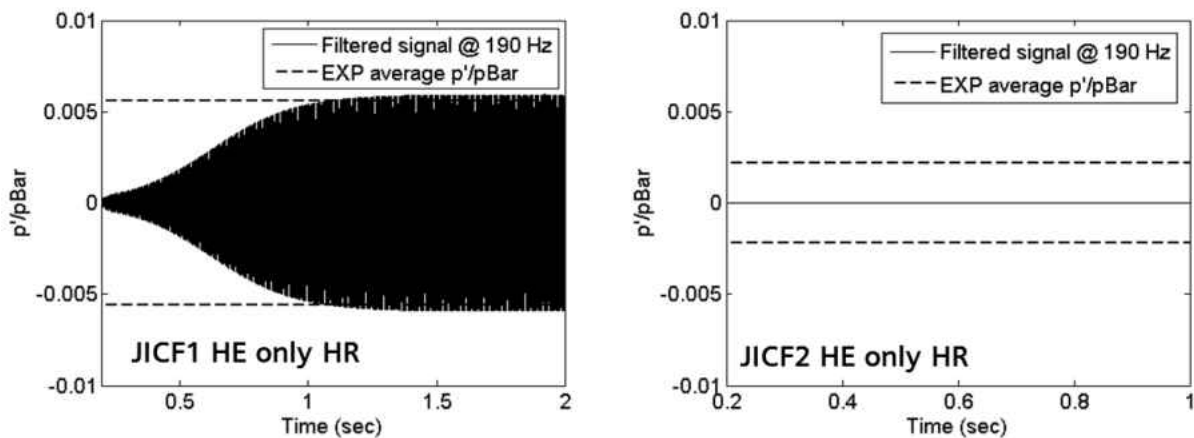


Figure 71: Filtered acoustic pressure signals for baseline JICF1 and JICF2 cases from TA3D, no JICF heat release model.

As expected, the dominant mode (near 200Hz) is driven to a limit cycle in the JICF1 case; however, it is apparent that this mode is basically non-existent in the JICF2 geometry. This suggests that the JICF2 geometry adds a significant amount of damping at 200Hz to the system. This is likely due to the fact that the geometry of the JICF2 configuration is such that it exhibits a resonant Helmholtz mode very close to the frequency of the dominant chamber mode. This results in a resonator effect that damps the signal near 200 Hz when a reaction is not occurring in

this region. If desired, it would be feasible to re-tune the head end heat release model such that enough driving of the 200Hz mode occurred from the head end that it would overcome the damping due to the JICF2 geometry and still achieve a limit cycle. However, for the sake of consistency, and because the desired stable/unstable trends can be predicted without matching the actual value of the limit cycle amplitude, this head end heat release model tuning was not further investigated in this study.

### ***Basic Heat Release Model***

Because the objective of this basic TA3D model was to predict the stability trends observed in the experiment and modeled in the simulations, a linear model was applied to the JICF while the non-linear model was left for the head end flame. Based on the proposed mechanism demonstrated in Figure 68, the two “time lags” that need to be accounted for are the time lag between the chamber pressure fluctuation and the resultant jet velocity fluctuation (jet impedance) and the time lag between the jet velocity fluctuation and the resultant heat release fluctuation (flame time lag). As stated above, the jet impedance is implicitly accounted through the TA3D solver, and thus, only the flame time lag needs to be included in the heat release model. From the LES simulations, this time lag was found to be approximately 285 degrees, or 3.958 ms for the 200 Hz mode. For this basic analysis, a gain factor of unity was applied, as no further insight on this parameter is currently available. The mean fields for heat release and velocity were mapped onto the acoustic mesh from the LES simulations and the fluctuating velocity field was averaged over the sender field, as described by Johnson (Johnson, 2013).

The flame time lag was introduced by assuming a simple  $q'-u'$  time lag model, where the heat release at the reacting JICF is calculated from the following relation

$$q'(x, y, z, t) = n\bar{q}(x, y, z)r(x, y, z)\frac{u'_s(x, y, z, t - \tau)}{\bar{u}_s} \quad (48)$$

where  $q'$  and  $\bar{q}$  represent the fluctuating and mean components of heat release, respectively,  $n$  represents the gain,  $u'$  represents the acoustic velocity field,  $\tau$  represents the time lag between the heat release fluctuation and the velocity fluctuation, and  $r$  and  $s$  represent the sender and receiver regions respectively (as described previously). The time lag was taken directly from the simulation results discussed previously and shown in Figure 69 as the gray symbols. The sender and receiver regions were defined using OpenFOAM's setFields utility based on the proposed mechanism that the acoustic perturbation originates at the exit of the jet and causes a fluctuation in heat release at the reacting JICF flame front. The sender and receiver regions for the basic heat release model are shown in Figure 72.

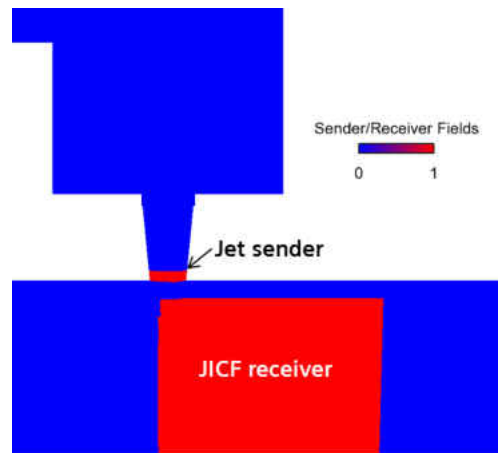


Figure 72: Sender and receiver regions for basic TA3D heat release model for the JICF

Because neither the gain nor the time lag in the heat release model are a function of the acoustic velocity fluctuation amplitude, the model is linear and will cause an unstable mode to grow unbounded while causing a stable mode to damp completely.

The same heat release model for the reacting JICF was applied to both the JICF1 and JICF2 configurations. The corresponding filtered pressure signals for each case are shown below in Figure 73.

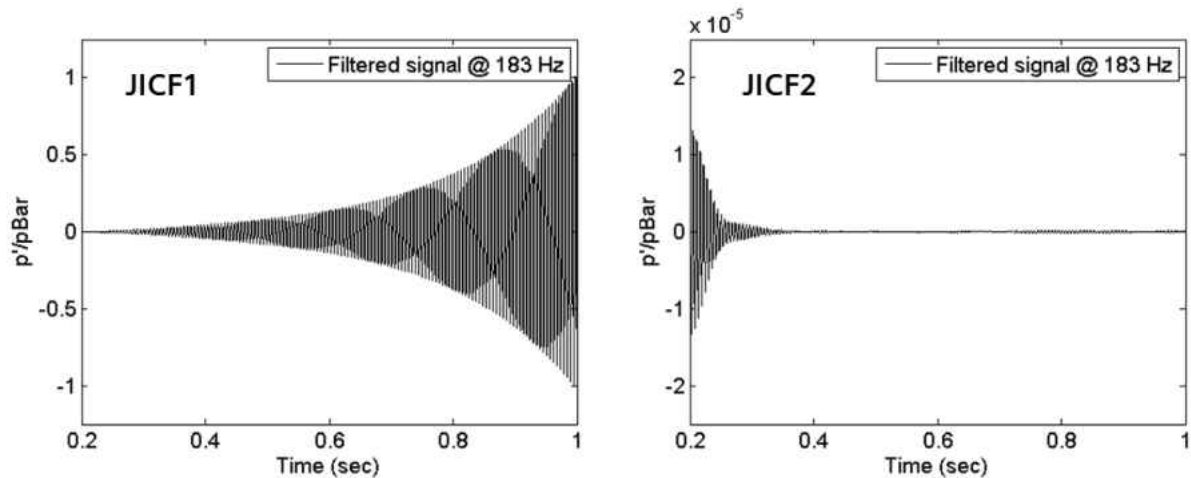


Figure 73: Filtered acoustic pressure signals for JICF1 and JICF2 cases from TA3D, with basic JICF heat release model (note the different axes for clarity).

The results clearly show that the dominant mode is strongly driven by the JICF1 case and completely damped by the JICF2 case, a difference that is solely due to the change in geometry between the two cases. This trend predicted by TA3D agrees well with the results observed in both the experimental rig and in the LES simulations, as discussed previously. This further validates the proposed mechanism and suggests that a lower order tool, like TA3D, can be used to further investigate the contributions to the mechanism of instability proposed here. It should be noted here that it was found that an incorrect JICF heat release model (for example, an

incorrect time lag) can result in the JICF2 geometry also strongly driving the dominant mode. Thus, it is evident that although the JICF2 configuration is known to provide significant damping to the system, an incorrect JICF heat release model can still result in the JICF2 geometry driving the dominant chamber mode and incorrectly predicting the trends observed in experimental data.

### ***Detailed Heat Release Model***

The detailed JICF heat release model derived above was implemented into the TA3D setup by adding two additional heat release models to the existing head end heat release model developed Johnson (Johnson, 2013). These additional heat release models relate the fluctuating heat release field to the fluctuating velocity field by applying an n-tau model based on Equation (47) to replace the basic JICF heat release model that was discussed previously.

### ***Time lag calculations***

The two time lags required for the JICF heat release model defined in Equation (47) were preliminarily determined from specific LES simulations. These specific simulations were run in an effort to identify the individual components that make up the JICF “global” flame time lag, calculated from the full, self-excited LES simulations. The individual time lags that were found to be important from the derivation of the heat release model shown in the preceding section include a fuel injection time lag (defined as the time from the fuel injection location to the corresponding heat release fluctuation at the flame front), and a burner, or jet time lag (defined as the time from the jet exit to the corresponding heat release fluctuation at the flame front).

These individual time lags were determined by running simulations that removed the contribution of individual effects. For example, the jet time lag was calculated directly by running a simulation where a constant mixture fraction boundary was applied to the jet flow

(perfectly premixed, PerPM). This resulted in a simulation with no equivalence ratio fluctuations, providing an accurate representation of the jet time lag.

An attempt to calculate the fuel injection time lag was initially done by subtracting the jet time lag from a time lag calculated from a partially premixed (ParPM) simulation. This requires the assumption that the fuel injection and jet time lags can be linearly superimposed. This assumption was found to be invalid, as the resultant injection time lag produced an incorrect prediction of the stability trends known from experimental and numerical results (i.e., both the JICF1 and JICF2 cases were unstable at 200 Hz with this time lag, instead of the JICF2 case being stable at 200Hz as is observed in the experimental results). Alternatively, a model to determine the injection time lag was proposed by defining this time lag as a function of the jet time lag and the mean velocity and length of the scoop, or mixing passage, between the fuel injection and the jet exit. This relation for the injection time lag becomes:

$$\tau_{injection} = \tau_{jet} + \frac{\ell_{scoop}}{\bar{u}_{scoop}} \quad (49)$$

The resultant time lags for the detailed heat release model defined in Equation (47) are summarized below in Table 7. Here, both methods used to calculate the injection time lag are shown for reference, however the acoustic modeling discussed below utilizes the injection time lag calculated from the 2<sup>nd</sup> method.



Table 7: Time lag calculations from LES simulations.

Time lag	Simulations/equation used	Value (@ 190Hz)
Fuel injection (method 1, found to be invalid)	ParPM – PerPM	$\tau_{injection} = 4.304ms$
Fuel injection (method 2)	$\tau_{injection} = \tau_{jet} + \frac{\ell_{scoop}}{\bar{u}_{scoop}}$	$\tau_{injection} = 1.349ms$
Jet exit	PerPM	$\tau_{jet} = 0.505ms$

### ***Gain factor calculations***

The relative gains of each of the terms in the JICF heat release model are determined using the constants in front of the perturbed variable terms in Equation (47). The quantities for each of these constants are approximated from the mean fields in the LES simulations (as necessary), and are summarized below in Table 8.

Table 8: Constants used to calculate the gain terms in the JICF heat release model.

Constants (mean quantities)	Region 1: fuel injection	Region 2: jet exit
Air density	4 kg/m <sup>3</sup>	3.5 kg/m <sup>3</sup>
Volume flow	0.010775 m <sup>3</sup> /s	-
Fuel fraction	0.036636	0.036636
Heating value	5e7 J/kg	5e7 J/kg
Velocity	25 m/s	60 m/s
Area	-	0.000201 m <sup>2</sup>
Sound Speed	535 m/s	535 m/s

Because only the relative gain between each of the terms in the heat release model is important, a gain of unity was assumed for the jet exit term and the injection component was

normalized with respect to this value. The expressions for each of the gain terms, along with their relative values, are provided below in Table 9. For reference, the gains of the neglected density fluctuation terms (or  $p'$  terms, assuming isentropic flow) are included to verify that they are indeed negligible. Also included in Table 9 are the values of the phase for the velocity gain terms, as calculated from the time lag information obtained from LES (shown in Table 8). It should be noted that because these terms can contribute to either driving or damping of a given mode, they should be included in the analysis of the system regardless of the phase, assuming the gains are of sufficient magnitude. Thus, the phases for the pressure gain terms are not included, as the relative gains for these terms are nearly two orders of magnitude smaller than the velocity gain terms.

Table 9: Gain expressions and relative values applied to JICF heat release model. Phase values are shown for reference and are calculated from the time lags shown in Table 8.

Term	Mathematical Expression	Relative value	Phase
Fuel injection – $u'$	$\frac{-\bar{m}H_f\bar{Y}}{\bar{u}_{air}}$	-2.450	97°
Jet exit – $u'$	$\bar{Y} \cdot \bar{\rho}A_{jet}H_f$	1.000	36°
Fuel injection – $p'$	$\frac{-\bar{m}H_f\bar{Y}}{\bar{\rho}_{air}c^2}$	-0.0535 (scaled with acoustic impedance)	N/A
Jet exit – $p'$	$\frac{\bar{Y} \cdot \bar{u}A_{jet}H_f}{c^2}$	0.0599 (scaled with acoustic impedance)	N/A

It is interesting to note from these results that the sign in front of the fuel injection term is negative, while the sign in front of the jet term is positive. This agrees with a fundamental

understanding of the flow physics, where an increase in the acoustic velocity results in a decrease in the heat release due to equivalence ratio fluctuations but an increase in the heat release due to the jet mass flow or velocity fluctuations.

These results also suggest that each of the velocity fluctuation terms have a similar contribution to the overall JICF heat release, as they are of the same order of magnitude. The pressure fluctuation terms are two orders of magnitude lower than the velocity terms when scaled by the acoustic impedance, which was estimated from the acoustic velocity and pressure fluctuations in the scoop. This confirms our initial assumptions that each of the velocity terms are important in constructing a model for the JICF heat release while the pressure terms can be neglected. It is important to note, however, that this assumption may not be valid for additional configurations. Each assumption made in this report should be re-evaluated before applying to additional configurations.

To validate the detailed heat release model that was developed, two additional TA3D cases were run, applying the detailed JICF heat release model to the jet flame while utilizing the same meshes and head end heat release model used previously for the cases with the basic JICF heat release model. Similar to the basic heat release modeling study, the only difference between the JICF1 and JICF2 detailed heat release model cases was the geometry, other than slight differences in the mean fields. This provides the most accurate comparison with experimental trends.

For the JICF heat release model, two sender regions were defined for each of the terms in Equation (47). The fuel injection sender region was defined at the location of the fuel nozzle and the jet sender region was defined at the exit of the jet. The receiver region for each of the two

modeled JICF terms was defined as a region enclosing the mean heat release field of the reacting JICF. These three regions are illustrated below in Figure 74.

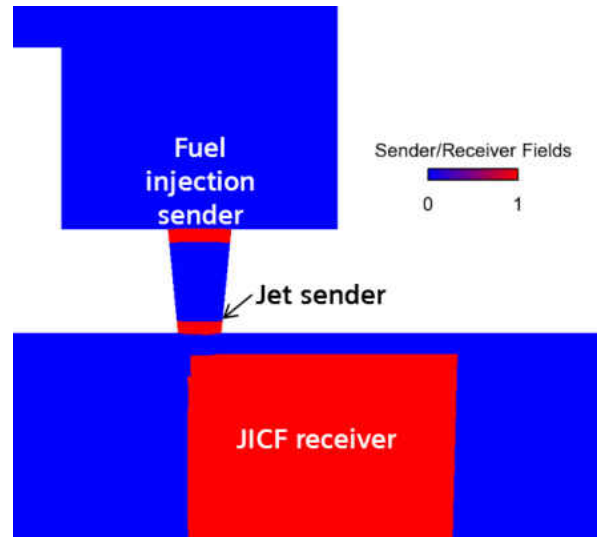


Figure 74: Sender and receiver regions used for detailed JICF heat release modeling in TA3D.

Filtered acoustic pressure signals for both cases with the detailed heat release model are shown below in Figure 75. Note that the only difference between the baseline head end only cases (Figure 71), the basic JICF heat release model cases (Figure 73), and these detailed JICF heat release model cases shown in Figure 75, is the heat release model that is applied for the JICF.

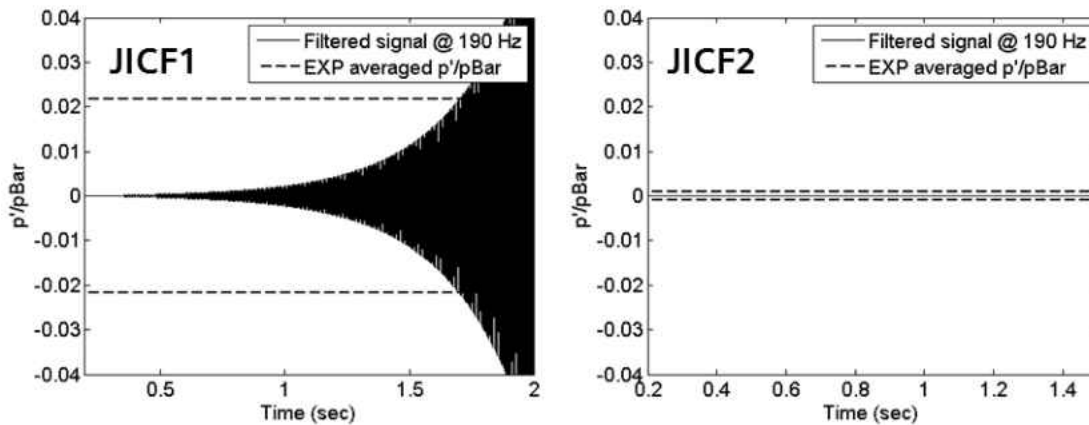


Figure 75: Filtered acoustic pressure signals for JICF1 and JICF2 cases from TA3D, with detailed JICF heat release model.

It is evident from these results that the trends observed in the experiments are correctly reproduced by TA3D with the implementation of the detailed JICF heat release model. The JICF1 geometry significantly drives the dominant head end mode above its baseline limit cycle amplitude when the JICF heat release model is applied, while the JICF2 geometry completely damps the head end mode. Because the detailed JICF heat release model is only linear, the unstable case grows unbounded. A non-linear JICF heat release model could be developed in the future with additional experimental data.

Figure 76 shows a summary of the filtered pressure signals from experimental results, compared to the corresponding TA3D cases that include the detailed JICF heat release model. The first column represents the JICF1 geometry, but with a baseline heat release model only applied for the head end reaction. This corresponds to experimental data that was taken with the same geometry but no fuel included in the jet flow (and therefore, no jet reaction). Here it is evident in both cases that the dominant mode near 200 Hz is driven to a limit cycle amplitude between 1 and 2% of the chamber pressure. The limit cycle amplitude in the experimental results

shows some variation due to transient effects that are not resolved in the TA3D model, however, the general behavior agrees well.

The second column also represents the JICF1 geometry, but now, with the detailed JICF heat release model turned on in the TA3D model and fuel added to the jet flow in the rig. Here a strong driving of the dominant mode is observed, to a limit cycle nearly three times higher than that observed with the HE only in the experimental data, and unbounded growth in the modeled data. Again, the unbounded growth in the modeled data is a result of a linear heat release model being applied for the reacting JICF, as opposed to a non-linear model where a limit cycle would be achieved.

Finally, the third column represents the JICF2 geometry, with the same detailed JICF heat release model applied to the TA3D model and fuel included in the jet flow in the rig. Here it is evident that the JICF reaction couples with the dominant mode in such a way that it nearly damps the dominant mode entirely. This trend is captured well with the modeled results.

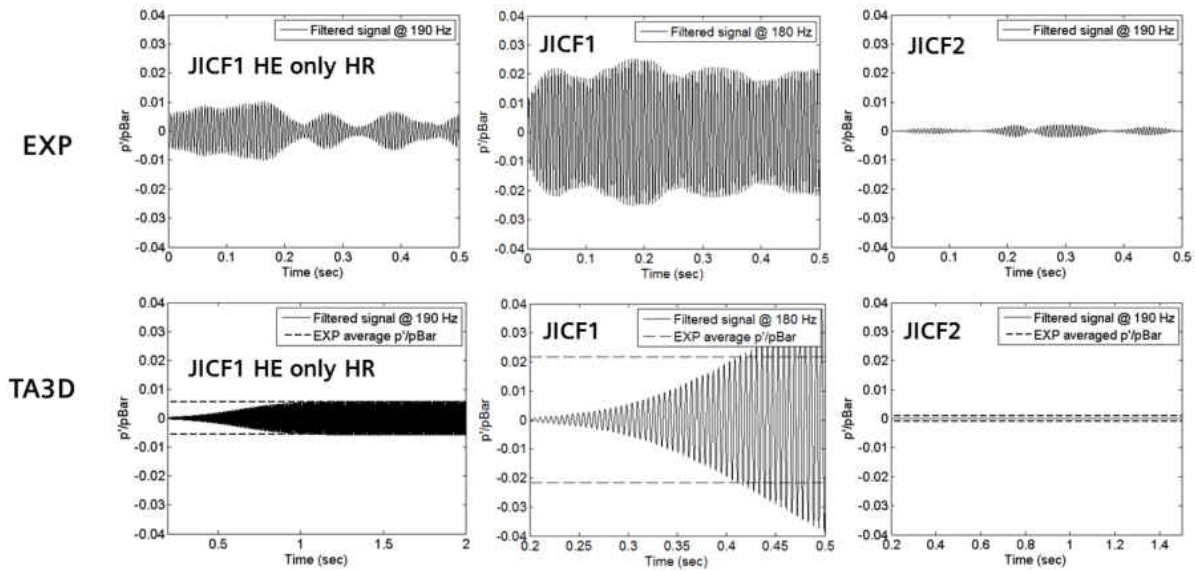


Figure 76: Summary of experimental data and TA3D results with detailed JICF heat release model.

### *Generalized Instability Model*

Additional reduced order modeling was done using the Generalized Instability Model (GIM) (Portillo, 2007) to develop stability maps for the two dominant modes present in the lab scale combustor. The purpose of this model was solely to investigate the effect of the JICF on the stability of the chamber modes, independent of the head end forcing. The model setup was based on the proposed mechanism that the combination of the jet impedance and the jet flame time lag contribute to the driving or damping of the JICF, as shown schematically in Figure 68.

Because the GIM tool is only quasi-3D (i.e., longitudinal and transverse modes are solved separately), it cannot capture the effect of the jet impedance implicitly, as was the case with TA3D. Thus, a  $p'$ - $q'$   $n$ - $\tau$  model was imposed at the location of the JICF and a stability map was generated by assuming that the  $p'$ - $u'$  time lag plus the  $u'$ - $q'$  time lag combine to form an overall  $p'$ - $q'$  time lag. A sweep of the overall  $p'$ - $q'$  time lag was performed for a total of two

periods of the selected mode and the results plotted on a stability map as a function of the  $p'$ - $u'$  time lag (jet impedance) and the  $u'$ - $q'$  time lag (flame time lag). No heat release model was applied for the head end flame, as the objective of this analysis was to investigate the effect of the JICF, independent of the head end forcing. The GIM model is represented schematically in Figure 77, which shows the 200 and 400 Hz mode shapes in the chamber and the location where the heat release model was applied, corresponding to the location of the JICF injection for the configurations investigated in this study.

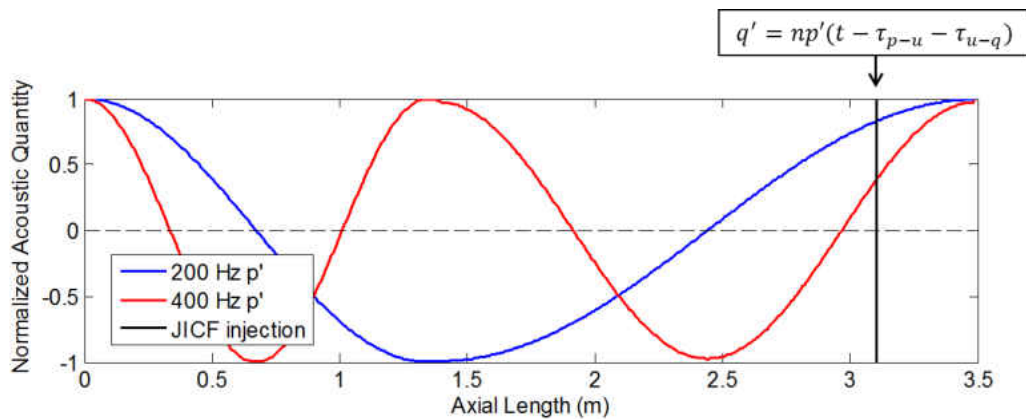


Figure 77: Schematic representation of the GIM model with the location of the applied heat release model shown relative to the 200 and 400 Hz pressure mode shapes.

Figure 78 shows a stability map for both the 200Hz and 400Hz normalized growth rates, as a function of the jet impedance and the flame time lag. Note that the growth rates calculated by the instability model are defined by the exponential factor that best fits the curve developed from the maximum points in the time series of the unsteady pressure signal. The heat release model applied in this study assumed that the combination of the jet impedance and flame time lags results in an effective time lag between the chamber pressure fluctuation and the reacting JICF heat release fluctuation. The location of the JICF1 and JICF2 configurations on the stability



maps, based on the calculated time lags from the LES simulations, are shown by the red and green points, respectively. Note that a growth rate of positive one represents the most unstable regions and a growth rate of negative one represents the most stable regions. These stability maps demonstrate how the proposed mechanism can be implemented into a low-order 1D acoustic tool and provide an understanding of the design parameters that can be used to develop a stable system.

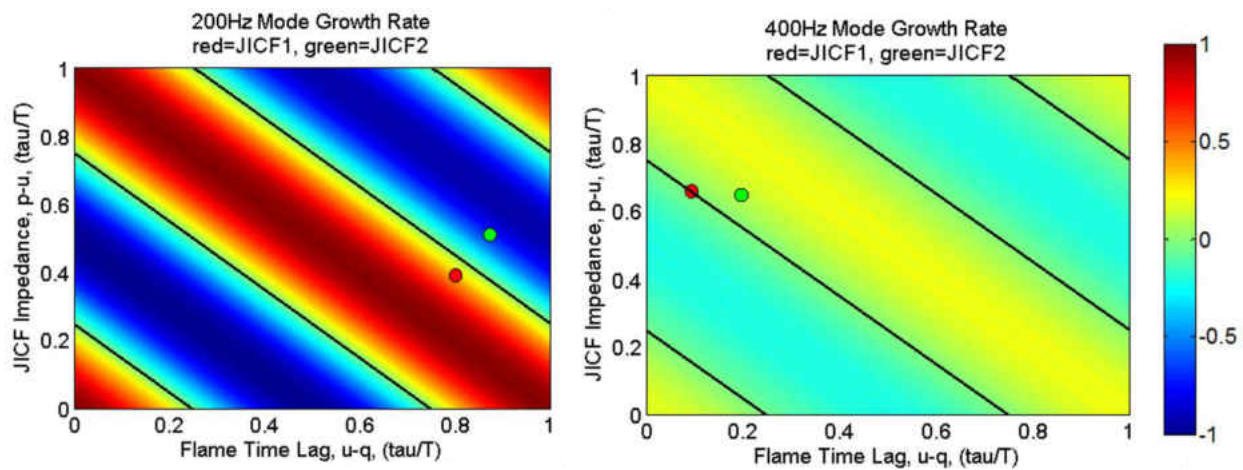


Figure 78: Normalized growth rate for 200 and 400 Hz modes using a 1D linear heat release model in GIM. Red and green points represent the JICF1 and JICF2 configurations, respectively, as calculated from SELES. Black lines represent stability boundaries.

The 200Hz stability map provides similar results to what was shown previously in Figure 69, where the JICF1 and JICF2 points bound the neutral stability line. This plot is also helpful in understanding the design space available for a stable system as a function of the jet impedance and flame time lag.

Because the color scale between the 200Hz and 400Hz stability maps is the same (scaled by the maximum of the absolute value of the growth rate in both plots), the relative growth rate can be compared between the two stability maps. Thus, it is evident that the 400Hz mode is not

nearly as sensitive to the JICF heat release as the 200Hz mode, and is actually close to neutrally stable throughout all operating regimes. This difference is due to the JICF injection location with respect to the pressure mode shape of each mode. It is important to note that the growth rate on these stability maps represents the effect of *only* the JICF reaction on the system stability, and thus, a neutrally stable system implies that the JICF will not have an effect on the mode already present from the head end reaction.

Experimental results agree with this trend, showing that the 400Hz mode is relatively insensitive to the JICF configuration, i.e., its amplitude was minimally affected between the HE only, JICF1, and JICF2 configurations. This is shown in the experimental pressure spectrum plotted in Figure 79, below.

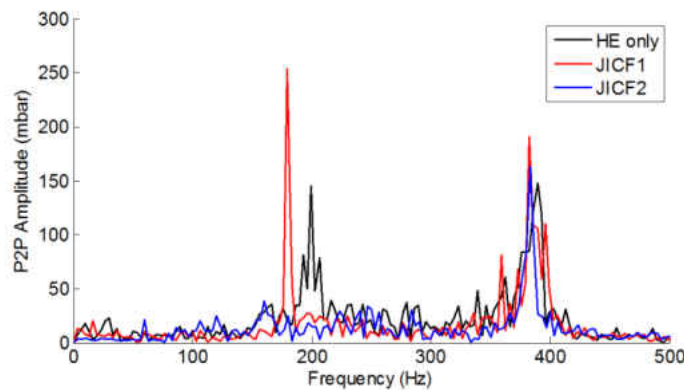


Figure 79: Experimental spectrum comparing the first two dominant modes in the HE only, JICF1, and JICF2 configurations.

## CHAPTER 6 – CONCLUSIONS AND RECOMMENDATIONS

### Summary and Conclusions

The overall objective of this study was to develop and validate a mechanism of instability that describes how a reacting JICF behaves when injected into an unstable cross flow at gas turbine operating conditions. There are many practical applications for this problem definition but specific focus was given to combustion staging in stationary gas turbines where the JICF is often used to promote mixing of fuel and oxidizer for combustion.

As a part of a related study, a lab scale dump combustor has been developed at Purdue University that provides an environment to inject a reacting jet into a cross flow that is made unstable by the head end flame. Experimental diagnostics include dynamic pressure measurements and high speed chemiluminescence imaging of the reacting jet to quantify the unsteady pressure and heat release, respectively. From the experimental tests, a three-point stability trend was identified, where a moderately unstable 2L mode in the combustion chamber during head end only operation was strongly driven by the reacting JICF for one configuration and strongly damped for another configuration. It was clear from the experimental results that the unsteady heat release from the JICF was coupling with the pressure waves present in the combustion chamber to either drive the head end only mode to a significantly higher unstable point, or damp the head end only mode to a nearly stable condition. These stability trends were used as validation data for a set of self-excited LES simulations of the reacting JICF, with the goal of obtaining an understanding of the physics governing the thermoacoustic stability of this combustion scenario.

The self-excited LES simulations were run using a solver implemented into OpenFOAM, an open source CFD toolbox for the numerical simulation of complex fluid flows including chemical reactions, turbulence, and heat transfer. A typical LES turbulence modeling setup was applied, with boundary conditions that were chosen to match the hydrodynamic and acoustic boundary conditions present in the experimental rig with as much accuracy as possible, given the available tools. A simplified combustion model was applied, using a 1-step chemical reaction and a turbulent flamespeed closure based reaction rate. This combustion model was applied under the assumption that it would provide modeling of the chemical kinetics that was accurate enough to capture the level of heat release oscillations necessary to drive the combustion instabilities at the frequencies of interest in this study.

A Rayleigh Index post-processing tool was developed in combination with a 3D DFT tool to calculate a three-dimensional Rayleigh Index field from the pressure and heat release fields generated by the self-excited LES simulations. These results provided a three-dimensional Rayleigh Index field as a function of frequency, and thus could be used to identify regions of driving or damping within the system at a specific frequency of interest. This post-processing technique was found to be especially useful when multiple reaction zones are present within the system, serving to clearly identify which reactions are driving the system and which are damping it. It was calculated that for the unstable case (JICF1) the reacting jet contributed an additional 32% of *driving* to the existing head end instability while the stable case (JICF2) contributed an additional 113% of *damping* to the existing head instability.

Extensive validation of the numerical methods applied to the LES simulations was done to identify the effects on the acoustics within the computational domain. These validation studies

quantified the effects of mesh resolution and refinement regions, temporal and spatial discretization schemes, combustion model parameters and extensions, and boundary conditions. Details of the validation results are provided in Appendix A. All of the numerical data was compared against the experimental results and any discrepancies or shortcomings in the modeling approaches were identified.

Additional reduced order acoustic modeling was included in this study to validate a proposed heat release model for the reacting JICF, based on the mechanism identified from experimental and numerical results. A three-dimensional thermoacoustic modeling tool and a quasi-3D Generalized Instability Model were used to model stability trends for the full geometry as well as generate stability maps that were used to further understand the design parameters that are important for the reacting JICF. One-dimensional full kinetic modeling was also applied to identify what kinetic mechanisms are important for thermoacoustic modeling of the given system at the conditions of interest.

It was found that the self-excited LES simulations were only able to match the stability trends observed in the experiments when a model for limiting the reaction rate due to strain was implemented into the combustion model. Based on 1D full kinetic modeling, however, it was determined that the actual effects of strain were not significant at the high pressures considered here, however, when an artificially high Markstein number was applied to the strain model, it reduced the reaction rate in the regions of high strain within the jet and delayed the overall flame time lag to the point that the stability trends from the simulations matched those of the experiment. Because the full kinetic modeling showed that the strain in the JICF was not high enough to cause a notable reduction in the overall reaction rate, it was determined that the strain

model in this study could only be viewed as a correction factor to the simplified combustion model and not as a physical representation of strain effects in the reacting JICF.

From an investigation into the natural coherent structures of the reacting JICF, it was found that these structures occurred at frequencies too high to result in any feedback cycle with the pressure and heat release oscillations that generated combustion instabilities at the frequencies of interest in this study (less than 500Hz). This conclusion was based on literature of non-reacting and reacting jets in cross flow, as well as LES simulations that were used in this study to quantify the frequencies of the shear layer of the JICF, as these coherent structures can have a direct effect on the flame surface and resultant heat release fluctuations in the jet. Further confirmation of this conclusion was given from experimental results, which found that changes to the hydrodynamic behavior of the JICF due to jet diameter, momentum ratio, and equivalence ratio had very little effect on the stability of the system.

By observing experimental and numerical animations of the transient flame behavior, a strong pulsing of the jet was identified to occur at the unstable frequency of interest when the jet was driving the baseline instability present in the combustion chamber. This pulsing behavior is similar to what has been observed in the literature when a premixed swirl stabilized flame is placed at a pressure anti-node of a mode sustained in the combustion chamber (O'Connor 2011 and 2012). Thus, a mechanism was developed, that included a mass flow fluctuation of reactants as well as an equivalence ratio of the mixture that resulted from the pressure oscillations present in the combustion chamber at the point of injection. These mass flow and equivalence ratio fluctuations result in heat release fluctuations in the JICF that can result in a feedback cycle with the pressure oscillations in the combustion chamber. Depending on the time lags between the

pressure oscillations in the chamber and the velocity oscillations in the JICF, and again between the velocity oscillations in the JICF and the heat release oscillations of the jet, a feedback cycle can develop that will cause the reacting JICF to either drive or damp the unstable mode generated by the head end flame and sustained in the combustion chamber. These time lags were identified from the LES simulations and implemented into the 3D thermoacoustic modeling tool as a “jet impedance time lag” and a “flame time lag”. The jet impedance is simply a function of the acoustic properties of the geometry being investigated while the flame time lag can be split into velocity, equivalence ratio, and strain fluctuations, depending on the operating conditions and setup. For the specific gas turbine application investigated in this study, it was found that the velocity and equivalence ratio fluctuations were important, however, the effect of the strain fluctuations on the heat release were minimal due to the high operating pressure.

The stability trends observed in the experiments were correctly captured with the 3D thermoacoustic tool, using a derived heat release model based on the proposed mechanism of instability as a function of the velocity and pressure oscillation present in the system. Using a detailed heat release model that included terms for both the velocity and equivalence ratio fluctuations of the JICF, it was found that the velocity fluctuations contributed to damping of the system, while the equivalence ratio fluctuations contributed to driving of the system. The jet impedance, or pressure-velocity time lag, contributed to driving for the unstable case (JICF1) and damping for the stable case (JICF2). Because only a linear heat release model was applied for the reacting JICF, the limit cycle amplitudes observed in experiment were not captured, but rather exponentially unstable growth rate was observed for the unstable case and complete damping was observed for the stable case. The gain factors derived from the governing equations

for the temporal heat release showed that the gain for the equivalence ratio fluctuations was approximately 2.5 times that of the velocity fluctuations, and with opposite sign when applied with a  $q'-u'$  heat release model. The density fluctuation terms were shown to be negligible in this case, due to their proportionality with the inverse of the square of the sound speed.

The Generalized Instability Model (GIM) results identified how a stable design could be achieved based on the two overall design parameters of the reacting JICF – the jet impedance and the overall flame time lag. The stable and unstable points investigated in this study were plotted on a 2D stability map generated using GIM, further confirming that the trends calculated with LES matched those observed in the experimental results. This model was also used to help explain why the 200 Hz mode was strongly affected by the JICF, while the 400 Hz mode was nearly oblivious to any design changes of the JICF. This was partly due to the fact that the jet was injected much close to a pressure anti-node for the 200 Hz mode, but also that the JICF configurations investigated in this study exhibited resonant frequencies quite close to the 200 Hz mode.

The original objectives of this study were summarized previously in Table 1 and are provided again in Table 10, with a brief statement summarizing how each objective was satisfied.



Table 10: Objectives of the current study and summary of results

	Objective	Result
1	Analyze and understand the flow phenomena related to a reacting JICF	Experimental and numerical data was investigated, along with a background of JICF literature, to analyze the flow field of the reacting JICF and identify the important parameters that contributed to the stability of the system.
2	Develop self-excited LES simulations of an unsteady dump combustor and validate with experimental data	Multiple head end only and reacting JICF simulations were run and validated with experimental dynamic pressure measurements and CH* chemiluminescence images. With appropriate extensions to the model, the trends observed in experiment were matched with the simulations. Shortcomings were identified and recommendations for further improvements were included.
3	Investigate the interaction between an unsteady cross flow and a reacting jet and identify a mechanism that contributes to the stability of the system	Using advanced post processing techniques applied to experimental and numerical data, a mechanism of instability was hypothesized and used to derive a heat release model that describes how the reacting JICF contributes to the overall system stability. The important physical parameters were identified and included in the model, while additional parameters were shown to be negligible at the operating conditions investigated in this study.
4	Identify the necessary tools and methods so that the fundamental study shown here can be extended to more specific engine design studies	While appropriate “tuning” of the LES model was shown to result in the correct prediction of stability trends, it was recommended that improvements to the acoustic boundary conditions and the combustion model be pursued to provide a design tool that can predict system stability a priori. However, by applying the heat release model developed in Objective 3, a 3D acoustic tool was shown to correctly predict the stability trends observed in the experiment, providing a method that can now be extended to a full engine style design.

### Recommendations for Future Work

One of the most significant assumptions in this study was that the chemical kinetics of the reactions present within the system could be captured using a global one-step reaction mechanism with a reaction rate based on turbulent flame speed closure modeling. While this approach has been extensively applied in the literature for co-flow jet flames, it often requires

extensions to model physical effects on the kinetics such as strain and heat loss, especially for more complex combustion scenarios such as swirl stabilized flames or reacting jets in cross flow, as was shown in this study. Thus, for these more complex combustion scenarios like the reacting jet in cross flow, it is recommended to improve the combustion modeling by applying more accurate kinetics information through methods such as tabulated chemistry lookup tables. Several variations of these tabulated chemistry combustion models are in the development phases and are described in recent literature. As more of the chemical kinetics can practically be included in the combustion modeling, it is expected that less “tuning” of the models will be required and a priori predictions will become more feasible.

For further increases in the accuracy of the combustion modeling, it is recommended to implement a method of including fuel flow fluctuations for non-premixed cases as a function of fuel line pressure drop or fuel nozzle impedance. In addition, a more accurate mixing profile for the fuel nozzles should be included, or, when practically possible, include the complete fuel nozzle geometry. Fuel source term modeling, such as the method applied here, provides a good way to introduce equivalence ratio fluctuations without a significant increase in the computational expense, however, depending on the setup being investigated and the simulation objectives, effects such as fuel flow fluctuations and mixing profiles can become important. These effects become increasingly important when investigating modes at higher frequencies where localized flame effects contribute as much to the stability behavior as the global flame effects investigated in this study.

By quantifying the reflection coefficients at the boundaries of the computational domain it was found that the method applied for a choked outlet matched the theory quite well, while the

method applied for a choked inlet exhibited a significantly lower reflection coefficient than the theoretical predictions. This was found to be the result of an inconsistency in the segregated pressure-velocity solver where the pressure and velocity are solved separately at the boundaries without an appropriate link between them. To correct this inconsistency, the pressure, velocity, and temperature at the boundaries would need to be solved together and then “frozen” throughout the rest of the PISO loop at the current time step. While this is a recommended improvement for cases in which choked inlets are present, it should be noted that these types of choked inlets are typically only present in lab-scale combustors and are uncommon in practical engine style rigs or full engines. In these practical cases, it is often necessary to include the actual geometrical features that result in the acoustic boundary conditions of the system.

One of the findings of this study was that due to differences in the hydrodynamic strain field between a co-flow jet flame and a JICF, the fluctuating strain resulting from acoustic velocity perturbations has the potential to effect the stability of the system, as it can cause a delay in the heat release at a localized point in the flame with high strain. While it was found that at gas turbine operating conditions, the high pressure effects cause the strain effects on the reacting JICF to be negligible, it is likely that strain effects can become significant at lower pressures, or in scenarios when the Markstein number is greater than 0.5. Thus, if a practical application becomes apparent, it is recommended to further investigate the stability effects of strain fluctuations through experimental testing, such as comparing the stability characteristics of a reacting jet injected at 90 degrees, 45 degrees, and 0 degrees.

## **APPENDIX A – LESSONS LEARNED**

## Analysis of Computational Domain Boundaries

### *Reflection coefficient calculations*

An unknown, and potentially significant, source of acoustic losses in the numerical simulations presented in this study comes from the inlet and outlet boundaries of the computational domain. In order to obtain an understanding of the behavior of these boundaries in the simulations, separate simulations of each boundary were run individually to quantify the reflection of acoustic waves at each boundary. These simulations were run by taking a small region of the computational domain near the boundary and calculating the magnitude and phase of the reflection coefficient at the inlet or outlet boundary. The condition at the boundary being measured was identical to that of the main simulations while the opposite boundary in the test domain was set to a sinusoidal overlay boundary with forcing applied to the pressure between 50 and 1000 Hz. This provided a forced boundary in the frequency range of interest where the two-microphone technique (ISO, 1998) could be applied to calculate the reflection coefficient with mean flow (Munjal, 1990).

The boundary test simulations were run using identical flow conditions, solver, and discretization schemes that were used in the main simulations to ensure that an accurate representation of the boundaries was determined. The two-microphone method with mean flow was applied to calculate the reflection coefficient at the boundary using Equation (50) (Munjal, 1990):

$$R = \frac{H_{12}e^{-Ms} - e^{-s}}{e^s - H_{12}e^{-Ms}} e^{2L} \quad (50)$$

where  $H_{12}$  represents the transfer function between the two probes,  $M$  represents the mach number, and  $L$  and  $s$  represent the dimensions shown in the schematic in Figure 80, below.

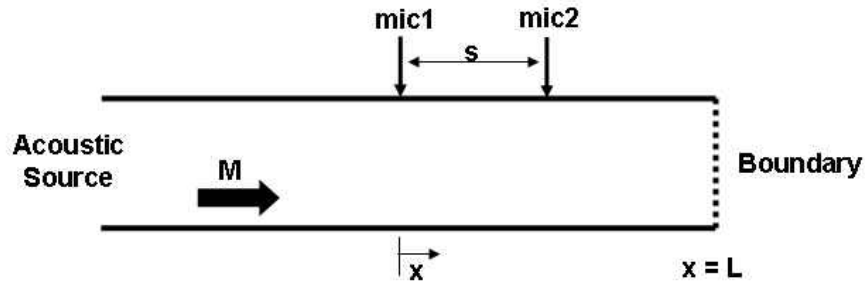


Figure 80: Schematic of two-microphone method setup applied to computational domain boundary analysis

Figure 81 shows the domain used for the inlet boundary reflection calculations.

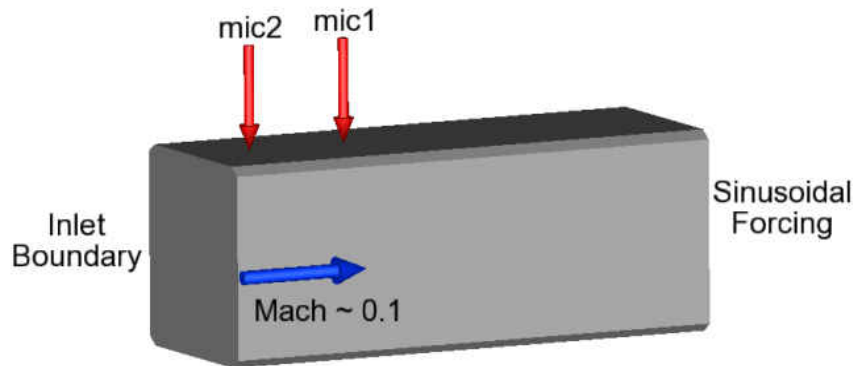


Figure 81: Domain used for inlet boundary reflection calculations

The reflection coefficient was calculated using both a constant mass flow inlet as well as a constant velocity inlet, for comparison. The results for calculating the reflection coefficient at the

inlet boundary are shown below in Figure 82. The theoretical reflection coefficient is also plotted in the figure, as derived by Lamarque and Poinso for a choked diffuser (Lamarque, 2008).

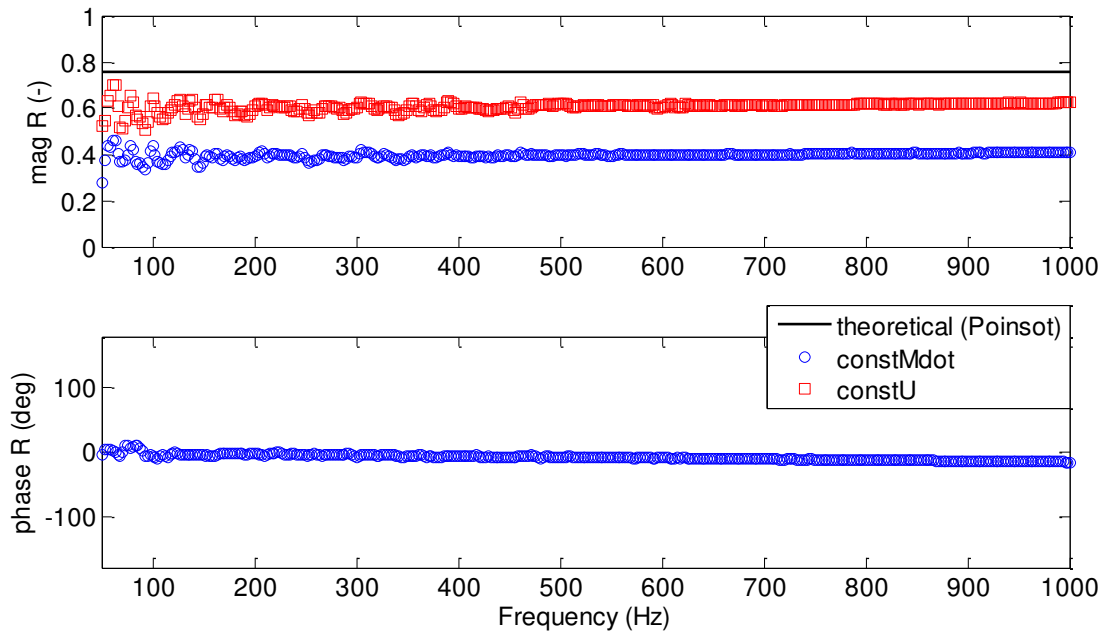


Figure 82: Calculated magnitude and phase of reflection coefficient for inlet boundary

There are several interesting observations that can be made from the data shown above. It is apparent that both of the numerical inlet conditions are less reflective than the theoretical value calculated using the relation from Lamarque and Poinso. It is also important to note here, that this theoretical value for a choked diffuser is actually a minimum approximation for the reflection at the inlet of the rig modeled in this study. This is because the actual inlet in this study consists of a choke plate, where the walls of the plate behave a rigid boundary ( $R=1$ ) and only the holes through the plate behave like a choked diffuser. This means that the actual reflection coefficient present in the rig is likely higher than this theoretical value. It can be concluded from the data shown here that the inlet boundary is an unavoidable source of acoustic losses, given the

resources available for this study, however, various methods were attempted to increase the physical accuracy of the inlet boundary which are described below.

Although the constant velocity inlet behaves closer to the theoretical condition with respect to its reflection coefficient, it was numerically unstable when applied with a pure second order temporal discretization scheme (Crank-Nicholson 1.0) and the full simulations would not run without crashing. It was also attempted to utilize a constant velocity inlet while applying an off-centering factor of 0.8 for the temporal discretization. While these simulations would run without crashing, they resulted in an interesting numerical feedback of combustion instabilities that drove the first and third longitudinal modes of the system, depending on the configuration. This behavior is evident in Figure 83, which shows representative pressure spectra for the head end only case, with a constant velocity inlet and an off-centering factor of 0.8 for the temporal discretization.

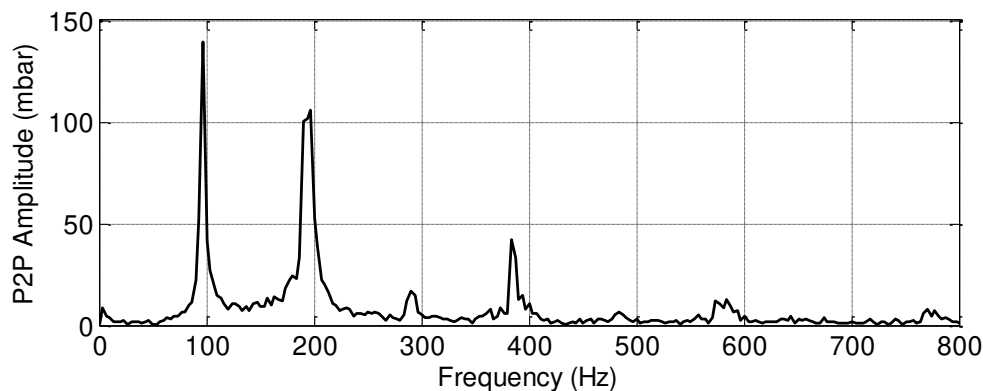


Figure 83: Representative pressure spectra for the head end only simulation with a constant velocity inlet boundary condition

While this simulation correctly predicted peaks near 200 and 400 Hz, it also excited a mode near 100 Hz, which corresponded to the first longitudinal mode of the system. The



amplitude of this mode increased in increments throughout the one second solution time that this simulation was run for. By calculating the mass flow rate through a plane 10 cm from the ox-post inlet, it was found that the reactant mass flow was fluctuating by at least 6-7% of the mean, an effect of the inlet boundary condition that was not physically correct. This mass flow fluctuation occurred as a result of the standing pressure waves within the system. Because the inlet of the domain is a pressure anti-node for any standing wave that exists in the system, the pressure fluctuations at the inlet resulted in density, and therefore mass flow rate fluctuations, as the velocity and temperature were fixed to constant values at the inlet. This fluctuation in the reactant mass flow convected downstream to the head end flame where it would cause fluctuations in heat release. These heat release fluctuations would then cause acoustic pressure fluctuations, thus closing the feedback loop necessary to drive the mode. While this presented a classic combustion instability phenomenon, it was not physically correct as the mass flow through a choked inlet cannot fluctuate, and thus, it was concluded that a constant velocity boundary condition could not be used to accurately model a choked inlet.

The final attempt at creating an accurate inlet boundary for the simulation was to resolve an inlet hole that had the same effective area as the nine holes present in the actual choke plate and apply a constant mass flow rate across this reduced area. The nine holes were merged into one hole so that the necessary mesh resolution would not need to significantly increase at the inlet, requiring both a larger number of cells and a smaller time step for numerical stability. Theoretically, this method should produce a much higher inlet reflection coefficient, as a significant portion of the inlet boundary becomes a rigid wall and the flow entering through the hole in this boundary would be choked. Upon running this simulation, however, it was found that

introducing a supersonic jet into the inlet of the domain resulted in large pressure oscillations that began to dominate over the acoustic pressure oscillations. While the supersonic jet should introduce a large amount of noise into the domain, it is unlikely that it would dominate over the acoustic pressure oscillations as the experimental data does not show this to be occurring. As a result, it was concluded that the correct behavior of a supersonic inlet could not be correctly captured by the solver being used.

To avoid this dilemma, the area of the inlet hole was slightly increased so that a transonic inlet flow would be introduced. This would eliminate the supersonic jet while still maintaining the acoustic accuracy of a high Mach number inlet. The transonic inlet condition was tested for a boundary analysis case similar to those used for the constant mass flow and constant velocity inlets which were defined over the entire face of the ox-post. The temporally averaged Mach number through this domain is shown below in Figure 84. It is evident from the figure that a transonic jet enters the domain through the inlet area, but due to the expansion immediately following the inlet boundary, the inlet does not choke, verifying that the desired results have been obtained for the velocity field. It should be noted here that the duct for this test case was lengthened to allow for probe measurements in a flow field that was uniform away from the inlet jet.

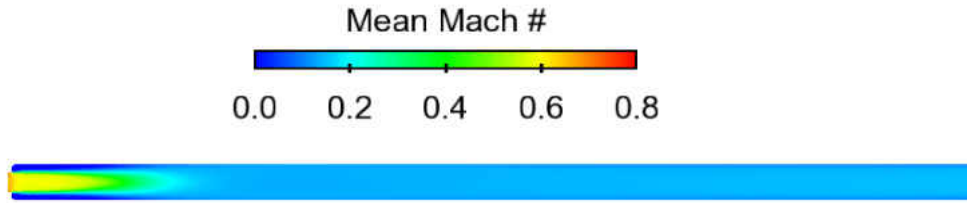


Figure 84: Domain used for transonic inlet boundary calculations, colored by temporal mean Mach number

Figure 85 shows the magnitude and phase of the calculated reflection coefficient for the transonic inlet case, using the same two-microphone method described above. Here the plot shows the calculated values for the transonic inlet compared to the values for the constant velocity and constant mass flow inlets, as well as the theoretical value of the reflection coefficient.

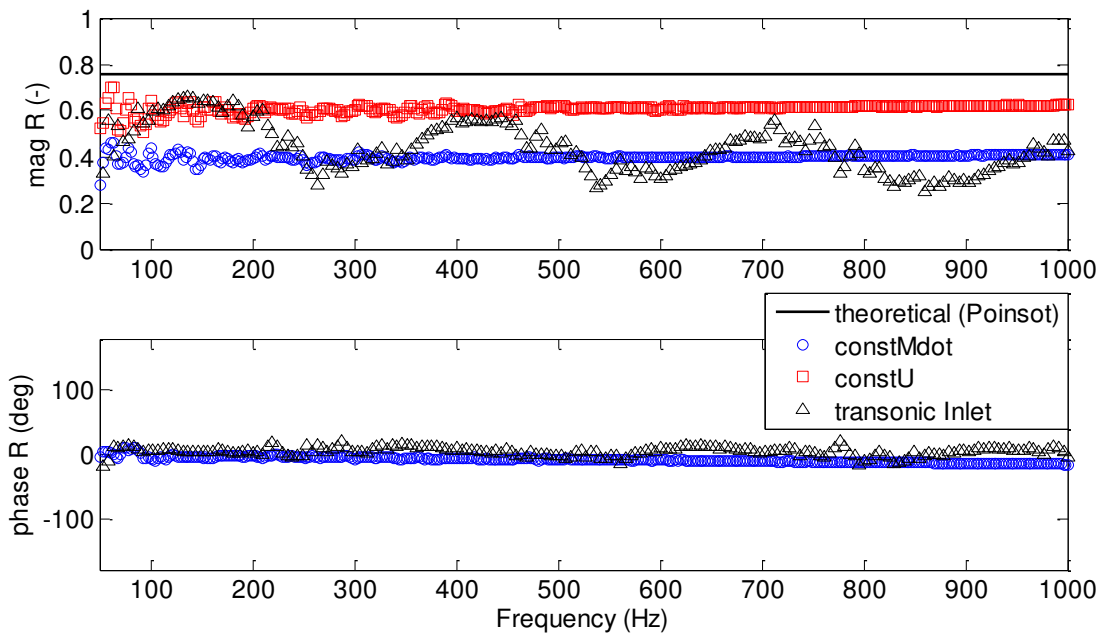


Figure 85: Calculated magnitude and phase of reflection coefficient for all inlet boundary configurations tested

It is evident that while the phase of the reflection coefficient behaves as it should, the magnitude of the reflection coefficient exhibits an oscillating behavior with frequency and generally does not result in a more accurate boundary. It is currently unknown whether this is a physical phenomenon, a numerical error, or an error due to the calculation method that may arise in non-uniform flow fields. A test case with double the mesh refinement was also run to determine if the unexpected results here were mesh dependent, however, it was found that the finer mesh resulted in almost identical results for the calculated reflection coefficient. It is recommended that this inlet be investigated in a future study, however, for the purpose of this work, we were interested in how this boundary effected the acoustic pressure amplitude seen in the chamber. This was determined by actually applying this transonic inlet boundary to the head end only case and running two simulations, using temporal discretization off-centering coefficients of 0.5 and 0.8. Representative pressure spectra for these simulations are compared with the corresponding baseline simulations in Figure 86, below.

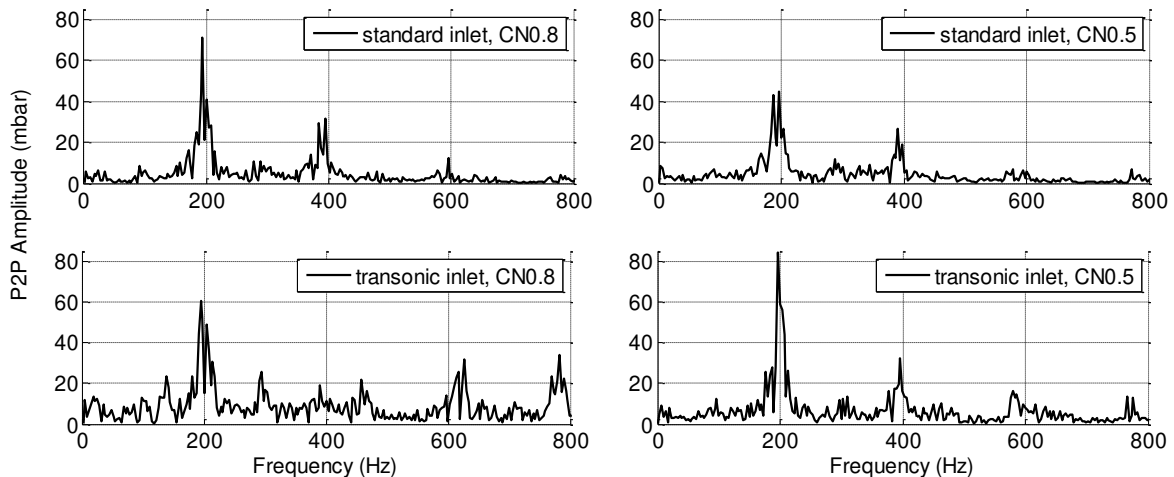


Figure 86: Representative pressure spectra for the head end only simulation comparing the standard inlet to a transonic inlet for various temporal discretization off-centering coefficients.

The pressure spectra show that the application of the transonic inlet actually decreases the limit cycle amplitude of the 200 and 400 Hz modes when an off-centering factor of 0.8 was used. This was attributed to numerical instabilities that developed from the high Mach number flow entering the domain, and thus, an off-centering factor of 0.5 was also run to minimize this effect. The pressure spectra show that with an off-centering factor of 0.5, the transonic inlet nearly doubled the amplitude of the 200 Hz mode and only slightly increased the amplitude of the 400 Hz mode. Given these results, the transonic inlet was determined to provide the most accurate results and was applied to the final simulations investigated in the study with an off-centering factor of 0.5 for the temporal discretization.

The domain for the outlet boundary, or choked nozzle, is shown below in Figure 87.

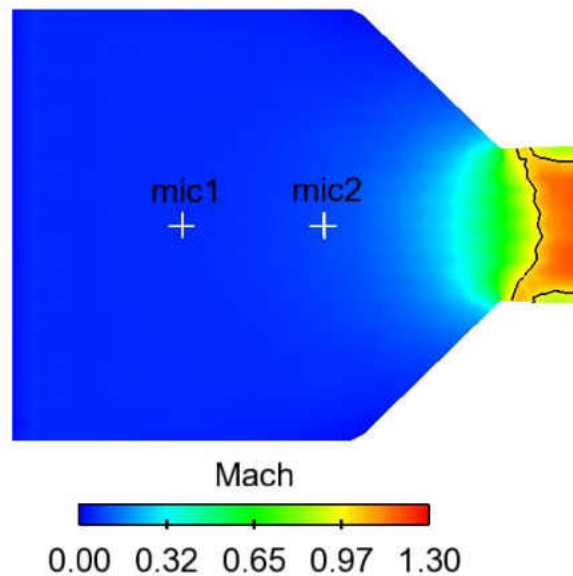


Figure 87: Domain used for exit boundary calculations, colored by Mach number. Black line represents isoline of Mach = 1.0

Here the domain is colored by Mach number, showing the acceleration of the flow in the nozzle and the choked condition at the throat. The black line in the throat represents an isoline of Mach number equal to one.

The calculated reflection coefficient for the exit nozzle is shown below in Figure 88. The theoretical value is again included in the plot, as derived by Lamarque and Poinsoot for a choked nozzle (Lamarque, 2008).

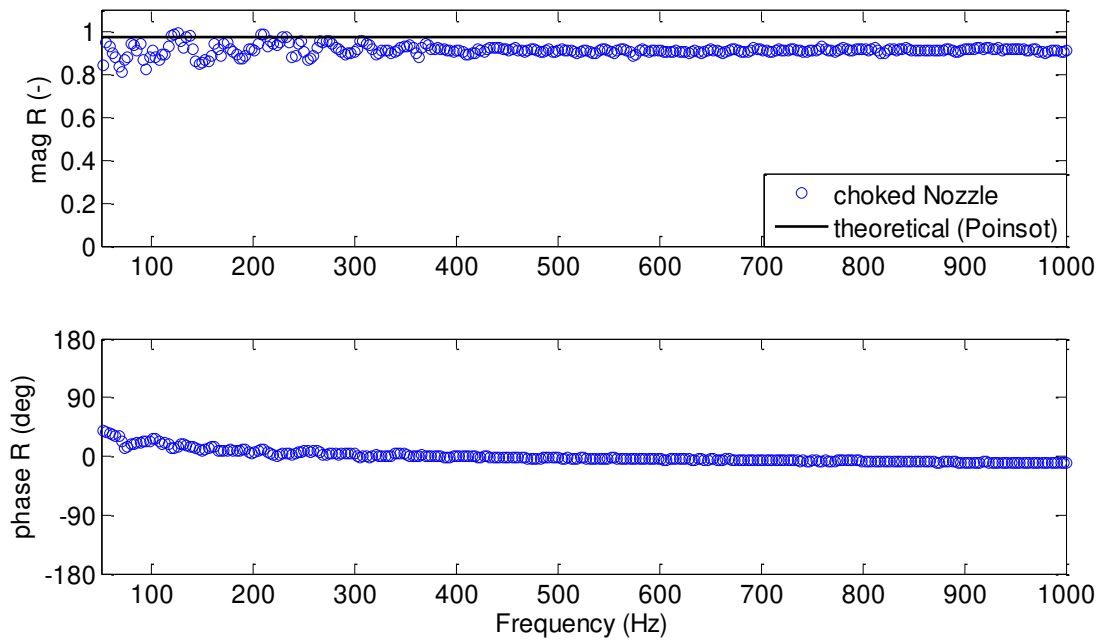


Figure 88: Calculated magnitude and phase of reflection coefficient for exit boundary

It is evident that the choked outlet of the computational domain behaves very closely to the theoretical approximation where over 90% of the acoustic waves that are incident to the nozzle are reflected back into the domain. It is concluded that utilizing a choked nozzle as an exit boundary for the simulations provides a good representation of the real exit nozzle and any acoustic losses through this boundary are expected to be less than 7%.

### *Boundary losses due to jet in cross flow geometry*

Because the inlet boundary conditions that were available for the simulations in this study were known to allow a significant amount of acoustic loss, as opposed to a nearly fully reflective choked inlet present in the experimental rig, a one-dimensional comparison was done between the HE only geometry and the JICF1 geometry to understand the differences in the acoustic losses that should be expected. This comparison was done using a one-dimensional transfer matrix code that could be used to quantify the damping present from a specified reflection coefficient at a boundary (Krebs, 1999). The network models used by the transfer matrix code are shown below in Figure 89 for the HE only and JICF1 models.

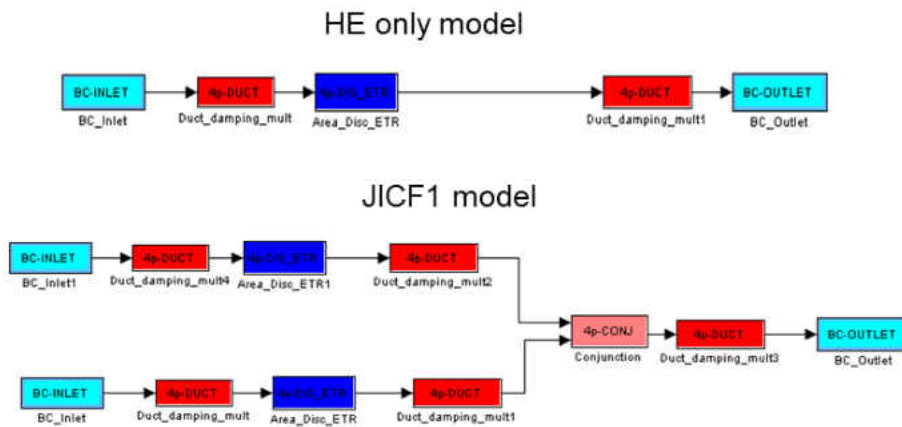


Figure 89: HE only and JICF1 network models used one-dimensional transfer matrix code to quantify boundary damping

Using the reflection coefficient calculations discussed previously, a relative damping coefficient was defined as the damping coefficient using the theoretically calculated reflection coefficient minus the damping coefficient using the reflection coefficient measured from the simulations. With this definition, a relative damping coefficient of zero would imply that the

simulated reflection coefficients match the theoretical values closely, while a relative damping coefficient greater than zero implies the presence of acoustic losses that are greater than the physical boundary losses. A plot of this relative damping coefficient is shown in Figure 90, comparing the HE only geometry to the JICF1 geometry for points at 200 and 400 Hz. The numerical damping present from the rhoPisoFoam solver is also shown on the plot for reference.

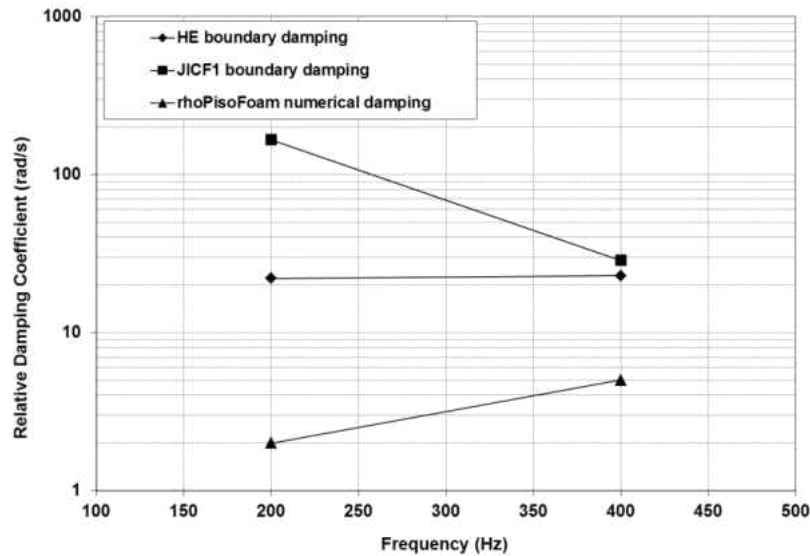


Figure 90: Relative damping coefficient at 200 and 400 Hz for HE only and JICF1 one-dimensional models. rhoPisoFoam numerical damping included for reference.

Several important points are evident from this data. First, the boundary losses for the HE only model are an order of magnitude higher than the numerical damping present in the rhoPisoFoam solver. This suggests that the development of a more accurate choked inlet boundary condition is much more important (in terms of minimizing unphysical damping in the simulations) than improving the order of accuracy of the solver itself. It is also important to note that for the HE only model, the relative damping coefficient is insensitive to the frequency, while the JICF1 model shows another order of magnitude increase in the relative damping coefficient at 200 Hz.



This is attributed to the fact that resonance occurs in the JICF geometry near 200 Hz, resulting in fluctuations in the acoustic pressure at the JICF inlet boundary that are even higher than those at the HE inlet boundary. This increases the inaccuracy of the JICF inlet boundary condition and adds a significant amount of additional damping to the JICF simulations. It is this additional damping that explains why the HE only simulations and the JICF simulations did not have comparable limit cycle amplitudes, as were seen in the experimental data. As a result, stability trends were only compared between JICF simulations, as the HE only simulations contained damping that was approximately an order of magnitude lower.

### **Effect of Choked Area on Chamber Pressure**

Because the exit of the rig modeled in this study is choked, the mean chamber pressure that is achieved within the rig is determined by the total mass flow of reactants and the area of the throat of the exit nozzle. Because an expanding section is required in the simulations to avoid numerical instability, the actual choked area in the simulations differs from the throat area in the experimental rig. It was also observed that the actual choked area in the simulations can change based on the length of the expansion section that is modeled. The effects of this actual choked area were investigated so that any deviation in mean chamber pressure could be properly understood. Two separate simulations were run, one with a long expansion section and one with a short expansion section after the throat. Clips through the long and short expansions are shown in Figure 91, where the black line represents an isoline of Mach number equal to one.

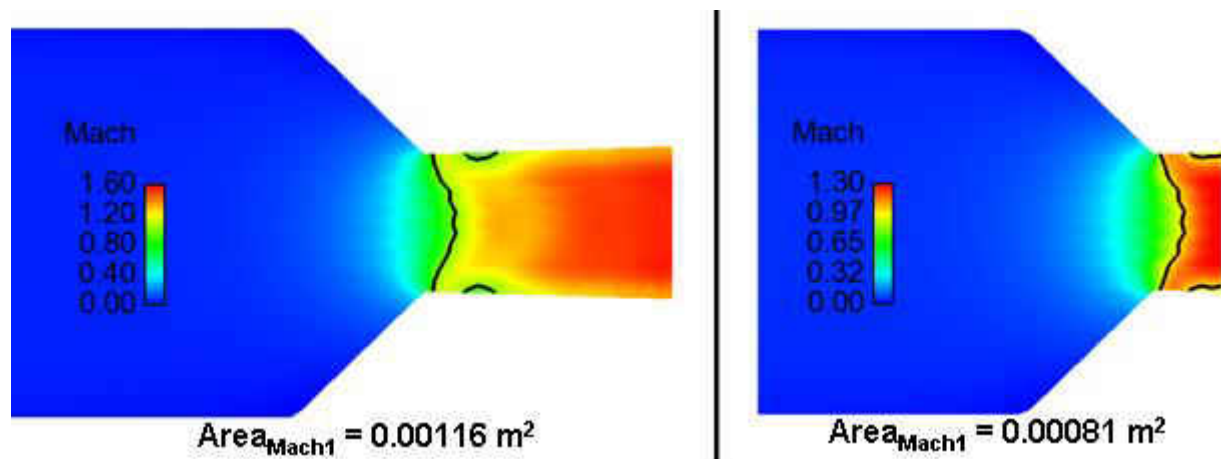


Figure 91: Comparison of choked area between long and short expansion section. Black line represents isoline of Mach=1.0.

It is evident that as the expansion length is increased in the simulations, the actual choked area also increases. This increase in choked area will result in a decrease in mean chamber pressure, as compared to the experimental results. Figure 92 shows two representative pressure traces from the short nozzle simulations compared to a corresponding case from the experimental data.

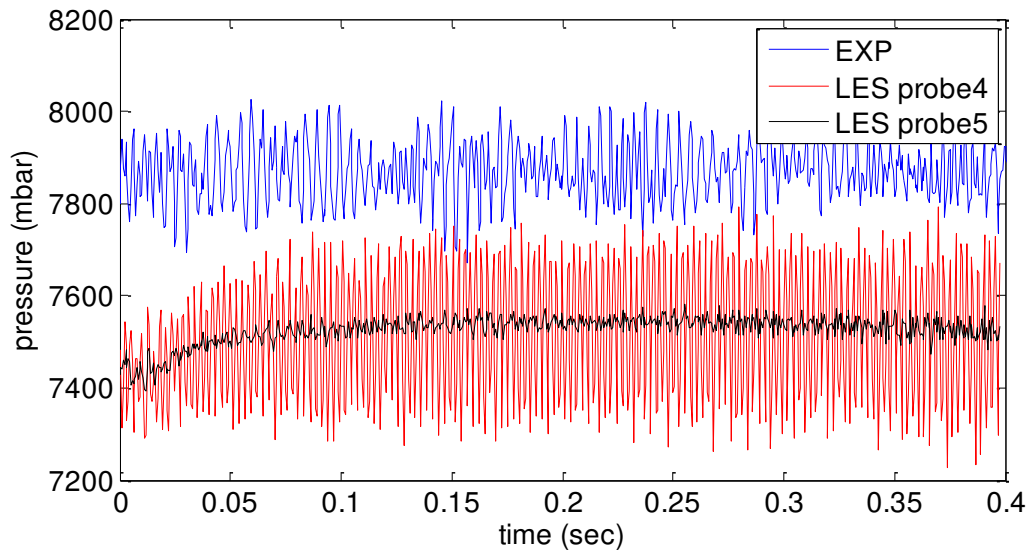


Figure 92: Representative pressure traces for short nozzle case, compared to experimental pressure

As expected, the mean chamber pressure in the simulations is approximately 4% lower for this case. This is attributed to the effective choked area in the simulations being larger than the actual throat area in the experiment, which is approximately  $0.00057 \text{ m}^2$ . All of the results shown in this study are obtained from simulations with the short nozzle, as this resulted in a more accurate mean chamber pressure and prevented numerical stability problems that were observed due to very low pressures that occurred in the exit of the long nozzle.

### Effect of Combustion Model Tuning Parameter

The combustion model that was utilized in this study requires a ratio between the turbulent and laminar flame speed to calculate the reaction rate of the mixture at every cell and timestep during the simulation. This reaction rate represents the source term in the reaction progress transport equation discussed above. This ratio between the turbulent and laminar flame

speed, or wrinkling factor, is determined from the Bradley correlation, which gives the following relation for the wrinkling factor,  $\Sigma$ , where  $A$  is a constant (Bradley, 1992):

$$\Sigma = 1 + \frac{(0.95A)}{Le} (\text{Re}_T \text{Pr})^{0.5} \quad (51)$$

Studies have shown that the value of  $A$  for methane/air flames should be set between 0.25 and 0.5 (Govert, 2011), however, it is important to understand the effect of this constant on the simulation results for the specific geometry and operating conditions investigated in this study. To determine this effect, four separate simulations were run where everything was kept constant between each simulation except for the values of this constant, which were set to 0.1, 0.3, 0.5, and 0.8. Figure 93 shows a clip plane through the head end flame for each of the four variations of the  $A$  constant, colored by instantaneous reaction progress variable.

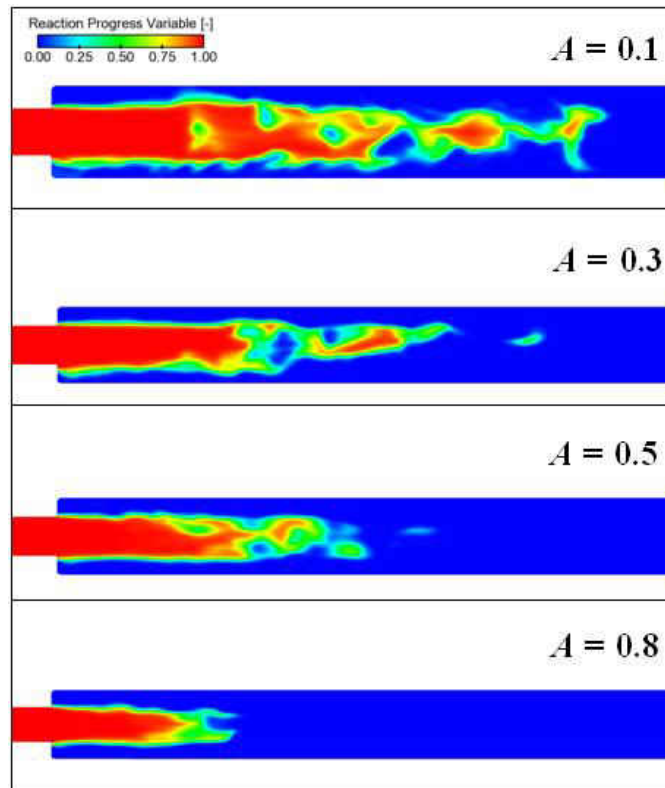


Figure 93: Clip plane through primary flame for four values of  $A$ , colored by instantaneous reaction progress variable

From this figure, it is clear that the value of the  $A$  factor has a direct effect on the flame shape and length, as expected from the equations. As the  $A$  factor is increased, it directly increases the wrinkling factor, which in turn increases the reaction rate, or the source term for the reaction progress transport equation. By increasing the reaction rate of a flame at fixed incoming velocity, the length and shape of the flame becomes shorter and more compact, as is apparent in Figure 93. This variation in flame behavior is expected to affect the combustion instabilities in the system, as the flame surface area, and thus the distribution of global and unsteady heat release, is affected by this flame shape and length.

Figure 94 shows the mean heat release profiles for each of the four cases tested here.

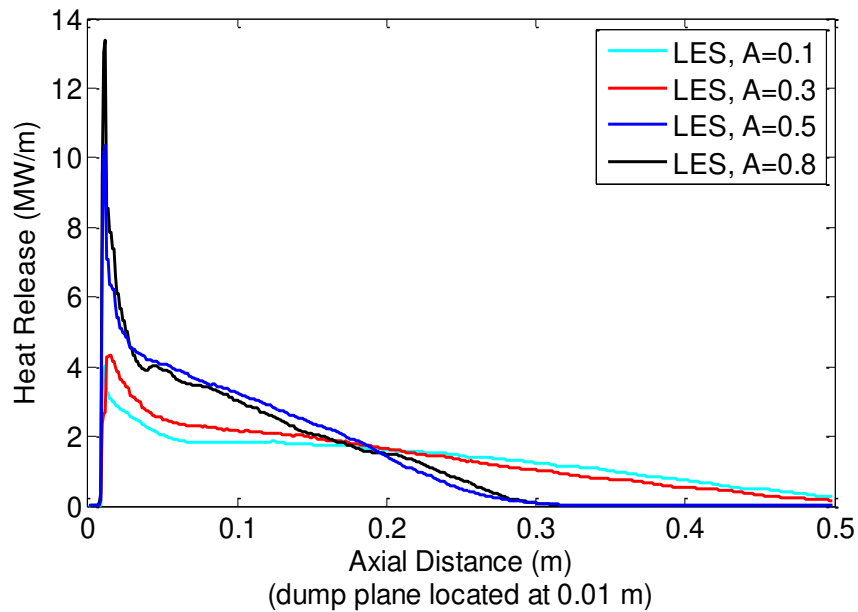


Figure 94: Mean heat release profiles for varying  $A$  factors

It is apparent from the figure that for low values of  $A$  (longer flame), the mean heat release is distributed up to 0.5 meters downstream from the dump plane, while the profile for higher values of  $A$  shows a much larger peak and a distribution that is less spread out. This distribution of heat release plays a direct role on the combustion instabilities present in the system, as it is the location of the unsteady heat release with respect to the acoustic modes of the system that either drives or damps the instabilities. This effect can be observed in Figure 95, which shows the mean heat release profiles for the two extreme cases ( $A=0.1$  and  $A=0.8$ ) plotted on the same horizontal axis as the first, second, and fourth longitudinal modes. Note that the amplitudes of the mode shapes (shown on the right vertical axis) are normalized by their individual maximum value in the combustion chamber.

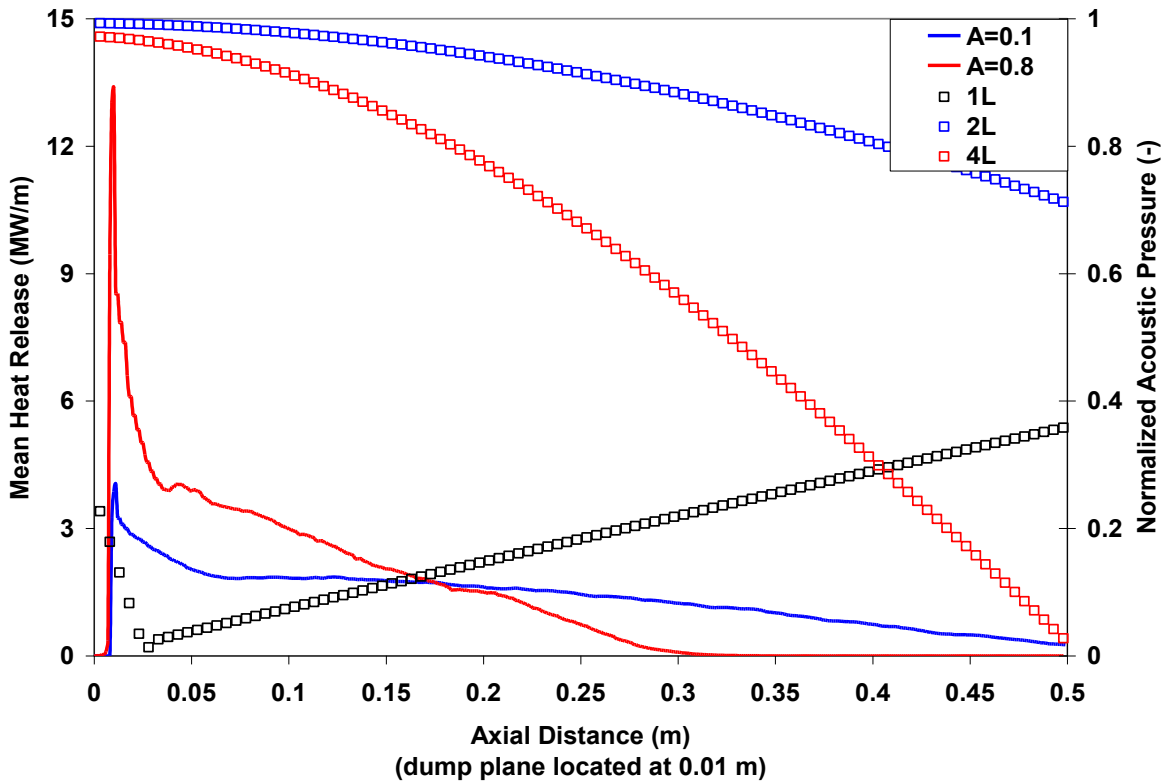


Figure 95: Axial location of mean heat release profiles with respect to 1L, 2L, and 4L acoustic pressure modes

As stated above, it is clear that the smaller value of the  $A$  constant results in a slower reaction rate, and thus, a much longer axial distribution of heat release. This causes the heat release to be distributed further away from the 2L and 4L pressure antinodes at the dump plane, and towards the 1L pressure antinode at the exit of the chamber. The effect on the stability of the modes can be seen in Figure 96, which shows representative pressure spectrum for the  $A=0.1$  and  $A=0.8$  cases.

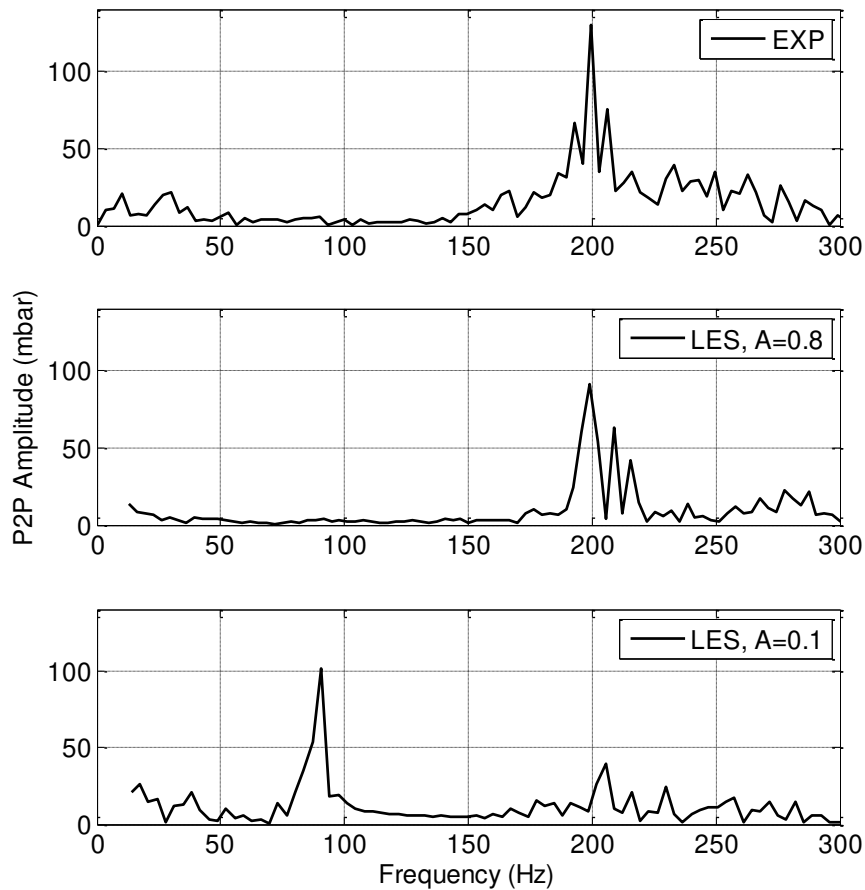


Figure 96: Representative pressure spectrum for minimum and maximum  $A$  factor cases

For the  $A=0.8$  case, the peak-to-peak amplitude of the 200 Hz mode is within approximately 30 mbar of that measured in the experiment, while the amplitude of the 200 Hz mode for the  $A=0.1$  case was significantly lower. It is clear, however, that the  $A=0.1$  case drives the 100 Hz mode which is not seen in the experiment or any of the other simulations. This is a result of the heat release being pushed downstream towards the 1L antinode at the exit of the chamber and away from the 2L antinode at the dump plane. It is evident from this analysis that an  $A$  factor must be chosen that provides the closest possible agreement with experimental data.



It was concluded, in part from the analysis discussed in this section, that an  $A$  factor of 0.5 should be used as the baseline constant for this study.

## **Understanding the Impact of Mesh Effects**

### *Mesh resolution*

An important factor in any numerical simulation is the resolution of the mesh and the regions of refinement that are applied throughout the computational domain. Although a mesh resolution study was performed on the computational domain, its goal was not necessarily to achieve a mesh independent solution, but rather to understand the role that the mesh resolution plays on the results of interest and to determine the optimum mesh resolution that should be used to achieve the desired results within a practical amount of required run time. Critical parameters for the two mesh resolutions tested in this analysis are shown in Table 11. The effect of mesh resolution was quantified by observing the flame shape and length as well as the peak-to-peak pressure amplitude and modeshapes of the first three unstable modes.

Table 11: Critical parameters for mesh resolution study

	<b>Elements</b>	<b>Cells/step height</b>	<b><math>\Delta x</math></b>
<b>Coarse</b>	840,200	36	$\sim 2.12$ mm
<b>Fine</b>	2,986,748	54	$\sim 1.41$ mm

It was observed that the mean flame length did not change significantly between the two mesh resolutions. By quantifying the flame length as the furthest downstream point where a reaction progress variable of 0.5 is observed, it was determined that the flame length for the coarse mesh was only 1.5% longer than the flame length for the fine mesh and was almost

indistinguishable when observing the flame images. A representation of the mean flame shape is shown below in Figure 97 and Figure 98 for the coarse and fine mesh, respectively. Clip planes through both the YZ and XZ planes are shown as the flame was always found to be asymmetric in the axial direction for every case run in this study. A discussion of this asymmetry is provided in a following section.

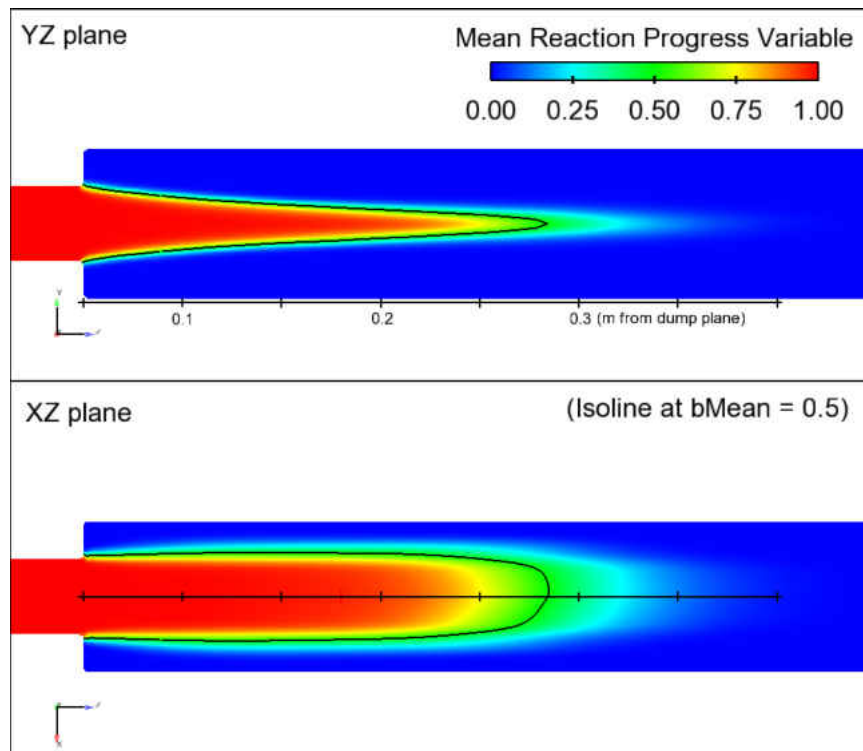


Figure 97: Coarse mesh YZ and XZ clip planes colored by mean reaction progress variable, representing the mean flame shape at the dump plane. Black isoline at  $bMean = 0.5$

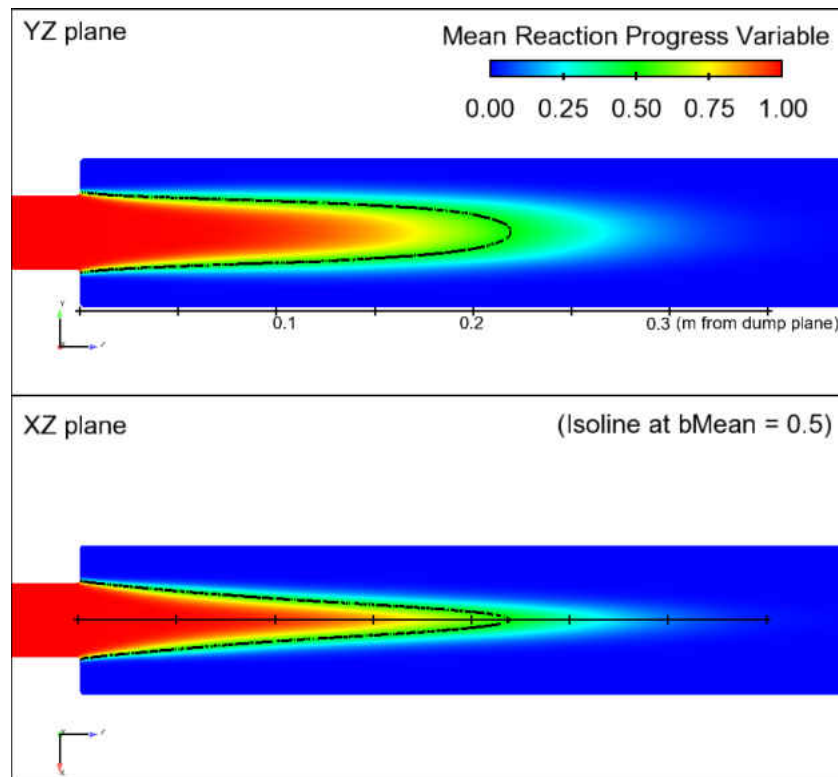


Figure 98: Fine mesh YZ and XZ clip planes colored by mean reaction progress variable, representing the mean flame shape at the dump plane. Black isoline at  $b_{\text{Mean}} = 0.5$

Although the overall flame length is very similar between the two meshes, there are a few differences that can be noted. First, it is observed that the flame rotates 90 degrees between the coarse and fine meshes. Consequently, the XZ plane in the coarse mesh should be compared with the YZ plane in the fine mesh and the YZ plane in the coarse mesh should be compared with the XZ plane in the fine mesh. It is currently unknown as to which (if either) of the orientations are more physical, as this rotational asymmetry could simply be a numerical error or a physical effect that could exist in either direction as the geometry is rotationally symmetric.

Another slight difference between the meshes is spread of the flame in the transverse directions. The coarse mesh exhibits a thinner cone shape flame in the YZ plane than the fine mesh exhibits in the XZ plane and a wider flame in the XZ plane than the fine mesh exhibits in the YZ plane. It is expected that the fine mesh resolves the hydrodynamic behavior at the dump plane more accurately, however, for the purpose of this study, the important mesh resolution effect was on the acoustic pressure waves within the chamber and how they were driven. Because the sole purpose of the head end flame in these results was to act a “speaker” to excite the chamber modes, a balance was sought between an accurate hydrodynamic solution at the head end but also a coarse enough mesh to provide reasonable solution times for the results that must be obtained.

A comparison of the peak-to-peak pressure amplitude is shown in Figure 99, comparing both the coarse and the fine mesh to the corresponding experimental results.

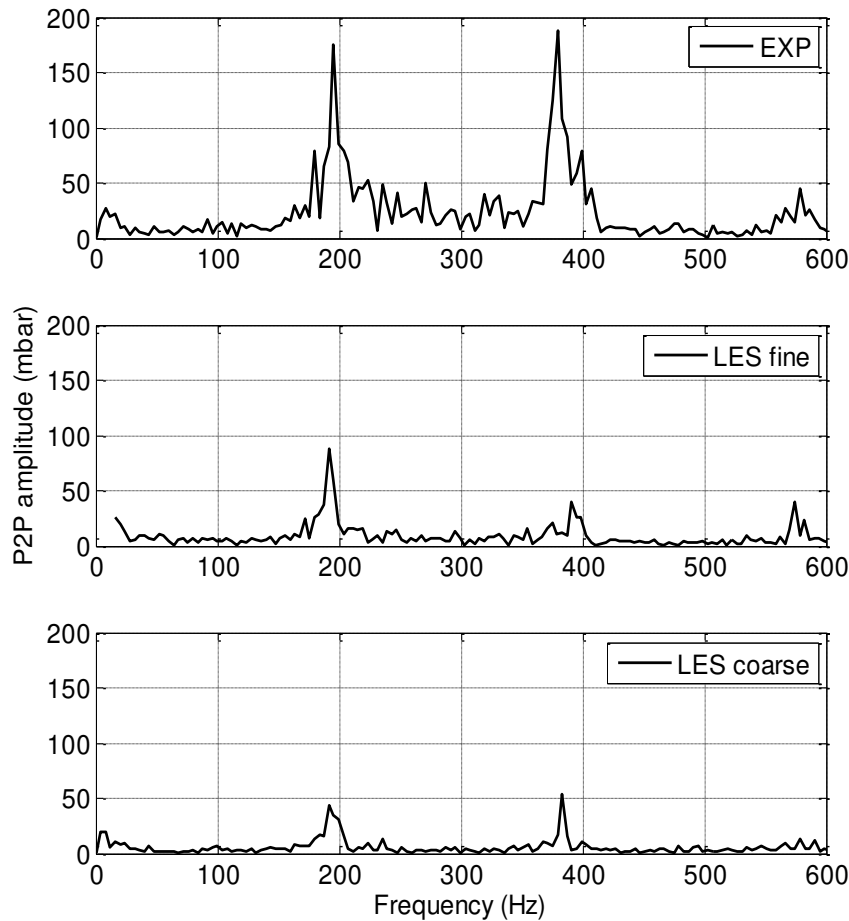


Figure 99: Representative pressure spectrum for mesh resolution study (Note that this data was taken from only 0.25 seconds of raw pressure data, compared to the standard 0.3 seconds of data used in other figures throughout this document)

It is apparent from the figure that although the simulation under predicts the amplitude of both the 200 and 400 Hz modes with both meshes, the fine mesh does predict a higher amplitude than the coarse mesh for both the 200 and 600 Hz modes. The amplitude of the 400 Hz mode, however, appears to be less affected by mesh resolution, and the coarse mesh may even predict a more accurate amplitude for this mode. It is likely that the effect of mesh resolution on each particular mode depends on the physical mechanism that is driving that mode. It was also

observed that the mode shapes for the 200 and 400 Hz modes, as calculated using a 3D discrete Fourier Transform (DFT), were nearly identical. Because the higher mesh resolution case was approximately three times slower than the coarse mesh case and did not provide a consistently improved result, it was concluded that the majority of the simulations run in this study would utilize the coarse mesh. For the JICF cases, a comparable resolution throughout the regions away from the JICF injection was applied, with additional refinement in the region of the reacting jet in cross flow.

### *Ox-post refinement*

Another important mesh parameter that was observed in this study was changing the level of mesh resolution in the ox-post, upstream of the dump plane. It was observed that if the refinement level was changed in the ox-post, the flow immediately preceding the dump plane was non-uniform and could have an effect on the flame and resulting dynamics of the system. This was due to inconsistencies that occurred in the mesh due to the change in refinement level, and is a problem specific to the mesh tool, snappyHexMesh, used in this study. The region of the ox-post that originally included a change in refinement level is shown in Figure 100, compared to the same region with a uniform mesh resolution throughout the ox-post.

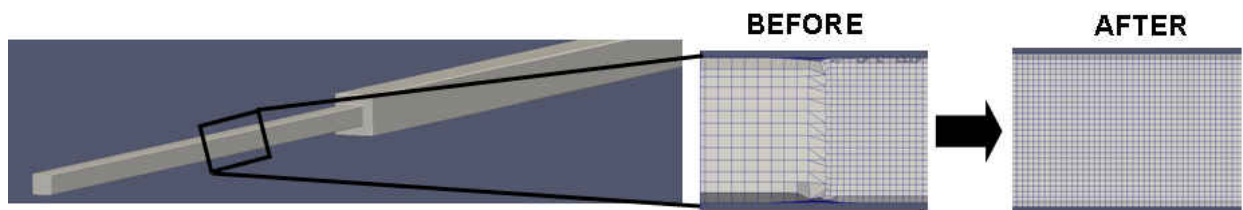


Figure 100: Ox-post mesh refinement levels

Although it required a slightly higher number of elements, it was found that ensuring a consistent and geometrically accurate mesh upstream of the dump plane was required to reasonably capture the flow physics of the incoming reactants. This is because the flame shear layer, which effects the mixing and dynamics of the flame, arises from the boundary layer that develops in the ox-post, and thus, is an important parameter to accurately model. Care should be given when modeling ducts and lines upstream of the reaction zone, as the resolution of these upstream components has a direct effect on the behavior of the flame.

### *Numerical damping of rhoPisoFoam solver*

A very basic study was performed to quantify the acoustic numerical damping of the rhoPisoFoam solver used in this study, as a function of the cells per wavelength resolved with the mesh. This study utilized a simple one-dimensional mesh where the velocity field within the domain was initialized with a  $\frac{3}{4}$  wave standing mode and the simulation was run long enough so that a consistent damping rate could be calculated from the pressure oscillations within the domain. Two sets of these simulations were run, using off-centering factors for the temporal discretization of 0.5 and 1.0 (see following section for a description of the off-centering factors). No mean fields were applied to the simulations so that the only result coming from this study was the direct effect of the temporal discretization scheme on the acoustic waves within the domain. The damping coefficient for each test case is shown in Figure 101 as a function of the cells per wavelength resolved with the mesh.

The results in Figure 101 show that the effect of the off-centering factor on the numerical damping of the acoustic waves within the system is almost negligible. It should be noted, however, that the order of the temporal discretization scheme can still have an indirect effect on

the acoustics of the system that would not be captured by this basic study. This indirect effect can arise, for example, when mean fields are included in the simulation.

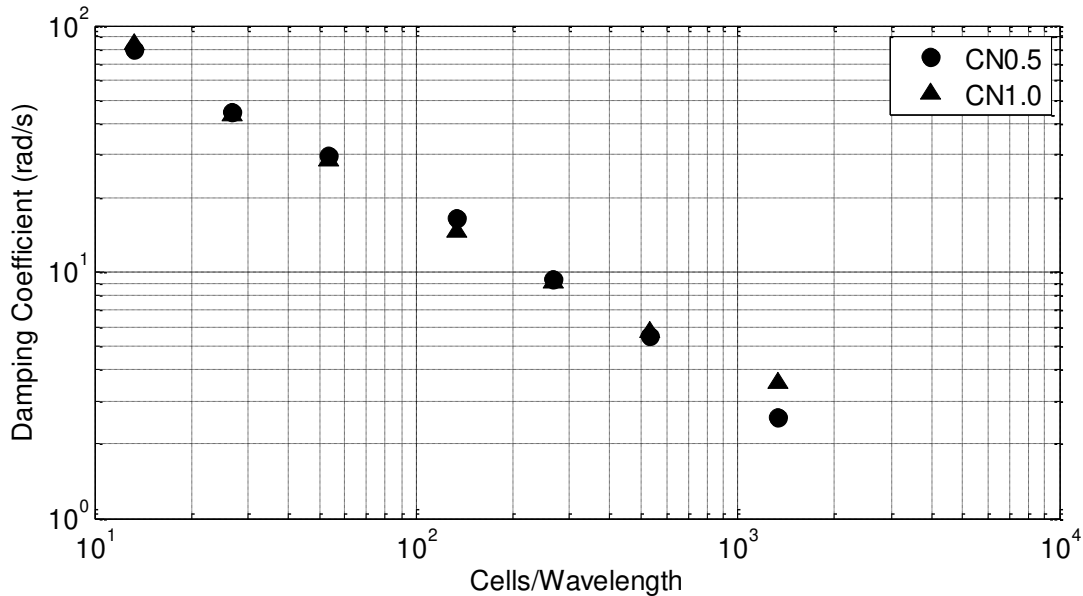


Figure 101: Damping coefficient versus cells per wavelength for rhoPisoFoam solver using two off-centering factors

Note that the two primary modes of interest in the Purdue acoustic rig modeled in this study had wavelengths of approximately 3.5 and 1.75 meters (the 200 and 400 Hz modes, respectively). The coarse mesh, which had approximately 1260 cells in the longitudinal direction, resulted in 1260 cells within the wavelength of the 200 Hz mode and 630 cells within the wavelength of the 400 Hz mode. Based on Figure 101, this correlates to a numerical damping between 2 and 5 rad/s on acoustics, due directly to temporal discretization errors.

To determine the relative effect of this numerical damping on acoustics, a one-dimensional transfer matrix analysis was performed to quantify the acoustic losses due to the inlet boundary errors in the reflection coefficient, and compare them to the numerical damping



from the temporal discretization, as determined in this test case. It was found from this analysis that the actual inlet boundary of the computational domain resulted in a damping coefficient of approximately 26 rad/s compared to the 4 rad/s of damping present if an inlet boundary reflection equal to the theoretical value was used. Thus, the damping, or acoustic losses from the errors in the inlet boundary condition contributed to a damping coefficient on acoustics that was nearly an order of magnitude higher than that observed from the temporal discretization errors. This suggests that a more accurate method to model the choked inlet would have a much more significant effect on the accuracy of the solution than implementing a higher order temporal discretization scheme, assuming sufficient cells per wavelength are included in the model.

#### **Effect of off-centering coefficient in the temporal discretization**

In any self-excited simulation where the results are largely dependent on the level of numerical damping present in the simulation, it is important to understand how critical discretization schemes affect the acoustics present in the simulation, as some numerical damping is required to achieve a numerically stable simulation. One of the critical discretization schemes is applied to the temporal derivatives in the simulation. This study utilized the Crank-Nicolson scheme for the temporal derivatives where an off-centering coefficient can be applied that blends the Crank-Nicolson scheme with an Euler scheme for more robust numerical stability. An off-centering coefficient of 1, for example, applies only the implicit Crank-Nicolson scheme and is second order accurate while an off-centering coefficient of 0 applies only the explicit Euler scheme and is first order accurate. Ideally, this coefficient should be set to 1 to limit the numerical damping and provide a solution that is second order accurate in time, however, this is often not feasible due to numerical instabilities. Several simulations were run in this study to

determine the effect of this off-centering coefficient on the numerical stability of the simulation and the limit cycle amplitude of the unstable acoustic modes of interest in the geometry. Both the baseline head end only simulation as well as the JICF simulations were run using off-centering coefficients of 0.5, 0.8, and 1.0. Each of the simulations discussed here were run using a mesh refinement level comparable to the baseline head end coarse mesh.

Figure 102 shows representative pressure spectrum for the baseline head end only simulations, comparing the off-centering coefficients of 0.5, 0.8, and 1.0 with the experimental pressure spectra.

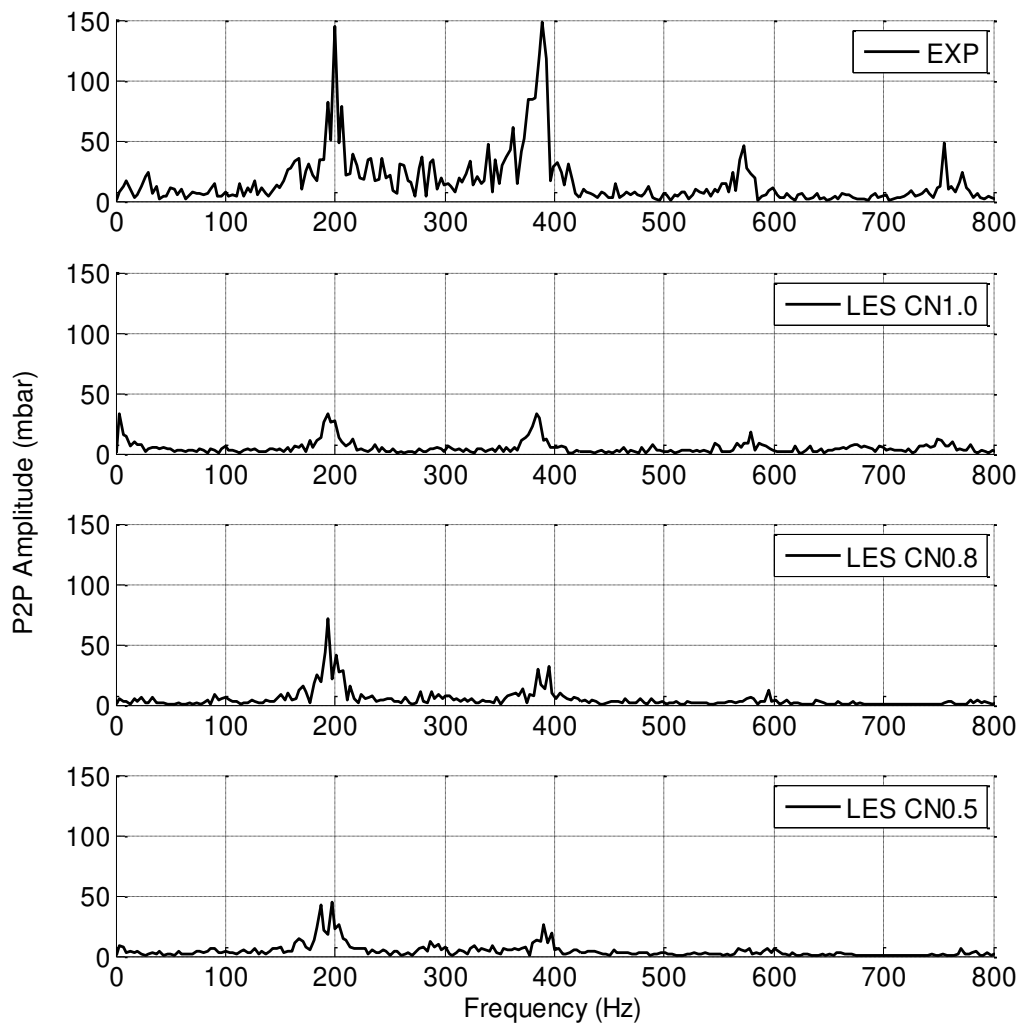


Figure 102: Representative pressure spectrum for temporal discretization study

From the figure it is apparent that each of the schemes tested here exhibit a peak near 200 and 400 Hz, where the frequency matches well with experiment and the amplitude is under predicted. The difference between the three different off-centering coefficients used here is more apparent in Figure 103, which shows the same data as Figure 102 but with a limited vertical axis for clarity.

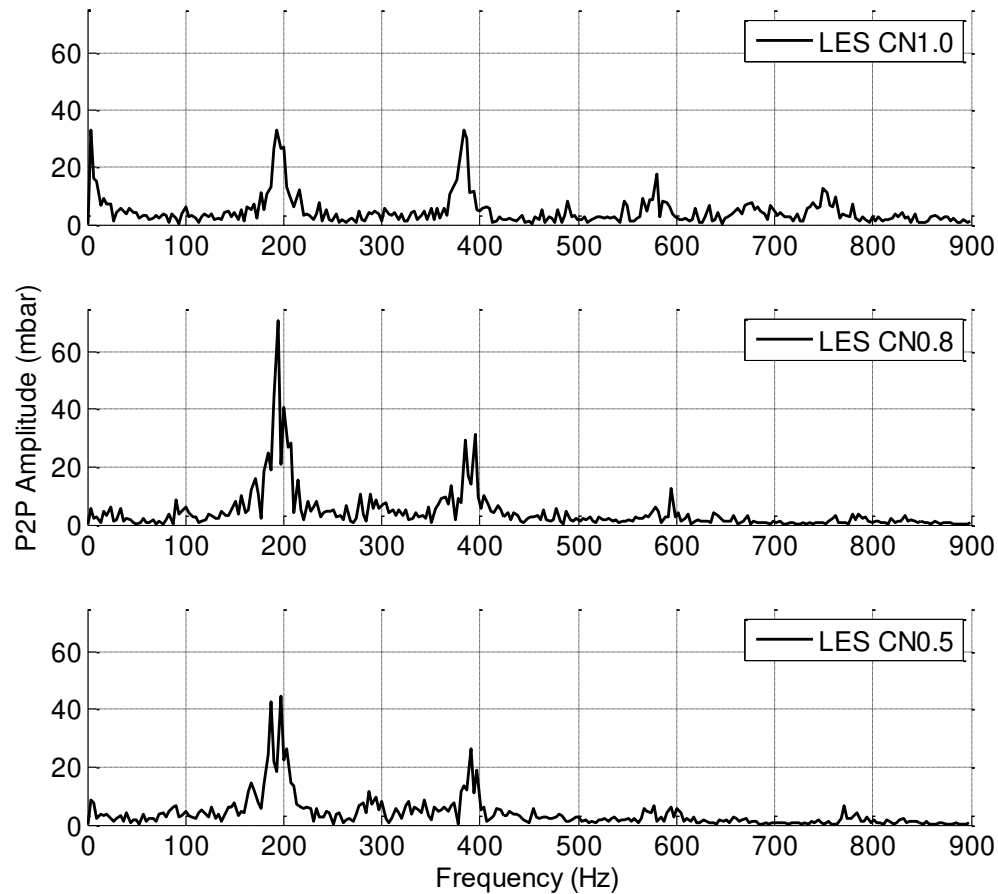


Figure 103: Zoomed in view of representative pressure spectrum for temporal discretization study

It is apparent from this figure that the CN0.8 scheme results in the highest amplitude for the 200 Hz mode while the 400Hz peak is slightly lower for the CN0.5 scheme. There are also small peaks visible at 580 and 750 Hz in the spectra for the CN1.0 scheme, however, these peaks are barely visible above the signal noise for the CN0.8 scheme and even less visible for the CN0.5 scheme. This data seems to suggest that the fidelity of the temporal discretization scheme appears to have a more significant effect with higher frequency modes. Note also that from the experimental data for this case, the peak amplitudes for the 200 and 400Hz modes are similar as

are the peak amplitudes for the 580 and 750 Hz modes. Although the simulation amplitudes are much lower than those seen in the experiment, the relative amplitudes between modes are similar to experiment for the CN1.0 scheme but are too low for the high frequency modes for the CN0.5 and 0.8 schemes. This again suggests that the blended schemes result in an increasing amount of numerical damping for higher frequency modes.

For the lowest frequency mode observed here at 200Hz, it is interesting to note that the less accurate blended scheme of CN0.8 actually results in a higher peak and thus, better agreement with experimental results. This result is counterintuitive, as one would expect a higher order of accuracy in the discretization scheme to result in less numerical damping, and thus a higher peak amplitude. While this appears to be the case for higher frequency modes, it clearly does not occur for the 200Hz mode. It is proposed that this is a result of the numerical instability that develops in the solution when using the CN1.0 scheme, as explained in more detail below. These numerical instabilities, which are an unphysical phenomenon, begin to dominate over the acoustic modes, resulting in a lower amount of energy being fed into the acoustic modes.

The effect of the temporal discretization scheme was also investigated for the JICF simulation, as this simulation adds the additional complexity of a secondary reaction zone in the combustion chamber and the effect of the temporal accuracy is potentially different than that seen in the more simple head end only case. Figure 104 shows the representative pressure spectra for the JICF case, comparing off-centering factors of 0.5, 0.8, and 1.0. Note that the vertical axis scales in this figure are different between the experimental data and the simulation data, as the peak-to-peak amplitude for the simulation data were an order of magnitude lower than the amplitude seen in the experiment.

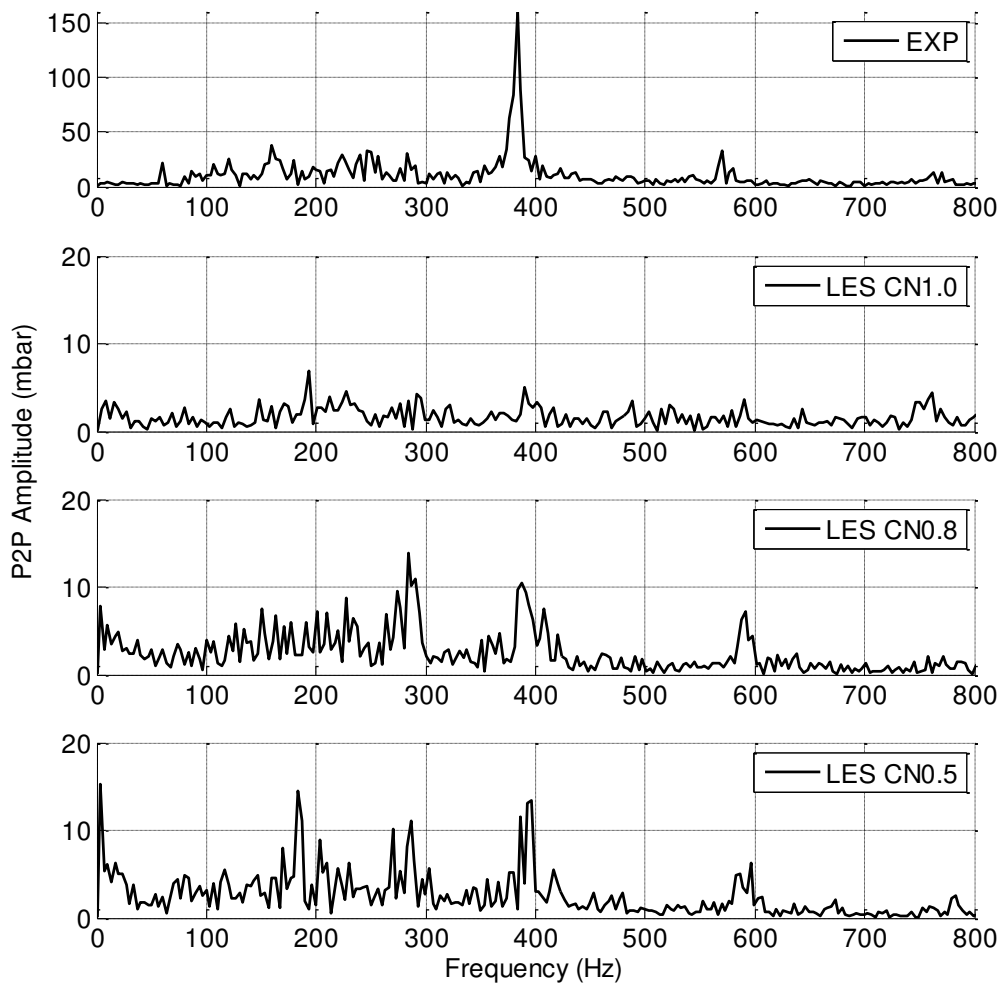


Figure 104: Representative pressure spectrum for JICF temporal discretization study (note the different scales on the simulation plots for clarity)

From the simulation spectrum, it is evident that the addition of the JICF to the computational domain essentially damped nearly all acoustics seen in the chamber. This does not agree with the experimental results, which clearly show that while the 200Hz mode was damped by the JICF for this condition, the 400Hz was still driven, and exhibits a peak-to-peak amplitude that is approximately equal to the corresponding amplitude seen in the baseline head end only

simulation. This simulation data provides unexpected results, especially since the head end conditions are the same between the head end only simulation and the JICF simulation. Thus, it is peculiar that the addition of the JICF in the simulations appears to significantly damp the acoustics when they were clearly driven in the head end only simulations. A necessary conclusion is that additional numerical damping, additional boundary losses, or inaccurate modeling of the JICF combustion/acoustic feedback arises with the addition of the JICF geometry.

Based on calculations of the volume integrated Rayleigh Index, it was determined that the JICF combustion/acoustic interaction was not damping the acoustics (specifically at 400Hz) in this configuration. The study of the temporal discretization scheme for the head end only simulation suggested that while the off-centering factor can have a damping effect on higher frequency modes, its effect was minimal at 400Hz, and thus, does not account for the significant damping that occurred in this JICF simulations. The only remaining explanations for the significant damping in the JICF simulations are either inaccuracies in the spatial discretization schemes that increase with the addition of the large gradients in the JICF flow fields, or the addition of boundary losses due to the JICF inlet boundary (which from the reflection coefficient analysis discussed above, the inlet boundaries are a known source of acoustic losses). Both of these factors were individually investigated and it was concluded that the additional damping in the JICF simulation could be attributed to combination of these two effects.

It was found that running the JICF simulations with an off-centering factor of 1.0 for the temporal discretization scheme resulted in so much numerical “noise” that the acoustic mode shapes were no longer clear when a DFT post processing technique was applied. This appeared

to be an effect of the secondary reaction zone in the combustion chamber, resulting in what could be considered numerical modes throughout the geometry that were not physical. An example of these numerical modes are shown in Figure 105, which shows plots of the normalized pressure amplitude and phase for the two dominant numerical modes at 93 and 455 Hz compared to the barely distinguishable acoustic modes at 193 and 392 Hz. Note that the color bars for the acoustic modes had to be limited to a maximum value of 0.2 to allow for any distinguishable mode to appear.

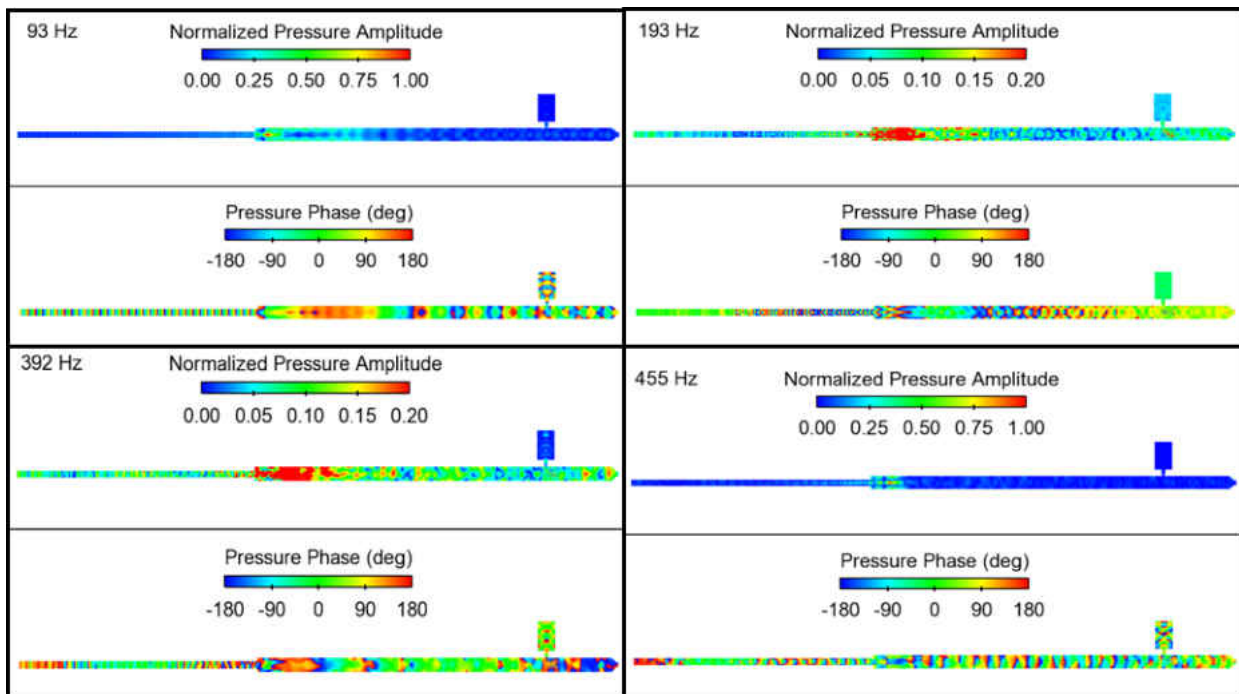


Figure 105: Comparison of numerical and acoustic modes for JICF case using the CN1.0 temporal discretization scheme

These numerical modes, which exhibited very high amplitudes in the region of the head end flame, are unphysical and contain no characteristics of any modes seen in the experimental measurements. The numerical mode shapes were significantly stronger than any acoustic modes seen in the JICF simulations, resulting in no useful results for the JICF simulations with an off-



centering factor of 1.0. This is a limitation of the numerical schemes that are available in OpenFOAM at this time, where the higher order temporal discretization schemes applied to more complex flow fields are numerically unstable. While the simulations run without crashing, the results are not useful for acoustic analysis.

### **Effect of Spatial Discretization Scheme**

What may have an even greater impact on the acoustics than the temporal discretization scheme discussed above is the spatial discretization scheme that is applied to the spatial derivatives in the solution. The current best practice approach is to use a Gauss linear second order scheme for the majority of the spatial derivatives that are solved, with specific limiting applied to derivatives that are prone to cause instability. One of the most important derivatives that requires limiting is the divergence of velocity, where a limiter is applied at cells where the gradients of velocity are high and numerical instabilities are likely. This limiter allows the discretization to reduce to first order in these regions of high gradients to maintain numerical stability. Because high velocity gradients are present in flame regions as well as the jet in cross flow region, it is important to understand what effect the reduced order of the spatial discretization of velocity will have on the acoustics present in the simulation.

This effect was investigated by running a full head end simulation where the discretization of the divergence of velocity terms were set to first order at all cells using an upwind scheme. Everything else was held constant and the results were compared to the baseline head end simulation using the limited second order scheme. The Crank-Nicholson temporal discretization scheme was applied with an off-centering coefficient of 0.8. Representative pressure spectra are shown below in Figure 106 for this comparison.

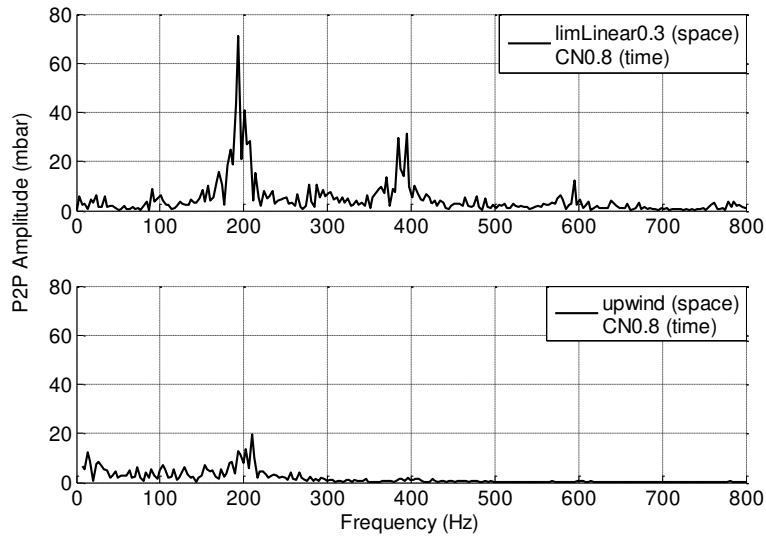


Figure 106: Representative pressure spectra for spatial discretization comparison

What is interesting to note from these results is that any frequency content in the signal above 300 Hz is almost completely eliminated when the first order discretization scheme is applied to the divergence of velocity terms. This is an important result when attempting to apply the self-excited LES approach to capture high frequency modes, as it is evident that if a sufficient portion of the cells require first order schemes to maintain stability, almost no acoustics will be captured. It is also clear that even the lower frequency modes, specifically the 200 Hz mode in this case, can be significantly damped as well, with the peak-to-peak amplitude using the upwind scheme barely reaching 25% of that seen using the limited linear scheme. These results suggest that if reasonable self-excited acoustics are to be captured using this technique, a spatial discretization scheme with at least second order accuracy is necessary throughout as much of the domain as possible. It is recommended that future work should investigate the implementation of a scheme that is higher than second order for specific application to self-excited LES, as it is likely that the errors coming from the spatial

discretization of the velocity terms result in a significant contribution to the numerical damping within the simulation.

### Asymmetric head end behavior

It was found that most of the simulations run in this study resulted in a mean head end flame shape that was not rotationally symmetric about the combustor axis. This phenomenon was first observed when orthogonal clip planes were taken through the data to observe the flame cross section. A representative example of this flame behavior is shown below in Figure 107. This example was taken from the fine mesh head end only simulation.

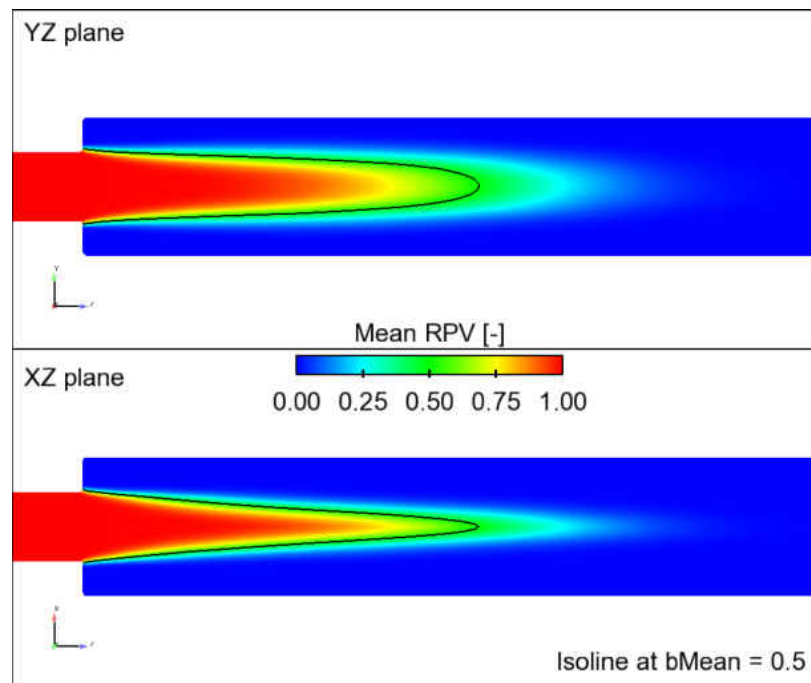


Figure 107: Orthogonal clip planes colored by mean reaction progress variable showing asymmetric mean flame shape. Isoline represents a value of 0.5.

It is apparent from the figure that the downstream region of the flame appears to be wider in the YZ plane than in the XZ plane, resulting in a flattened, or “screwdriver” shaped flame.

Many exploratory simulations were run to try and determine the source of this flame asymmetry, including RANS and LES, reacting and non-reacting, coarse and fine mesh resolutions, as well as a variety of initial conditions and solver parameters. With sufficient simulation time, the solution always seemed to converge to an asymmetric flame shape, even though extra care was taken to ensure an axisymmetric mesh, initial conditions, and boundary conditions. It should be noted here that the reacting RANS simulation took over 35,000 iterations before the flame became asymmetric while the LES simulations tended to result in asymmetric flames almost immediately after achieving a converged solution. This is likely due to the additional turbulence modeling present in the RANS simulation that resulted in a delay of the asymmetric effect. Figure 108 shows two orthogonal views of the coarse mesh used in this study, demonstrating that the mesh is symmetric with 18 cells in both directions across the ox-post and 36 cells in both directions across the combustion chamber.

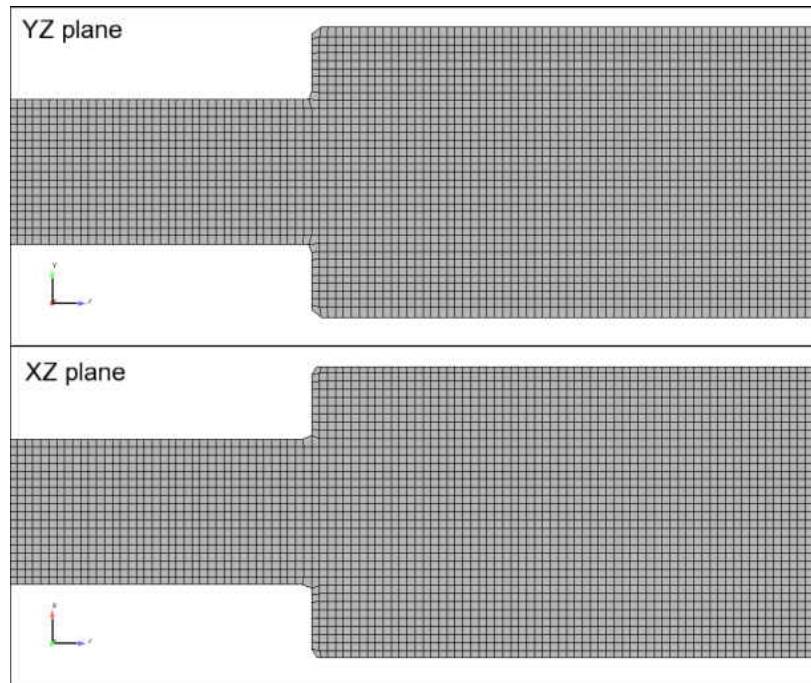


Figure 108: Orthogonal views of the coarse mesh in the head end region

Figure 109 shows orthogonal clip planes through the head end region colored by mean axial velocity for a non-reacting LES simulation. The white isoline represents a mean axial velocity of zero, or the boundary of the recirculation region behind the area change.

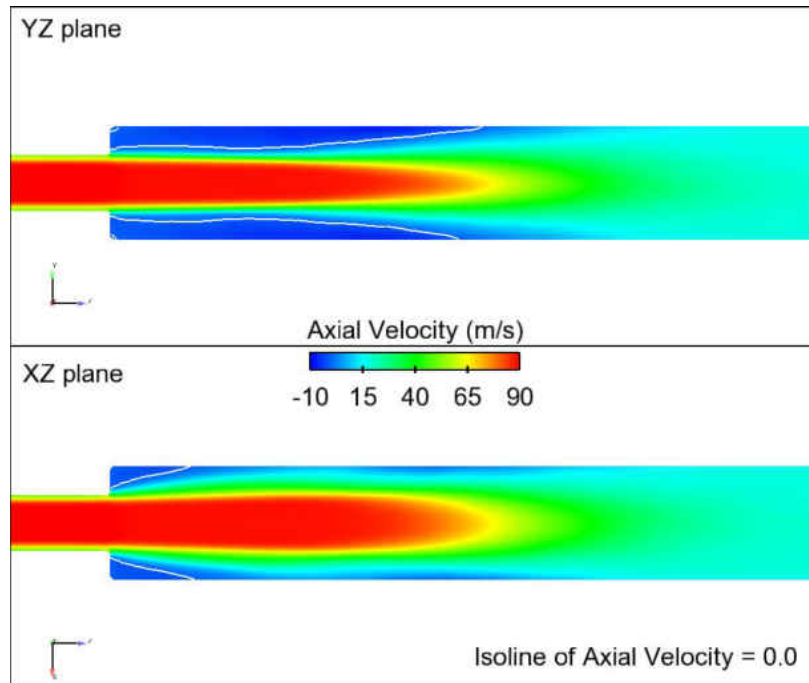


Figure 109: Orthogonal clip planes colored by mean axial velocity showing asymmetric recirculation region. Isoline represents a value of 0.

These contours of axial velocity from the non-reacting simulation clearly show that the flow downstream of the dump plane is not rotationally symmetric about the combustor axis, but rather is characterized by very long recirculation regions in the YZ plane and very short recirculation regions in the XZ plane. Because this same asymmetric phenomenon was observed in the non-reacting simulation, it was concluded that the phenomenon was not a result of the reaction or the combustion model, but rather a hydrodynamic effect.

Although future experimental data will include optical diagnostics of the head end flame for validation purposes, there is currently no data that can be used to verify whether the asymmetric flame behavior is a real phenomenon or simply a numerical simulation error. One possible explanation is that the effect is actually physical, due to the square cross section of the ox-post and combustion chamber, however, this would have to be verified through experimental

measurements which are currently unavailable. Because the focus of this study is on the behavior of the reacting jet in cross flow and the related combustion instabilities present in the overall system, it was determined that further analysis of the asymmetric head end flame was outside of the scope of this work and will be left for future investigations, if deemed necessary or of interest.

## **APPENDIX B – PRE AND POST PROCESSING METHODS**



### Calculating time lag information from simulations

In order to be able to accurately quantify the phase between arbitrary variables in the simulation, it was necessary to develop a method to extract the necessary data during the simulation run time that could be used to calculate the phase between these variables. This data is important for quantifying the phase, or time lag, between quantities that play a role in the feedback cycle of combustion instabilities, specifically the velocity, pressure, and heat release. The accurate calculation of these values will provide important information in validating the simulation data with experimental trends.

Due to the unsteady and three-dimensional nature of the flow in the self-excited LES simulations, point sampling of any of the fields would not be a practical way to identify the phase information between the variables of interest. Instead, volume integrations were performed of the three-dimensional fields within localized regions of heat release or velocity. These integrations were performed during the simulation run time to allow for sufficient time resolution without an extensive disk space requirement. This method also ensured that the quantities that were compared from a given simulation were “in-sync” with each other so that the calculated phases would be physically accurate.

The phase calculation method applied here utilized several built in features in OpenFOAM. Before beginning the simulation, the geometrical regions for the volume integrations were input into the `cellSetDict` and then setup using the `cellSet` and `setsToZones` commands. The region of integration for the heat release from the JICF reaction zone was simply specified so that it fully enclosed the mean heat release profile of the jet flame. A representation of this region is shown in Figure 110, which outlines the volume used for the integration of the JICF heat release.

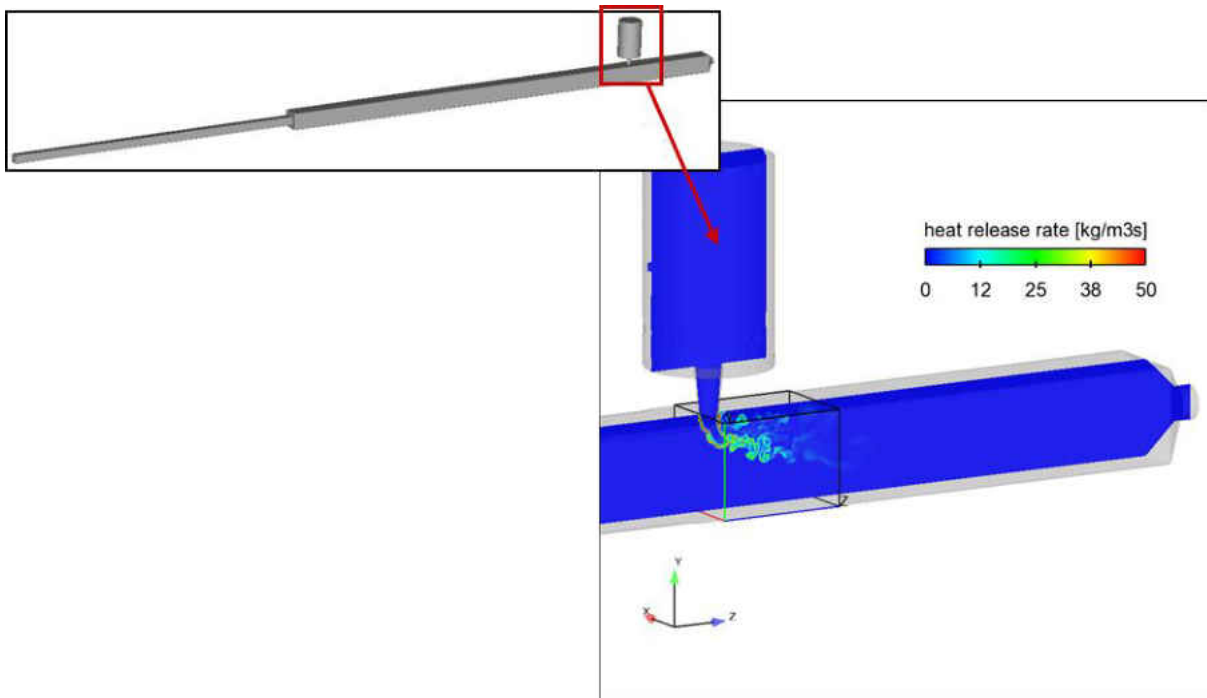


Figure 110: Representation of the volume used for calculating the temporal signals of reacting JICF heat release and jet nozzle pressure. Instantaneous contours of heat release rate included in lower plot

By integrating the transient heat release field in this localized region, a signal for the JICF heat release as a function of time could be obtained. It was assumed for the purposes of this study, that the heat release from the JICF could be represented as a compact flame, with respect to the acoustic modes in the combustion chamber. This is a valid assumption considering that the JICF flame was typically only about 2-3% of the length of the chamber acoustic modes. It also is a sufficient approximation considering the objective of this study, which is to quantify a mechanism of instability of a reacting JICF. As stated previously, this study seeks to identify the global effect of the jet flame and how it relates to the overall system stability, not necessarily the localized behavior within the jet flame.

This same volume (shown in Figure 110) was also used to quantify the chamber pressure at the exit of the jet nozzle. Similar to the heat release signal, this method of integrating the pressure into a single 1D pressure signal as a function of time assumes that the pressure at the jet exit can be approximated by the volume integration of the pressure field within this domain. This assumption is valid due to the relatively low pressure gradient within this volume and must be done to ensure that the phase between the heat release and pressure signal is maintained through the data extraction process.

The final variable that plays a direct role in the combustion instability feedback cycle is the velocity of the JICF. A separate volume was specified in the region of the jet scoop and is shown below in Figure 111.

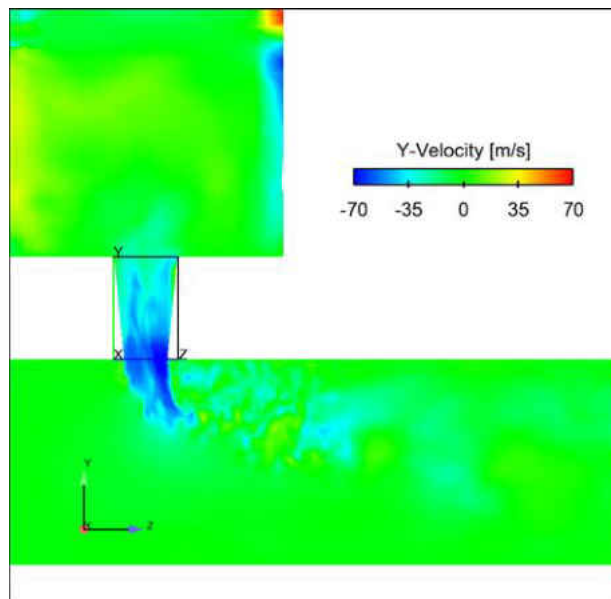


Figure 111: Representation of the volume used for calculating the temporal signals of jet velocity, including instantaneous contours of y-velocity

Calculating the volume integral of the y-velocity in the scoop, in-sync with the previously described heat release and pressure signals, allowed for a quantitative understanding of the relation between the pressure fluctuations at the exit of the jet and the resultant velocity fluctuations in the scoop, as well as the relation between the velocity fluctuations in the scoop and the resultant heat release fluctuations from the jet flame.

Figure 112 shows signals of the velocity fluctuation from the scoop integration zone and the pressure fluctuation from the JICF heat release zone, filtered at 200Hz. It is evident from the signals that they are nearly 180 degrees out of phase. This is confirmed by the calculation of the transfer function phase between the two raw signals, shown in the lower plot of Figure 112, where the phase between the signals at 200Hz is just below 180 degrees.

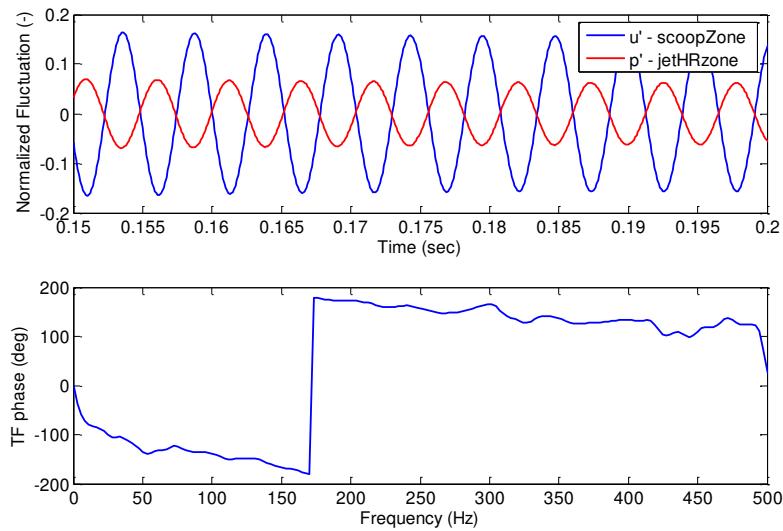


Figure 112: Velocity and pressure fluctuation signals filtered at 200Hz (upper) and corresponding transfer function phase calculated from the corresponding raw signals (lower)

A similar plot is shown below in Figure 113, comparing the velocity fluctuation from the scoop integration shown and the heat release fluctuation from the JICF heat release zone.

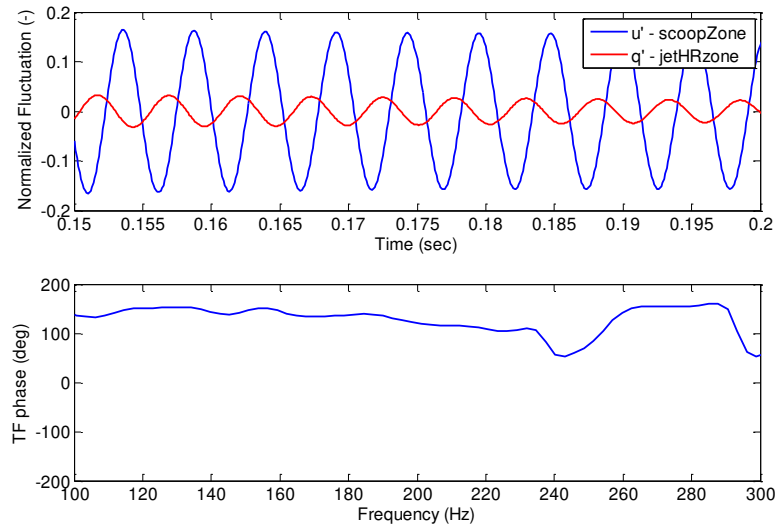


Figure 113: Velocity and heat release fluctuation signals filtered at 200Hz (upper) and corresponding transfer function phase calculated from the corresponding raw signals (lower)

These signals, again filtered at 200 Hz, are less than 180 degrees out of phase. This is confirmed by the phase of the transfer function, which shows a phase between the signals of 123 degrees near 200Hz. These signals and resultant transfer function phases are representative of the data that was used throughout this study to quantitatively identify the phases between the variables that contribute to the combustion instability feedback cycle of the reacting JICF.

Some general trends were identified when calculating the phase, or time lag, between the velocity fluctuations in the scoop and the resultant heat release fluctuations from the jet flame. In general, the phase between two signals is linearly related to frequency, that is,  $\phi = \omega\tau = (2\pi\tau)f$ . From this relation, it is evident that the slope of the phase-

frequency curve is proportional to the time lag (in seconds). This linear relation is evident below in Figure 114, which shows the phase-frequency curves for several different configurations where the distance from the choked point of the air supply line to the jet flame was varied (i.e., the impedance of the JICF configuration).

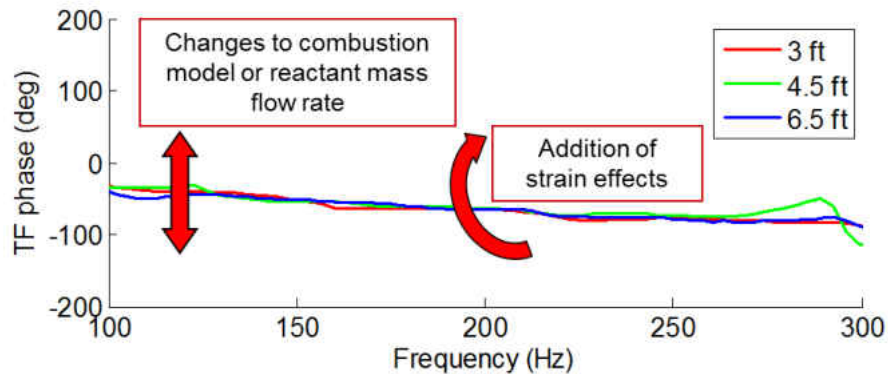


Figure 114: Phase-frequency relation for various jet air supply line choke points (distance specified from jet manifold)

It is evident that the changes in the impedance of the JICF configuration due to moving the air supply line choke point do not change the slopes of the curves. This agrees with the physical understanding of this “flame” time lag, as the time between reactant velocity fluctuations to the resultant heat release fluctuations is more a function of chemical kinetics than the impedance of the jet geometry. It was found that changes to the combustion model or variations in the reactant mass flow rate could cause shifts of the curve in the vertical direction, while the addition of strain to the combustion model resulted in a different slope altogether.

### Calculation of three-dimensional Rayleigh Index fields

One of the benefits of utilizing three-dimensional LES simulations is that the transient 3D fields are available for post-processing, as opposed to the limited data obtained from experimental diagnostics. The transient three-dimensional pressure and heat release fields from the simulations were utilized to calculate the Discrete Fourier Transform (DFT) of a three-dimensional Rayleigh Index field. This data resulted in a “mean” Rayleigh Index field, filtered at specific frequencies, providing an understanding of the driving and damping regions within each reaction zone at a given frequency.

The first step in this calculation was to create  $p'$  and  $q'$  fields from the pressure and heat release fields, respectively. This was done by simply subtracting the temporally averaged fields from a given simulation from the 3D pressure and heat release fields at each time step. Next, a DFT was taken of each fluctuating field at each cell throughout all time steps. This provided a real and imaginary component of each fluctuating quantity at each cell as a function of frequency. A Rayleigh field was defined as the complex conjugate of  $p'$  multiplied by the complex  $q'$ , or

$$rayleigh = \hat{p}'^c \cdot \hat{q}' = (\hat{p}'_{real} - \hat{p}'_{imag}) \cdot (\hat{q}'_{real} + \hat{q}'_{imag}) \quad (52)$$

Expanding the above expression and re-grouping by real and imaginary terms gives the following expression

$$rayleigh = rayleigh_{real} + rayleigh_{imag} \cdot i = (\hat{p}'_{real} \cdot \hat{q}'_{real} + \hat{p}'_{imag} \cdot \hat{q}'_{imag}) + (\hat{p}'_{real} \cdot \hat{q}'_{imag} - \hat{p}'_{imag} \cdot \hat{q}'_{real}) \cdot i \quad (53)$$

where the first and second terms represents the real and imaginary parts of the Rayleigh field, respectively. The amplitude and phase of the Rayleigh field are defined as

$$rayleighA = \sqrt{rayleigh_{real}^2 + rayleigh_{imag}^2}$$
(54)

and by the tangent half angle formula

$$rayleigh\Theta = 2 \tan^{-1} \left[ \frac{rayleigh_{imag}}{\sqrt{rayleigh_{real}^2 + rayleigh_{imag}^2} + rayleigh_{real}} \right] \cdot \frac{\pi}{180}$$
(55)

Finally, the Rayleigh Index field was determined as a function of the amplitude and phase of the Rayleigh field

$$rayleighIndex = rayleighA \cdot \cos\left(\frac{\pi \cdot rayleigh\Theta}{180}\right)$$
(56)

It is this Rayleigh Index field that is shown plotted in Figure 59 for the JICF configurations investigated in this study.

### **Modeling the jet in cross flow fuel nozzle**

A specially designed “engine-style” nozzle was used in the experimental rig testing that provided efficient mixing of the fuel and air feeding the reacting JICF. This nozzle was located between the manifold section and the converging section, or scoop, that led into the combustion chamber, as demonstrated in Figure 115.



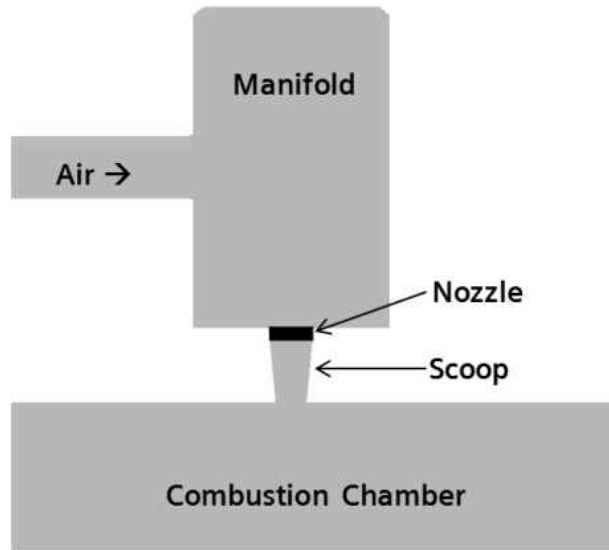


Figure 115: Schematic of air and fuel supply to reacting JICF

The JICF air supply was fed into the manifold before passing through the nozzle, while fuel was fed directly into the nozzle. Based on this setup, the air flow passing through the nozzle will fluctuate when exposed to acoustic oscillations, while the fuel flow can be assumed to be constant, due to the small contribution that it has on the overall equivalence ratio fluctuations. This relative contribution of the fuel fluctuations to the overall equivalence ratio fluctuations was calculated by linearizing the fuel and air mass flow rates for the JICF about their mean values to solve for the fluctuating components. The air mass flow rate through the nozzle is given as

$$\dot{m}_{air} = (\rho UA)_{air} \quad (57)$$

with the fluctuating quantity defined as

$$\dot{m}'_{air} = (\bar{\rho}u' + \bar{u}\rho')A = \bar{\rho}Au' \quad (58)$$

where the density fluctuations are assumed to be negligible, relative to the velocity fluctuations (see Table 9).

The fuel mass flow is approximated based on the fuel line pressure drop

$$\dot{m}_{fuel} = A_{nozzle} \sqrt{2(p_{fuelline} - p_{nozzle})} \rho_{fuel} \quad (59)$$

with the fluctuating quantity defined as

$$\dot{m}'_{fuel} = -\frac{1}{2} \frac{A_{nozzle} \sqrt{2\rho_{fuel}}}{\sqrt{p_{fuelline} - p_{nozzle}}} p'_{nozzle} \quad (60)$$

Using the fuel line and chamber dynamic pressure measurements from experiment, it was estimated that the air fluctuations through the nozzle contribute to more than 85% of the overall equivalence ratio fluctuations. Future development may include the fuel mass flow as a function of the fuel line pressure drop or impedance, however, for the purposes of this study, the fuel mass flow through the nozzle was assumed to be constant.

Thus, to avoid the expense of fully resolving the nozzle within the computational mesh, some simplifications were made so that the model would still be able to capture the effects of a partially premixed system without requiring mesh refinement more than five times higher than what was required in the region of the jet injection, where approximately 25-30 cells per diameter were used.

Instead of fully resolving the nozzle, a mixture fraction source term region was added immediately downstream of the nozzle location. A mass flow rate of fuel was added to the conservation equations through the cells in this region, based on the fuel flow rate in the rig tests.

This method allowed the air flow rate through the nozzle region to fluctuate while the fuel “flow” was held constant, resulting in physically realistic equivalence ratio fluctuations that would be expected in a partially premixed system. This mixture fraction source term is represented below and was applied within a pre-specified volume,  $V_{nozzle}$ , immediately downstream of the physical nozzle location. Here the fuel flow rate,  $m_{fuel}$ , is constant and equal to the value measured during the rig test.

$$\dot{f}_T = \frac{\dot{m}_{fuel}}{\int dV_{nozzle}} \quad (61)$$

This mixture fraction source term was added to the transport equation for the mixture fraction,

$$\frac{\partial(\bar{\rho} \tilde{f}_T)}{\partial t} + \frac{\partial(\bar{\rho} \tilde{u}_i \tilde{f}_T)}{\partial x_i} = \frac{\partial^2}{\partial x_i \partial x_i} \left( \bar{\rho} \bar{D} + \frac{\mu_T}{S_c} \tilde{f}_T \right) + \dot{f}_T \quad (62)$$

as well as the pressure equation (mass):

$$\frac{\partial \bar{\rho}}{\partial t} + \frac{\partial(\bar{\rho} \tilde{u}_i)}{\partial x_i} = \dot{f}_T \quad (63)$$

Contours of instantaneous mixture fraction for a representative partially premixed case compared to a perfectly premixed case are shown in Figure 116. Note that the scales are different for clarity.

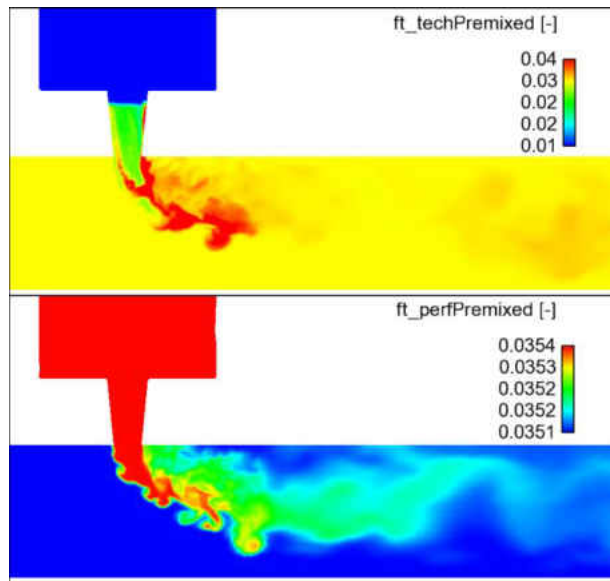


Figure 116: Contours of instantaneous mixture fraction, demonstrating the difference between a partially, or technically, premixed JICF and perfectly premixed JICF (note different scales for clarity).

It is evident that the partially premixed case contains no fuel upstream of the nozzle. At the location of the nozzle, the mixture fraction source term “injects” a constant rate of fuel into the conservation equations, while the air flow through this region is allowed to fluctuate due to the natural hydrodynamics of the flow. This explains why the partially premixed case shows a much larger range of mixture fraction in the region of the jet, where lean pockets are created where the local air flow is high and rich pockets are created where the local air flow is low. Conversely, the perfectly premixed case only introduces two constant mixture fractions, one from the cross flow and one from the jet flow. Mixing occurs in the combustion chamber between these two limits.

To understand the potential discrepancies in the fuel/air mixing that could be introduced by modeling the nozzle in this way, normalized contours of the mixture fraction at the exit of the

scoop are shown in Figure 117 for the JICF1 case in this study, compared to a RANS mixing study of only the honeycomb nozzle.

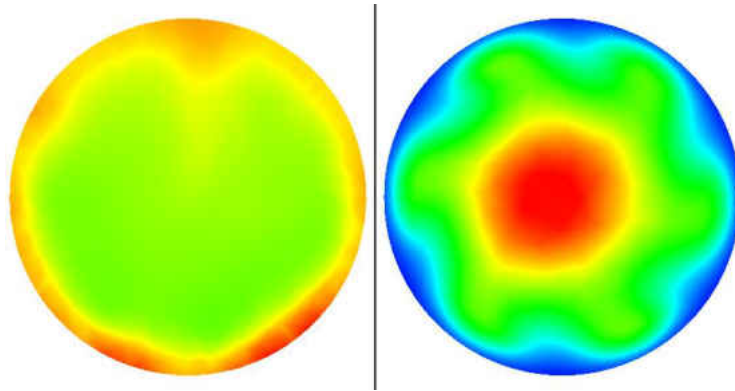


Figure 117: Normalized mixing profiles at scoop exit for JICF case with mixture fraction source term (left) and a honeycomb nozzle mixing study computed using CFX RANS (right).

Two primary differences are apparent in the mixing profiles. The first is that the JICF profile does not have the richer region in the center of the plane. This rich region in the actual nozzle is due to a fuel only passage that injects through the center of the nozzle. The second difference is that the JICF profile exhibits a rich region around the outside circumference of the scoop, while the actual nozzle exhibits a lean region around the outside circumference. This lean region is due to bypass air that flows around the outside of the honeycomb nozzle which was not accounted for in the JICF model. It is recommended that future work investigate the effect of this mixing profile on the overall flame time lag, as it could make a noticeable difference, depending on the combustion model begin applied. For the purposes of this report, however, the uniform profile was sufficient.

To check that energy was conserved with the new formulation of the mixture fraction source term, a simple energy balance was performed using the mean fields from the JICF1

simulation. The energy into the system included the energy from the air flow as well as the energy of the reacted fuel, assuming complete combustion. The energy out of the system included the heat loss through the walls of the geometry and a mass flow average of the temperature of the burnt gases exiting the domain, both calculated from the mean fields from the JICF1 simulation. This energy balance is represented by Equation (64).

$$\left(\dot{m}c_p T\right)_{inlets} + \dot{m}_{fuel}H_f = \left(\dot{m}c_p \bar{T}\right)_{outlet} + Q_{loss,walls} \quad (64)$$

It was found that the calculated energy out of the system (1017 kW) was in good agreement with the energy into the system (1053 kW), with an error less than 3.5%.

**APPENDIX C – DERIVATION OF HEAT RELEASE MODEL WITH  
STRAIN TERM**

A mathematical heat release model was developed from the governing equation for the unsteady heat release at the flame front of the jet. Based on the findings that the fluctuating strain field may be an important parameter in the instantaneous heat release fluctuation of the reacting JICF, an effective strain rate,  $\sigma$ , was added as a multiplier to the governing equation for the heat release. This effective strain rate was defined similar to the strain model from Tay, et al that was included in the LES combustion model, and represents the ratio between the strained and unstrained laminar flame speed (Tay, 2009). The only difference between the term included in the derivation of the heat unsteady release model and the term modeled in the LES simulations is that the heat loss parameter was assumed to be negligible in the derivation. This assumption was verified using LES. Thus, the relation for the instantaneous heat release at the flame front of the jet is defined as:

$$q(t) = Y \cdot \dot{m} \cdot H_f \cdot \frac{\sigma}{\bar{\sigma}} \quad (65)$$

where  $Y$  represents the fuel concentration,  $\dot{m}$  represents the jet mass flow rate,  $H_f$  represents the lower heating value of the fuel, and  $\sigma$  represents the effective strain rate. Here the effective strain rate is normalized by its mean value to ensure that the integral of the temporal heat release over time is solely a function of the fuel mass flow rate and heating value.

Three regions of importance were defined for the derivation of the local heat release fluctuation: the location of the fuel injection, the exit of the jet, and the flame front, as shown in Figure 118.



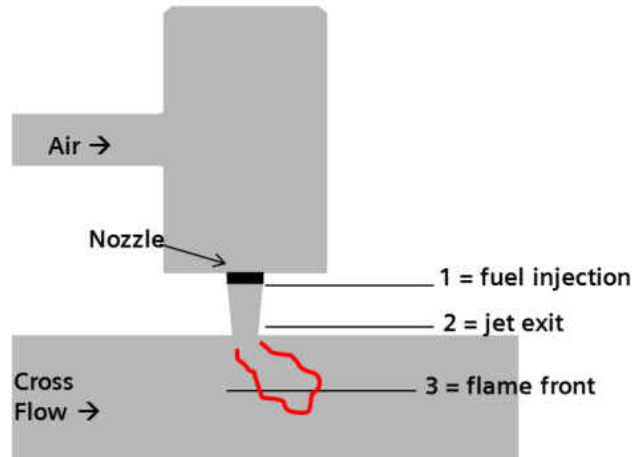


Figure 118: Regions defined for heat release derivation.

The instantaneous heat release is divided into a mean and fluctuating component and then linearized about the mean value to develop a function for the fluctuating heat release as a function of the fluctuating fuel concentration, mass flow rate, and effective strain rate:

$$q'(t) = [\bar{m} \bar{\sigma} H_f Y']_1 + [\bar{Y} \bar{\sigma} H_f \dot{m}']_2 + [\bar{Y} \cdot \bar{m} H_f \sigma']_3 \quad (66)$$

Here, the subscripts listed for each of these terms represents the location where the quantities are to be evaluated, as defined above in Figure 118. Note that Equation (66) has been multiplied through by the mean effective strain rate for the sake of consistency. Each of these terms are then expanded about their mean values and related to acoustic quantities.

The first term on the right hand side in Equation (66) is expanded by defining the fuel concentration as a function of the fuel and air mass flow rates, but for simplicity, neglecting the contribution of the fuel mass flow to the total mass flow:

$$Y = \frac{\dot{m}_f}{\dot{m}_f + \dot{m}_{air}} \approx \frac{\dot{m}_f}{\dot{m}_{air}} = \frac{\dot{m}_f}{\rho_{air} u_{air} A_{air}} \quad (67)$$

Here, the fuel mass flow rate is assumed to be constant based on the pressure drop that occurs across the fuel nozzle orifices and the resulting contribution of the fuel fluctuations to the equivalence ratio fluctuations. By linearizing about the mean air density and velocity, an expression for the fluctuating fuel concentration can be defined as a function of acoustic quantities:

$$Y' = \frac{-\dot{m}_f}{\bar{\rho}_{air} \bar{u}_{air} A_{air}} \left( \frac{u'_{air}}{\bar{u}_{air}} \right) - \frac{\dot{m}_f}{\bar{\rho}_{air} \bar{u}_{air} A_{air}} \left( \frac{\rho'_{air}}{\bar{\rho}_{air}} \right) = \frac{-\bar{Y}}{\bar{u}_{air}} u'_{air} - \frac{\bar{Y}}{\bar{\rho}_{air}} \rho'_{air} \quad (68)$$

Assuming isentropic flow, the density fluctuations can be related to the pressure fluctuations, giving the following expression for the fluctuating fuel concentration:

$$Y' = \frac{-\bar{Y}}{\bar{u}_{air}} u'_{air} - \frac{\bar{Y}}{\bar{\rho}_{air} c_{air}^2} p'_{air}$$

It is assumed that the second term in Equation (68) can be neglected, as this term is several orders of magnitude lower than the velocity term (this assumption was verified previously). Thus, an expression for the fluctuating fuel concentration can be substituted into the first term in Equation (66),

$$\bar{\dot{m}} \bar{\sigma} H_f Y' = \frac{-\bar{\dot{m}} \bar{\sigma} H_f \bar{Y}}{\bar{u}_{air}} u'(t - \tau_{injection}) \quad (69)$$

where these terms are evaluated at the location of fuel injection, or region 1 in Figure 118.

The second term in Equation (66) is expanded by linearizing the mass flow rate about its mean value to develop an expression for the fluctuating mass flow rate:

$$\bar{Y}\bar{\sigma}H_f\dot{m}' = \bar{Y}\bar{\sigma}H_f(\rho'\bar{u}A_{jet} + \bar{\rho}u'A_{jet}) \quad (70)$$

Assuming isentropic flow, the density fluctuation can again be related to the pressure fluctuation, resulting in a relation for the fluctuating mass flow rate as a function of acoustic quantities:

$$\dot{m}' = \left( \frac{p'\bar{u}A_{jet}}{c^2} + \bar{\rho}u'A_{jet} \right) \quad (71)$$

Again, the pressure term in Equation (71) is several orders of magnitude lower than the velocity term, and thus, the fluctuating mass flow rate can be approximated as:

$$\dot{m}' \approx \bar{\rho}u'A_{jet} \quad (72)$$

The second term in Equation (66) then becomes:

$$\bar{Y}\bar{\sigma}H_f\dot{m}' = \bar{Y}\bar{\sigma}\bar{\rho}A_{jet}H_f u'(t - \tau_{jet}) \quad (73)$$

where these quantities are evaluated at the jet exit, or region 2 in Figure 118.

The third term in Equation (66) is expanded by linearizing the expression used to model the effective strain rate from Tay et al, which was defined previously as:

$$\sigma = \frac{S_L}{S_L^0} = \exp(-Ka(Ma - \chi)) \quad (74)$$

As verified with LES, the heat loss term,  $Ka\chi$ , can be neglected, as it has a much smaller impact on the fluctuating heat release than the corresponding strain term. The Markstein number is calculated using a 1D counterflow model as described previously.

Here, the Karlovitz number,  $Ka$ , which represents the ratio between the chemical and turbulent timescales, is defined as,

$$Ka = \frac{\alpha\kappa}{S_L^{02}} \quad (75)$$

where  $\alpha$  represents the thermal diffusivity and  $\kappa$  represents the strain rate. By neglecting the heat loss term and linearizing about the mean strain rate, an expression for the fluctuating effective strain rate can be derived from Equation (74):

$$\sigma' = -\frac{\alpha Ma}{S_L^{02}} \exp\left(-\frac{\alpha\bar{\kappa}Ma}{S_L^{02}}\right) \kappa' \quad (76)$$

Relating this expression to acoustic quantities is not as straightforward as the previous terms, however, it was assumed that the fluctuating strain rate is proportional to the acoustic velocity, divided by a length scale:

$$\kappa' \propto \frac{u'}{\ell} \quad (77)$$

To confirm the validity of this assumption, as well as to determine an appropriate length scale, the transient LES data was used to compare the fluctuating strain field at the flame front to the fluctuating velocity field in this same region. This comparison was done by creating an

isosurface of reaction progress variable at 0.1 (representing the flame front) and averaging both the fluctuating strain magnitude as well as the fluctuating velocity magnitude over this isosurface at each timestep. A representative image of the flame front isosurface, colored by the strain magnitude, is shown in Figure 119.

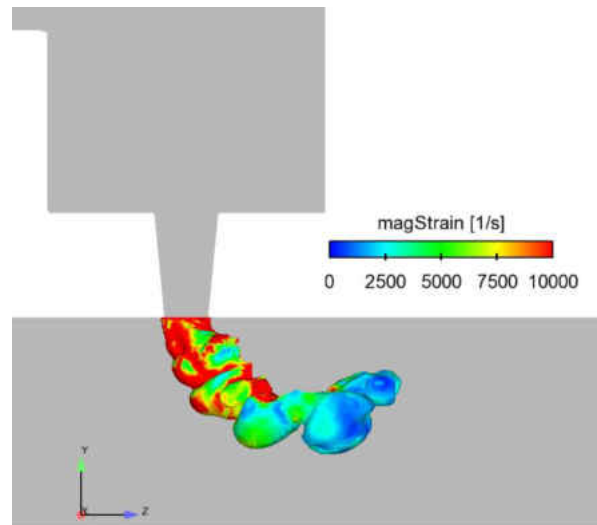


Figure 119: Representative instantaneous isosurface of reaction progress variable at 0.1, used to calculate fluctuating strain and velocity fields at the flame front. Colored by strain magnitude.

The fluctuating quantities from these calculations are plotted below in Figure 120, where the velocity fluctuations are scaled by one-quarter of the jet exit diameter. It was found that this length scale provided a good correlation between the fluctuating strain and velocity at the flame front.

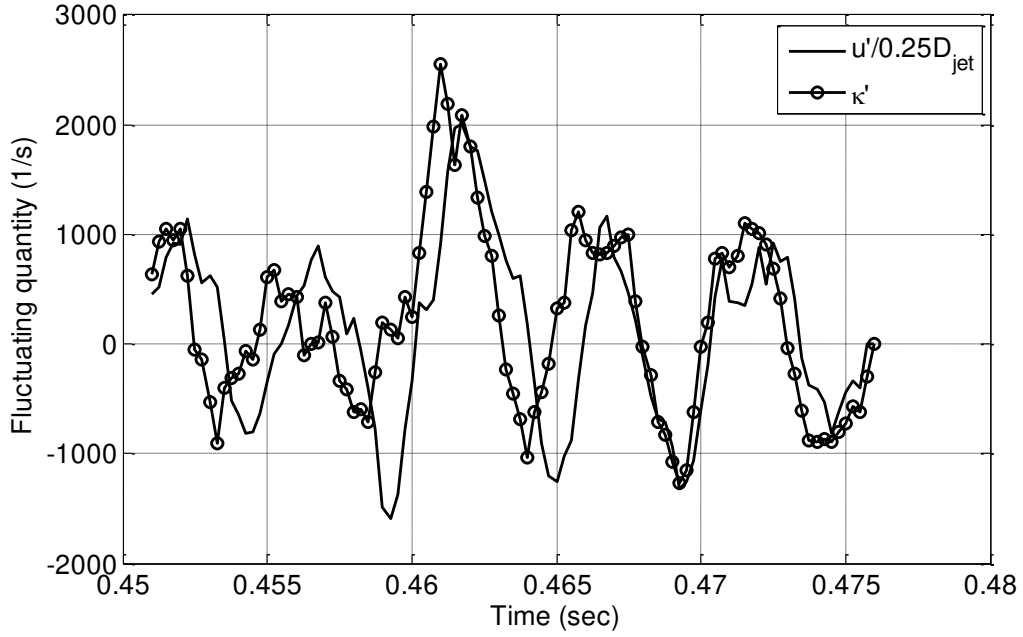


Figure 120: Fluctuating strain and scaled velocity fields, used verify to proportionality between fluctuating strain and acoustic velocity.

It is evident that there is a proportionality between the fluctuating strain and the acoustic velocity scaled by one-quarter of the jet diameter. This provided a relation between the fluctuating strain rate and the acoustic velocity, which was then applied to the third term in Equation (66):

$$\bar{Y} \cdot \bar{m} H_f \sigma' = -\bar{Y} \cdot \bar{m} H_f \left[ \frac{\alpha Ma}{S_L^{0^2}} \exp\left(-\frac{\alpha \bar{\kappa} Ma}{S_L^{0^2}}\right) \right] \frac{u'(t - \tau_{strain})}{\ell} \quad (78)$$

For the JICF, these quantities are evaluated at the flame front, or region 3 in Figure 118. Based on the scaling procedure shown in Figure 120, the length scale was taken as one-quarter of the jet exit diameter.

Substituting Equations (69), (73), and (78) back into Equation (66) produces a final expression for the instantaneous heat release fluctuation of the JICF, as a function of acoustic quantities:

$$q'(t) = \left[ \frac{-\bar{m}\bar{\sigma}H_f\bar{Y}}{\bar{u}_{air}} u'(t - \tau_{injection}) \right]_1 + \left[ \bar{Y}\bar{\sigma} \cdot \bar{\rho}A_{jet}H_f u'(t - \tau_{jet}) \right]_2 - \left[ \bar{Y} \cdot \bar{m}H_f \left[ \frac{\alpha Ma}{S_L^{0.2}} \exp\left(-\frac{\alpha\bar{\kappa}Ma}{S_L^{0.2}}\right) \right] \frac{u'(t - \tau_{strain})}{\ell} \right]_3 \quad (79)$$

Note that the subscripts listed for each of these terms represent the location where the quantities are to be evaluated, as defined above in Figure 118. A summary of the assumptions made in deriving this model is provided below:

- Reacting JICF can be assumed to be a “thin” flame, with respect to the chamber acoustic wavelengths of interest (jet flame length is less than 1% of 2L wavelength)
- Isentropic flow
- Density/pressure terms can be neglected (see Table 9)
- Heat loss parameter in strain model can be neglected (based on LES simulations with and without heat loss parameter)
- The contribution of the jet fuel mass flow to the total jet flow can be neglected (fuel mass flow is ~ 3% of total jet flow)
- Jet fuel mass flow is constant (based on pressure drop across the nozzle orifices and resultant contribution to equivalence ratio fluctuations of less than 15%)
- Fluctuating strain is proportional to the acoustic velocity divided by a length scale equal to one-quarter of the jet exit diameter (see Figure 120)

## LIST OF REFERENCES

- Fric, T.F., Roshko, A., "Vortical Structure in the Wake of a Transverse Jet", *Journal of Fluid Mechanics*, Vol. 279, pp. 1-47, 1994.
- Karagozian, A., "Transverse Jets and their Control", *Progress in Energy and Combustion Science*, Vol. 36, pp. 531-553, 2010.
- Kelso, R.M., Lim T.T., Perry, A.E., "An Experimental Study of Round Jets in Cross Flow", *Journal of Fluid Mechanics*, Vol. 306, pp. 111-144, 1996.
- Smith, S.H., Mungal, M.G., "Mixing, Structure, and Scaling of the Jet in Cross Flow", *Journal of Fluid Mechanics*, Vol. 357, pp.83-122, 1998.
- Cortelezzi, L., Karagozian, A.R., "On the Formation of the Counter-Rotating Vortex Pair in Transverse Jets", *Journal of Fluid Mechanics*, Vol. 446, pp. 347-373, 2001.
- Baker, C.J., "The Turbulent Horseshoe Vortex", *Journal of Wind Engineering and Industrial Aerodynamics*, Vol. 6, pp. 9-23, 1980.
- Kelso, R., Smits, A., "Horseshoe Vortex Systems Resulting from the Interaction between a Laminar Boundary Layer and a Transverse Jet", *Physics of Fluids*, Vol. 7, pp. 153-158, 1995.
- Muppidi, S., Mahesh, K., "Direct Numerical Simulation of Round Turbulent Jets in Cross Flow", *Journal of Fluid Mechanics*, Vol. 574, pp.59-84, 2007.
- Alves, L.S., "Transverse Jet Shear Layer Instabilities: Linear Stability Analysis and Numerical Simulations. PhD Thesis. University of California, Los Angeles, Department of Mechanical and Aerospace Engineering, March 2006.
- Bagheri, S., Schlatter, P., Schmid, P.J., Henningson, D.S., "Global Stability of a Jet in Cross Flow", *Journal of Fluid Mechanics*, Vol. 624, pp. 33-44, 2009.
- Pratte, S.D., Baines, W.D., "Profiles of the Round Turbulent Jet in a Cross Flow", *Journal of Hydraulics Division ASCE*, Vol. 92, pp. 53-64, 1967.
- Hasselbrink, E., Mungal, M.G., "Transverse Jets and Jet Flames. Part 1. Scaling Laws for Strong Transverse Jets", *Journal of Fluid Mechanics*, Vol. 443, pp. 1-25, 2001.
- Hasselbrink, E., Mungal, M.G., "Transverse Jets and Jet Flames. Part 2. Velocity and OH Field Imaging", *Journal of Fluid Mechanics*, Vol. 443, pp. 27-68, 2001.
- Kadota, T., Wang, J.X., Kawaoka, T., "Structure of Propane Jet Diffusion Flame in a Cross Flow", *JSME International Journal Series II*, Vol. 33, pp. 575-581, 1990.



- Ronald, M., So, C., Ahmed, S. A., “Characteristics of Dump Combustor Flows”, *International Journal of Heat and Fluid Flow*, Vol. 10, No. 1, pg. 66-74, 1989.
- Pitz, R.W., Daily, J.W., “Combustion in a turbulent mixing layer formed at rearward facing step”, *AIAA Journal*, Vol. 21, pp. 1565-1570, 1983.
- Ahmed, S. A., Nejad, A. S., “Premixed Turbulent Combustion of Axisymmetric Sudden Expansion Flows”, *International Journal of Heat and Fluid Flow*, Vol. 13, No. 1, pg. 15-21, 1992.
- Schadow, K.C., Gutmark, E., “Combustion Instability Related to Vortex Shedding in Dump Combustors and their Passive Control”, *Progress in Energy and Combustion Science*, Vol 18, pp. 117-132, 1991.
- Rayleigh, J.W.S., “The Theory of Sound”, *Dover Publications*, New York, 1945.
- Smith, D.A., Zukoski, E.E., AIAA Paper 85-1248, 1985.
- Sterling, J.D., Zukoski, E.E., AIAA Paper 87-0220, 1987.
- Roux, A., Gicquel, L., Reichstadt, S., Bertier, N., Staffelbach, G., Vuillot, F., Poinso, T. “Analysis of Unsteady Reacting Flows and Impact of Chemistry Description in Large Eddy Simulations of Side-Dump Ramjet Combustors”, *Combustion and Flame*, Vol. 157, pp. 176-191, 2010.
- Wolf, P., Staffelbach, G., Roux, A., Gicquel, L., Poinso, T., Moureau, V., “Massively Parallel LES of Azimuthal Thermo-Acoustic Instabilities in Annular Gas Turbines”, *C.R. Mecanique*, Vol. 337, pp. 385-394, 2009.
- Roux, S., Lartigue, G., Poinso, T., Meier, U., Berat, C., “Studies of Mean and Unsteady Flow in a Swirled Combustor Using Experiments, Acoustic Analysis, and Large Eddy Simulations”, *Combustion and Flame*, Vol. 141, pp. 40-54, 2005.
- Staffelbach, G., Gicquel, L., Boudier, G., Poinso, T., “Large Eddy Simulation of Self Excited Azimuthal Modes in Annular Combustors”, *Proceedings of the Combustion Institute*, Vol. 32, pp. 2909-2916, 2009.
- Xia, G., Harvazinski, M., Anderson, W., Merkle, C.L., “Investigation of Modeling and Physical Parameters on Instability Prediction in a Model Rocket Combustor”, 47<sup>th</sup> *AIAA/ASME/SAE/ASEE Joint Propulsion Conference and Exhibit*, San Diego, 2011.
- Lorstad, D., Lindholm, A., Alin, N., Fureby, C., “Experimental and LES Investigation of a SGT-800 Burner in a Combustion Rig”, *Proceedings of the ASME Turbo Expo*, Glasgow, 2010.
- Beck, C., “LES Combustion Modeling Peer Review”, Internal Report, Siemens Energy, Inc. 2009.
- Jemcov, Aleksander. “Re: training follow up questions.” E-mail to Jared Pent. 7 June, 2011.

- Poinsot, T., Veynante, D., "Theoretical and Numerical Combustion", RT Edwards Inc, Philadelphia, 2005.
- Derksen, M., "On the Influence of Steam on Combustion", PhD Thesis, University of Twente, 2005.
- Bradley, D., Lau, A.K.C., Lawes, M., "Flame Stretch Rate as a Determinant of Turbulent Burning Velocity", *Philosophical Transactions: Physical Sciences and Engineering*, Vol. 338, No 1650, pp. 359-337, 1992.
- Beck, C. "Documentation of OpenFOAM Combustion Model", Internal Report, Siemens Energy, Inc. 2010.
- Stokes ARCC "High Performance Computing IBM Stokes Cluster", University of Central Florida, <http://stokes.ist.ucf.edu> May 09, 2014.
- SGI, Inc. "Mesh generation with the snappyHexMesh utility", <http://www.openfoam.com/docs/user/snappyHexMesh.php> Oct. 15, 2011.
- Smith, R., "Computational Modeling of a High Frequency Combustion Instability in a Single Element Liquid Rocket Engine", MS Thesis. Purdue University. 2006.
- MediaWiki, "HowTo Using the Wave Transmissive Boundary Condition", 4. [http://openfoamwiki.net/index.php/HowTo\\_Using\\_the\\_WaveTransmissive\\_Boundary\\_condition](http://openfoamwiki.net/index.php/HowTo_Using_the_WaveTransmissive_Boundary_condition) Oct. 15, 2011.
- Panhandle Energy, "Pandhandle Eastern Pipe Line Company, LP", 11. <http://infopost.panhandleenergy.com/InfoPost/jsp/frameSet.jsp?pipe=pepl> Oct. 15, 2011.
- Sisco, J.C., Yu, Y.C., Sankaran, V., Anderson, W.E., "Examination of Mode Shapes in an Unstable Model Combustor", *Journal of Sound and Vibration*, Vol. 330, 2011.
- Fugger, C., Anderson, W., Pent, J., Krebs, W., Portillo, E., "Investigation of a Pre-mixed Reacting Jet in an Unstable Transverse Flow Field", 47th AI-AA/ASME/SAE/ASEE Joint Propulsion Conference and Exhibit, San Diego, 2011.
- Gentemann, A., Hirsch, C., Kunze, K., Kiesewetter, F., Sattelmayer, T., Polifke, W., "Validation of flame transfer function reconstruction for perfectly premixed swirl flames", *Proceedings ASME Turbo Expo, GT2004-53776*, Vienna, 2004.
- Crocco, L., "Aspects of Combustion Stability in Liquid Propellant Rocket Motors .1. Fundamentals - Low Frequency Instability with Monopropellants," *Journal of the American Rocket Society*, Vol. 21, No. 6, 1951, pp. 163-178.
- Martin, C.E., Benoit, L., Sommerer, Y., "Large-Eddy Simulation and acoustic analysis of a swirled staged turbulent combustor", *AIAA Journal*, Vol. 44, No. 4, 2006, pp. 741-750.
- Siemens Energy, "Gas Turbine SGT5-8000H", <http://www.energy.siemens.com/hq/en/power-generation/gas-turbines/sgt5-8000h.htm#content=Technical%20Data> Oct. 15, 2011

- Ibrahim, Z.M., Williams, F.A., Buckley, S.G., “A Review of Previous Studies of Oscillatory Combustion in Gas Turbines”, University of California – Progress Report, San Diego, 2005.
- SGL, Inc. “OpenFOAM: The open source CFD toolbox”, <http://www.openfoam.com> Oct. 15, 2011.
- Spalart, P.R., Allmaras, S.R., “A One-Equation Turbulence Model for Aerodynamic Flows”, *Recherche Aerospatiale*, Vol. 1, pp. 5-21, 1994.
- Portillo, J.E., Sisco, J.C., Yu, Y., Anderson, “Application of a Generalized Instability Model to a Longitudinal Mode Combustion Instability”, *43<sup>rd</sup> AIAA/ASME/SAE/ASEE Joint Propulsion Conference and Exhibit*, Cincinnati, 2007.
- Portillo, J.E., Sisco, J.C., Corless, M.J., Anderson, W.E., and Sankaran, V., “Generalized Combustion Instability Model”, *42<sup>nd</sup> AIAA/ASME/SAE/ASEE Joint Propulsion Conference and Exhibit*, Sacramento, 2006.
- Noble, D.R., Dubsy, S., Periagaram, K., Sullivan, R., Jones, M., Seitzman, J., Lieuwen, T., “Imaging of a Reacting Fuel Jet in 6 Atm Vitiated Cross Flow”, *7<sup>th</sup> US National Combustion Meeting of the Combustion Institute*, Atlanta, 2011.
- Lam, K.M., Xia, L.P., “Experimental simulation of a vertical round jet issuing into an unsteady cross flow”, *Journal of Hydraulic Engineering*, Vol. 127, pp. 369-379, 2001.
- Xia, L.P., Lam, K.M., “Unsteady Effluent Dispersion in a Round Jet Interacting with an Oscillating Cross Flow”, *Journal of Hydraulic Engineering*, Vol. 130, pp. 667-677, 2004.
- Blossey, P.N., Narayanan, S., Bewley, T.R., “Dynamics and Control of Jets in Cross Flow”, *IUTAM Symposium on Turbulent Mixing and Combustion*, Chapter 1, pp. 1-10, 2002.
- Versteeg, H.K., Malalasekera, W., "An Introduction to Computational Fluid Dynamics: The Finite Volume Method", Longman, 1995.
- Govert, S., “Analysis of Unsteady Flow Phenomena in Gas Turbine Combustion Systems Based on Large Eddy Simulations”, Masters Thesis, Institute of Fluid Dynamics and Thermodynamics, 2011.
- Krediet, H., “Prediction of Limit Cycle Pressure Oscillations in Gas Turbine Combustion Systems using the Flame Describing Function”, PhD Thesis, University of Twente, 2012.
- Munjal, M.L., Doige, A.G., “The two-microphone method incorporating the effects of mean flow and acoustic damping”, *Journal of Sound and Vibration*, Vol. 137, pp. 135-138, 1990.
- ISO 10534-2:1998 – Acoustics, “Determination of sound absorption coefficient and impedance in impedance tubes – Part 2: Transfer-function method”, 1998.
- Lamarque, N., Poinot, T., “Boundary conditions for acoustic eigenmode computations in gas turbine combustion chambers”, *AIAA Journal*, Vol. 46, pp. 2282-2292, 2008.

- Tay, L., Chong, W., Komarek, T., Zellhuber, M., Lenz, J., Hirsch, C., Polifke, W., "Influence of strain and heat loss on flame stabilization in a non-adiabatic combustor", *Proceedings of the European Combustion Meeting*, 2009.
- Doost, S., "Validation and application of a CFD based tool for the prediction of carbon monoxide emissions in a gas turbine combustion system using tabulated chemistry", Master's Thesis, Technical University of Darmstadt, 2013.
- Johnson, P., "Thermoacoustic Riemann Solver Finite Volume Method with Application to Turbulent Premixed Gas Turbine Combustion Instability", Master's Thesis, University of Central Florida, 2013.
- Lyons, K. M., "Toward an understanding of the stabilization mechanisms of lifted turbulent jet flames: Experiments", *Progress in Energy and Combustion Science*, Vol. 33, pp. 211-231, 2007.
- Hallum, Z., "The Use of Proper Orthogonal Decomposition in the Research of Combustion Instability", Master's Thesis, Purdue University, 2012.
- O'Connor, J. and T. Lieuwen, "Disturbance Field Characteristics of a Transversely Excited Burner," *Combustion Science and Technology*, p. 427-443. 2011.
- O'Connor, J. and T. Lieuwen, "Further Characterization of the Disturbance Field in a Transversely Excited Swirl-Stabilized Flame," *Journal of Engineering for Gas Turbines and Power*, 2012.
- Schlegel, F., Ghoniem, A., "Simulation of a high Reynolds number reactive transverse jet and the formation of a triple flame", *Combustion and Flame*, 2013.
- Megerian, S., Davitian, J., Alves, L., Karagozian, A., "Transverse jet shear layer instabilities. Part 1. Experimental studies.", *Journal of Fluid Mechanics*, Vol. 593, pp93-129, 2007.
- Krebs, W., Walz, G., Hoffmann, S., "Thermoacoustic analysis of annular combustor", *5<sup>th</sup> AIAA Aeroacoustics Conference*, AIAA 99-1971, 1999.
- Weller, H. G., Tabor, G., Gosman, A. D., Fureby, C., "Application of a Flame-Wrinkling LES Combustion Model to a Turbulent Mixing Layer", *27th International Symposium on Combustion/The Combustion Institute*, pp. 899-907, 1998.
- Tabor, G., Weller, H. G., "Large Eddy Simulation of Premixed Turbulent Combustion Using Flame Surface Wrinkling Model", *Flow Turbulence and Combustion*, Vol. 72, pp. 1-28, 2004.
- Di Domenico, M., Beck, C., Lammel, O., Krebs, W., Noll, B., "Experimental and Numerical Investigation of Turbulent, Lean, High-Strained, Confined, Jet Flames", *49th AIAA Aerospace Sciences Meeting*, Orlando, 2011.